

## Fouling in Membrane Processes for Water Treatment

Jafari Eshlaghi, M.

**DOI**

[10.4233/uuid:3fdd3c36-38cc-4e38-a5ac-c6445c4857d5](https://doi.org/10.4233/uuid:3fdd3c36-38cc-4e38-a5ac-c6445c4857d5)

**Publication date**

2021

**Document Version**

Final published version

**Citation (APA)**

Jafari Eshlaghi, M. (2021). *Fouling in Membrane Processes for Water Treatment*. [Dissertation (TU Delft), Delft University of Technology, Universiteit Gent]. <https://doi.org/10.4233/uuid:3fdd3c36-38cc-4e38-a5ac-c6445c4857d5>

**Important note**

To cite this publication, please use the final published version (if applicable). Please check the document version above.

**Copyright**

Other than for strictly personal use, it is not permitted to download, forward or distribute the text or part of it, without the consent of the author(s) and/or copyright holder(s), unless the work is under an open content license such as Creative Commons.

**Takedown policy**

Please contact us and provide details if you believe this document breaches copyrights. We will remove access to the work immediately and investigate your claim.

# **Fouling in Membrane Processes for Water Treatment**



# **Fouling in Membrane Processes for Water Treatment**

Dissertation

for the purpose of obtaining the degree of doctor

at Delft University of Technology

by the authority of the Rector Magnificus Prof.dr.ir. T.H.J.J.van der Hagen,

chair of the Board for Doctorates

to be defended publicly on

Thursday 7 October 2021 at 10:00 o'clock

by

**Mohammadreza JAFARI ESHLAGHI**

Master of Science in Chemical Engineering, University of Bologna, Italy

born in Tehran, Iran



This dissertation has been approved by the promotor.

Composition of the doctoral committee:

Rector Magnificus	chairman
Prof.dr.dr.h.c.ir. M.C.M. van Loosdrecht	Delft University of Technology, Promotor
Prof.dr.ir. C. Picioreanu	Delft University of Technology, Promotor
Prof.dr.ir. A.R.D. Verliefde	Ghent University, Promotor

Independent members:

Prof.dr. M.D. Kennedy	Delft University of Technology
Prof.dr.ir. E. Meers	Ghent University
Prof. dr. M. Elimelech	Yale university
Prof. dr.ir. W.G.J. van der Meer	University of Twente
Prof.dr.ir. L.C. Rietveld	Delft University of Technology, <i>reserved</i>



This doctoral research has been carried out in the context of agreement on joint doctoral supervision between Ghent University, Belgium and Delft University of Technology, the Netherlands.

Printed by: ProefschriftMaken || [www.proefschriftmaken.nl](http://www.proefschriftmaken.nl)

Copyright © 2021 by M. Jafari Eshlaghi

ISBN 978-94-6423-472-5

# Table of Contents

<b>Summary</b>	<i>i</i>
<b>Samenvatting</b>	<i>iii</i>
<b>Chapter 1</b> General Introduction	<b>1</b>
<b>Chapter 2</b> Effect of biofilm structural deformation on hydraulic resistance during Ultrafiltration	<b>15</b>
<b>Chapter 3</b> Biofilm compressibility in ultrafiltration: A relation between biofilm morphology, mechanics and hydraulic resistance	<b>39</b>
<b>Chapter 4</b> A Comparison Between Chemical Cleaning Efficiency in Lab-scale and Full-Scale Reverse Osmosis Membranes	<b>61</b>
<b>Chapter 5</b> Bringing laboratory to full-scale RO installation: A novel approach for membrane fouling analysis and CIP protocol development	<b>79</b>
<b>Chapter 6</b> Cost of fouling in full-scale RO & NF installations in The Netherlands	<b>95</b>
<b>Chapter 7</b> A techno-economic analysis of fit-for-multi-purpose Effluent Reclamation Plant (ERP)	<b>119</b>
<b>Chapter 8</b> Conclusions & outlook	<b>145</b>
<b>Supplementary Information</b>	<b>155</b>
<b>List of Abbreviations</b>	<b>185</b>
<b>References</b>	<b>187</b>
<b>Acknowledgments</b>	<b>207</b>
<b>List of Publications</b>	<b>209</b>
<b>Curriculum vitae</b>	<b>210</b>



# Summary

Membranes are widely applied in water and waste water treatment as they provide an absolute barrier against the contaminants. Membranes are offered in wide pore size range and they are applied vastly due to their versatile and cost effective operation in dealing with wide range of streams. However, membranes, like any other filtration systems, suffer from fouling. Fouling layer, accumulation of rejected materials over time on membrane surface, is often called the main bottleneck of membrane processes. Fouling formation reduces water flux, increases energy consumption and leads to the early membrane replacement.

To better control and mitigate fouling layer formation, better understanding of fouling mechanism and properties are required. Fouling properties can be categorized into hydraulic properties, mechanical properties, structural properties, chemical properties. These properties can be impacted by operational conditions, feed water quality and membrane properties. Moreover, these properties influence membrane performance parameters such as water flux, energy consumption and eventually the plant expenses. Therefore, the fouling properties, their inter-relations, their impacts on performance parameters should be further studied. We used novel modelling techniques and experimental measurements in laboratory and full-scale plants to study fouling properties and their impacts on membrane performance parameters. We also discussed the opportunities and challenges for future fouling study.

**Chapter 2.** To evaluate the relation between structural, hydraulic and mechanical properties of fouling layer in the membrane systems, a novel method to extract these properties was developed to extract fouling properties in a non-destructive and in-situ technique. The performance parameters of a dead-end UF system with integrated OCT imaging (in-situ) was coupled with a fully-coupled fluid-structural interaction (FSI) model. The dead-end UF was operated under a compression-relaxation cycle to evaluate how fouling properties changes under different applied pressure. Several mechanical models were evaluated to find the most suitable mechanical model to explain the fouling layer behaviour under compression-relaxation cycle in the dead-end UF.

The results indicate that the hydraulic resistance of homogeneous biofilms under UF was much more affected by change in permeability than by the fouling layer thickness. Interestingly, we also found that even a poroelastic model (relatively simple model) can fairly good explain behaviour of the fouling layer in this study under different applied pressures. Compression of the fouling layer in UF systems can significantly increase hydraulic resistance of the membrane systems. In **Chapter 2**, a new technique was developed to extract fouling properties of the smooth surface biofilms. In **Chapter 3** the new technique was further expanded to extract the mechanical properties of rough surface fouling layer under dead-end UF. We observed for the fouling layer which is fed with real surface water (i.e., river water), a dual-layer fouling structure with a thin and dense base layer and a thick and porous top layer could best explain the observed results. We also introduced a new fouling structure indicator, the fraction of exposed base layer, as a good indicator in the determination of water flux in UF systems.

In *Chapter 4* the chemical properties of fouling layer (e.g., composition) and their impacts on chemical cleaning efficiency in Reverse Osmosis (RO) systems were evaluated. Chemical cleaning protocols (often referred as CIP protocols) are usually developed under laboratory conditions (synthetic feed water, short-term experiments) and then are applied in the full-scale RO installations. This often leads to significant differences in CIP efficiency in the lab and full-scale installations. Thus, we compared the fouling layer properties and CIP efficiency of typical laboratory conditions RO and several full-scale RO plants. The results show that CIP efficiency in the full-scale RO plants are much lower than lab conditions RO. Later, we correlated such differences in CIP efficiency to their significantly different extracellular polymeric substance (EPS) properties. The EPS extracted from lab RO had different composition and adherence properties than the EPS extracted from full-scale RO. Therefore, we concluded that CIP protocols should not be developed under lab conditions. In the *Chapter 5* we suggested a new method to better develop CIP protocols and study fouling properties with more industrial applications. We installed several new RO modules in the full-scale installation and they were operated for 30 days under identical conditions as the full-scale installation. Later, the fouling properties and CIP efficiency (in-situ measurement of permeability and pressure drop recovery) were compared between new RO modules (after 30 days of operation) and old RO modules (>2 years of operations). The new proposed fouling simulation method show promising results in both CIP efficiency results and fouling properties.

Although fouling is inevitable part of filtration processes, its economic impacts on membrane systems is not well evaluated. In *Chapter 6* cost of fouling in several RO and NF systems in The Netherlands has been calculated using plant performance data. All the cost factors contributing to cost of fouling such as CIP cost, energy cost, down cost were considered. We observed that for the RO plants, around a quarter of OPEX is caused by fouling, as oppose of around 10% for anoxic NF plants. The most important factor in the cost of fouling was considered the early membrane replacement cost, followed closely by additional energy cost. CIP costs have a minor contribution to the overall cost of fouling.

Reuse of municipal wastewater effluent is part of solution to deal with water scarcity challenges. In *Chapter 7* a fit-for-purpose approach to water reuse was proposed. We developed full techno-economic analysis on membrane-based Water reuse plant for municipal wastewater treatment effluent in the Netherlands. The impact of fouling and its properties and fouling cost have been integrated in all the membrane systems. A novel approach on design of water reuse plant has been offered to not only inherently reduce fouling impact but also increase plant robustness and water recovery. In *chapter 8* a summarized and generalized conclusions of the previous chapters is presented. We also presents our suggestions and opportunities for the future membrane and fouling research.

# Samenvatting

Membranen worden op grote schaal toegepast bij de behandeling van afvalwater en het zuiveren van proces- en drink-water omdat zij een barrière vormen tegen verontreinigende stoffen. Membranen hebben, net als alle andere filtratiesystemen, te lijden onder vervuiling. De ophoping van materialen die worden tegengehouden door het membraanoppervlak leiden tot een vervuilingslaag. Deze laag is veelal het belangrijkste knelpunt van membraanprocessen omdat de waterdoorstroming wordt verminderd, hetgeen leidt tot verhoogd energieverbruik en vroegtijdig vervanging van het membraan.

Om meer controle te krijgen over de vorming van deze vervuilingslaag is een beter begrip nodig van (i) de mechanismes die aan de vervuiling ten grondslag liggen en (ii) de eigenschappen van de vervuilingslaag. De kenmerken en samenstelling van de vervuilingslaag hangen nauw samen met de operationele omstandigheden van het filtratieproces, de kwaliteit van het instromende water, en de membraaneigenschappen. De eigenschappen van de vervuilingslaag kunnen worden onderverdeeld in vier categorieën: hydraulische, mechanische, structurele en chemische eigenschappen. Tezamen beïnvloeden deze eigenschappen de prestaties van het membraan, zoals de waterdoorstroming, het energieverbruik en uiteindelijk de installatiekosten. Daarom moeten de vervuilingseigenschappen, hun onderlinge relaties en hun invloed op de prestatieparameters verder bestudeerd worden. We hebben nieuwe modelleringstechnieken en experimentele metingen in laboratorium opstellingen en installaties op grote schaal gebruikt om de vervuilingseigenschappen en hun impact op de membraan prestaties te bestuderen. Verder bespreken we ook de mogelijkheden en uitdagingen voor voortvloeiend onderzoek naar vervuiling.

Om de relatie tussen structurele, hydraulische en mechanische eigenschappen van de vervuilingslaag in membraansystemen te evalueren, werd een nieuwe methode ontwikkeld om deze eigenschappen te bepalen in een niet-destructieve en *in-situ* techniek. De prestatieparameters van een afgesloten ultrafiltratie (“dead-end” UF) systeem met geïntegreerde (*in-situ*) optische coherentietomografie (OCT) werden gekoppeld aan een vloeistof-structuur interactie model (Fluid-structure Interaction: FSI).

Het afgesloten UF-systeem werd uitgevoerd onder een compressie-relaxatie cyclus om te evalueren hoe de eigenschappen van de vervuilingslaag veranderen onder verschillende toegepaste druk. Verschillende mechanistische modellen zijn geëvalueerd om het meest geschikte mechanistische model te vinden om het gedrag van de vervuilingslaag onder compressie-relaxatiecyclus in het afgesloten UF-systeem te verklaren. De resultaten tonen aan dat de hydraulische weerstand van homogene vervuilingslagen veel meer beïnvloed werd door de verandering in permeabiliteit dan door de dikte van de vervuilingslaag. Interessant is ook dat we ontdekten dat zelfs een poro-elastisch model (relatief eenvoudig model) het gedrag van de vervuilingslaag in deze studie redelijk goed kan verklaren voor verschillende toegepaste drukken. Samendrukking van de vervuilingslaag in UF-systemen kan de hydraulische weerstand van de membraansystemen aanzienlijk verhogen. In **hoofdstuk 2** is een nieuwe techniek ontwikkeld om de vervuilingseigenschappen van vervuilingslagen met een glad oppervlakte te bepalen. In **hoofdstuk 3** werd de nieuwe techniek verder uitgebreid om ook de mechanische eigenschappen van vervuilingslagen met een ruw oppervlakte te bepalen. We stelden vast dat, voor vervuilingslagen die gevoed worden met echt oppervlaktewater (bv. rivierwater),

een model met een tweelaagse structuur bestaande uit een dunne en dichte onderlaag en een dikke en poreuze toplaag het best overeenkomt met de waargenomen resultaten. Hierop gebaseerd introduceerden we ook een nieuwe indicator voor de bepaling van de waterflux in UF-systemen: de fractie van de blootgestelde onderlaag.

In **hoofdstuk 4** werden de chemische eigenschappen van de vervuilingslaag (bijv. samenstelling) en hun invloed op de chemische reinigingsefficiëntie in Omgekeerde Osmose (reverse osmosis: RO) systemen geëvalueerd. Chemische reinigingsprotocollen (vaak CIP-protocollen genoemd) worden meestal ontwikkeld onder laboratorium condities (synthetisch voedingswater, experimenten op korte termijn) en worden dan toegepast in RO-installaties op ware grootte. Dit leidt vaak tot significante verschillen in efficiëntie tussen laboratorium en grote schaal installaties. Daarom hebben we de eigenschappen van de vervuilingslaag en de CIP-efficiëntie van een typisch laboratorium RO-systeem vergeleken met die van een aantal grote schaal RO-installaties. De resultaten laten zien dat de CIP-efficiëntie in de grote schaal RO-installaties veel lager is dan die van laboratoriuminstallaties.

Later hebben we deze verschillen in CIP-efficiëntie gecorreleerd aan de significant verschillende compositie van de extracellulaire polymeren (extracellular polymeric substances: EPS) in de vervuilingslaag. Het EPS geëxtraheerd uit lab RO-systeem had een andere samenstelling en hechtingseigenschappen dan het EPS geëxtraheerd uit grote schaal RO-systemen. Daarom concludeerden we dat CIP-protocollen niet onder laboratorium condities ontwikkeld zouden moeten worden. In **hoofdstuk 5** stelden we een nieuwe methode voor om CIP-protocollen beter te ontwikkelen en de vervuilingseigenschappen met meer industriële toepassingen te bestuderen. We installeerden verschillende nieuwe RO-modules in grote schaal installaties en deze werden gedurende 30 dagen onder identieke condities bedreven als de grote schaal installatie. Later werden de vervuilingseigenschappen en CIP-efficiëntie (in-situ meting van permeabiliteit en herstel van de drukval) vergeleken tussen nieuwe RO-modules (na 30 dagen in dienst) en oude RO-modules (>2 jaar in dienst). De nieuwe voorgestelde vervuiling simulatiemethode laat veelbelovende resultaten zien in zowel de CIP efficiëntie resultaten als de vervuilingseigenschappen.

Hoewel vervuiling een onvermijdelijk onderdeel is van filtratie processen, is de economische impact op membraan systemen niet goed geëvalueerd. In **hoofdstuk 6** zijn de kosten van vervuiling in verschillende RO en nanofiltratie systemen (NF-systemen) in Nederland berekend met behulp van gegevens over de prestaties van de installatie. Alle kostenfactoren die bijdragen aan de kosten van vervuiling, zoals CIP kosten, energiekosten en aanloopkosten zijn in beschouwing genomen. We hebben waargenomen dat voor de RO-installaties ongeveer een kwart van de OPEX wordt veroorzaakt door vervuiling, in tegenstelling tot ongeveer 10% voor anoxische NF-installaties. De belangrijkste factor in de kosten van vervuiling waren de kosten van vroegtijdige membraanvervangings, op de voet gevolgd door extra energiekosten. CIP-kosten dragen slechts in geringe mate bij tot de totale kosten.

Hergebruik van stedelijk afvalwater is een deel van de oplossing om hoofd te bieden aan waterschaarste. In **hoofdstuk 7** stellen we een passende oplossing van waterhergebruik voor. We hebben een volledige, technisch-economische analyse gemaakt van een membraan-gebaseerde installatie voor het hergebruik van gemeentelijk afvalwater in Nederland.

De invloed van de vervuiling en de eigenschappen en kosten van vervuiling zijn geïntegreerd in alle membraansystemen. Een nieuwe benadering van het ontwerp van de water hergebruik installatie is voorgesteld om niet alleen de impact van vervuiling te verminderen maar ook om de robuustheid van de installatie en de water terugwinning te verhogen. In *hoofdstuk 8* worden de conclusies van de voorgaande hoofdstukken samengevat en gegeneraliseerd. Ook worden suggesties en mogelijkheden voor toekomstig membraan- en vervuilingsonderzoek gepresenteerd.





# 1

## General Introduction

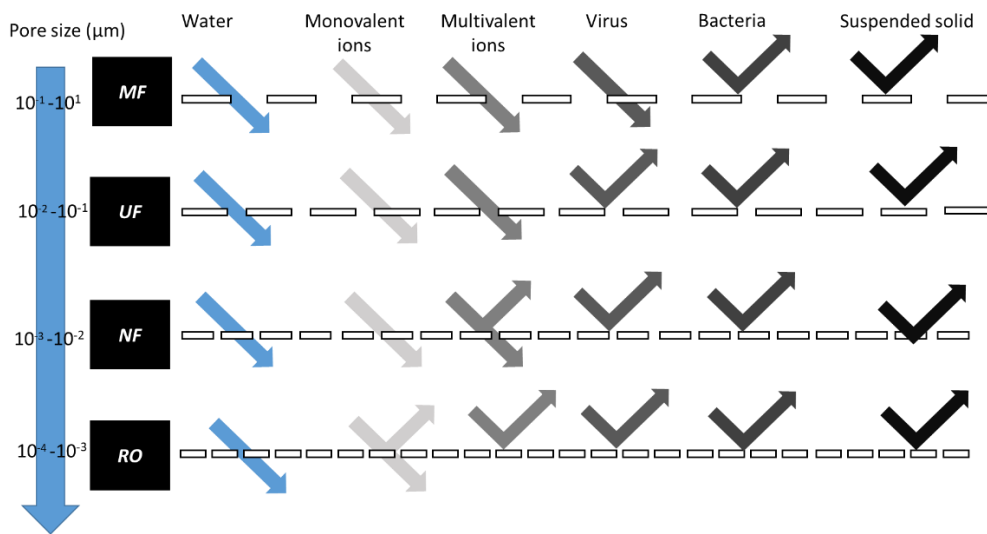
I may not have been sure about what really did interest me, but I was absolutely sure about what didn't.

Albert Camus

### 1.1 Global water outlook and applications of membrane processes

The fresh water availability is vital for meeting human needs and steady growth in industrial and agriculture sectors (FAO 2017). World population is growing fast and fresh water consumption is expected to increase significantly (Boretti and Rosa 2019). Uneven distribution of available fresh water accompanied by extensive population growth in water-stress regions forced humans to search for alternative water sources (Boretti and Rosa 2019). Alternative water sources such as seawater (Namboodiri and Rajagopalan 2014) and municipal reclaimed wastewater (Asano and Levine 1996) attracted huge attention in the last decades. Drinking water production via seawater desalination is becoming popular for water-stress regions such as middle eastern countries and North Africa. Seawater desalination for potable use is already in practice for decades in countries like Israel, Saudi Arabia, United States, Australia and even Spain (Eke et al. 2020). Even some of North European countries such as Belgium are looking into possibilities of widespread seawater desalination plants to combat seasonal drought (Gaublomme et al. 2020). To meet high hygienic standards of potable and industrial water, membrane technologies are widely used as separation physical barrier. Pressure-driven membrane-based technologies are currently extremely popular for seawater desalination (Namboodiri and Rajagopalan 2014). These membranes operate as a physical barrier rejecting the contaminants based on their nominal pore size and the driving force of the separation process is the applied hydraulic pressure (**Figure 1.1**). Reverse Osmosis (RO) is the most common in industrial seawater desalination. In addition, other membrane technologies such as microfiltration (MF) and ultrafiltration (UF) are often used in seawater desalination as a pre-treatment steps.

The share of municipal reclaimed wastewater in total water production is rapidly growing in many countries as the pressure to find alternative water source is mounting (Lyu et al. 2016, Silva et al. 2020). Potable use as well as industrial and agricultural applications are common in water-stress regions such as Singapore and United States (Lee and Tan 2016, Olivieri et al. 2020). Again, as for water desalination, pressure driven membrane systems such as (MF, UF, RO) are commonly employed as the main purification steps in water reuse treatment trains.

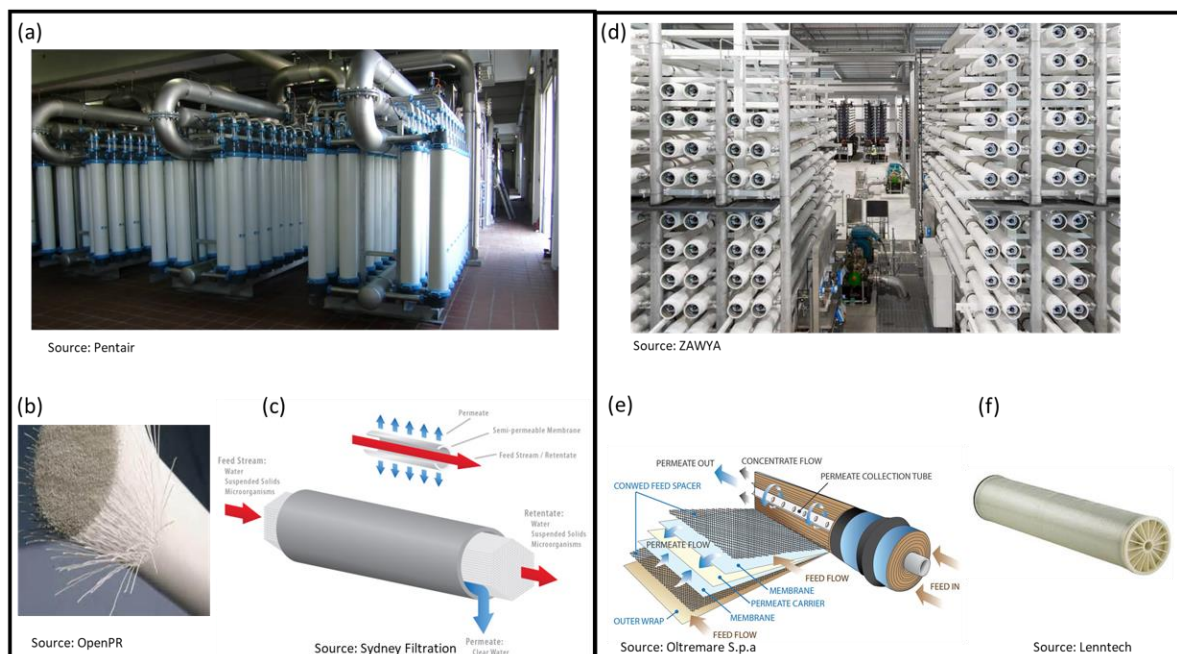


**Figure 1.1** Pore size and rejection of different membrane systems.

## 1.2 Membrane processes in water treatment

Membranes are vastly applied in different sectors due to their robustness and versatility (Cui et al. 2010). In sectors with heat-sensitive products such as food and pharmaceutical industries, where evaporation process is not an option, membranes are widely applied as an alternative process for separation and concentrating the final products (Tew et al. 2019). Pressure driven membranes are also widely employed in water and wastewater treatment. Development of cost-effective membranes with superior performances (e.g., high water flux, high rejection) made membrane systems available option in the several industrial sectors (Pal 2017). UF membranes are already widespread in drinking water sector due to their high removal rate and low energy consumption (Pal 2017). Recently, due to the rise of emerging pollutants (e.g., pharmaceuticals and organic micro pollutants) in drinking water sources, many utility companies decided to install RO and NF in their drinking water production train to ensure the high standard of water quality. Pressure-driven membrane systems are often divided to low pressure membrane systems (MF and UF) and high pressure membrane systems (NF and RO). MF and UF are often applied as pre-treatment, while NF and RO applied as the main purification step (Cui et al. 2010).

Membrane module configurations are categorized as hollow-fibre membranes (typically for MF and UF), spiral wound membranes (typically for NF and RO), tubular membranes and plate-and-frame membranes. The hollow-fibre and spiral wound are the most common configurations due to their high surface to volume ratio (Pal 2017). Flat sheet design is often used in the laboratory set-ups due to its simplicity of operation, sampling and monitoring. The schematic representation of spiral wound membrane module and hollow fibres are represented in **Figure 1.2**. This thesis focuses on UF and RO systems for brackish water.



**Figure 1.2** Ultrafiltration (UF) and Reverse Osmosis (RO) systems. a) full-scale UF installation, b) hollow fibre UF membrane module, c) Scheme of hollow fibre UF; d) full-scale RO installation, e) Scheme of spiral wound RO, f) spiral-wound RO module.

The operational conditions for UF and RO are very different as their aim and removal range is very different. RO modules are often operated in high transmembrane pressure (TMP=7-60 bar) and in cross-flow velocity. However, UF modules are mainly operated in low transmembrane pressure (TMP=1-3 bar) and under both cross-flow or dead-end modes (Pal 2017). In cross-flow mode, the feed water flows parallel to the membrane: part of the water passes through the membrane (called permeate) and the other part exits the module as concentrate/retentate. In dead-end mode, all the feed water will eventually pass through as permeate (Cui et al. 2010, Pal 2017). These characteristics are summarized in **Table 1.1**.

**Table 1.1** Typical characteristics of UF and RO systems

	Ultrafiltration (UF)	Reverse Osmosis (RO)
Driving force	Hydraulic pressure	Hydraulic pressure
Pore size	~0.1-0.01 ( $\mu\text{m}$ )	~0.1-1 ( <b>nm</b> )
Configuration	Hollow-fibre	Spiral-wound
Operating mode	Cross-flow/Dead-end	Cross-flow
Operating pressure (bar)	2-5	10-60

### 1.3 Membrane fouling: Bottleneck of membrane processes

Accumulation of rejected materials over time on membrane surface and feed spacer is called membrane fouling (Voutchkov 2017). Membrane fouling reduces the process performance and leads to frequent cleanings and ultimately early membrane replacement (Meng et al. 2017, Porcelli and Judd 2010a). Actually, fouling is inherently part of any filtration processes, however, especially for optimal membrane operation fouling is the biggest challenge. There are several types of fouling, classified based on the origin and nature of the deposited material: organic (mainly polymeric material), inorganic (usually as salt crystals, but also colloidal particles) and biofouling (caused by microorganisms growing on the membrane). Fouling leads to an increase in feed channel pressure drop and a reduction in water flux by imposing an additional hydraulic resistance. The effects of fouling layers on different membrane processes can be diverse, related to the nature of the foulant but also to the membrane properties and operation mode. For example, the additional hydraulic resistance induced by fouling is the primary reason for water flux reduction in MF and UF (Dreszer et al. 2013). In reverse osmosis (RO) and forward osmosis (FO), where the hydraulic resistance of membrane is dominant, biofouling (for example) decreases the flux mainly by enhancing the concentration polarization (thus decreasing the net pressure by causing extra osmotic pressure) (Herzberg and Elimelech 2007, Kim et al. 2009b). On the other hand, the formation of a biofouling layer can also have positive impacts on some membrane processes such as Gravity-driven membrane (GDM) and Membrane bioreactors (MBR) (Meng et al. 2017, Pronk et al. 2019). In these systems, the fouling layer enhances permeate quality by either degradation of assimilable Organic Carbon (AOC) (Derlon et al. 2014) or by greater rejection of biopolymers and humic matter (as an additional filtration

layer with smaller pore size) (Desmond et al. 2018d). Therefore, knowledge of how fouling occurs and of its effects is necessary to understand, predict and control fouling for optimal operation of membrane systems.

#### **1.4 Types of fouling**

Four major types of fouling can occur in membrane systems: biofouling is excessive formation of biofilms in the membrane system; colloidal fouling, caused by accumulation of particulate matter; organic fouling, caused by deposition of macromolecules and natural organic matters such as humic acid; scaling, associate with precipitation and crystallization of salts.

*Biofouling.* Biofouling occurs due to the growth of microorganisms and formation of extracellular polymeric substances (EPS) excreted by the microbes (Flemming 2011, 2020, Flemming 2002). Biofouling is the “Achilles heel” of membrane process because even if the pre-treatment is extremely successful (>99.99% removal of microbes), the microorganisms still multiply over time and a fouling layer of biological origin will accumulate (Bucs et al. 2018, Flemming 2002). Biofouling is estimated to be the major fouling factor in all membrane problems, with a share of ~ 45% of all fouling types (Flemming 2020). The greatest challenge that biofouling poses for a membrane system is attributed to EPS and its hydraulic and mechanical properties (Desmond et al. 2018a, Herzberg et al. 2009). The negative effects of biofouling on the process and its treatment are considered to cost around 30% of a plant OPEX in industrial RO plants (Flemming 2020).

*Scaling.* Formation of mineral deposits (mainly inorganic salt crystals) on the membrane surface (Voutchkov 2017, Warsinger et al. 2015) is called scaling. As feed water passes through the membrane module, salt concentration increases along the module due to rejection and also towards the membrane due to concentration polarization – both effects leading to precipitation of poorly soluble salts as they reach their solubility limits. Scaling in RO and NF membranes often include calcium carbonate, calcium sulphate, calcium phosphate and silica (Antony et al. 2011). Membrane system recovery is often limited (for RO system ~ 80%) due to high scaling potential of the concentrate streams under elevated recovery rate (> 80%) (Antony et al. 2011, Tang et al. 2016). Dosing of in-line antiscalant or installation of softener as pre-treatment can reduce the risk of scaling (Vanoppen et al. 2016).

*Colloidal fouling.* Deposition of particles in colloidal size range (1 nm-10 µm) causes colloidal fouling, in a similar way cake layers form in other filtration processes. Common colloidal fouling in NF/RO plants occurs due to aluminium silicate clays, silica, iron and manganese oxides (Tang et al. 2011).

*Organic fouling.* Deposition and adsorption of macromolecules such as polysaccharides, humic acids and proteins on the membrane surface can lead to organic fouling. This is often observed in NF/RO plants fed with shallow surface water and wastewater effluent (Elimelech 2009, Li and Elimelech 2004)

However, it is many times possible that all these fouling mechanisms would occur simultaneously, especially in industrial plants, which makes a clear distinction between the types of fouling very difficult in a particular water production plant. Usually, organic fouling accompanies with colloidal fouling results in much higher fouling potential. Similarly, (Radu et al. 2015a, Thompson et al. 2012) reported an increase in scaling potential in presence of biofouling. Therefore, in practice we are mainly dealing with systems that are either a combination of all fouling types or partly dominated by one form (but never purely one fouling type). Evidently,

this combined fouling only makes more difficult to find efficient methods to restore the membrane process after fouling.

### **1.4.1 Fouling characterization: first step to mitigate the fouling**

Membrane fouling is extensively analysed in membrane literature. Fouling studies focus on biomass analysis (Hijnen et al. 2011a, Vrouwenvelder et al. 2008), concentration of elemental metals (Beyer et al. 2014, Shen et al. 2018), analysis of microbial community (Al Ashhab et al. 2017, Bereschenko et al. 2011, Bereschenko et al. 2010, Yu et al. 2017) and EPS properties (Al Ashhab et al. 2017, Desmond et al. 2018a, Herzberg et al. 2009, Lin et al. 2014, Sweity et al. 2011). Optical techniques are also applied to evaluate fouling layer morphology and structure (Valladares Linares et al. 2016). Different microscopic techniques with various characteristics are used to provide better overview of fouling layer morphology at different spatial scales (Blauert et al. 2015, Valladares Linares et al. 2016). Stability of fouling layer under elevated shear forces is also often measured to estimate the efficiency of physical cleaning (Ang et al. 2006, Vrouwenvelder et al. 2010b, Wibisono et al. 2014). Many studies has been performed to evaluate the mechanical properties of biofilms in general and of biofouling layers in particular (Allen et al. 2018, Billings et al. 2015, Korstgens et al. 2001a, Laspidou 2007, Laspidou et al. 2014, Peterson et al. 2015). Most of the time, however, these properties are extracted using ex-situ and destructive methods, which also raise questions regarding the applicability of these data in practice.

Generally, fouling analyses are often carried out using destructive sampling methods (e.g., membrane autopsy), which may limit the applications in industrial cases. To avoid destructive sampling, researchers attempted to correlate feed water properties to the fouling characteristics (Peiris et al. 2013, Wang and Tang 2011). In addition, fouling properties are extensively studied on “membrane fouling simulators” (MFS) using laboratory flow cells and under lab conditions (e.g., synthetic feed water, high concentrations of nutrients, short operational time)(Bucs et al. 2016, Farhat et al. 2019, Miller et al. 2012, Vrouwenvelder et al. 2010b, Vrouwenvelder et al. 2009). The analysis of industrial-scale fouling layer is often carried out via membrane autopsy (Bereschenko et al. 2011, Beyer et al. 2014, Tang et al. 2016, Yu et al. 2017). Many times, the analyses made in full-scale are oriented to problem solving and less to understanding the fouling mechanism. Recently, there have been reports about the discrepancy between fouling impacts and its properties, as obtained in laboratory and full-scale installations (Tew et al. 2019). Therefore, we believe that further studies should go beyond the artificial conditions created in the lab and gather more comprehensive knowledge of fouling under full-scale conditions.

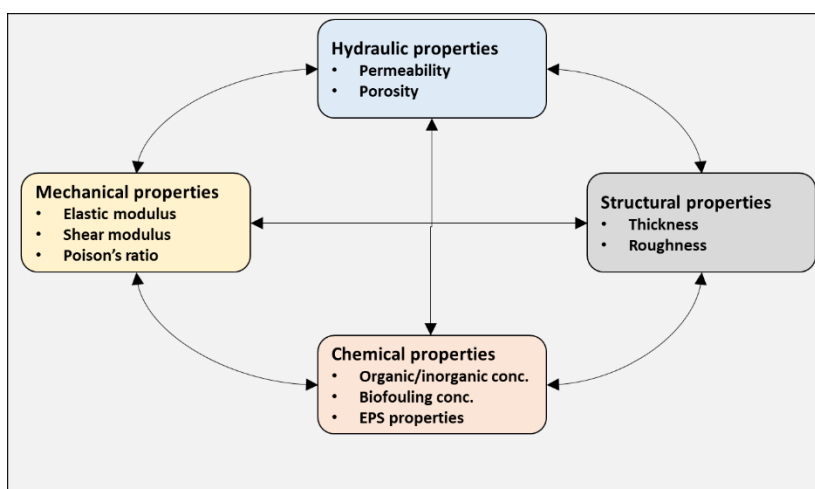
## **1.5 Importance of fouling properties**

Biofouling can be characterized by four main categories of properties:

1. Hydraulic properties
2. Mechanical properties
3. Structural properties
4. Chemical properties

The membrane fouling properties can be impacted by operational conditions, growth time, feed water quality and membrane properties.

The fouling properties are all inter-connected and cannot be fully distinguished from each other (**Figure 1.3**), with the result that a change in any of these properties would lead to a change in other properties. For instance, a change in chemical properties (i.e., calcium concentration) would lead to a stronger fouling layer (i.e., greater elastic modulus) thus affecting also its mechanical properties. Moreover, Valladares Linares et al. (2015) reported that a biofilm with higher EPS concentration (again a chemical property) would have a lower porosity and permeability (which is strongly related to the hydraulic properties). A change in the structural properties (e.g. thickness or roughness of the fouling layer) will lead to a change in hydraulic characteristics and also mechanical resistance – for example, uniformly flat biofilms have a stronger mechanical stability than those with a rough surface (Picioreanu et al. 2018).



**Figure 1.3** A scheme with several classes of properties for the fouling layers (chemical, hydraulic, structural and mechanical) and their close interconnection.

### 1.5.1 Hydraulic properties

The main hydraulic property of fouling is its permeability for water, which in turn is highly affected by the effective porosity of the fouling layer. Often reported for the fouling layer is also the hydraulic resistance, which correlates permeability and thickness (Dreszer et al. 2013, Martin et al. 2014). The relation between fouling permeability, porosity and hydraulic resistance is discussed in (Martin et al. 2014, Valladares Linares et al. 2015). The combined hydraulic resistance is calculated using a “resistance model”, by measuring water flux of fouled and of virgin membranes (Dreszer et al. 2013, Poorasgari et al. 2015). Several empirical models were developed to explain fouling mechanics in UF and MF and their relations to hydraulic resistance reduction (Poorasgari et al. 2016, Poorasgari et al. 2015). The change in operational conditions, such as increase in applied pressure or operating flux, can lead to compression of the fouling layer and consequently to the elevation of hydraulic resistance (Desmond et al. 2018d, Dreszer et al. 2013, Poorasgari et al. 2016, Poorasgari et al. 2015). However, the impact of compression on hydraulic resistance is mainly observable in MF and UF systems and not in NF and RO (Dreszer et al. 2013). This is due to the fact that in UF and MF systems, the fouling hydraulic resistance has a significant share in total system resistance, that is the sum of membrane and fouling resistances.



Therefore, a dead-end UF system has been selected in this thesis to study the impact of compression on fouling hydraulic resistance.

Biofilm compression causes a structural rearrangement of the biofouling layer, leading to change in density and porosity and consequently to an increase in hydraulic resistance (Derlon et al. 2016, Dreszer et al. 2013, Valladares Linares et al. 2015). The reversibility of compression depends on fouling layer morphology and composition (Valladares Linares et al. 2015). The extent of biofilm compression will be the result of a balance between forces generated by the permeate flow (i.e., pore pressure and permeate drag) and structural forces within the biofouling layer that oppose its deformation (i.e., elastic, viscous). Valladares Linares et al. (2015) reported a significant increase in hydraulic resistance in UF systems under compression and correlated it to potential structural rearrangements of fouling layer such as macro-porosity reduction (i.e., collapse of mushroom-like biofilm structures). However, the information on structural properties of fouling (i.e., thickness and roughness) was measured ex-situ.

To study the behaviour of fouling layer hydraulic resistance under compression, accurate information of membrane permeability and fouling structural parameters (thickness and surface roughness) is required. Dreszer et al. (2013) observed a change in hydraulic resistance under step-wise flux change in MF and correlated the change in hydraulic resistance to the fouling structure. They reported a clear time-dependent biofilm deformation under compression/relaxation scheme which implied a viscoelastic behaviour of biofilm .

Several other studies analysed the time dependency of fouling hydraulic resistance under different operating conditions (Derlon et al. 2016, Derlon et al. 2008, Desmond et al. 2018a, Desmond et al. 2018d). However, no clear correlation could be found for the fouling structural changes during compression, mainly due to the lack of in-situ measurement of biofilm structure. Recently, the biofilm compression in gravity-driven membrane filtration (GDM) has been recorded in-situ with optical coherence tomography (OCT) (Desmond et al. 2018d). They reported that biofilm hydraulic resistance increases with increasing TMP/flux.

Fouling layer porosity also plays a significant role in fouling layer hydraulic resistance . However, biofilm porosity measurement is very challenging due to the limitation in application of ex-situ and destructive techniques (due to fragile structure of fouling layer) and potential ambiguity in pore distinction in the in-situ non-destructive methods (i.e., the way image processing is used will bias the results). Better, a coupled approach between computational and optical techniques could be required to measure biofilm porosity during compression – which was proposed in this thesis.

## **1.5.2 Structural properties**

Fouling structure can be divided into fouling layer internal structure and surface structure. From the internal structure point of view, the fouling is often described as a porous medium consisting of several layers with different properties, such as density and porosity. In general, biofilm porosity has been observed to increase with the distance from substratum (Gao et al. 2011b, Okabe et al. 1998, Zhang and Bishop 1994), whereas the biofilm elastic modulus (or rigidity) seems to have an opposite trend (Aravas and Laspidou 2008, Picioreanu et al. 2018). Thus, the biofilm close to the support material (membrane here) is in general more compact, denser and more rigid, while the biofilm close to the liquid is more porous, less dense and more elastic. The spatial

distribution of porosity and mechanical properties affect the biofilm permeability, as well as the structural responses under compressive forces (Derlon et al. 2016, Dreszer et al. 2013, Poorasgari et al. 2015, Valladares Linares et al. 2015). In cases where the biofilm structure is clearly variable over its thickness, it has been reported that biofilm hydraulic resistance in UF membrane is dominated by a thin and dense base layer of fouling (Derlon et al. 2016, Desmond et al. 2018d).

In general, the biofilms can be observed to develop diverse structures. They can have a smooth surface and appear rather flat in the direction parallel to the membrane surface (that is, a rather constant thickness along their support surface). Other biofilms present a rough surface, with fluffy outgrowth, and have different macroporosity values due to the different number of macro-colonies. The main parameters often used to describe the structural properties of biofilm surface are the average thickness and surface roughness (Desmond et al. 2018d, Martin et al. 2014, Wagner et al. 2010, Zhang and Bishop 1994). These two parameters are often used to describe fouling layer surface structure. Development of imaging techniques has enabled the measurement of biofilm structural parameters (i.e., thickness and roughness) with higher accuracy (Valladares Linares et al. 2016, Wagner and Horn 2017, Wagner et al. 2010). Different optical techniques have different optical scales, which provide broad information about fouling morphology at several spatial levels. Many studies measured hydraulic resistance and structural parameters in an uncoupled and *ex-situ* manner (Derlon et al. 2016, Dreszer et al. 2013, Poorasgari et al. 2015). However, later developments of *in-situ* imaging techniques such as optical coherence tomography (OCT) enabled researchers to study biofilm development and structural rearrangement in real time and at meso-scale (Dreszer et al. 2014, Fortunato et al. 2017, Wagner and Horn 2017, Wagner et al. 2010). Integration of OCT imaging with the membrane fouling simulator has enabled researchers to correlate biofouling structural deformation to the change in fouling layer hydraulic resistance (Desmond et al. 2018d, Valladares Linares et al. 2015). Desmond et al. (2018d) studied the *in-situ* biofilm structure deformation (surface roughness and thickness) under compression and correlated it to hydraulic resistance. However, the relation between structural deformation and hydraulic resistance during compression of biofilms with different morphologies (e.g., surface roughness) is not still clear and the relations with operational conditions has still to be determined.

### **1.5.3 Mechanical properties**

Fouling mechanical properties play an important role in the efficiency of physical cleaning strategies such as shear cleaning (Ang et al. 2006), air-bubble cleaning (Cornelissen et al. 2007) and backwash cleaning (Shao et al. 2018). Mechanical properties of the fouling layer govern the biofilm structural response to any changes in the operational conditions, such as changes in applied pressure and cross-flow velocity (Paramonova et al. 2009). In turn, the biofouling mechanical properties are determined by chemical composition and morphology. Valladares Linares et al. (2015) reported an increase of mechanical resistance of biofilms causing biofouling with a higher EPS content. Moreover, other studies observed higher stiffness of biofilms at higher calcium concentrations (Kim and Jang 2006, Shen et al. 2018).

Several mechanical models such as elastic, viscoelastic and elastoplastic were applied to describe biofilm mechanical behaviour (Gloag et al. 2020). The classical elastic model attracted most of the attention due to simplicity, while several viscoelastic models were used to describe time-dependent response biofilm to

mechanical forces (Blauert et al. 2015, Gloag et al. 2020, Klapper et al. 2002, Özkaya et al. 2012, Picioreanu et al. 2018). Poroelastic models, coupling elastic mechanical models with hydrodynamics in porous media, can be formulated to describe the biofilm response to applied forces. From the multitude of mechanical properties, the elastic modulus  $E$  (also known as Young's modulus) is most commonly measured. Interestingly, the reported values for elastic moduli in literature vary significantly, anywhere between 10 and 6000 Pa (Aravas and Laspidou 2008, Blauert et al. 2015, Cense et al. 2006, Galy et al. 2012, Gloag et al. 2020, Klapper et al. 2002, Korstgens et al. 2001a, Laspidou et al. 2014, Özkaya et al. 2012, Peterson et al. 2012). The significant variation in elastic modulus is attributed to the different type of applied forces (tensile, shear, compressive) (Blauert et al. 2015, Korstgens et al. 2001a, Laspidou 2007, Stoodley et al. 1999), the measurement techniques (rheometer, Nano indentation and image processing) (Blauert et al. 2015, Cense et al. 2006) and type of biofilms under study (Jones et al. 2011, Peterson et al. 2012).

Moreover, the mechanical properties are also spatially distributed within the biofilm. (Picioreanu et al. 2018, Zhang and Bishop 1994) reported higher mechanical properties for the biofilms near substratum compared to biofilm surface. This is usually explained by biofilm consolidation close to substratum over time (Casey 2007, Derlon et al. 2016). (Laspidou 2007, Paramonova et al. 2007) reported an increase in mechanical stiffness of biofilms during compression tests, which would support the definition of effective mechanical properties in a way integrated with biofilm material properties.

In general, biofilm mechanical properties are measured using destructive ex-situ techniques (rheometry, etc.). Coupling imaging techniques with a mathematical model describing the observed deformation provided a new approach to extract mechanical properties in a non-destructive way. Picioreanu et al. (2018) developed a Fluid-Structure Interaction (FSI) model to extract biofilm mechanical properties from the OCT images of the biofilm developed in a laboratory flow cell. Although this constitutes a beginning, further integration of imaging techniques and mathematical models is required to extract mechanical properties in-situ and non-destructive and to couple the mechanical parameters to other properties such as porosity (a structural property) and permeability (a hydraulic measure).

#### **1.5.4 Chemical properties**

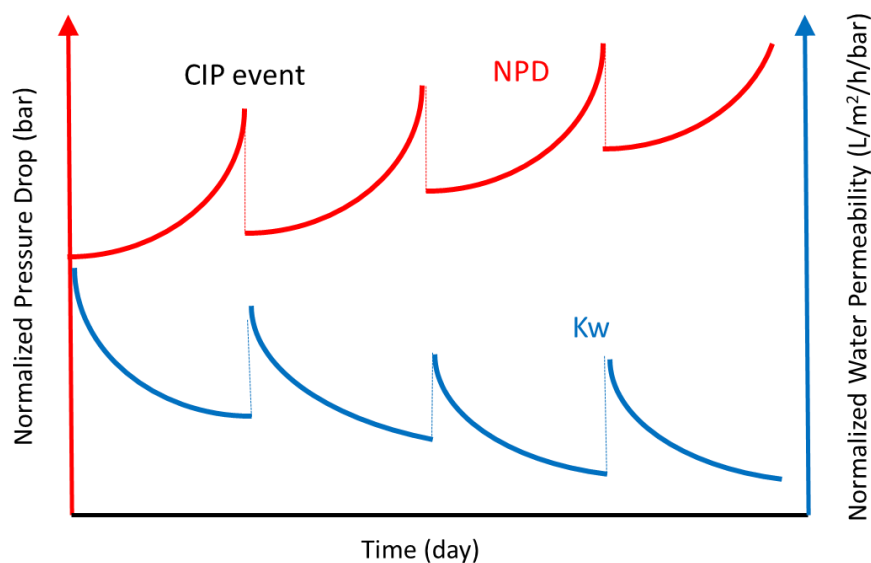
Fouling layer chemical composition plays a major role in optimal operation of the membrane systems including selection of suitable pre-treatment steps and chemical cleaning protocols (Al Ashhab et al. 2017, Ang et al. 2006, Bereschenko et al. 2011, Elimelech 2009). Biofilm composition determines efficiency of cleaning during a chemical cleaning event. Fouling layer composition (i.e., chemical and biological properties) is often characterized by the concentration of living matter (i.e., biological content, microbial dynamic population), organic content and concentration of elemental cations (e.g., calcium, magnesium, iron) (Beyer et al. 2014, Farhat et al. 2019, Miller et al. 2012, Shen et al. 2018, Vrouwenvelder et al. 2008). Moreover, the organic polymers in biofouling (EPS) act as a matrix, which plays a distinctive role in biofouling cleanability in membrane processes (Flemming 2020). Solubilizing the EPS forming the biofilm on the membrane would enhance fouling removal and cleaning efficiency (Sanawar et al. 2018). The EPS from biofilms developed on membrane surfaces (i.e. membrane biofilm EPS) are evaluated based on their main composition (i.e., polysaccharide, protein) and adherence properties to the membrane surface (Al Ashhab et al. 2017, Desmond

et al. 2018a, Herzberg et al. 2009, Sweity et al. 2011). EPS composition is mainly studied for biofilms grown under laboratory conditions. Al Ashhab et al. (2017) analysed EPS adherence properties and composition of lab-grown biofilm after several rounds of chemical cleaning. EPS composition is significantly impacted by feed water composition (e.g., nutrient limitation), growth time and operating conditions (Al Ashhab et al. 2017, Desmond et al. 2018a, Farhat et al. 2019, Herzberg et al. 2009). Other studies reported considerable discrepancy between the CIP efficiency of the lab-grown biofilms compared to the CIP efficiency of fouling developed in full-scale plants (Tew et al. 2019). Beyer et al. (2017) measured the EPS composition for three full-scale RO installations and reported polysaccharide-rich EPS within the developed biofouling. Studies of EPS from membrane biofilms have been mainly focused on the biofouling developed in the lab conditions (typically, young biofilms), usually fed with synthetic feed water for short periods of time (Al Ashhab et al. 2017, Bereschenko et al. 2011, Bereschenko et al. 2010, Herzberg et al. 2009). EPS properties of biofilms developed in full-scale installations (i.e., “old” biofilms, formed under nutrient limitation) are not well explored. To be able to optimize chemical cleaning protocols compatible with full-scale installations, EPS properties of full-scale biofilms need to be better studied.

## 1.6 Fouling properties and operational parameters

It is widely acknowledged that fouling formation on membrane surface leads to a decline in membrane performance parameters (Flemming 2020). Fouling increases the required pressure in the membrane systems in two ways: it increases feed channel pressure drop and also the needed transmembrane pressure (Vrouwenvelder et al. 2009, Wang and Tang 2011). Biofilm accumulation in the feed channel (on membranes and spacer) causes channel blockage and therefore would increase the cross flow velocity which leads to higher axial pressure drop. Moreover, the fouling layer acts as an additional hydraulic resistance in series with that of the membrane, leading to decrease in TMP and consequently flux decline (Al Ashhab et al. 2017, Farhat et al. 2019, Herzberg and Elimelech 2007, Herzberg et al. 2009). In industrial plants where a certain water production has to be guaranteed, membranes are operated under constant-flux mode. This means the feed channel pressure drop and decrease in transmembrane pressure have to be compensated with an additional pressure to ensure the constant water flux (Beyer et al. 2017, Beyer et al. 2014, Pearce 2008). In addition, fouling accumulation will lead to increased salt concentration polarization (called cake-enhanced concentrationpolarization) and consequently increased transmembrane osmotic pressure and reduced permeate flux (Beyer et al. 2014, Herzberg and Elimelech 2007, Kim et al. 2009b).

Membrane operational parameters such as feed channel pressure drop, membrane permeability and salt passage (mainly for NF and RO) are often measured in the industrial plants. These parameters are frequently normalized to standard conditions to allow a fair comparison between these parameters over time and among different plants (Beyer et al. 2017, Beyer et al. 2014). A typical profile of membrane performance parameters for industrial RO plants is shown in **Figure 1.4**.



**Figure 1.4** Typical profile of plant performance parameters (pressure drop and water permeability) over time and impact of chemical cleaning events on their recovery.

### 1.7 Fouling control and mitigation strategies

To control fouling formation, membrane cleaning is often applied in the membrane systems. The goal of all the cleaning techniques is to restore the membrane original performance properties (Ang et al. 2006, Bucs et al. 2018). Membrane cleaning approaches are divided into chemical and physical cleaning.

Chemical cleanings include dosage of antiscalants to prevent nuclei formation (scaling) and frequent chemical cleaning-in-place (CIP) routines using acid and alkaline solutions. Alkaline cleanings are often successful in organic fouling removal (Li and Elimelech 2004), while acid cleaning is often employed for the removal of inorganic scale (Kim et al. 2020, Lyster et al. 2010). However, biofouling is the most challenging type of fouling from the cleaning point of view (Bucs et al. 2018). Several types of non-oxidant biocides (such as 2,2-Dibromo-3-nitropropionamide (DBNPA) and Sodium bisulfite (SBS)) are applied to control biofouling in membrane systems (Creber et al. 2010). Moreover, extensive pre-treatment is normally applied to remove biodegradable substrate in the feed water to reduce the biofouling potential (Anis et al. 2019). However, practice shows that biofouling can be delayed but not prevented (Flemming 2020). Chemical cleanings are often successful in killing microorganisms, but not in their removal from the membrane system. Therefore, the residual biofilm after cleaning can still be used as feed for other incoming microorganisms (Bereschenko et al. 2011). What is worse, Al Ashhab et al. (2017) showed that the frequent chemical cleanings can lead to formation of resilient fouling and consequently lower cleaning efficiency (e.g., self-limiting mechanism).

Physical cleanings such as by backwash (Shao et al. 2018), by air-bubble (Wibisono et al. 2015) or by air-scouring cleaning (Cornelissen et al. 2007) are also applied as they are less harmful for the membrane integrity. Although physical cleanings are commonly employed in UF and MF membranes, their application in spiral wound RO and NF is rather limited due spiral wound configuration of these systems. Nevertheless, Cornelissen et al. (2007) showed that air-scouring in vertical RO can save energy up to 10% and chemical consumption up to 90%.

Alternative methods such as membrane surface modification (Bucs et al. 2017, Miller et al. 2012), novel pre-treatment steps (e.g., application of softener as RO pre-treatment) (Prihasto et al. 2009, Vanoppen et al. 2015), novel feed channel spacer geometries (Haaksman et al. 2017) have also been proposed to reduce biofouling potential – however without significant industrial impact to date.

In general, chemical and physical cleaning protocols are often developed in the laboratory conditions and their removal efficiency was not optimized in the full-scale operations. This is where this thesis brings its contributions.

## **1.8 Scope and outline of the thesis**

The main objective of this thesis is to evaluate the impact of fouling properties on reverse osmosis and ultrafiltration membrane systems using both experimental and computational approaches. Three aims can be formulated: i) develop reliable methods to extract the most important fouling properties; ii) evaluate the inter-relation between the fouling properties, performance parameters and operating conditions in RO and UF systems; iii) quantify the economic impact of fouling in the membrane plants.

The thesis is structured in six research chapters, supplemented by this introduction and the conclusion and outlook chapters. The objectives of the main research chapters are here summarized.

**Chapter 2.** To evaluate the impact of fouling layer properties in membrane systems, a reliable method to extract the hydraulic, mechanic, structural and chemical properties is required. Fouling properties should be measured, preferably, by non-destructive in-situ techniques. The coupling of mechanical models and optical imaging methods such as OCT provides an excellent opportunity to extract the mechanical (i.e., elastic modulus) and hydraulic (i.e., permeability, porosity) properties of the fouling layer. In this chapter, the performance results (i.e., water flux and hydraulic resistance) of a dead-end UF system with in-situ OCT imaging was coupled with a fully-coupled fluid-structural interaction (FSI) model. In this way, mechanical, hydrological, and morphological properties of the fouling layer can be determined simultaneously in a non-destructive manner. The technique was developed and applied on a fouling layer with smooth surface (i.e., with low surface roughness), to extract fouling properties under compression for the biofilms grown under lab conditions as well as for the ones fed with real (complex composition) feed water.

**Chapter 3.** Compression of fouling layer in UF systems can significantly increase the hydraulic resistance of the membrane process. While in **Chapter 2** a non-destructive technique was developed to determine properties for smooth surface fouling layers, here the FSI-OCT method was expanded on fouling layers with high surface roughness. The fouling layer was formed in a dead-end UF system fed with real surface water under different operational pressures. The cultivated fouling layers presented different morphologies and properties. In this respect, a correlation between fouling layer structure (morphology) and its behaviour under compression was determined.

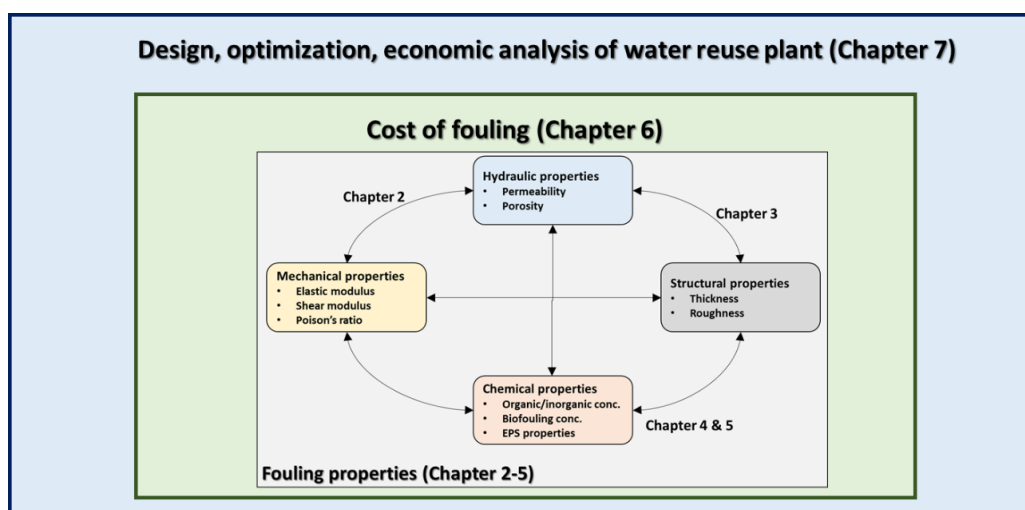
**Chapter 4.** Chemical cleaning is frequently applied in membrane systems to remove fouling and restore membrane original performance parameters. The chemical properties (composition) of fouling layers significantly dominate the fouling removal and chemical cleaning efficiency. However, the chemical cleaning protocols are often developed for fouling formed under lab-conditions (i.e., short operational time and synthetic

feed water). It has been shown that EPS composition plays a crucial role in the degree of solubilisation and fouling removal. A conventional chemical cleaning protocol was applied to lab-scale RO systems fed with synthetic water and operated for a short time. Moreover, RO membranes from full-scale installations fed with complex water and under a long operational time were analysed. The cleaning efficiency of lab-scale fouling and full-scale fouling were compared and correlated to its biomass indicators and EPS properties.

**Chapter 5.** To fairly compare the chemical properties and the chemical cleaning efficiency of fouling from full-scale and lab-scale RO systems, a number of new RO modules were installed in a full-scale installation and they were operated for short period of time. In this way, all the operational parameters (feed water, TMP, etc.) were all similar except the duration of the operation (operational time). This allows to evaluate the impact of operational time on industrial RO systems and it gives a better understanding of the optimal conditions in which the cleaning protocols should be developed.

**Chapter 6.** Although fouling is an inevitable part of the filtration processes, its economic impacts on membrane systems is not well evaluated. In this study, the cost of fouling in several RO and NF systems in The Netherlands has been calculated using plant performance data. This allows to identify the major cost factors such as energy consumption, membrane replacement and chemical cleaning – and it is expected to have a significant impact in further development of cleaning protocols.

**Chapter 7.** Reuse of municipal wastewater effluent is part of solution to deal with water scarcity challenges. A fit-for-purpose approach to water reuse that provides different water quality for different applications (potable, industrial, irrigation) would be a good method to taking into account the main drivers for water reuse. We developed a full techno-economic analysis on a membrane-based water reuse plant for municipal wastewater treatment effluent in the Netherlands. The impact of fouling and its properties and fouling cost have been integrated in all the membrane systems. By this, a novel approach on the design of water reuse plants has been offered, which not only inherently reduces the fouling impact, but also increases the plant robustness and water recovery factor.



**Figure 1.5** A scheme integrating the objectives of the current thesis and approaches used in its different chapters.

# 2

## **Effect of biofilm structural deformation on hydraulic resistance during Ultrafiltration**

“Where there is power, there is resistance”.

Michel Foucault

---

This chapter published as: Jafari, M., Desmond, P., van Loosdrecht, M.C.M., Derlon, N., Morgenroth, E. and Picioreanu, C. (2018) Effect of biofilm structural deformation on hydraulic resistance during ultrafiltration: A numerical and experimental study. *Water Res* 145, 375-387.



## **Abstract**

Biofilm formation in membrane systems negatively impacts the filtration system performances. This study evaluated how biofilm compression driven by permeate flow increases the hydraulic resistance and leads to reduction in permeate flux. We analysed the effect of biofilm compression on hydraulic resistance and permeate flux through computational models supported by experimental data. Biofilms with homogeneous surface structure were subjected to step-wise changes in flux and transmembrane pressure during compression and relaxation tests. Biofilm thickness under applied forces was measured non-invasively *in-situ* using optical coherence tomography (OCT). A numerical model of poroelasticity, which couples water flow through the biofilm with biofilm mechanics, was developed to correlate the structural deformation with biofilm hydraulics (permeability and resistance). The computational model enabled extracting mechanical and hydrological parameters corresponding to the experimental data. Homogeneous biofilms under elevated compression forces experienced a significant reduction in thickness while only a slight increase in resistance was observed. This shows that hydraulic resistance of homogeneous biofilms was affected more by permeability decrease due to pore closure than by a decrease in thickness. Both viscoelastic and elastoplastic models could describe well the permanent biofilm deformation. However, for biofilms under study, a simpler elastic model could also be used due to the small irreversible deformations. The elastic moduli fitting the measured data were in agreement with other reported values for biofilm under compression. Biofilm stiffening under larger flow-driven compression forces was observed and described numerically by correlating inversely the elastic modulus with biofilm porosity. The importance of this newly developed method lies in estimation of accurate biofilm mechanical parameters to be used in numerical models for both membrane filtration system and biofouling cleaning strategies. Such model can ultimately be used to identify optimal operating conditions for membrane system subjected to biofouling.

## 2.1 Introduction

In the recent decades, membrane processes have become established technologies in drinking water and wastewater treatment. Production of stable water quantity and quality are now usual characteristics for membrane systems. However, due to the non-sterile conditions, microorganisms are present in water and formation of biofilms is inevitable, leading to biofouling (Vrouwenvelder et al. 1998), reduction of water production (Li and Elimelech 2004) and life time reduction of membrane modules (Martin et al. 2014). Biofilms developed on membranes have a negative impact on both cross flow (i.e., increased axial pressure drop; Vrouwenvelder et al. (2009)) and on permeate flow (i.e., reduced water flux; Lee et al. (2010)). The additional hydraulic resistance induced by biofilms (Dreszer et al. 2013) reduces permeate flux in microfiltration (MF) and ultrafiltration (UF) (Martin et al. 2014). In reverse osmosis (RO) and forward osmosis (FO), where the hydraulic resistance of membrane is dominant, biofilms decrease the flux mainly by enhancing the concentration polarization (thus decreasing the net pressure by causing extra osmotic pressure) (Herzberg and Elimelech 2007, Radu et al. 2010). The hydraulic resistance, in turn, depends on the biofilm thickness and permeability. On the other hand, biofilm permeability depends on biofilm porosity and tortuosity. It has been reported that water permeation through biofilms can cause a structural re-arrangement, increasing biofilm density (Casey 2007), decreasing the porosity and eventually increasing the hydraulic resistance (Derlon et al. 2016, Dreszer et al. 2013, Valladares Linares et al. 2015). The extent of biofilm compression will be the result of a balance between forces generated by the permeate flow (i.e., pore pressure and permeate drag) and structural forces opposing biofilm deformation (i.e., elastic, viscous). At the same time, the biofilm compression caused by permeation would lead to an elevated mechanical strength, with biofilms more difficult to be removed during the cleaning. Other studies also observed biofilm hardening behaviour under elevated stress (Laspidou 2007, Paramonova et al. 2009). Compression of organic fouling layers developed on FO and RO by permeate drag force membranes has been reported (Xie et al. 2015). Therefore, it appears important to relate the biofilm hydraulic resistance both with the applied hydrodynamic conditions and with the biofilm mechanical behaviour. A better understanding of the link between the hydrodynamic conditions, the biofilm mechanical properties and its resulting hydraulic resistance is required to properly define operating strategies for membrane processes. An optimal operation of membrane systems should aim at maximizing permeate flux while minimizing compression of the biofilms.

Recently, the biofilm compression in gravity-driven membrane filtration (GDM) has been recorded with optical coherence tomography (OCT) (Desmond et al. 2018d). During dead-end ultrafiltration, the biofilm experiences only compression forces. Several studies correlated biofilm mechanical behaviour and properties (e.g., Young modulus, bulk modulus, relaxation time, etc.) to the different flow conditions: shear forces (i.e., flow parallel to biofilm surface caused by axial flow; (Blauert et al. 2015)), compression forces (i.e., permeate flow perpendicular to biofilm and membrane surfaces; (Derlon et al. 2016)) and simultaneous compression and shear (Valladares Linares et al. 2015)). However, there is still no theoretical description of biofilm deformation under compression forces caused by water permeation.

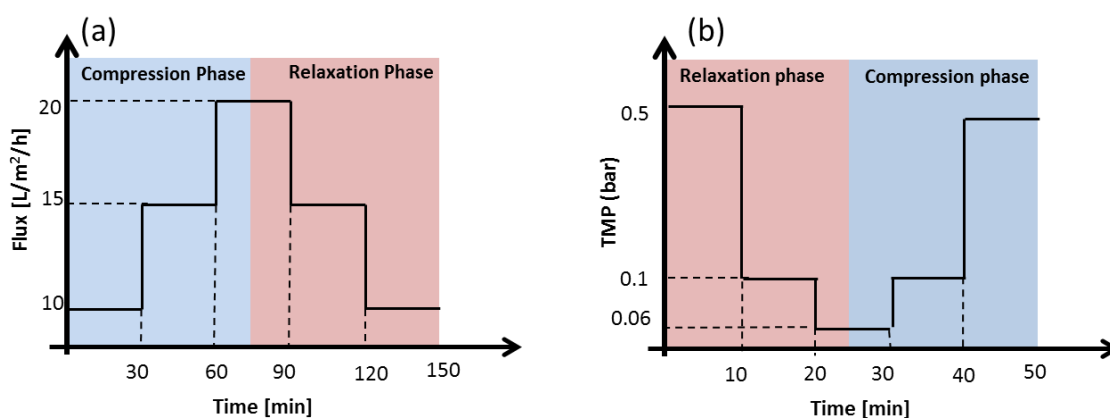
To improve our understanding of biofilm compression and its effect on hydraulic resistance in membrane filtration processes, we formulated a numerical model coupling the permeate flow with the biofilm mechanics.

The numerical model was used to explain experimental observations of changing biofilm thickness and hydraulic resistance under compression and relaxation generated by different applied fluxes and transmembrane pressure in a dead-end ultrafiltration system. Model simulations were also used to extract mechanical and hydrological parameters corresponding to the experimental data. Finally, we evaluated the effect of different mechanical and structural properties of biofilms on the hydraulic response of biofilms to applied permeate flux.

## 2.2 Experimental set-up

### 2.2.1 Biofilm growth and compression setup

Biofilms were grown for 20 days under constant transmembrane pressure (TMP) of 0.06 bar in Membrane Fouling Simulators (MFS) according to Desmond et al. (2018c). Feed waters with different compositions (i.e., river water and synthetic water with phosphorous limitation) were used for the cultivation of the biofilms on membrane surfaces (see **supplementary Information Table 2.S1**). The phosphorous limitation was considered as it is a known strategy for biofouling control in membrane systems (Vrouwenvelder et al. 2010a). The compression/relaxation experiments were performed by step-wise increase/decrease of the permeate flux ( $L/m^2/h$ ) (**Figure 2.1a**) or TMP (bar) (**Figure 2.1b**) to defined values. TMP controlled experiments have been carried out by monitoring pressure at the feed and permeate side, while permeate flux was controlled using permeate mass measurements and PID control.



**Figure 2.1** Schemes of applied loads on the biofilms in this study. a) Step-wise change of permeate flux in time intervals of 30 min for the P-limiting biofilm. b) Step-wise change of transmembrane pressure (TMP) in time intervals of 10 min for the river water biofilm. The time intervals were selected long-enough to collect representative permeate for hydraulic resistance calculation.

### 2.2.2 Compression set-up and membrane preparation

Biofilms which were developed for 20 days under constant TMP of 0.06 bar in six MFS in a gravity driven membrane were subjected to a compression/relaxation scheme in an automated filtration system, as described in details by Desmond et al. (2018c). The automated filtration system was fed with feed waters reflective of the biofilm growth conditions. The filtration system mainly consisted of a gear pump, a transparent MFS (in which biofilms were already developed), measurement scales and PID control system.

Ultrafiltration membranes (UP150, MicrodyN Nadir, Wiesbaden, Germany) with molecular weight cut-off MWCO=150kDa and the equivalent pore size of 30-40 nm were used in MFS units. Membrane coupons were cut and rinsed with 40% ethanol prior to use in MFS.

### 2.2.3 Hydraulic parameters

The biofilm hydraulic resistance  $R_{bio}$  [1/m] was calculated as the difference between the total hydraulic resistance  $R_{tot}$  and membrane resistance  $R_{mem}$ . The total filtration resistance is a function of transmembrane pressure,  $TMP$  [Pa], water viscosity,  $\mu$  [Pa·s] (at 15 °C) and the measured permeate flux  $J$  [m/s] in the presence of biofilm (Darcy's law):

$$R_{tot} = \frac{TMP}{J \mu} \quad (2.1)$$

The bare membrane resistance,  $R_{mem}$ , is the intrinsic resistance measured with nanopure water prior to fouling. The permeate flux in [L/m<sup>2</sup>/h] was calculated from mass measurements of permeate collection, as follows:

$$J = \frac{\Delta m}{\rho_w A \Delta t} \quad (2.2)$$

with  $\Delta m$  the mass of collected permeate [kg],  $\rho_w$  the water density [kg/L],  $A$  the membrane active area [m<sup>2</sup>] and  $\Delta t$  the permeate collection time [h].

### 2.2.4 Biofilm morphology quantification

The morphological response of the membrane biofilms to increasing and decreasing compressive force was measured by means of optical coherence tomography (OCT) (model 930 nm Spectral Domain, Thorlabs GmbH, Dachau, Germany) with a central light source wavelength of 930 nm and refractive index of 1.33 (Desmond et al. 2018c). Quantification of average biofilm thickness and surface roughness were conducted using a customized MATLAB routine (MathWorks, Natick, US).

## 2.3 Model description

A mathematical model was developed to evaluate the effects of biofilm deformation (compression and relaxation) on the biofilm hydraulic resistance under step-wise flux or TMP in dead-end ultrafiltration. The model couples fluid flow in the biofilm considered as porous medium with the structural mechanics of biofilm. The liquid pressure in biofilm pores affects the effective stress in the biofilm and leads to deformation, while the structural deformation changes the permeability and consequently the pore pressure.

### 2.3.1 Model geometry

The biofilms investigated in this study presented mostly a uniform thickness. This implies the main property gradients (e.g., pressure, stress, porosity, permeability) would develop only in the permeate flow direction, i.e., perpendicular to the membrane and biofilm surface (the  $y$  direction). A one-dimensional model would therefore be sufficient to describe both water flow and biofilm mechanics. Uniaxial strain for biofilm mechanics would be consistent with the assumption that no deformation (strain) occurs in the lateral directions  $x$  and  $z$ . However,

in order to conveniently use the computational resources already build in COMSOL Multiphysics, we used a two-dimensional model geometry. A rectangular domain was created with the biofilm thickness expanding in the  $y$ -direction, taking  $L_0$  as initial thickness. The domain was made very short ( $5 \mu\text{m}$ ) in the  $x$  direction parallel with the membrane. When applying symmetry boundary conditions on the lateral boundaries, this is equivalent with a one-dimensional geometry. Finally, the biofilm depth in the neglected third dimension  $z$  was considered large enough to apply the two-dimensional plane-strain simplification. Therefore, we describe here the model equations in the used two-dimensional setup, while the equivalent one-dimensional reduction is presented in the Supplementary Information. The model considered homogeneous biofilm properties in the whole rectangular domain.

### 2.3.2 Fluid flow

The biofilm was assumed a porous medium, where Darcy's law, equation (2.3), and continuity equation (2.4) were applied to compute fluid (i.e., water) velocity and pressure (Helmig et al. 2013, Pintelon et al. 2012)

$$\mathbf{u} = \frac{-K\varphi}{\mu} \nabla p \quad (2.3)$$

$$\frac{\partial \varphi}{\partial t} + \nabla \cdot \mathbf{u} = 0 \quad (2.4)$$

with the local water velocity vector  $\mathbf{u}$ , pressure  $p$ , water viscosity  $\mu$ , biofilm permeability  $K$  and biofilm porosity  $\varphi$ . Biofilm porosity and permeability had to be correlated to the biofilm deformation, in order to represent the effect of structural deformation on the hydraulic resistance and flux. Suppose that the average biofilm porosity scales with biofilm thickness,  $\varphi(t) / \varphi_0 = L(t) / L_0$ , and that compression mainly affects the pores in the permeation direction (i.e., the quasi-1-D assumption). With these assumptions, the average biofilm porosity at each moment of time can be calculated from equation (2.5)

$$\varphi(t) = \varphi_0 \frac{L_0 - \int_0^{L(t)} \varepsilon_y(t) dy}{L_0} \quad (2.5)$$

where  $\varphi_0$  and  $L_0$  are the initial biofilm porosity and thickness, respectively (i.e., under zero-stress conditions). The total biofilm deformation at a certain time,  $\Delta L$ , results from integrating the local strain,  $\varepsilon_y(t)$ , over the whole biofilm thickness  $L$ .

Furthermore, the biofilm permeability was calculated from the power-law relation between porosity and permeability as equation (2.6) proposed by Millington and Quirk (1960b):

$$K = A\varphi^n \quad (2.6)$$

with a biofilm permeability coefficient  $A$  and permeability exponent  $n$ .

In case of the applied step-wise permeate flux, the velocity  $\mathbf{u}=(0, u_y)$  was imposed on the biofilm base at  $y=0$ , where  $u_y$  is the applied velocity (permeate flux) taking several values. A constant pressure ( $p=p_{top}=1$  bar) was set on the biofilm-liquid interface. In case of the applied step-wise TMP, the biofilm-liquid interface was subjected to different pressure values to reach the defined TMP. On the biofilm base the flux was set to values

calculated from  $J = \frac{TMP}{\mu(R_{bio} + R_{mem})}$  as also in (Martin et al. 2014). No-flow conditions were set on the

lateral boundaries in all cases.

### 2.3.3 Solid mechanics

The reversible response of the biofilm under compression and relaxation experiments implies an elastic behaviour (Korstgens et al. 2001a, Paramonova et al. 2009, Stoodley et al. 1999), while the irreversible deformation may be caused by viscous (Galy et al. 2012, Peterson et al. 2015, Safari et al. 2015, Towler et al. 2003) or plastic (Korstgens et al. 2001a) components. The time-dependent response to an applied stress is often described by a viscous term. Therefore, based on the experimental observations, we attribute three mechanical behaviours to the biofilm structural response to normal compression and relaxation: elastic, viscoelastic and elastoplastic.

#### 2.3.3.1 Elastic model

We present here the equations in the general tensor form, while the possible one-dimensional reduction to uniaxial strain is given in Supplementary Information. The biofilm structural mechanics is governed by quasi-static balance of momentum of a linear elastic material, equation (2.7):

$$\nabla \cdot \boldsymbol{\sigma} = 0 \quad (2.7)$$

with  $\boldsymbol{\sigma}$  the effective stress tensor in the biofilm (Lubliner and Papadopoulos 2013, Richards 2000). The constitutive equation (8) relates the stress to elastic forces determined by the stiffness tensor  $\mathbf{C}$  (i.e. Hooke's law, here function of elastic modulus  $E$  and Poisson's ratio  $\nu$ ), but also to internal forces caused by the fluid pressure  $p$  (Coussy 2004):

$$\boldsymbol{\sigma} = -\alpha \mathbf{I} p + \mathbf{C}(E, \nu) : \boldsymbol{\varepsilon} \quad (2.8)$$

In the following it was assumed a Biot-Willis proportionality coefficient  $\alpha=1$ . The strain tensor  $\boldsymbol{\varepsilon}$  can be expressed from the relative biofilm deformation  $\boldsymbol{\delta}$  with respect to the initial biofilm structure, as in equation (2.9):

$$\boldsymbol{\varepsilon} = \frac{1}{2} \left[ (\nabla \boldsymbol{\delta}) + (\nabla \boldsymbol{\delta})^T \right] \quad (2.9)$$

The values of biofilm mechanical properties (i.e.,  $E$  and  $\nu$ ) are highly variable as a result of different biofilm composition (i.e., polymers, cells, etc.) and various types of applied stress (i.e., compression/tensile, shear) (Cense et al. 2006, Galy et al. 2012, Klapper et al. 2002, Peterson et al. 2015, Towler et al. 2003). Therefore, these values need to be estimated directly based on the experimental data obtained in this study. The model parameters are presented in **Table 2.1**.

In case of the applied step-wise permeate flux, a constant pressure  $p_{top}$  was applied on the top boundary, while the biofilm base was fixed (i.e. zero deformation). When a step-wise increase/decrease TMP was applied, the biofilm-liquid interface was subjected to variable pressure  $p_{top}$ , while the biofilm base was also fixed. On the lateral boundaries the deformation was considered parallel to the applied stress (i.e., symmetry conditions). These boundary conditions were applied for all three mechanical models (i.e., elastic, elastoplastic and viscoelastic).

### 2.3.3.2 Elastoplastic model

The permanent plastic deformation occurs when the biofilm is subjected to a stress higher than a threshold value called “yield stress”. The plastic strain  $\boldsymbol{\varepsilon}_p$  must be subtracted from the total strain when used in the constitutive equation (2.10), leading to:

$$\boldsymbol{\sigma} = -\alpha \mathbf{I} p + \mathbf{C}(E, \nu) : (\boldsymbol{\varepsilon} - \boldsymbol{\varepsilon}_p) \quad (2.10)$$

The constitutive description of plastic behaviour included the yield condition ( $F_p = 0$ ) in which the plastic flow begins when von Mises stress  $\sigma_M$  reaches the initial yield stress  $\sigma_{ys0}$  (Öchsner 2016):

$$F_p = \sigma_M - \sigma_{ys0} \quad (2.11)$$

We considered here only the case of ideal plasticity (constant  $\sigma_{ys0}$ , no hardening rule), which described sufficiently well the experimental data. The increment of plastic strain  $d\boldsymbol{\varepsilon}_p$  was calculated using the “associated” flow rule equation (2.12) (Bland 1957, Kelly 2008)

$$d\boldsymbol{\varepsilon}_p = d\lambda \frac{\partial F_p}{\partial \boldsymbol{\sigma}_M} \quad (2.12)$$

which reduces to  $d\boldsymbol{\varepsilon}_p = d\lambda$  for ideal plasticity, with a consistency parameter  $\lambda$  that satisfies the condition

$$F_p = 0.$$

### 2.3.3.3 Viscoelastic model

Mechanical behaviour of biological tissues and especially biofilms is often described by a viscoelastic model (Cense et al. 2006, Galy et al. 2012, Klapper et al. 2002, Peterson et al. 2015, Towler et al. 2003). The viscoelastic behaviour is mainly distinguished by a time-dependent deformation under a constant stress. In linear viscoelastic materials the deviatoric stress ( $\mathbf{C} : \boldsymbol{\varepsilon}$ ) depends on strain history. In this study, we used the *Single-branch Generalized Maxwell* model (Peterson et al. 2015) which consists of a spring and dashpot in series (the viscous term), in parallel with the main branch spring (the elastic term). The main branch stiffness is  $E$ , while the Maxwell branch is characterized by shear modulus  $G_v$  (the spring) and relaxation time  $\tau_v$  (the dashpot). The total stress is thus augmented by viscoelastic stress  $\boldsymbol{\sigma}_v$ :

$$\boldsymbol{\sigma} = -\alpha \mathbf{I} p + \mathbf{C}(E, \nu) : \boldsymbol{\varepsilon} + \boldsymbol{\sigma}_v \quad (2.13)$$

The viscoelastic stress is calculated in terms of strains in spring  $\boldsymbol{\varepsilon}$  and strain in dashpot  $\gamma_v$ :

$$\sigma_v = 2G_v(\epsilon - \gamma_v) \quad (2.14)$$

with the time-dependent dashpot strain calculated from the differential equation:

$$\tau_v \frac{d\gamma_v}{dt} + \gamma_v = 0 \quad (2.15)$$

### 2.3.4 Model solution

The two-dimensional hydro-mechanical model was solved in COMSOL Multiphysics (v5.2, COMSOL Inc., Burlington, MA). The fluid flow in porous media was coupled with plane strain structural mechanics (**Figure 2.2**). Moving mesh accounted for the biofilm deformation. A time-dependent solver was applied on a mapped finite element mesh (a mesh size of 10  $\mu\text{m}$  ensures the mesh convergence). The parameter fitting was implemented by minimizing the error between experimental and model results, using a MATLAB optimization function through the LiveLink™ for MATLAB.

**Table 2.1** Model parameters for biofilm compression/relaxation tests under step-wise permeate flux and TMP.

Parameter	Symbol	P-limiting biofilm	River water biofilm	Unit	Source
Biofilm length	$l$	5	5	$\mu\text{m}$	Chosen <sup>a</sup>
Initial biofilm thickness	$L$	980	157	$\mu\text{m}$	Experimental <sup>b</sup>
Elastic modulus	$E$	324 $\pm$ 7	196	Pa	Fit <sup>b</sup>
Poisson's ratio	$\nu$	0.42	0.42	-	Kundukad et al. (2016)
Initial yield stress	$\sigma_{ys0}$	1900	-	Pa	Fit <sup>c</sup>
Viscous shear modulus	$G_v$	1007.8	-	Pa	Fit <sup>d</sup>
Viscous relaxation time	$\tau_v$	17.4	-	s	Fit <sup>d</sup>
Permeability coefficient	$A$	$\sim 9.9 \times 10^{-16}$	$1.9 \times 10^{-16}$	$\text{m}^2$	Fit <sup>b</sup>
Permeability exponent	$n$	1.3	1.3	-	(Millington and Quirk 1960a)
Biofilm hardening coefficient	$m$	0	0.88	-	Fit
Liquid viscosity	$\mu$	0.001	0.001	Pa.s	Water at 25 °C
Biofilm initial porosity	$\phi_{b0}$	0.99	0.99	-	Chosen

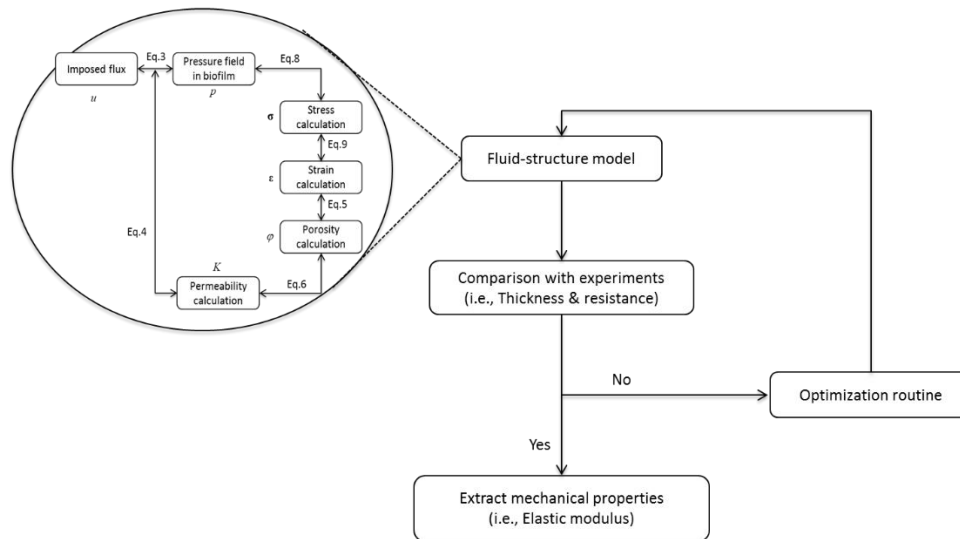
<sup>a</sup> Quasi-one-dimensional model assumption

<sup>b</sup> Values averaged for the three applied models, with standard deviation

<sup>c</sup> Parameters fitted in the elastoplastic model

<sup>d</sup> Parameters fitted in the viscoelastic model





**Figure 2.2** Flowchart of modelling approach used in this study to extract biofilm mechanical properties. Relation between variables in the fully coupled Fluid-structure model were illustrated in an insert. Reverse arrows indicate that model variables are solved simultaneously (parallel).

## 2.4 Results

The biofilm hydraulic resistance depends on biofilm average thickness (depending on local thickness and surface roughness) and permeability. Compression will decrease the biofilm thickness (decreasing resistance), but also decrease the biofilm porosity and permeability (increasing resistance). An increase in biofilm hydraulic resistance decreases in turn the permeate flux.

### 2.4.1 Deformation of P-limiting biofilm under controlled permeate flux

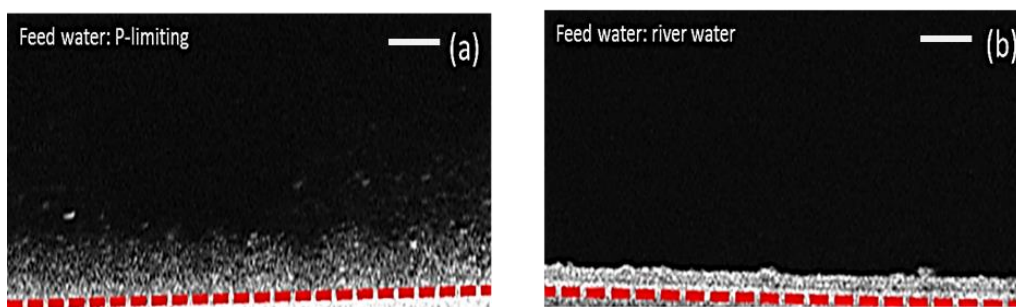
The P-limiting biofilm in this study had a smooth surface structure with very low relative roughness, which could be related to the nutrient-limited growth conditions. The river water biofilm selected for this study had also an smooth surface. **Table 2.2** shows the relative biofilm roughness, growth condition and extracellular polymeric substance concentration (EPS) and **Figure 2.3** presents cross-section images of the studied P-limiting and river water biofilms. The smooth surface biofilm provides a more uniform structural deformation distribution than a biofilm with rough surface. Hence, the homogeneous surface of the biofilms under study provides a valid ground for the plain strain and quasi-one-dimensional model assumptions.

**Table 2.2** Growth condition, roughness for the studied biofilms.

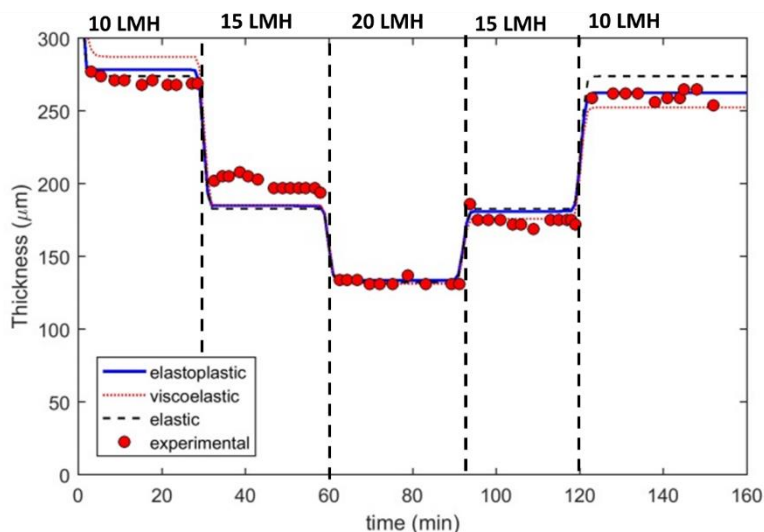
Biofilm	Growth condition C/N/P	Relative surface roughness	EPS Concentration (mg C/m <sup>2</sup> )*
P-limiting biofilm	100/30/0	0.21	676±100
River biofilm	~100/10/10	~0.2	541±15

\*based on measurements by Desmond et al. (2018c)

The measured average thickness of the P-limiting biofilm under step-wise flux change over time is presented in **Figure 2.4**. The biofilm thickness changed immediately after each applied step change in flux and remained constant during each time interval of 30 minutes. During the relaxation phase, the biofilm almost recovers its thickness attained during compression at the same fluxes. This demonstrates the strong elastic component of the biofilm mechanical behaviour. However, a small irreversible biofilm deformation of  $\sim 20\ \mu\text{m}$  is visible during flux change from 10 to 15  $\text{L}/\text{m}^2/\text{h}$  (relaxation phase). The permanent biofilm deformation can be explained by a plastic behaviour. An elastoplastic model was therefore applied to explain the experiments. On the other hand, the permanent deformation can also be explained by a viscous behaviour. However, the fact that the thickness reached the stationary value almost immediately after the change in flux indicates that the viscous relaxation time ( $\tau_v$ ) is smaller than the data acquisition time ( $\sim 3\ \text{min}$ ). Thus, both elastoplastic and viscoelastic models are capable to explain observed results.



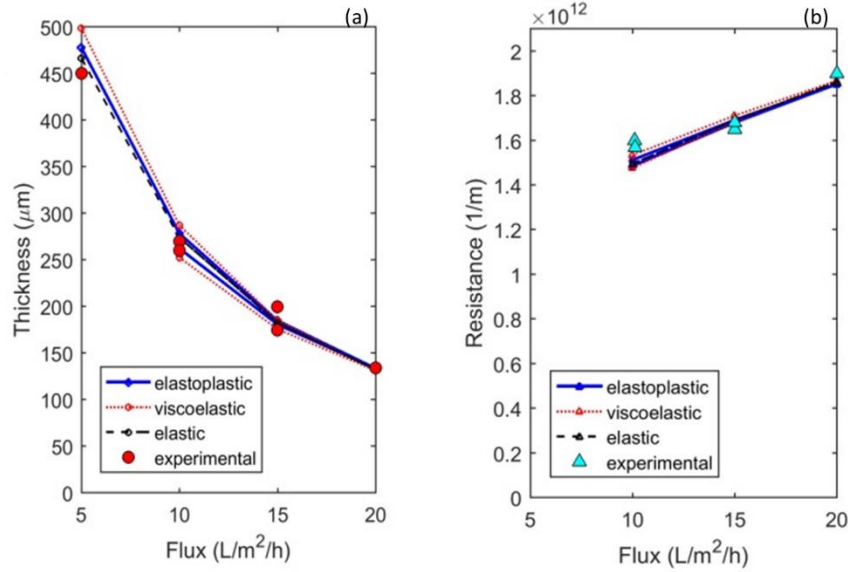
**Figure 2.3** Two-dimensional cross-section images of (a) P-limiting biofilm (at TMP 0.06 bar) and (b) pre-compressed river water biofilm (at TMP 0.5 bar). Both biofilms show a homogenous surface structure. Dashed-line illustrates the biofilm-membrane interface. Scale bar 200  $\mu\text{m}$ .



**Figure 2.4** Experimental (circles) and modelled (lines) thickness of the P-limiting biofilm under step-wise change in permeate flux in a dead-end ultrafiltration (UF) system. The elastic model ( $E=317$  Pa) can explain the reversible deformations, while the elastoplastic ( $E=320$  Pa,  $\sigma_{ys0} = 1900$  Pa) and viscoelastic ( $E=339$  Pa,  $G_v=1008$  Pa,  $\tau_v=17$  s) models describe in addition the irreversible deformation observed in the relaxation phase.

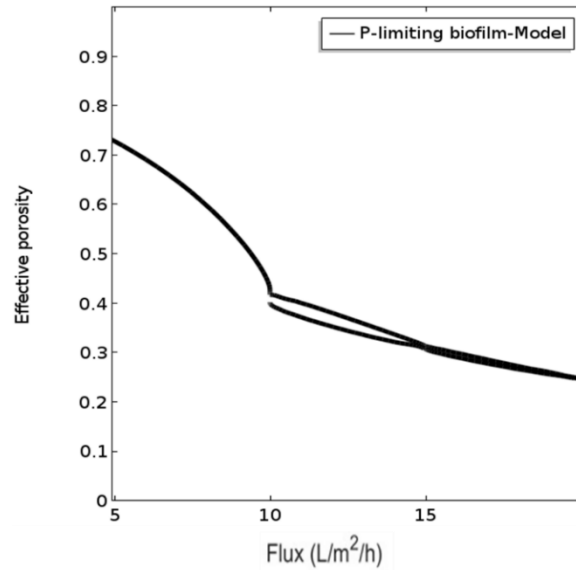
The elastic model represents the data reasonably well and it requires the least number of parameters. The determined value of elastic modulus was 317 Pa with the square root of the averaged sum of squares of errors,  $SRSSE=13.2$   $\mu\text{m}$ . When using the elastoplastic model, a better fit was obtained ( $SRSSE=10.6$   $\mu\text{m}$ ) with  $E = 320$  Pa and  $\sigma_{ys0} = 1900$  Pa. The viscoelastic model also fitted well the data ( $SRSSE=11.3$   $\mu\text{m}$ ) with  $E = 339$  Pa,  $G_v = 1008$  Pa and  $\tau_v = 17$  s. Therefore, in membrane biofilm studies in which a long-term response of biofilm is considered, both viscoelastic and elastoplastic behaviours can equally explain the biofilm response to applied fluxes. However, a simpler elastic model could also describe the observation with only one adjustable parameter instead of two or three.

**Figure 2.5a** demonstrated that thickness reduction of P-limiting biofilm in each identical flux interval is decreased during compression phase ( $\sim 180$ , 80 and 60  $\mu\text{m}$ ). This behaviour indicates a biofilm stiffening phenomenon (“strain hardening”) (Paramonova et al. 2009, Rmaile et al. 2013) during compression. The biofilm compression can be attributed to the permeate drag force, which is induced by the liquid flow (driven by a pore pressure drop across the biofilm). **Figure 2.5a** also shows the initial biofilm thickness  $L_0=450$   $\mu\text{m}$  under the growth conditions at permeate flux around 5 LMH.



**Figure 2. 5** Structural and hydrological properties of the P-limiting biofilm as a function of permeate flux. a) Time-averaged biofilm thickness during a flux step as a function of flux, experimental and evaluated by three mechanical models; b) Hydraulic resistance of the P-limiting biofilm compared with the model calculations. The biofilm thickness at flux 5 LMH is the biofilm thickness under the growth conditions.

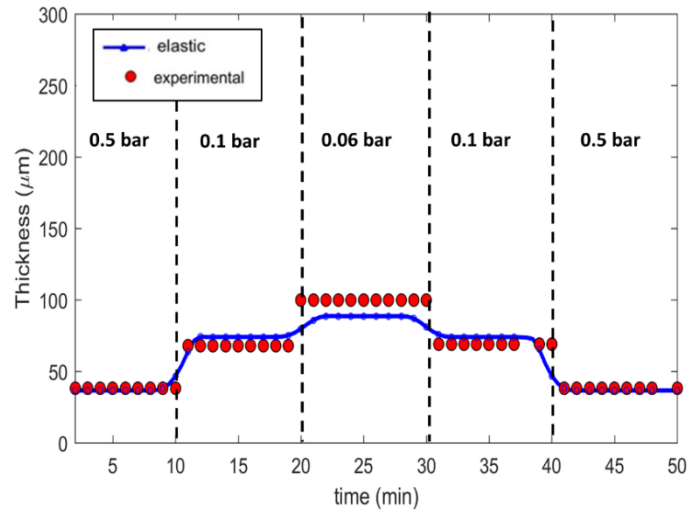
The hydraulic resistance of P-limiting biofilm increases with an increase in permeate flux (**Figure 2.5b**). The biofilm resistance only slightly increased from  $1.5 \times 10^{12}$  to  $1.9 \times 10^{12} \text{ m}^{-1}$  during the flux increase from 10 to 20 LMH. This relatively minor rise in hydraulic resistance while the biofilm underwent significant structural deformation indicates that the decrease in permeability had a greater effect on hydraulic resistance than the biofilm thickness reduction. Consequently, all the proposed mechanical models were able to describe the effect of flux on the biofilm resistance (**Figure 2.5b**). The permeability change under compression can be attributed to biofilm structural re-arrangement and void closure, leading to biofilm porosity decrease. Porosity variation was calculated by eq.(5) and permeability function of porosity was computed by eq.(6). The exponent  $n$  in eq.(6) tunes the slope of the resistance vs. flux curve, with higher  $n$  leading to steeper resistance rise (see Sensitivity Analysis section). The actual porosity change, as calculated, is represented in **Figure 2.6**. The porosity decreased by  $\sim 50\%$  in the compression phase while it could be recovered to nearly its initial value in the relaxation phase (**Figure 2.6**).



**Figure 2.6** Computed (elastoplastic model) porosity variation of P-limiting biofilm under step-wise flux changes in a dead-end ultrafiltration system

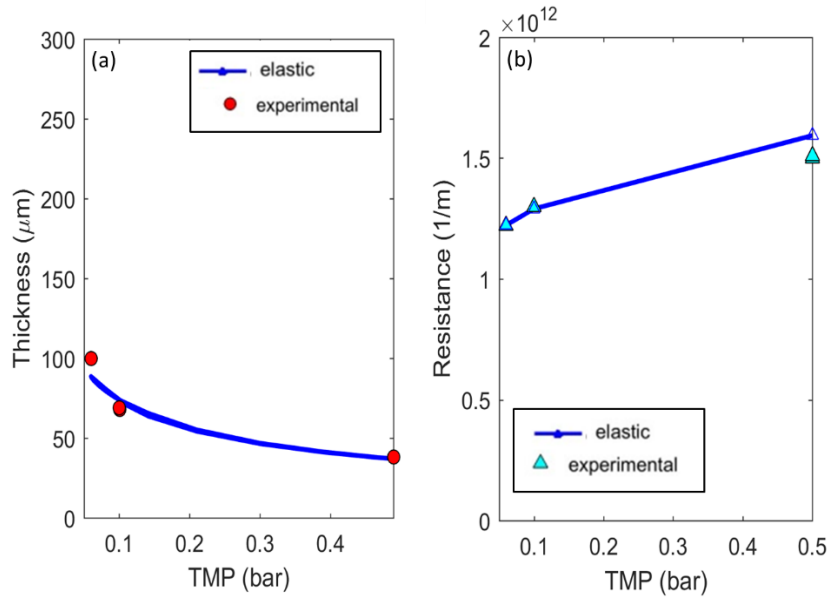
#### 2.4.2 Deformation of river water biofilm under controlled transmembrane pressure

The river water biofilm grown in this study consisted of a mixture of extracellular polymeric substance and cells, as well as particulate matter originating from the influent. The river water biofilm grown in this study included particulate matter originating from the influent, in addition to the typical biofilm composition (mixture of EPS and cells). Biofilms grown under different conditions and influent compositions have different EPS concentration and composition (Desmond et al. 2018c). **Table 2.2** shows the measured EPS concentration of both P-limiting and river water biofilms. EPS concentration was higher for the P-limiting biofilm ( $\sim 676$  mg C/m<sup>2</sup>) compared to the river biofilm with an EPS concentration of  $\sim 541$  mg C/m<sup>2</sup>. The river water biofilm was grown under 60 mbar TMP in a dead-end UF and it has been subjected to the relaxation/compression scheme presented here (**Figure 2.1b**). A cross-section image of river water biofilm structure is illustrated in **Figure 2.3b**. Similar to the P-limiting biofilm, the river water biofilm expresses a reversible structural response and recoverable deformation during the step-wise unload/load cycle, which can be well described by an elastic model (**Figure 2.7**).



**Figure 2.7** Thickness of the river water biofilm exposed to step-wise changes in transmembrane pressure (TMP) in a dead-end UF system. The biofilm response to relaxation and compression caused by applied TMP has been evaluated with the elastic model including material stiffening.

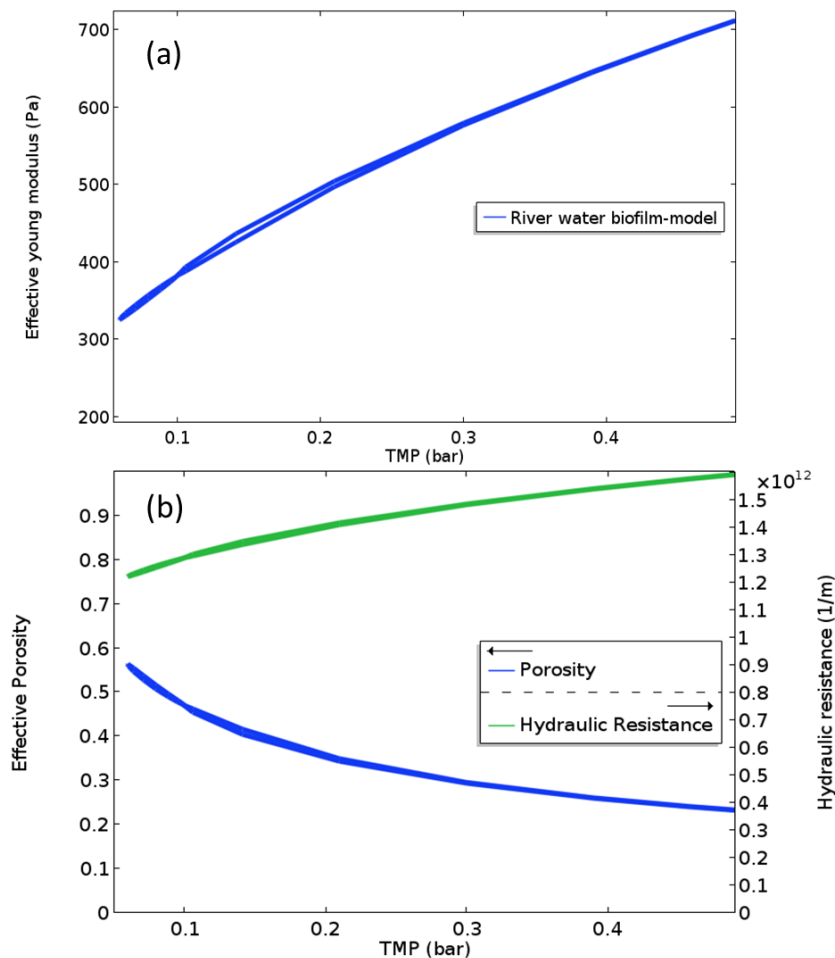
As the applied TMP increased from 0.06 bar to 0.5 bar the biofilm thickness decreases from ~100 to 40  $\mu\text{m}$  (**Figure 8a**). The same strain-hardening mechanism in which biofilm stiffness increases as biofilm deforms can be noted here (i.e., less relative deformation as the TMP increases). The fully reversible biofilm deformation measured in this case implies a fully elastic behaviour. However, due to the nonlinear relationship between stress and deformation, the elastic modulus should increase with a decrease in biofilm porosity. Therefore, we proposed an effective Young modulus  $E_{eff} = E \varphi^{-m}$ . The fitted biofilm hardening coefficient  $m$  was 0.88 and the  $E = 196$  Pa. In this way, the effective Young modulus (i.e., biofilm stiffness) increases from ~300 Pa ( $\varphi = 0.6$ ) to 700 Pa ( $\varphi = 0.25$ ) when TMP increases from 0.06 to 0.5 bar, respectively (**Figure 2.9**).



**Figure 2.8** A comparison between experimental data (symbols) and fluid-structural model results with elastic material behaviour (lines) for the river water biofilm thickness and hydraulic resistance as a function of TMP. a) Time-averaged thickness of the biofilm during TMP steps and model evaluation; b) Hydraulic resistance during TMP steps and model evaluation.

**Figure 2.8b** also shows that the river water biofilm hydraulic resistance increases from  $1.2 \times 10^{12}$  to  $1.5 \times 10^{12} \text{ m}^{-1}$  during TMP change from 0.06 to 0.5 bar. Similar to P-limiting biofilm, a decrease in biofilm porosity due to structural deformation causes a slight increase in hydraulic resistance.

Both homogeneous biofilms in this study presented a reversible and recoverable deformation under applied stress (caused either by controlling the flux or the TMP). The deformation in thickness leads to a change hydraulic resistance due to porosity variation.



**Figure 2.9** a) Computed effective elasticity modulus function of applied transmembrane pressure (TMP). River water biofilms showed stain-hardening properties, in which the biofilm stiffness (Young modulus,  $E$ ) increased at elevated TMP. b) Calculated effective porosity and hydraulic resistance of the river biofilm under step-wise TMP. As TMP increases, the biofilm porosity calculated function of biofilm compression would decrease. Pore closure would lead to an increase in biofilm hydraulic resistance.

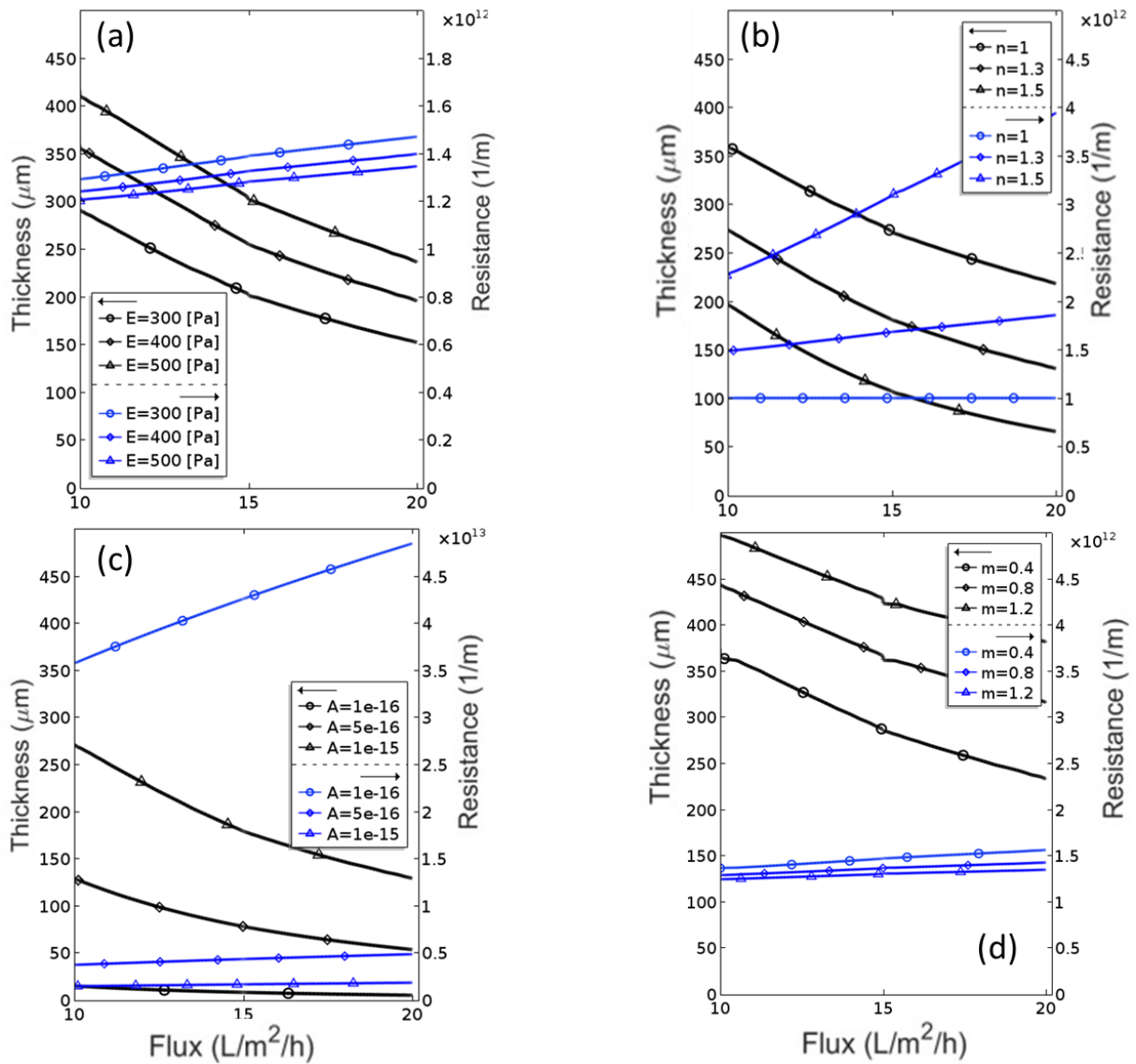
### 2.4.3 Sensitivity analysis

Biofilm thickness and hydraulic resistance are the main structural and hydrological properties determined experimentally in this study. To evaluate how mechanical and permeability properties of the biofilm could influence the biofilm thickness and hydraulic resistance, parametric sensitivity simulations were performed with changes in the Young modulus  $E$  and hardening coefficient  $m$  for the elastic model, shear modulus  $G_v$  and relaxation time  $\tau_v$  for the viscoelastic model, initial yield stress  $\sigma_{ys0}$  for the plastic behaviour, and permeability coefficient  $A$  and exponent  $n$  for the hydraulic model (**Figure 2.10**).

*Mechanical parameters.* Biofilms with a higher value of the elastic modulus  $E$  have greater stiffness and therefore should undergo smaller structural deformation at a given load (i.e. imposed flux or TMP). Increasing  $E$  from 300 to 500 Pa resulted a significant increase in biofilm thickness from  $\sim 150$  to  $250 \mu\text{m}$  at applied flux of 20 LMH (**Figure 2.10a**).



The biofilm hydraulic resistance only slightly decreased for the similar change in elastic modulus (from  $1.45 \times 10^{12}$  to  $1.35 \times 10^{12} \text{ m}^{-1}$ ). The effects of biofilm hardening coefficient,  $m$ , on biofilm thickness and resistance are shown in **Figure 2.10d**, for a river-water biofilm case. Increasing the biofilm hardening coefficient from 0.4 to 1.2 would result in larger biofilm stiffness during the compression phase and a calculated biofilm thickness reduction from 50 to 100  $\mu\text{m}$ , respectively. However, a change in hardening coefficient had only a minor effect on hydraulic resistance, as shown in **Figure 2.10d**. A variation in the other biofilm mechanical properties (i.e. shear modulus  $G_v$  and relaxation time  $\tau_v$  for the viscoelastic model, or the initial yield stress  $\sigma_{y,0}$  for the plastic behaviour) in the range often reported for biofilms had only minor influences on the computed biofilm thickness and resistance (**Figure S1**).



**Figure 2.10** Parametric study of biofilm thickness and resistance over a flux range for different model parameters: a) elastic modulus,  $E$ ; b) permeability exponent,  $n$ ; c) permeability coefficient,  $A$ ; d) hardening coefficient,  $m$ . Black lines refer to biofilm thickness variation and blue line show hydraulic resistance. For

interpretation of the references to colour in this figure legend, the reader is referred to the Web version of this article.

*Hydraulic parameters.* Biofilm hydraulic parameters (i.e. permeability coefficient  $A$  and exponent  $n$  in the permeability dependence on the biofilm porosity, eq. (6)) greatly affected biofilm thickness and resistance during step-wise flux change. Increasing the permeability exponent,  $n$ , from 1 to 1.5 leads to decrease in the biofilm thickness from  $\sim 350$  to  $200 \mu\text{m}$  at  $10 \text{ LMH}$  permeate flux, for the P-limiting biofilm case (**Figure 2.10b**). Practically, the larger the permeability exponent  $n$  the steeper the slope of resistance elevation becomes during permeate flux increase. As expected, the change in biofilm permeability coefficient,  $A$ , lead to an important thickness and resistance variation (**Figure 2.10c**). For example, increasing permeability coefficient from  $1 \times 10^{-16}$  to  $1 \times 10^{-15} \text{ m}^2$  resulted in a biofilm thickness of  $\sim 280$  to  $40 \mu\text{m}$  at permeate flux equal to  $10 \text{ LMH}$ .

## 2.5 Discussion

*Observed relation between biofilm deformation and hydraulic resistance.* It is well experimentally proven that biofilm compression increases the hydraulic resistance and consequently reduces the water permeation through the membrane (Derlon et al. 2016, Desmond et al. 2018c, Dreszer et al. 2013, Dreszer et al. 2014, Valladares Linares et al. 2015). The reversibility in biofilm compression during permeation at changing fluxes or TMPs is related to biofilm composition and morphology (Valladares Linares et al. 2015). *Ex-situ* measurements of biofilm deformation do not provide adequate information on structure dynamics and its effects on biofilm hydraulic resistance, as these only occur in permeation conditions. Thus, applications of microscopy and image processing techniques, particularly OCT but also confocal laser microscopy, for *in-situ* biofilm deformation measurements have attracted attention recently (Blauert et al. 2015, Fortunato et al. 2017). *In-situ* biofilm deformation was measured without permeation under shear forces only (Blauert et al. 2015) or under both permeation and shear force in microfiltration (MF) to evaluate the effect of biofilm compression on the hydraulic resistance (Dreszer et al. 2013). Dreszer et al. (2014) measured biofilm compression and relaxation under step-wise flux change in UF and they observed that biofilm hydraulic resistance significantly increased at elevated permeate fluxes. Later, Valladares Linares et al. (2015) observed biofilm deformation and correlated biofilm thickness under step-wise flux changes in MF to biofilm hydraulic resistance. They observed a clear time-dependent biofilm deformation under permeate flux and interpreted this as a viscoelastic mechanical behaviour. Recently, (Desmond et al. 2018c) measured biofilm thickness using OCT in dead-end ultrafiltration under a step-wise change in permeate flux and TMP. The biofilm in their study was exposed only to compression forces and the effect of shear force could be neglected due to dead-end conditions in the membrane filtration process.

*Biofilm mechanical model.* In the present study, we observe reversible compression for both biofilms (**Figure 2.4** and **Figure 2.7**), which could be explained by a simple elastic model. However, for the P-limiting biofilm some small permanent deformation was recorded, which could be interpreted both as viscoelastic and as elastoplastic behaviour. A viscoelastic biofilm is recognized by the time dependency of deformation under constant load (Peterson et al. 2015). However, data from **Figure 2.4** and **Figure 2.7** demonstrate that the biofilm thickness remained constant under constant applied stress. Still, one should note that in our membrane biofouling study the data acquisition time interval ( $\sim$ minutes) was much larger than the biofilm relaxation time

(~seconds) derived from the experiments by (Valladares Linares et al. 2015). Thus, the permanent biofilm deformation could still be described by a viscoelastic model, while remaining in agreement with a plastic characteristic too. All these lead to the conclusion that the observed mechanical behaviour of the biofilm not only depends on biofilm composition and morphology, but also on the type of applied stress (e.g., shear by flow over the biofilm, compression by permeation flow, etc.) and on the time-scale of observations.

*Biofilm hydraulics.* Hydraulic resistance of biofilms depends on the biofilm structure (e.g., thickness, surface roughness and porosity) and permeability characteristics. **Figure 2.5b** and **Figure 2.8b** demonstrate that biofilm compression is accompanied by a small increase in biofilm hydraulic resistance under elevated flux or TMP. Assuming that the biofilm permeability does not vary due to compression, the biofilm hydraulic resistance should decrease as a result of its thickness reduction. The slight increase in hydraulic resistance clearly indicates that the effect of permeability reduction due to pore closure determines biofilm hydraulic resistance instead of biofilm shrinkage (i.e., shortening the permeation distance). The proposed models thus imply that the biofilm compression mainly occurs by pore shrinkage and that the pores are partially restored during the relaxation phase. Dreszer et al. (2013) and Valladares Linares et al. (2015) reported much stronger increase in hydraulic resistance under elevated fluxes than results of this study presented. Such deviation could be explained by the differences in biofilm morphology among these investigations. Heterogeneous biofilms (i.e., fluffy, filamentous, “mushroom-like”, etc.) in these studies would collapse under applied stress, leading to macro-pore closure or channel blocking, ultimately resulting in a significant rise of hydraulic resistance. Moreover, biofilm structure collapse would lead to irreversible biofilm compression. Since the biofilms in our study had only a low surface roughness, demonstrating reversible and recoverable deformation under compression, accompanied by a slight increase observed in the hydraulic resistance. Therefore, for a biofilm with homogeneous surface (i.e., planar, flat, smooth, etc.), the compression could mainly affect the structural deformation, not the hydrological properties (i.e. hydraulic resistance).

*Biofilm porosity.* The calculated porosity changed significantly during the compression and relaxation cycles (mostly between 0.75 and 0.25, **Figure 2.6** and **Figure 2.9b**). In order to better estimate the model parameters (mechanical and hydraulic), the biofilm porosity would have to be determined independently during the permeation experiments. Measurements of biofilm porosity were reported by Blauert et al. (2015), who estimated a change in 5 to 10% porosity during their shear flow tests – but such measurements would also be needed under permeation conditions. However, it should be noted that biofilm porosity measurement is really challenging for multiple reasons. First, the biofilm fragile structure can be damaged in *ex-situ* techniques. Second, the pore distinction in *in-situ* techniques using image processing can be ambiguous (i.e., grey-scale thresholding, non-repetitive image brightness/contrast, interpretation of grey-scale image, pore distinction criteria, etc.). Finally, the porosity observed by visual/microscopic/imaging techniques - i.e., apparent voids in the biofilm structure - may not be directly correlated with the hydraulic porosity. Thus, back-calculation of biofilm porosity using structural and hydrological properties (i.e., thickness and hydraulic resistance) might lead to more reliable porosity values.

*Biofilm structural hardening.* Biofilm thickness during compression/relaxation phases depends on biofilm composition (i.e., cells, polymers, mineral inclusions, all with different mechanical properties), biofilm

morphology (i.e., surface roughness and porosity) and applied load magnitude and direction (i.e., shear or normal forces). Several studies show how biofilm mechanical properties depend on biofilm composition and morphology (Dreszer et al. 2013, Peterson et al. 2015, Stoodley et al. 1999). Laspidou et al. (2014) demonstrates with a numerical model that the biofilm mechanical properties change during compression and tension tests. They also showed that biofilm mechanical properties can vary with the biofilm structure. All these observations and theories support the definition of effective mechanical properties which integrate biofilm material properties (intrinsic Young modulus, but probably also viscoelastic or elastoplastic parameters) with biofilm hydrological and structural properties (i.e. porosity).

The step-wise flux change experiments showed that biofilm stiffness increases at greater permeation fluxes, leading to smaller thickness reduction during compression. Biofilms in this study showed a strain hardening behaviour that can be represented quantitatively by the hardening coefficient,  $m$ . Biofilm with higher values of hardening coefficient become stiffer under applied load (**Figure 2.9a**) and consequently smaller deformation occurs under elevated fluxes (**Figure 2.10d**). The strain-hardening behaviour of biofilms was already reported by (Paramonova et al. 2009) for dental biofilms, similarly described before for rubber-like materials. This tendency could be explained by the fact that at mild compression forces the biofilm pores take up the stress and gradually close, while at higher loads the polymers and cells (harder biofilm constituents) would oppose the applied load. In this respect, Valladares Linares et al. (2015) demonstrated that EPS concentration in the biofilm is a dominant factor in determining mechanical properties and biofilm thickness variation. We proposed here a simple power-law correlation of the elasticity modulus with the porosity,  $E_{eff} = E \varphi^{-m}$ . However, in the literature there are several other alternatives, such as, the Ryshkewitch-Duckworth equation (Ryshkewitch 1953) proposed for porous sintered materials,  $E_{eff} = E \exp(-m \varphi)$ , or the Phani-Niyogi equation (Phani and Niyogi 1987) using another power-law formulation  $E_{eff} = E \left(1 - \varphi / \varphi_{crit}\right)^m$  which implies the existence of a critical porosity at which the Young modulus becomes zero (Blauert 2017).

*Mechanical properties.* Values of Young (elastic) modulus reported in literature vary in a wide range between ~10 to 6000 Pa (Korstgens et al. 2001a, Mohle et al. 2007, Peterson et al. 2015, Stoodley et al. 1999) based on biofilm type and applied mechanical tests. For example, Stoodley et al. (1999) reported elastic moduli between 17 and 240 Pa for biofilms exposed to different shear levels, while (Paramonova et al. 2009) reported similar values of ~ 20 to 200 Pa for dental biofilms also under variable shear. Blauert et al. (2015) reported a shear modulus of around 30 Pa for biofilm under shear stress using OCT and deformation angles, which corresponds to  $E = 80$  Pa when Poisson ratio is 0.4. However, under uniaxial compression, much higher values were reported,  $E \approx 6500$  Pa (Korstgens et al. 2001b). In this study we found elastic moduli  $E$  of ~320 Pa for P-limiting biofilm and ~200 Pa for river water biofilm, well in the range reported in literature. The variation of measured Young modulus can be attributed to different biofilm composition, different mechanical tests (compression, tensile, shear) and also different measurements techniques (rheometer, image processing, etc.). One should note that mechanical properties in this work were calculated for biofilms under compression forces, for which (Aravas and Laspidou 2008) demonstrated that larger values should be obtained compared to shear tests. Moreover, viscoelastic properties fitting data from this study were shear modulus  $G_v \approx 1000$  Pa and biofilm relaxation time

$\tau_v \approx 17$  s. The biofilm relaxation times often reported in literature are in the order magnitude of seconds, in-line with the value reported here (Towler et al. 2003, Valladares Linares et al. 2015). Moreover, biofilm shear modulus ( $G_v \approx 1000$  Pa) is well in the range of the value reported for Maxwell shear modulus for two type of biofilm by Jones et al. (2011).

*Permeability properties.* Although, biofilm structure response to applied forces is greatly influenced by the elastic modulus, its impact on hydraulic resistance did not appear considerable in our study. This again can be explained by the fact that, in homogeneous biofilms, the hydraulic resistance is mainly governed by porosity change by pore closure and not by thickness decrease. On the other hand, sensitivity analysis simulations showed that the biofilm permeability coefficient,  $A$ , and permeability exponent,  $n$ , determine the biofilm hydraulic resistance (**Figure 2.10b,c**). Increasing values of  $A$  and  $n$  would result in higher permeability and therefore higher stress exerted on the biofilm leading to a considerable structural deformation, as well as permeability change. The correlation proposed here between biofilm permeability and porosity can be applied for biofilms with high surface roughness but with a higher value of exponent coefficient,  $n$ .

*Future research.*

To increase accuracy of experimental results and model validation more number of TMP steps need to be evaluated. In the current study, TMP steps selection were facing three main problems: 1) make sure that compression would occur in the smaller range of TMP; 2) lower TMP steps would result a very small change in the collected permeate mass (used in the calculation of biofilm resistance) and, consequently, the changes in hydraulic resistances for different TMP steps would be negligible and results would become doubtful; 3) another issue for smaller TMP steps was that reaching a stable TMP value in a small step was difficult with the existing PID control system. Therefore, the proposed approach in the study of biofilm compressibility should be evaluated for a wider TMP range and more TMP steps.

Knowledge of biofilm mechanics is essential to optimize physical cleaning strategies such as shear cleaning (i.e., order of forward flush and backwash cleaning depending on fouling layer compressibility) (Hilal et al. 2005), air bubble cleaning (Wibisono et al. 2014), air/water jet cleaning (Fabbri et al. 2016, Safari et al. 2015). Such Non-invasive methodologies to obtain biofilm mechanical properties should be developed. For this aim, OCT data coupled with a fluid-structure numerical model can provide an opportunity to estimate biofilm mechanical properties in a non-destructive way. The present work focused on uniaxial biofilm compression driven by flow. A fully coupled fluid-structural model for heterogeneous surface biofilm also needs to be developed, in order to use the two- or three-dimensional datasets obtainable by OCT. In this way, the spatial variation of mechanical properties within heterogeneous biofilms could be estimated. For such a goal, experimental determination of local deformations in the biofilm is needed (for example, by using embedded particles (Galy et al. 2012) or other particle tracking methods). Development of more complex material models to simulate deformation non-linearity may be required. Coupling biofilm mechanics with flow, would also need the development of reliable experimental techniques to measure biofilm hydraulic porosity.

## 2.6 Conclusions

- A poroelastic computational model which couples water permeation through the biofilm with the biofilm mechanics was developed to correlate the structural deformation with biofilm hydraulic resistance.
- Mechanical and hydraulic biofilm properties were estimated based on the data obtained in compression/relaxation cycles, with a fully coupled fluid-structural model.
- The hydraulic resistance of the smooth surface biofilms (e.g., grown in P-limiting conditions) under compression was affected more by permeability decrease due to pore closure than by a decrease in thickness.
- In membrane biofilm compression studies with sampling time step larger than the biofilm relaxation time, both viscoelastic and elastoplastic models could describe the permanent biofilm deformation. For biofilms under study, due to the small irreversible deformation, a simpler elastic model could also be used.
- The elastic moduli fitting the measured data were in agreement with other reported values for biofilm under compression. Biofilm stiffening under larger flow-driven compression forces was observed and described numerically by correlating inversely the elastic modulus with biofilm porosity.

## 2.7 Acknowledgements

This study was funded by European Union's Horizon 2020 research and innovation programme under the Marie Skłodowska-Curie grant agreement No. 676070 and the Swiss National Science Foundation BIOMEMBRA project, grant No. 149648. This communication reflects only the authors' view and the Research Executive Agency of the EU is not responsible for any use that may be made of the information it contains.



# 3

## **Biofilm compressibility in ultrafiltration: A relation between biofilm morphology, mechanics and hydraulic resistance**

“Science may be described as the art of systematic over-simplification”

Karl Popper

---

This chapter published as: Jafari, M., Derlon, N., Desmond, P., van Loosdrecht, M.C.M., Morgenroth, E. and Picioreanu, C. (2019) Biofilm compressibility in ultrafiltration: A relation between biofilm morphology, mechanics and hydraulic resistance. *Water Res* 157, 335-345.



## Abstract

Poroelastic fluid-structure interaction models were coupled to experimental data to determine the effects of biofilm spatial distribution of mechanical and hydraulic properties on the biofilm hydraulic resistance and compressibility in membrane filtration processes. Biofilms were cultivated on ultrafiltration membranes for 20 and 30 days under high (0.28 bar) and low (0.06 bar) transmembrane pressure (TMP), in dead-end filtration mode. Subsequently, biofilms were subjected to a compression/relaxation cycles by step-wise TMP changes. Structural deformation of biofilms during compression was observed *in-situ* using optical coherence tomography.

Experimental results show that the observed increase in the biofilm hydraulic resistance during compression is not necessarily accompanied by a detectable biofilm thickness reduction. A dual-layer biofilm model with a dense base and porous top layer could explain these observed results. Because porosity controls indirectly the mechanical response of biofilms under compression, results could be described without assuming a gradient in mechanical properties within the biofilm. The biofilm surface roughness did not significantly influence the water flux in this study. However, the fraction of biofilm base layer directly exposed to bulk liquid could be a good indicator in the determination of water flux. The main implications of this study for the design and operation of low-pressure membrane systems (e.g., MF and UF with fouling layer being the main filtration resistance) lays in the selection of favorable operational TMP and biofilm morphology.

### 3.1 Introduction

Biofilm formation causes additional hydraulic resistance that adversely impacts water production in membrane systems (McDonogh et al. 1994, Radu et al. 2010). In membrane systems such as microfiltration (MF) and ultrafiltration (UF), biofilm resistance is the main filtration resistance (Dreszer et al. 2013, Ko and Pellegrino 1992, Martin et al. 2014). Biofilms are often described as porous media consisting of several layers with different properties, such as density (Zhang and Bishop 1994), porosity (Gao et al. 2011a, Okabe et al. 1998, Rosenthal et al. 2018) and elastic modulus (Aravas and Laspidou 2008, Picioreanu et al. 2018). In general, biofilm porosity increases with the distance from substratum, whereas the biofilm elastic modulus (or rigidity) seems to have an opposite trend.

The spatial distribution of porosity and mechanical properties affect the biofilm permeability, as well as the structural responses under compressive forces. Biofilm compression has been often described as the main cause of changes in biofilm hydraulic resistance during water filtration (Derlon et al. 2016, Dreszer et al. 2013, Jorgensen et al. 2017, Poorasgari et al. 2016, Valladares Linares et al. 2015). Indeed, as biofilms are subjected to larger forces (e.g., higher transmembrane pressure, TMP) biofilms undergo a decrease in thickness and surface roughness (Derlon et al. 2016, Derlon et al. 2014, Desmond et al. 2018d, Dreszer et al. 2014, Valladares Linares et al. 2015) leading to a reduction in biofilm porosity (Blauert et al. 2015) and permeability (Derlon et al. 2016, Desmond et al. 2018d). The magnitude of the increase in hydraulic resistance upon compression depends on biofilm composition (e.g., EPS concentration and composition) (Desmond et al. 2018a, Herzberg et al. 2009), growth conditions (e.g., operational TMP and growth time) (Derlon et al. 2016, Dreszer et al. 2014, Poorasgari et al. 2015) and operation mode (e.g., dead-end and cross flow). Poorasgari et al. (2015) reported an increased hydraulic resistance of the fouling layer under elevated TMP during dead-end filtration, without correlating this to the physical structure of the fouling layer. Dreszer et al. (2013) also reported that biofilm hydraulic resistance increases at higher permeate fluxes. However, Dreszer et al. (2013) calculated the biofilm thickness based on biofilm weight per specific area, meaning that compression effects on biofilm morphology could not be detected.

Later developments of *in-situ* imaging techniques such as optical coherence tomography (OCT) enabled researchers to study biofilm development (Wagner et al. 2010, Wang et al. 2017) and structural deformation in real-time during compression (Blauert et al. 2015, Desmond et al. 2018d). Biofilm thickness and hydraulic resistance were correlated using *in-situ* OCT imaging techniques during MF process (Dreszer et al. 2014). It was observed that the biofilm hydraulic resistances increased at larger permeate fluxes and the resistance returned almost to its original value as compression forces were released. However, in the study of Dreszer et al. (2014) the severe changes in resistance were only accompanied by a slight change in biofilm thickness. Valladares Linares et al. (2015) also related the change in hydraulic resistance of MF biofouling to the biofilm thickness and structural deformation through OCT imaging. Furthermore, Derlon et al. (2016) measured increased biofilm hydraulic resistance with increasing TMP during a dead-end UF system. The correlation between biofilm resistance, biofilm thickness and biofilm roughness was later studied by Desmond et al. (2018d) in a gravity-driven membrane (GDM) system. They observed that the increase in hydraulic resistance is accompanied by a reduction of biofilm relative roughness (based on OCT images) during compression of

several model biofilms. Interestingly, they also reported that the increase in hydraulic resistance of a river water biofilm could not be correlated to changes in biofilm thickness and roughness. Recently, Jafari et al. (2018) proposed a fluid-structural model that can explain the structural and hydrological responses of a smooth surface biofilm to compression during water filtration in membrane systems. The numerical model enabled the quantification of mechanical and hydrological properties of different biofilms.

The relation between structural deformation and hydraulic resistance during compression of biofilms with different morphologies (e.g., surface roughness) is not still clear. Therefore, this study aims at evaluating membrane biofilm compressibility and the corresponding changes in biofilm hydraulic resistance as a function of: i) biofilm growth conditions (i.e., growth time and growth TMP); ii) spatial distribution of mechanical and hydrological properties in the biofilm, and iii) biofilm surface roughness. To this goal, a computational model was developed and supported by experimental results.

## 3.2 Experimental set-up

### 3.2.1 Biofilm cultivation and growth conditions

Biofilms were cultivated in a flow cell under dead-end ultrafiltration mode with the membrane effective area of 18.75 cm<sup>2</sup>. Biofilms developed from filtration of river water (Chriesbach river, Dübendorf, Switzerland) during winter, under growth conditions listed in **Table 3.1**. The detailed characteristics (Total organic carbon, dissolved organic carbon, assimilable organic carbon, etc.) of feed water used for biofilm growth can be found in (Derlon et al. 2013) and in supplementary information **Table 3.S1**. In the first experiment, we evaluated the effect of biofilm age (20 and 30 days), when grown under constant transmembrane pressure (TMP = 0.06 bar). In the second experiment, the effect of TMP (0.06 and 0.28 bar) during biofilm growth was studied. To evaluate data reproducibility, biofilms were grown in several parallel flow cells in each growth condition.

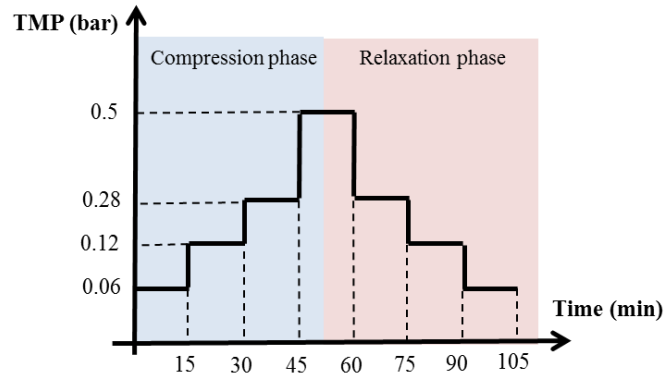
**Table 3.1** Experimental conditions used in this study.

Experiment	Name	Growth time [days]	Growth TMP [bar]	Number of parallel flow cells
(1) Effect of growth time	<i>E1</i>	20	0.06	4
	<i>E2</i>	30		3
(2) Effect of growth TMP	<i>E2</i>	30	0.06	3
	<i>E3</i>		0.28	3

### 3.2.2 Biofilm compression experiments

The biofilms grown in parallel flow cells were subjected to the compression/relaxation tests consisting of gradual increase/decrease of TMP to specific values, as defined in **Figure 3.1**. Biofilms were subjected to an identical compression and relaxation cycle regardless of their growth TMP. The TMP range (between 0.06 to 0.5 bar) was selected based on practical implications and construction limitations GDM systems. Biofilms were

discarded after one compression/relaxation test. All compression tests were done in a 20 °C temperature-controlled room.



**Figure 3.1** Loads were applied on the biofilms by a step-wise change of TMP (compression/relaxation phases) in intervals of 15 minutes.

### 3.2.3 Hydraulic parameters

The permeate flux in [L/m<sup>2</sup>/h] was calculated from mass measurements of collected permeate. The biofilm hydraulic resistance  $R_{bio}$  [m<sup>-1</sup>] resulted from the difference between the total hydraulic resistance  $R_{tot}$  and membrane resistance  $R_{mem}$ , as explained in Martin et al. (2014). The total filtration resistance was calculated through Darcy's law based on applied TMP and the measured permeate flux in the presence of biofilm (Jafari et al., 2018). The intrinsic membrane resistance,  $R_{mem}$ , was measured with nanopure water for 24 hours prior to fouling.

### 3.2.4 Biofilm morphology quantification

The morphological response of biofilms to compression forces was determined by means of optical coherence tomography (OCT) (Ganymede GAN210, Thorlabs GmbH, Dachau, Germany), light source center wavelength of 930 nm and refractive index of 1.33. In order to improve statistical certainty of biofilm morphological properties, at least 10 images were taken at random locations in each flow cell, at each pressure step. Mean biofilm thickness and surface roughness were quantified using a customized MATLAB routine (MathWorks, Natick, US). Mean absolute surface roughness ( $\delta_{abs}$ ) shows biofilm thickness variability averaged for a number of image locations, according to equation (3.1). Moreover, mean roughness coefficient ( $\delta_{rough}$ ) was calculated, which indicates biofilm thickness distribution normalized to mean biofilm thickness based on equation (3.2) (Murga et al. 1995)

$$\delta_{abs} = \frac{1}{n} \sum_{i=1}^n |L_f - \overline{L_f}| \quad (3.1)$$

$$\delta_{rough} = \frac{1}{n} \sum_{i=1}^n \frac{|L_f - \overline{L_f}|}{\overline{L_f}} = \frac{\delta_{abs}}{\overline{L_f}} \quad (3.2)$$

where  $n$  is the number of measurements,  $L_f$  is biofilm local thickness and  $\overline{L_f}$  is the mean biofilm thickness.

### 3.3 Model description

#### 3.3.1 Model geometry and physics

The mathematical model used to correlate the biofilm structural deformation with the corresponding changes in hydraulic resistance during compression was presented in details in (Jafari et al. 2018), therefore the model is here only briefly described. In this poroelastic model, fluid flow in the biofilm was reciprocally coupled to the structural mechanics of the biofilm. The gradient of liquid pressure in biofilm pores affects the effective stress in the biofilm and leads to structural deformation, while the deformation changes the permeability and consequently the pore pressure.

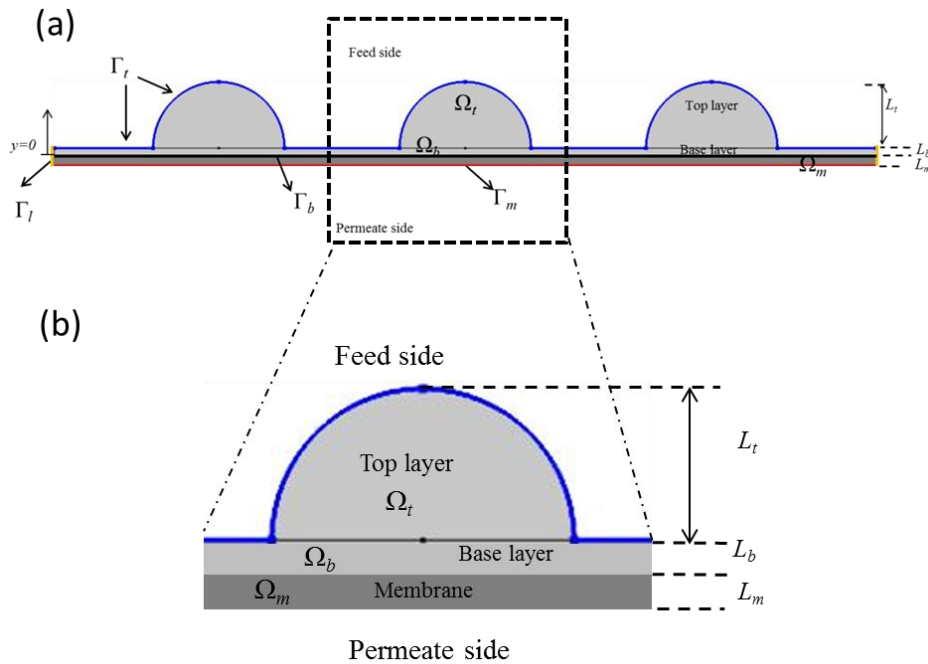
Due to the dead-end filtration mode, the biofilm properties would change mainly in the direction of permeate flow (i.e., perpendicular to the membrane). However, a two-dimensional (2-D) model was developed to evaluate the effect of biofilm surface roughness on permeate flux and biofilm deformation (**Figure 3.2**). Two different geometries were used to represent both smooth (cases 1 and 2) and rough surface biofilms (cases 3 to 6 in **Table 3.2**). Average biofilm thickness ( $L_f$ ) and biofilm length ( $L_x$ ) of the model biofilms were based on experimental results. The membrane was represented by an additional layer with thickness,  $L_m$ . The biofilm base layer thickness  $L_b$  and top layer thickness  $L_t$  in the bi-layer model biofilm were constructed so that the sum ( $L_b+L_t$ ) equals the average thickness ( $L_f$ ). In case of smooth-surface biofilm (cases 1 and 2) the model could in principle be reduced to one-dimension (Jafari et al. 2018), however, for consistency, we kept the 2-D model geometry for all six cases. Finally, the biofilm depth in the third dimension ( $z$ ) was considered to be large enough to apply the 2-D plane-strain simplification (Coussy 2004).

The velocity and pressure fields for water flow through the biofilm were calculated from Darcy's law, with permeability  $K$  being related to biofilm porosity  $\varphi$  by a linear relationship  $K=A\varphi$  in which  $A$  is the biofilm permeability coefficient. Under compression, local biofilm porosity  $\varphi(x,y)$  is related to the porosity prior to compression,  $\varphi_0$ , and biofilm displacement gradient in the compression direction (i.e., local strain in y-direction,  $\varepsilon_y$ ) through equation (3.3) (MacMinn et al. 2016)

$$\frac{\delta d_y}{\delta y} = \varepsilon_y = \frac{\varphi - \varphi_0}{1 - \varphi_0} \quad (3.3)$$

The biofilm displacement tensor  $\mathbf{d}$  resulted from the balance of momentum for a saturated porous material (Biot poroelasticity, (Coussy 2004)). The linear elastic response depends on the elastic modulus  $E$  and Poisson's ratio  $\nu$  of the biofilm. In case of bilayer biofilms, different hydraulic and/or mechanical properties

were applied in each layer. Applied boundary conditions are presented in **Figure 3.2** and all model parameters are in **Table 3.3**.









**Figure 3.2** General model geometry for rough-surface biofilm.  $\Omega_t$ : top layer domain;  $\Omega_b$ : base layer domain and  $\Omega_m$ : membrane domain (not represented at scale here). Liquid flow was calculated in all the domains while structural mechanics was applied only to  $\Omega_b$  and  $\Omega_t$  domains.  $\Gamma_t$ : top layer boundary was set to constant pressure (0.5 bar);  $\Gamma_b$ : base layer boundary conditions were set to zero deformation;  $\Gamma_m$ : permeate side subjected to zero relative pressure so that the TMP matched the value used in the experiment and  $\Gamma_l$ : symmetry conditions were applied to the lateral boundaries. The zoomed geometry shows part of the model geometry including one cluster with different domains.

### 3.3.2 Model cases and their structure

Six biofilm cases were selected based on their morphology (rough or smooth surfaces) and structures (mono-layer or bi-layer). Biofilms have different surface roughness properties and multi-layer structure depending on their growth conditions, as reported by Desmond et al. (2018d). They also observed during dead-end filtration that biofilms developed under phosphate limitation had smooth surface and mono-layer structure as opposed of river water biofilms that had rough surface and bi-layer structure (Desmond et al. 2018b). Existence of base layer can be explained by biofilm stratification (densification) adjacent to the substratum (e.g., membrane) caused by different growth condition parameters such as hydrodynamic strengths, carbon sources, organic loading rate and culture time (Bishop et al. 1995, Derlon et al. 2008, Okabe et al. 1996). In addition, biofilm porosity and elastic modulus were selected as distinctive properties in determination of biofilm hydraulic and mechanical behaviour (Jafari et al. 2018). Thus, in this study we selected smooth surface (case 1 and 2) and rough surface biofilms (case 3 to 6). To evaluate the importance of the bi-layer structure, four biofilm cases with different porosity and/or elastic modulus among the layers were set up (cases 2, 4, 5 and 6). **Table 3.2** shows biofilm morphologies and specifications of the six chosen cases.

**Table 3.2** Biofilm geometries and specifications of six case study biofilms.

Case No.	Case 1	Case 2	Case 3
Name	1-F	2-F-(E,φ)	1-R
Model geometry			
specifications	$E = \text{Const.}$ $\phi = \text{Const.}$	$E_b > E_t$ $\phi_b < \phi_t$	$E = \text{Const.}$ $\phi = \text{Const.}$
Case (cont.)	Case 4	Case 5	Case 6
Name (cont.)	2-R-φ	2-R-E	2-R-(E, φ)
Model geometry			
specifications	$E = \text{Const.}$ $\phi_b < \phi_t$	$E_b > E_t$ $\phi = \text{Const.}$	$E_b > E_t$ $\phi_b < \phi_t$

### 3.3.3 Model solution

The 2-D fluid-structure interaction model was solved in COMSOL Multiphysics (v5.3.a, COMSOL Inc., Burlington, MA). The fluid flow in porous media was coupled with plane strain structural mechanics and computed through a stationary solver. Triangular mesh elements had a maximum size of 2 μm, to ensure the solution independency on mesh size.

**Table 3.3** Model parameters for biofilm grown 20 days under TMP = 0.06 bar.

Parameter	Symbol	River water biofilm	Unit	Source
Biofilm length	$L_x$	1000	$\mu\text{m}$	Experimental <sup>***</sup>
Average biofilm thickness before compression (initial)	$L_f$	~40	$\mu\text{m}$	Experimental <sup>***</sup>
Initial top biofilm layer	$L_t$	80	$\mu\text{m}$	Experimental <sup>***</sup>
Initial base biofilm layer	$L_b$	10	$\mu\text{m}$	Experimental <sup>***</sup>
Membrane thickness	$L_m$	200	$\mu\text{m}$	Experimental
Membrane resistance	$R_m$	$4 \times 10^{11}$	$\text{m}^{-1}$	Experimental
Biofilm permeability coefficient	$A$	$1 \times 10^{-17}$	$\text{m}^2$	Fitted
Initial top layer porosity	$\varphi_{t0} (= \varphi_0)^{**}$	0.8	-	Chosen
Initial bottom layer porosity*	$\varphi_{b0}$	0.5	-	Chosen
Elastic modulus of top layer	$E_t (= E)^{**}$	5	kPa	Fitted
Elastic modulus of base layer*	$E_b$	7.5	kPa	Fitted
Poisson's ratio	$\nu$	0.48	-	(Kundukad et al. 2016)

\*Values used in applicable cases

\*\*Values for top layer were used in the cases with constant properties

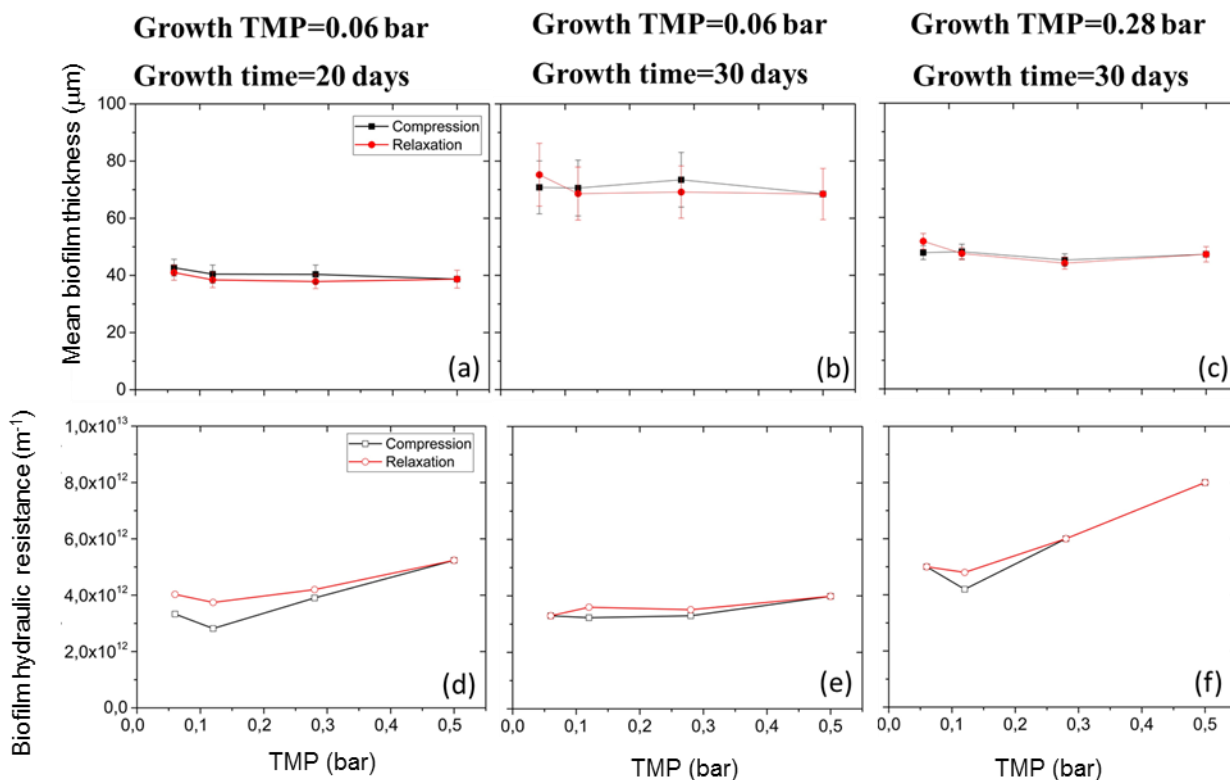
\*\*\* Based on OCT images of the specified biofilm

## 3.4 Results

### 3.4.1 Correlation between biofilm hydraulic resistance and the structural deformation

River water biofilms were cultivated in parallel flow cells, under three different conditions. **Figure 3** shows the biofilm mean thickness and hydraulic resistance measured during a compression and relaxation cycle. As expected, biofilms grown for longer time (30 days) were thicker ( $70 \pm 10 \mu\text{m}$ , average thickness) than younger biofilms ( $40 \pm 3 \mu\text{m}$  after 20 days), under the same growth TMP (0.06 bar) (**Figure 3.3a,b**). Furthermore, biofilms grown under high TMP (0.28 bar) were thinner ( $50 \pm 3 \mu\text{m}$ , average thickness) compared to the low TMP (0.06 bar) biofilms, at the same age (30 days) (**Figure 3.3b,c**). Interestingly, when subjected to compression and relaxation phases, the river water biofilms did not undergo a significant structural deformation (i.e., change in thickness and roughness) (**Figure 3.3a-c**). A relatively constant biofilm thickness is also observed in the time-lapse videos in Supplementary Information, **3.SI-V1** and **3.SI-V2**, while the membrane displacement clearly indicates the applied pressure steps. However, biofilm hydraulic resistance increases significantly during compression over TMP range of 0.06 to 0.5 bar (**Figure 3.3d-f**): from  $3 \times 10^{12}$  to  $5 \times 10^{12} \text{m}^{-1}$  for the biofilm grown at 0.06 bar for 20 days and from  $3 \times 10^{12}$  to  $4 \times 10^{12} \text{m}^{-1}$  for the biofilm developed for 30 days. Biofilms grown under high TMP (0.28 bar) showed greater hydraulic resistance change from  $5 \times 10^{12}$  to  $8 \times 10^{12} \text{m}^{-1}$  during compression tests. These measurements clearly confirm that biofilms grown under higher TMP were more compact (thinner) (**Figure 3.3b,c**) and associated higher hydraulic resistance (**Figure 3.3e,f**).

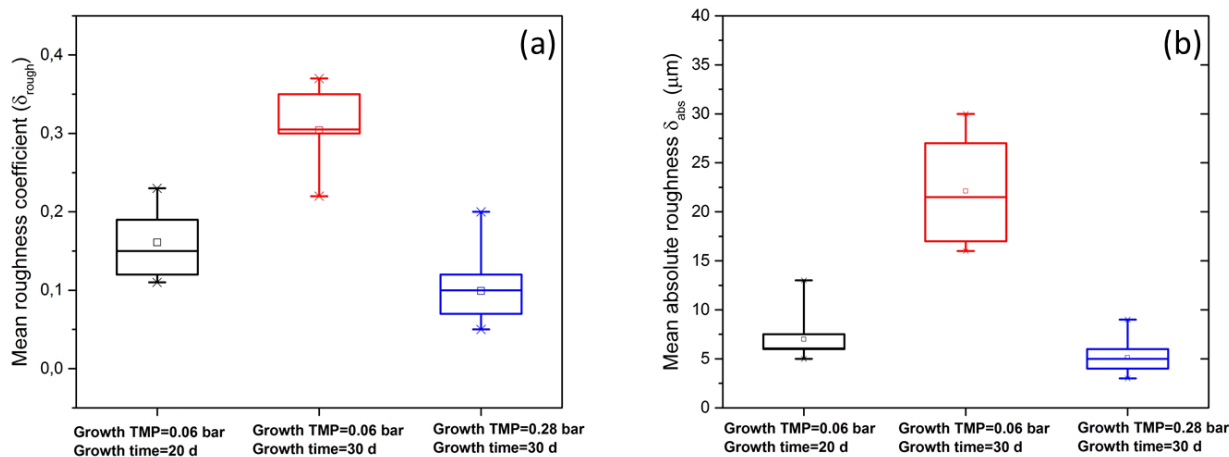




**Figure 3.3** Change in mean biofilm thickness (a-c) and hydraulic resistance (d-f) of river water biofilms during compression/relaxation tests. Biofilms were grown in three conditions: (a,d) TMP = 0.06 bar for 20 days, (b,e) TMP = 0.06 bar for 30 days, (c,f) TMP = 0.28 bar for 20 days. Biofilm thickness was calculated based on minimum of 10 images taken at random locations. See Supplementary Information **Figure S2** for mean biofilm thickness and hydraulic resistance in other parallel flow cells, showing similar trends.

### 3.4.2 Effect of growth conditions on biofilm surface morphology

Experiments in UF flow cells have shown that the growth conditions affect not only the biofilm thickness, but also the biofilm surface roughness. **Figure 3.4** displays biofilm surface morphology properties (i.e., mean absolute roughness and mean relative roughness coefficient) developed in different conditions. Clearly, the biofilms after 30 days of cultivation showed higher roughness coefficient ( $\delta_{\text{rough}} = 0.3 \pm 0.05$ ) than after 20 days ( $\delta_{\text{rough}} = 0.16 \pm 0.05$ ) when grown under TMP = 0.06 bar (**Figure 3.4a**). Moreover, the biofilms grown at larger pressure were smoother ( $\delta_{\text{rough}} = 0.11 \pm 0.05$ ) compared to biofilms grown at low pressures (**Figure 3.4a**). Similar trend was observed in biofilm mean absolute roughness (**Figure 3.4b**). However, change in the biofilm roughness measured during compression of river water biofilms did not follow any clear trend (as also reported in other studies, e.g. Desmond et al (2018)).

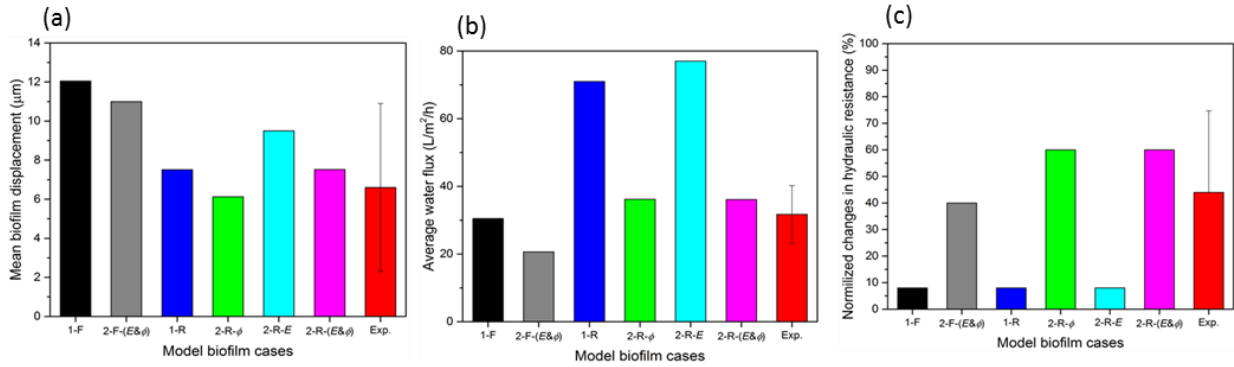


**Figure 3.4** Effect of cultivation TMP (0.06 and 0.28 bar) and biofilm age (20 and 30 days) on the biofilm roughness properties. (a) Mean roughness coefficient and (b) mean absolute roughness, both increase with cultivation time and decrease with cultivation TMP. Results represent deviations for minimum 10 images taken at different locations in the same flow cell.

### 3.4.3 Selection of a fluid-structure biofilm model correlating thickness and resistance under compression

Experimental measurements of river water biofilms under compression showed a considerable increase in hydraulic resistance (up to  $\sim 60\%$ ), while biofilm thickness only slightly changed. To explain the correlation between biofilm thickness and resistance during compression, we developed a fluid-structural model and evaluated several biofilm possible structures with different morphological, mechanical and hydrological properties (**Table 2**). Three main variables (mean biofilm displacement, change in hydraulic resistance and water flux) were calculated and compared with experimental results of biofilm grown for 20 days under TMP=0.06 bar (**Figure 3.5**). The fitting parameters (**Table 3.3**) were selected for each model biofilm individually, so that the three measured variables are optimally represented.

The model results of mean biofilm displacement obtained by *one-layer-rough* (case 3), *dual-porosity-rough* (case 4) and *dual-porosity-elasticity-rough* biofilm models (case 6) are in agreement with experimental results. However, the mean displacement in other model cases was still within range of experimental results (**Figure 3.5a**). Furthermore, the measured water flux was around 20 to 35  $\text{L}/\text{m}^2/\text{h}$ , which is compatible with the calculated flux for *one-layer-flat* (case 1), *dual-porosity-elasticity-flat* (case 2), *dual-porosity-rough* (case 4) and *dual-porosity-elasticity-rough* biofilm models (case 6), **Figure 3.5b**. Finally, **Figure 3.5c** indicates that *dual-porosity-elasticity-flat* (case 2), *dual-porosity-rough* (case 4) and *dual-porosity-elasticity-rough* (case 6) biofilm models could explain a significant increase in hydraulic resistance (40 to 60 %) during compression. Considering all three criteria, the dual-layer rough biofilms (Cases 4 and 6) are the most suitable to explain the experimental results. The difference between cases 4 (constant mechanical properties across the biofilm) and 6 (layers of different elasticity) shows that a gradient of initial biofilm porosity is more important than a gradient of mechanical properties in determination of biofilm deformation and hydraulic resistance during compression. Therefore, case 4 (*dual-porosity-rough*) was selected to further evaluate biofilm local properties during compression, due less model parameters required compared with case 6.



**Figure 3.5** Comparison between the six different models and experimental results of biofilm grown 20 days under  $TMP=0.06$  bar and compressed under  $TMP=0.5$  bar in dead-end UF. This experiment condition was selected as the biofilm under this condition had relatively high surface roughness and a clear change in hydraulic resistance was observed. (a) biofilm mean displacement, (b) water flux and (c) changes in biofilm hydraulic resistance, normalized to the initial membrane resistance.

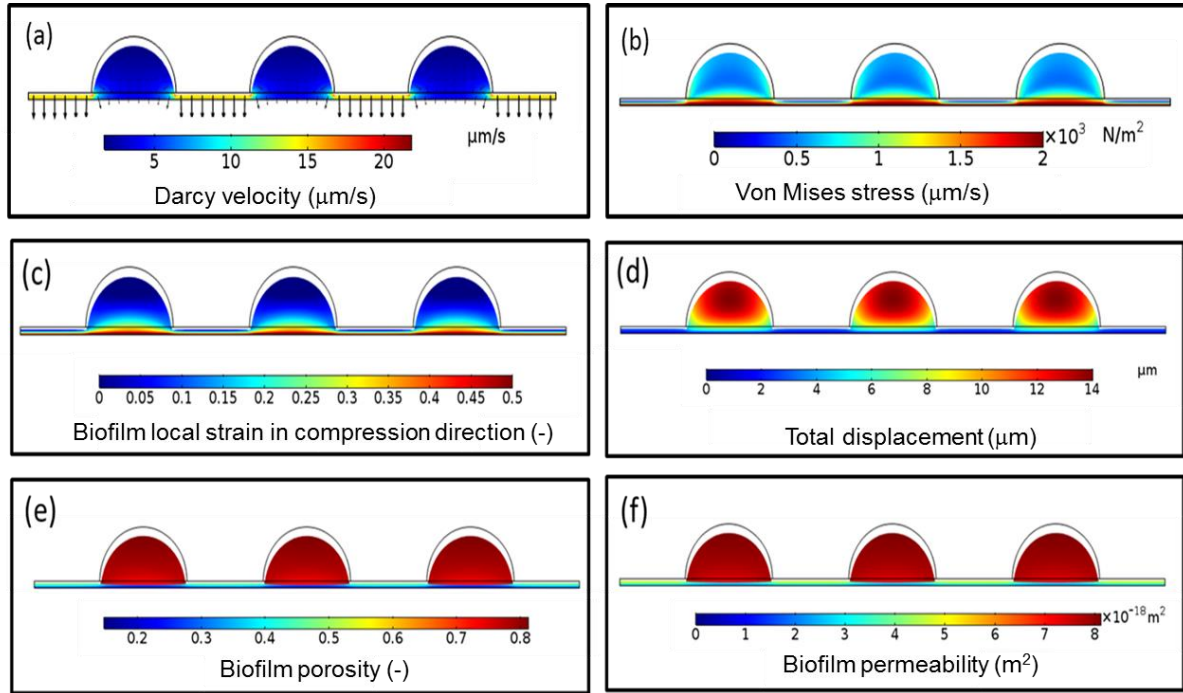
### 3.4.4 Model calibration and parameters estimation

All the model cases were calibrated with experimental results of biofilms grown for 20 days under  $TMP=0.06$  bar. Model parameters used in this study are shown in **Table 3.3**. Geometric parameters (i.e., biofilm average thickness, base and top layers thickness and top layer coverage area) were selected based on OCT images and biofilm morphological properties of the specific biofilm. Initial porosity of top and base layers (if applicable) were chosen with the assumption that porosity of base layer is lower than top layer porosity prior to compression (Gao et al. 2011b). The porosity values and distribution in biofilms were in accordance with the observations reported by (Blauert et al. 2015, Gao et al. 2011b, Wagner et al. 2010). In the model calibration procedure, initial biofilm porosity of both layers (if applicable) was kept constant and only fitting parameters (permeability coefficient, elastic modulus) were changed to calibrate the models. Moreover, during model selection procedure (**Figure 3.5**), a model was considered acceptable only if the model results were within the range of experimental data (considering experimental deviations). For example, in **Figure 3.5a** all the models were acceptable for biofilm deformation due to the large spreading of data in the experiments. Sensitivity analysis of the proposed fluid-structure model to different parameters has been presented in our previous work (Jafari et al. 2018).

### 3.4.5 Local biofilm properties during compression

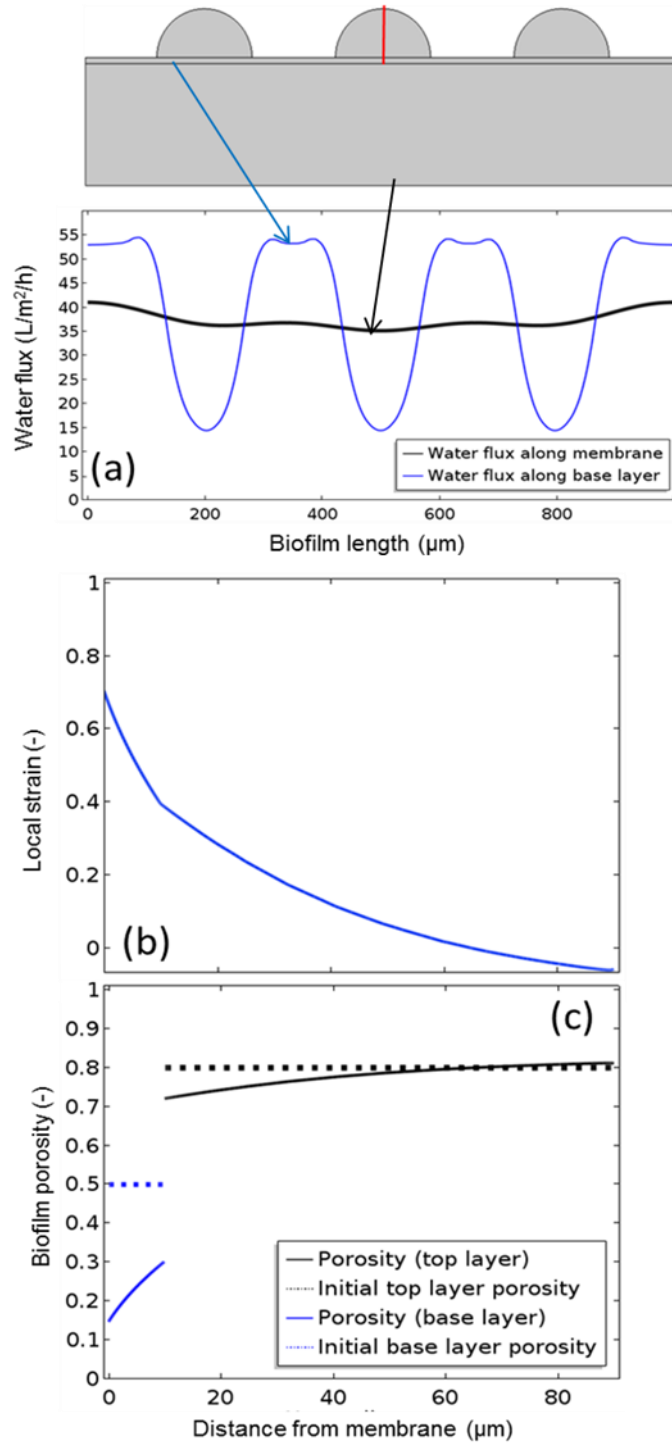
Computed 2-D distributions of the main model variables during compression ( $TMP=0.5$  bar) are presented in **Figure 3.6**. The water flows at higher velocity through the thin biofilm sections ( $\sim 14 \mu\text{m/s}$ ), while the water velocity in the thicker parts (i.e., top layer) is much lower ( $\sim 2 \mu\text{m/s}$ ) (**Figure 3.6a**). As expected, lower biofilm thickness results in lower hydraulic resistance and higher fluxes. The biofilm experiences the highest stress ( $2500 \text{ N/m}^2$ , Von Mises stress) near the membrane, compared to the top layer ( $570 \text{ N/m}^2$ ), as shown in **Figure 3.6b**. In addition, due to large pressure drop, the stress is higher in the thick biofilm parts. Considering the relation of stress and strain, thus, greater local strain is observed in the biofilm next to the membrane (**Figure 3.6c**). The top biofilm layer displaces more ( $13 \mu\text{m}$ ) than the base layer ( $1 \mu\text{m}$ ), due to the cumulative effect of

strain on displacement (**Figure 3.6d**). Higher local strain leads to lower biofilm porosity (**Figure 3.6e**) based on eq.(3) and, consequently, to reduced permeability (**Figure 3.6f**). Although the biofilm top layer porosity remains almost constant ( $\phi=0.8$ ), the base layer undergoes a significant reduction of porosity after compression ( $\phi=0.3$  to 0.15). Similarly, biofilm permeability in top layer remained around  $14 \times 10^{-18} \text{ m}^2$  after compression, while the permeability decreased to  $\sim 1 \times 10^{-18} \text{ m}^2$  in the base layer.



**Figure 3.6** Calculated biofilm local variables after compression. (a) water velocity magnitude and direction in biofilm and membrane; (b) Von Mises stress developed in the biofilm; (c) biofilm strain in compression direction; (d) total biofilm displacement; (e) biofilm porosity; (f) biofilm permeability. Results are based on dual-porosity-rough model (Case 4), with parameters determined for the biofilm grown 20 days under  $\text{TMP}=0.06 \text{ bar}$  and compressed under  $\text{TMP}=0.5 \text{ bar}$ . Membrane domain is not shown.

Spatial distributions of biofilm porosity, permeability and physical structure (i.e., thickness) along the membrane surface cause heterogeneity of water flux along the membrane. **Figure 3.7a** shows a pronounced difference in the calculated water flux at the biofilm base along the flow cell ( $\sim 15$  to  $50 \text{ L/m}^2/\text{h}$ ), whereas the flux is homogenized by flow through the membrane ( $37$  to  $41 \text{ L/m}^2/\text{h}$ ). This considerable difference in flux distribution between biofilm and membrane boundaries (**Figure 3.7a**) is correlated to flux homogenization in membrane domain, caused by lower membrane resistance and greater thickness compared to the biofilm).



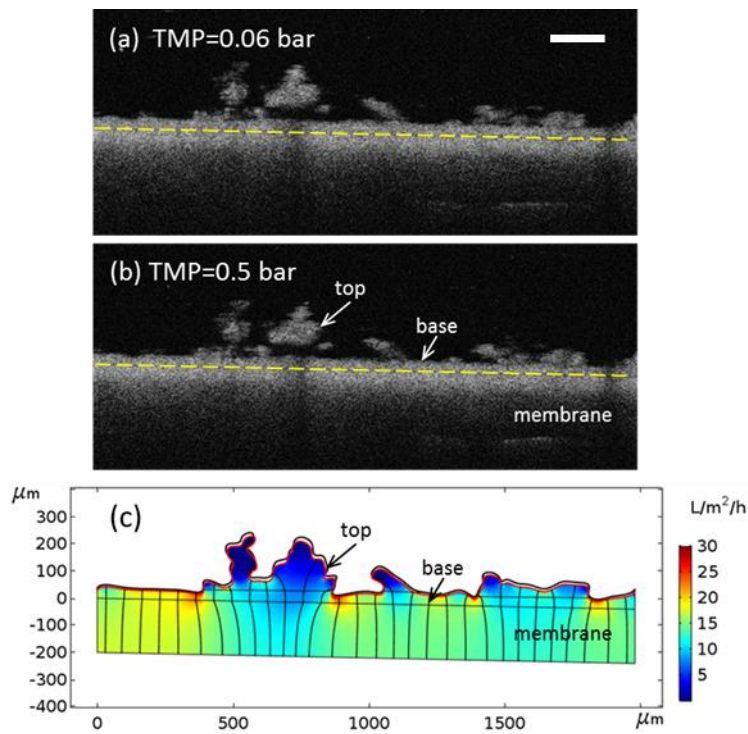
**Figure 3.7** (a) Local permeate flux along the biofilm base (blue line) and permeate side of the membrane (thick black line); (b) Strain in the compression direction in base and top biofilm layers, along the cut line shown in red in (a); (c) Biofilm porosity in base and top layers, along the same cut line. Dotted lines show initial values and solid lines values after compression. Arrows demonstrated the boundaries which water fluxes were computed. Simulation conditions as in **Figure 3.6**.

A more detailed analysis demonstrates that due to distinct biofilm properties in the top and base layers, porosity and permeability undergo different behaviors during compression. **Figure 3.7b** shows biofilm strain in the

compression direction,  $\varepsilon_y$ , across the biofilm depth, after compression at TMP=0.5 bar. The strain decreases from 0.7 at the membrane side to zero at the liquid side. The small change in strain gradient at the base layer/top layer interface is caused by the difference in porosity of the two layers. **Figure 3.7c** demonstrates that the top layer porosity remains almost constant after compression, while biofilm porosity in base layer drastically decreases from its initial value (0.5) to 0.3 in top of base layer and 0.15 at the membrane surface.

### 3.4.6 Evaluation of flux and deformation from OCT biofilm images

Exact biofilm surface geometries (initial and after compression) were extracted from OCT images and the water flux and biofilm deformation were calculated on these geometries using the *dual-porosity-rough model* (case 4). **Figures 3.8a,b** show OCT images of the biofilm under transmembrane pressure of 0.06 and 0.5 bar, respectively. **Figures 3.8a,b** demonstrate that the biofilm underwent a very small deformation during compression (max. 10  $\mu\text{m}$  at the top), while a significant change in hydraulic resistance was observed. Coupling of OCT images with the fluid-structural model allows for the computation of water flux and biofilm deformation under compression on the exact biofilm geometries. Negligible biofilm deformation was calculated under compression, in accordance with OCT results: red line in **Figure 3.8c** shows biofilm surface under compression of 0.5 bar.



**Figure 3.8** (a),(b) OCT images of biofilm structure at TMP=0.06 and 0.5 bar, respectively. The biofilm was grown under TMP=0.06 bar for 30 days. The yellow dashed line represents the membrane/biofilm interface. Scale bar: 200  $\mu\text{m}$ . (c) Computed water flux (colored surface) and streamlines (black lines), using the dual-porosity-rough model (case 4). Black thick line: biofilm surface at 0.06 bar; Red thick line: biofilm surface under compression at 0.5 bar.

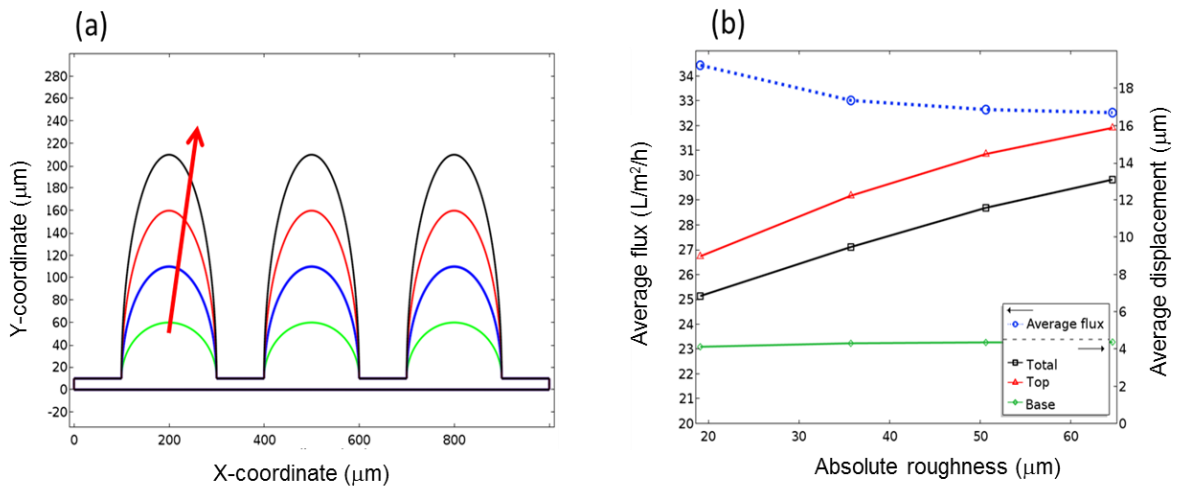


### 3.4.7 Effect of biofilm surface morphology on flux and deformation during compression

#### 3.4.7.1 Biofilm roughness (effect of cluster height)

The numerical model developed for the Case 4 (*dual-porosity-rough biofilm*) was also used to evaluate the effect of biofilm surface roughness on the hydraulics and structural response of the biofilm to the same compression conditions (TMP=0.5 bar). To ensure that the area of base layer in contact with the liquid remained constant, the roughness was increased by changing the half-circular colonies into half-ellipses with increasing semi-major axes (four structures, shown in **Figure 3.9a**).

Increasing the biofilm surface roughness from 20 to 80  $\mu\text{m}$  (i.e., peaks 50 to 200  $\mu\text{m}$  high) resulted in a total deformation from 8 to 13  $\mu\text{m}$ , respectively. **Figure 3.9b** shows that the total biofilm average displacement is mainly determined by the top layer (displaced 10-16  $\mu\text{m}$ ), while the base layer is less compressed (4  $\mu\text{m}$ ). However, more biofilm surface roughness just slightly decreases water flux during compression, from 34  $\text{L}/\text{m}^2/\text{h}$  ( $\delta_{\text{abs}}=20 \mu\text{m}$ ) to 32  $\text{L}/\text{m}^2/\text{h}$  ( $\delta_{\text{abs}}=80 \mu\text{m}$ ). Water flux approached a constant value as the surface roughness increased above 35  $\mu\text{m}$ , which implies that the contribution of top sections to the water flux becomes negligible at high roughness.



**Figure 3.9** (a) Biofilm geometries used to evaluate effect of morphology (arrow shows increased surface roughness) on water flux and biofilm deformation during compression; (b) average water permeate flux and average displacement of different sections of the biofilm. Simulation conditions as in **Figure 3.6**.

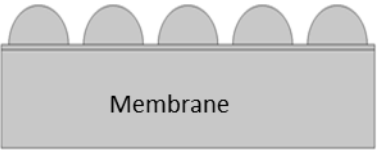
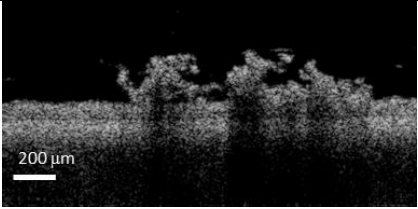
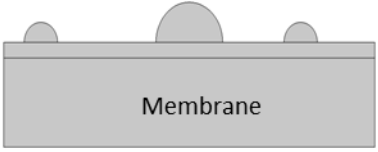
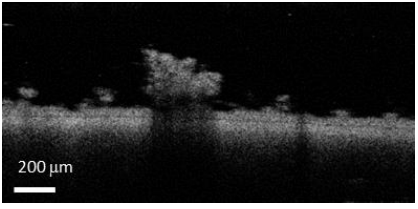

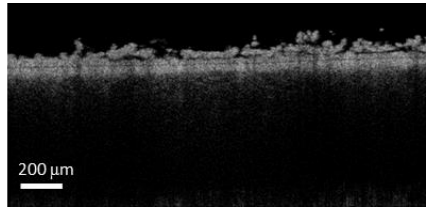
#### 3.4.7.2 Fraction of exposed base layer

Since the biofilm roughness does not significantly impact the permeate flux accordingly to our model results, we also evaluated other potential morphological parameters. The permeate flux during compression was calculated for three biofilm geometries with different morphologies (**Table 3.4**). Biofilm geometries were selected in which have identical average thickness and roughness values, but different fractions of base layer exposed to bulk liquid. To satisfy the mentioned criteria, different top / base layers thickness values were chosen. Fraction of exposed base layer was defined as area of biofilm base layer divided by the total biofilm surface area. The *dual-porosity-rough model* (Case 4) was applied and permeate fluxes were calculated under

TMP=0.5 bar. Model results clearly demonstrate that configurations with higher fraction of exposed base layer (i.e., 0.71 for config. II) allow higher water flux (27.4 L/m<sup>2</sup>/h) compared to 10 and 20.7 L/m<sup>2</sup>/h for config. I and config. III, respectively (**Table 3.4**).



**Table 3.4** Three model biofilm configurations (geometries) with similar morphological properties (average thickness and surface roughness). Biofilms with greater fraction of exposed base layer lead to higher permeate flux. Results are based on dual-porosity-rough model (Case 4 parameters) and compression under TMP=0.5 bar.

Configuration	Model configuration	OCT image	Average thickness	Roughness coefficient	Absolute roughness	Fraction of exposed base layer	Water flux (L/m <sup>2</sup> /h)
Config. I			~53 (μm)	0.48	~25 (μm)	0.2	14
Config. II			~53 (μm)	0.48	~25 (μm)	0.71	27.4
Config. III			~53 (μm)	0.48	~25 (μm)	0.33	20.7

### 3.5 Discussion

*Biofilm hydraulic resistance and structural deformation.* Biofilms grown under high TMP showed higher hydraulic resistance and lower thickness compared to biofilms developed under low TMP (**Figure 3.3**). In addition, biofilms grown under high TMP showed lower roughness values compared to biofilm developed under low TMP (identical growth time) (**Figure 3.4**). This could be explained by higher drag force (induced by higher flux) and consolidation effect caused by the long-term continuous compression under high TMP. These results agree with other reported observations (Casey 2007, Derlon et al. 2016, León Ohl et al. 2004). Biofilms developed under high TMP are likely more compact (i.e., lower porosity), which reduces the biofilm permeability and ultimately increases its hydraulic resistance. In this study we consistently observed that the increase in biofilm hydraulic resistance during compression was accompanied by limited biofilm deformation (**Figure 3.3** and **Supplementary Information, 3.SI-V1 to 3.SI-V2**). A similar trend was also reported previously (Desmond et al. 2018a, Dreszer et al. 2014). One possible explanation for the increased hydraulic resistance would be a reorganization of the biofilm material (McCarthy et al. 2002) at a scale lower than the OCT resolution (thus not observable by OCT), while the biofilm thickness remains approximately constant. Other authors related the larger hydraulic resistance during compression to the collapse of the mushroom-like biofilm structure (Valladares Linares et al. 2015) and the corresponding loss in macro-porosity (Fortunato et al. 2017), with a significant reduction in biofilm thickness. In our study, due to the small measured deformation during compression, we propose that the hydraulic resistance increase was caused by pore/particle reorganization at a scale lower than the OCT detectable threshold. In addition, simulation results confirm that in case of the base layer deformation equal to OCT detectable threshold ( $\sim 3 \mu\text{m}$ ), biofilm hydraulic resistance would rise by 110%, in agreement with the observed results.

*The biofilm model selection.* A bi-layer morphology with a porous layer on top of a thin and dense base layer was observed by Derlon et al. (2016) and Desmond et al. (2018b) for biofilms developed under dead-end GDM. In order to explain the observed trend in biofilm structural deformation and the corresponding hydraulic resistance, several biofilm models were evaluated. The poroelastic numerical model proposed in Jafari et al. (2018) for smooth surface biofilms was extended here to include rough surface with dual-layer properties. **Figure 3.5** confirms that only cases 4 and 6 (i.e., rough and double-layer biofilm, as observed in experimental results from **Figure 3.5**) could explain the small total biofilm deformation associated with significant rise of hydraulic resistance under compression.

*The gradient of porosity across the biofilm is more important than the gradient of elastic modulus for fluid-structural models.* Gradients in biofilm porosity (Blauert et al. 2015, Okabe et al. 1998, Zhang and Bishop 1994) or biofouling layer porosity (Gao et al. 2011a) were reported, with generally a dense base layer and more porous top layer. In this study, both model cases 4 and 6 can explain the observed trends in biofilm compressibility (**Figure 3.5**). However, the model case 4 (i.e., same elastic modulus across both layers) would be preferable as it contains less parameters and thus it is simpler (**Table 3.2**). The comparison between model cases shows that the biofilm deformation is mainly a result of pore compression, and the variable mechanical properties can be achieved by a gradient in porosity. This observation can further be used to simplify development of fluid-structure models. However, one should note that when water is not forced through the biofilm (e.g., biofilm

developed on pipe walls) a gradient in elastic modulus could be important for the mechanical response (as permeate flux and porosity are not relevant) (Picioreanu et al. 2018).

*Biofilm local properties.* Water permeates mostly through the thin parts of the biofilm due to lower hydraulic resistance (**Figure 3.6a 3.7a, 3.8**). This is in accordance with the computations by Martin et al. (2014) for model biofilm in GDM. Fortunato et al. (2017) reported unusual calculation results in which the permeate flux through biofilm peaks is larger than the flux through the thinner parts (biofilm cavities), in a submerged membrane biofilm reactor. They claimed this observation is due to the effect of liquid vortices in biofilm cavities leading to lower pressure gradient. However, their result is physically unrealistic because small axial velocities would only lead to negligible pressure drop compared to the trans-membrane pressure gradient.

During compression, the biofilm porosity decreases mainly in the base layer (near the membrane) (**Figure 3.6e and 3.7c**), which is in agreement with reported results by MacMinn et al. (2016) and Radu et al. (2015b) for soft porous materials under deformation. Thus, during compression of the fouling layer, the base layer permeability decreases much more than in the top layer (due to local porosity reduction). Therefore, the base layer becomes even more important in the determination of water flux. However, not all biofilms may display this bi-layered structure. Desmond et al. (2018b) observed that for biofilms with smooth surface (i.e., synthetic biofilm developed under phosphate-limiting conditions), biofilm hydraulic resistance is determined by the whole biofilm structure and not by a dense base layer.

*Effect of biofilm surface roughness on permeate flux.* Although biofilm surface roughness affected the structural response during compression, its impact on the total permeate flux was not significant (**Figure 3.9**). Again, this could be explained by the fact that the magnitude of the permeate flux is mainly dictated by the base layer. Derlon et al. (2012) reported that predation by eukaryotic microorganisms leads to heterogeneous biofilm structure with larger surface roughness accompanied by lower membrane coverage. The reduced membrane coverage caused higher values of the measured permeate flux at greater biofilm surface roughness.

*Fraction of exposed base layer.* Although biofilm surface properties, such as roughness coefficient and thickness, are generally useful when characterizing biofilm morphology (Li et al. 2016, Zhang et al. 1994), these measures are not adequate when water flux is concerned. Biofilms with identical roughness and thickness might lead to different water fluxes during compression (**Table 3.4**). Fraction of exposed base layer proves to be a better indicator to correlate permeate flux and biofilm surface morphology in membrane systems. A greater fraction of exposed base layer would result in a higher permeate flux through the biofilm.

*Practical implications.* The findings of this chapter is practical for the operational of GDM systems. In GDMs, a formation of biofilm with high surface roughness is preferred as they offer high AOC removal while, maintain high water flux (due to its high fraction of exposed base layer). This chapter offer better understandings for optimal operation of GDM systems.

### 3.6 Conclusions

- An increased biofilm hydraulic resistance during compression is not necessarily accompanied by large structural deformation (i.e., not observable by OCT). The rise in resistance could be explained by micro-scale particle/pore reorganization of biofilms under pressure;
- Hydraulic resistance of membrane biofilm formed from river water is mainly governed by properties of their base layer (i.e., density, porosity and fraction of base layer exposed to bulk liquid), while deformation is governed by biofilm roughness;
- A poroelastic fluid-structural model was proposed to explain various biofilm behaviors under compression. The dual-layer biofilm with a porous top layer and a dense base layer can explain the observed increase in hydraulic resistance coupled with minor structural deformation;
- Model simulations indicate that, when developing fluid-structural models for membrane systems, considering a gradient in biofilm initial porosity is more important than a gradient in the elastic modulus. This allows to reduce complexity of poroelastic models;
- Biofilm surface roughness alone does not impact significantly water permeate flux under compression. The fraction of exposed base layer could be a better biofilm morphology indicator in determination of permeate flux.

### 3.7 Acknowledgements

This study was funded by European Union's Horizon 2020 research and innovation programme under the Marie Skłodowska-Curie grant agreement No. 676070 and the Swiss National Science Foundation BIOMEMBRA project, grant No. 149648. This communication reflects only the authors' view and the Research Executive Agency of the EU is not responsible for any use that may be made of the information it contains.



# 4

## **A Comparison Between Chemical Cleaning Efficiency in Lab-scale and Full-Scale Reverse Osmosis Membranes**

“I do not know how to teach philosophy without becoming a disturber of the peace”.

Spinoza

---

This chapter published as: Jafari, M., D'Haese, A., Zlopasa, J., Cornelissen, E.R., Vrouwenvelder, J.S., Verbeken, K., Verliefe, A., van Loosdrecht, M.C.M. and Picioreanu, C. (2020) A comparison between chemical cleaning efficiency in lab-scale and full-scale reverse osmosis membranes: Role of extracellular polymeric substances (EPS). *Journal of Membrane Science* 609, 118-189.

## **Abstract**

Chemical cleaning is vital for the optimal operation of membrane systems. Membrane chemical cleaning protocols are often developed in the laboratory flow cells (e.g., Membrane Fouling Simulator (MFS)) using synthetic feed water (nutrient excess) and short experimental time of typically days. However, full-scale Reverse Osmosis (RO) membranes are usually fed with nutrient limited feed water (due to extensive pre-treatment) and operated for a long-time of typically years. These operational differences lead to significant differences in the efficiency of chemical Cleaning-In-Place (CIP) carried out on laboratory-scale and on full-scale RO systems. Therefore, we investigated the suitability of lab-scale CIP results for full-scale applications. A lab-scale flow cell (i.e., MFSs) and two full-scale RO modules were analysed to compare CIP efficiency in terms of water flux recovery and biofouling properties (biomass content, Extracellular Polymeric Substances (EPS) composition and EPS adherence) under typical lab-scale and full-scale conditions. We observed a significant difference between the CIP efficiency in lab-scale (~50%) and full-scale (9-20%) RO membranes. Typical biomass analysis such as Total Organic Carbon (TOC) and Adenosine triphosphate (ATP) measurements did not indicate any correlation to the observed trend in the CIP efficiency in the lab-scale and full-scale RO membranes. However, the biofilms formed in the lab-scale contains different EPS than the biofilms in the full-scale RO modules. The biofilms in the lab-scale MFS have polysaccharide-rich EPS (Protein /Polysaccharide ratio=0.5) as opposed to biofilm developed in full-scale modules which contain protein-rich EPS (Protein /Polysaccharide ratio=2.2). Moreover, EPS analysis indicates the EPS extracted from full-scale biofilms have a higher affinity and rigidity to the membrane surface compared to EPS from lab-scale biofilm. Thus, we propose that CIP protocols should be optimized in long-term experiments using the realistic feed water.

## 4.1 Introduction

Biofouling is an undesired accumulation of microorganisms on surfaces due to the deposition of organic compounds and/or growth of microorganisms (biofilm formation) (Flemming 2002, Vrouwenvelder et al. 2008). Biofouling adversely impacts membrane filtration systems by causing an additional hydraulic resistance (Dreszer et al. 2013, Martin et al. 2014), reduction in apparent membrane permeability and selectivity (Herzberg et al. 2009, Huertas et al. 2008), and higher feed channel pressure drop (Beyer et al. 2014, Farhat et al. 2019, Vrouwenvelder et al. 2008). Physical and chemical cleaning routines are periodically applied to reduce biofouling impacts on membrane systems. Physical cleaning is applied frequently in membrane systems (i.e., UF, MF) using different approaches such as back-wash cleaning (Basu 2015), shear cleaning (Vrouwenvelder et al. 2010b, Wibisono et al. 2015) and air-bubble cleaning (Cornelissen et al. 2007). Chemical cleaning protocols include chemically-enhanced backwash and Cleaning-In-Place (CIP) typically using acid and base solutions. The goal of both physical and chemical cleanings is to remove foulants and restore membrane performance as close as possible to virgin membranes. In dense membrane systems (RO, NF) in spiral wound configuration, hydraulic cleaning options are limited because the membranes cannot be backwashed.

The efficiency of CIP cleaning routines depends on type of cleaning solvents, solvent concentration, contact time, temperature and hydraulic parameters (kinetic or static cleaning) (Madaeni and Mansourpanah 2004a, Shi et al. 2014). The CIP cleaning mechanisms can be concluded namely such as hydrolysis, solubilisation, dispersion and chelating (Beyer et al. 2017). Chemical agents such as acids, bases, surfactants, chelating agents, oxidizing agents, and enzymes are used in CIP cleaning of RO membranes (Beyer et al. 2017). Generally, acids (e.g., HCl) and bases (e.g., NaOH) are among the most popular chemical agents used in RO membranes thanks to their economic advantages. Acids are used to dissolve precipitate of inorganic salts while alkaline agents can promote protein and polysaccharide hydrolysis and weaken membrane-foulant bonds (Shi et al. 2014)

Although periodical CIP cleanings are vital for a stable membrane operation, CIP cleanings are only partially successful in the recovery of both water permeability and pressure drop (Beyer et al. 2017, Beyer et al. 2014, Madaeni and Mansourpanah 2004a, Sanawar et al. 2018). Residual biofilm has been observed to remain on the membrane surface even after several cycles of CIP cleanings, leading to biofilm regrowth (Bereschenko et al. 2011). The membranes cleaned by CIP have a higher biofouling potential compared to the virgin membranes, due to nutrient availability resulting from the lysis of killed cells (Bereschenko et al. 2010). Chemical cleaning leads to changes in biofouling layer properties such as microbial community composition and extracellular polymeric substances (EPS) properties. Al Ashhab et al. (2017) suggested that several rounds of CIP in reverse osmosis (RO) membranes leads to formation of biofilms with limited microbial diversity and higher adherence to the membrane surface.

Novel CIP protocols (e.g. biocides, chelating agents and enzymes) already demonstrated superior recoveries of water permeability and feed channel pressure drop (Hijnen et al. 2012, Porcelli and Judd 2010a, Sanawar et al. 2018). Often, the novel CIP routines enhance EPS solubilisation leading to more effective and long-term biomass removal by higher degree of protein denaturation (Sanawar et al. 2018). Often, these CIP protocols are developed and optimized in the lab conditions using Membrane Fouling Simulator (MFS) (Bucs et al. 2015,



Creber et al. 2010, Farhat et al. 2019, Hijnen et al. 2012, Hijnen et al. 2011a, Madaeni and Mansourpanah 2004a, Miller et al. 2012, Sanawar et al. 2018, Sanawar et al. 2017). MFS is widely used in fouling and CIP studies due to its similarity in hydrodynamics to spiral wound RO membranes as well as its practicality in terms of low amount of water and chemicals required (Vrouwenvelder et al. 2006).

The EPS, forming the biofilm matrix, play a distinctive role in biofouling cleanability in membrane processes. The EPS from biofilms developed on membrane surfaces (i.e. membrane biofilm EPS) are evaluated based on their main composition (i.e., polysaccharide, protein) and adherence properties to the membrane surface (Al Ashhab et al. 2017, Sweity et al. 2011). Herzberg et al. (2009) reported EPS with high concentration of polysaccharide for biofilms developed in lab RO flow cells using synthetic wastewater. Similarly, the EPS extracted from the biofilms grown in the MFS has a protein/polysaccharide ratio of around 0.5 (i.e., polysaccharide-rich EPS) (Sanawar et al. 2018). Desmond et al. (2018a) reported that the protein/polysaccharide ratio in EPS increases with the biofilm age in a dead-end UF system fed with synthetic wastewater. A similar trend was observed with increasing Solid Retention Time (SRT) in a lab-scale Membrane Bioreactor (MBR) (Sweity et al. 2011). Bucs et al. (2017) reported that amphiphilic coating of reverse osmosis membrane would increase the formation of protein-rich EPS on the membrane surface. Al Ashhab et al. (2017) studied the EPS properties (composition, adherence) for biofilms grown in lab-scale RO systems subjected to several rounds of CIP and they reported a polysaccharide-rich EPS. Recently, Farhat et al. (2019) observed that a protein-rich EPS is formed for the biofilms growing under phosphate limitation. However, Beyer et al. (2017) measured the EPS composition for three full-scale RO installations and they reported polysaccharide-rich EPS from biofilms developed in full-scale RO plants. It is therefore apparent that the EPS composition depends on the biofilm age, nutrient availability in the feed water, and membrane surface properties.

The studies of EPS from membrane biofilms have been mainly focused on biofouling developed in lab conditions (typically, fast grown biofilms), usually fed with synthetic feed water for short periods of time (Al Ashhab et al. 2017, Bereschenko et al. 2011, Bereschenko et al. 2010, Herzberg et al. 2009). However, EPS properties of biofilms developed in full-scale installations (i.e., “old” biofilms and under nutrient limitation) are not well explored, probably due to time limitations, sampling difficulty, and diversity in plant operational conditions. Surprisingly, researchers reported significantly different results for the lab-scale CIP cleaning efficiency compared to full-scale plants (Tew et al. 2019).

The aim of this study was to evaluate the applicability of CIP results from typical lab-scale MFS to full-scale RO plants. Therefore, we investigated i) the difference between biofilm removal and water flux recovery after conventional chemical cleaning of full-scale modules and lab-scale MFSs, and ii) the difference in EPS properties (i.e., composition and, adherence) for biofilms formed in full-scale RO modules and lab-scale MFSs. These objectives allow for a better understanding of the correlation between the CIP efficiency and the properties of EPS in biofilms formed in membrane processes.

## **4.2 Materials and Methods**

### **4.2.1 Experimental set-up and fouling protocol**

Laboratory set-up for “natural biofouling” growth in a MFS includes a feed pump, nutrient pump, level controller, pressure safety valve, by-pass valve, mass flow meter, back pressure valve, and a MFS (Miller et al.

2012). A back-pressure valve was installed to prevent degassing by pressurizing the set-up. A MFS with flow channel dimensions of 250×50×1 mm and a membrane with active area of 124.14 cm<sup>2</sup> were used. The RO membrane used in the MFS was provided by DOW FILMTEC (**Table 4.1**). The MFS was operated under transmembrane pressure TMP=2 bar and in cross-flow mode with linear velocity of 0.15 m/s, representative of practical operation (Vrouwenvelder et al. 2009). Such MFS operation (i.e., at TMP ~ 1-6 bar) has been vastly reported for studies of model fouling development and membrane cleaning (e.g, CIP) in RO processes (Farhat et al. 2019, Hijnen et al. 2011a, Miller et al. 2012, Sanawar et al. 2018, Sanawar et al. 2017, Tew et al. 2019). The MFS retentate was partially recirculated (200 mL/min equivalent of 75% of feed flow rate) to ensure the availability of fresh tap water in the feed storage. Tap water in city of Ghent, Belgium, with minimal residual chlorine was used as feed water for “natural biofouling” growth (no inoculation). Feed water characteristic are listed in **Table 1**.

Biofilm development in the MFS was accelerated by dosing a nutrient solution containing sodium acetate, sodium nitrate and sodium dihydrogen phosphate in a mass ratio C:N:P of 100:20:10 to the feed water (Miller et al. 2012). The phosphate concentration was considered in excess to prevent the risk of phosphate limitation (which can be applied as a biofouling control strategy). The concentration of acetate added to the feed water was 1 mg/L (Miller et al. 2012, Sanawar et al. 2018). During operation, the MFS was covered to prevent any growth of phototropic microorganisms. The nutrient stock solution was replaced every 2 days. The nutrient solution was dosed using a calibrated peristaltic pump with the flow rate of 0.03 L/h. The nutrient flow rate was set much lower than feed flow rate to ensure the effect of nutrient dosage on feed solution pH is negligible (Sanawar et al. 2018, Sanawar et al. 2017). As previously reported by Vrouwenvelder et al. (2006) the MFS test-rig installed in parallel to full-scale RO (identical feed water) delivered comparable results (i.e., feed channel pressure drop) for spiral-wound RO and MFS. However, due to practical considerations, fouling studies and CIP protocol developments are often carried out in lab conditions (e.g., synthetic feed water, short-term) (Farhat et al. 2019, Hijnen et al. 2011a, Miller et al. 2012, Sanawar et al. 2018, Sanawar et al. 2017, Tew et al. 2019). Although the difference in operational parameters between MFS and the full-scale plants such as flux and recovery would lead the possible formation of different fouling layers, the MFS operational conditions in current study have been selected based on the rationale that such conditions are widely reported in the literature, thus, the results can be compared to existing data.

**Table 4.1** Feed water characteristics and operational conditions of the MFS and the full-scale plants in Belgium (Plant A) and in The Netherlands (Plant B).

Case studies	MFS	Plant A	Plant B
<i>Membrane properties and operational condition</i>			
Location	Ghent, Belgium	Veurne, Belgium	Rotterdam, Netherlands
Manufacturer	DOW FILMTEC	Toray	DOW FILMTEC
Membrane elements	XLE BW30	TM720D-400	ECO-PRO 440-i
Water permeability <sup>a</sup> (L/m <sup>2</sup> /h/bar)	7.49± 0.77	3.01	4.7
Salt rejection	~97%	90.3%	99.4%
Operational time	20 days	2 years	1.5 years
Historical CIP protocol	N.A.	Caustic/ Citric acid <sup>b</sup>	Hydrochloric acid/Caustic <sup>c</sup>
Days since last CIP	N.A.	35 days	60 days
<i>Feed water characteristics</i>			
Type of feed water	Tap water	Industrial effluent	Surface water
TOC (mg/L)	<0.2	7±0.3	4.3±0.06
pH	7.5	6.5	9.3
Total Hardness (mmol/L)	1.2	4.9	0.06
Conductivity (µS/cm)	453	3140	547

<sup>a</sup> Virgin membrane permeability based on supplier data

<sup>b</sup> The CIP protocol of Plant A consists of four steps: 1) NaOH (pH 12) at 20-32°C for 4 hours, 2) rinsing with permeate water, 3) Citric acid (pH 2.5-3) at 20-32°C for 2h and followed by the final rinsing with permeate water. This protocol “Historical CIP” is only practiced during full-scale operation.

<sup>c</sup> The CIP protocol of Plant B consists of four steps: 1) HCl (pH 2) at 5-25°C for 2 hours, 2) rinsing with demineralized water, 3) NaOH (pH 12) at 40°C for 2h and followed by the final rinsing with demineralized water. This protocol is only practiced during full-scale operation.

#### 4.2.2 Full-scale membrane modules autopsy

Two full-scale Reverse Osmosis (RO) installations in Belgium (Plant A) and in The Netherlands (Plant B) which both are operating at constant flux using surface water as feed water were studied. The feed water characteristics of the full scale plants are listed in **Table 4.1**.

Plant A is a water reuse plant for a potato chips and snack factory (PepsiCo) in Veurne, Belgium. The installation consists of ultrafiltration (UF) as a pre-treatment and a one-stage RO as a main purification step. The Plant B

is a demineralized water production plant in Rotterdam, The Netherlands, providing a demineralized water to a broad range of industries in the Rotterdam harbour area. Pre-treatment steps at Plant B include a Dissolved Air Flotation sand Filtration (DAFF), Water softener and two-stages RO (as the main purification steps). The post-treatment consists of a mixed-bed ion exchange resins to remove the residual ions. Periodical CIP was performed in both full-scale plants as the feed channel pressure increased by 20%. From each full-scale installation, one membrane element (lead module) was taken and opened for autopsy.

Membrane modules were transported for autopsy within 3 hours of extraction from the pressure vessels. Membrane modules were refrigerated at 7 °C. Biofouling samples were taken from membrane sheets randomly (at least 3 locations along the module). The samples size vary between 10-30 cm<sup>2</sup>. The results of all the analysis were normalized by samples area for further comparative assessment.

### 4.2.3 Water permeability and chemical cleaning

Water flux was measured to evaluate membrane performance before and after CIP. Water permeability

[L/m<sup>2</sup>/h/bar] ( $\frac{Flux[Lm^{-2}h^{-1}]}{TMP[bar]}$ ) and CIP recovery [%] ( $\frac{Flux_{afterCIP} - Flux_{beforeCIP}}{Flux_{beforeCIP}}$ ) were calculated

before and after CIP to investigate water permeability recovery by such a cleaning. To determine the water permeability, membrane samples (i.e., membrane sheet and feed spacer) which were cut from the membrane modules and the MFS were placed in a high pressure flow cell with identical dimensions as mentioned above. Water permeability measurements were carried out using deionized water under transmembrane pressure of 5 bar in the cross-flow mode (with cross flow velocity 0.15 m/s, from practice). Water flux/permeability measurements were carried out in duplicate before and after CIP. Water permeability data were recorded at least 15 min after stable water flux was recorded.

A conventional chemical cleaning was applied in both MFS and full-scale modules which includes the following steps *i*) alkaline cleaning (NaOH, pH 12, 0.01 M, 35 °C, 1hour), *ii*) Rinsing with DI water for 15 min, *iii*) Acid cleaning (HCl, pH 1, 0.1 M, room temperature, 1 hour), *iv*) final rinsing with DI water for 15 min. The chemical solutions were circulated with an identical flow rate as used for feed water (Sanawar et al. 2018).

### 4.2.4 Biomass quantification

The membrane sheets and spacers were cut to quantify biomass in lab-scale MFS and full-scale plants. Membrane and spacer samples were cut from membrane sheets and places in a centrifuge tube containing 30 mL sterile tap water for Adenosine triphosphate (ATP) measurements and in the ultrapure water for Total Organic Carbon (TOC) analysis. The centrifuge tubes with membrane samples were placed in an ultrasonic water bath (5510E-DTH, Branson, Danbury, CT) for 2 min and 1 min of vortex mixer to detach biofilm from membrane and spacer surfaces (Farhat et al. 2019). The procedure was repeated three times and the solution in the centrifuge tube was used to measure ATP and TOC. ATP measurements have been carried out to quantify the active biomass accumulated on both spacer and membrane surfaces before and after chemical cleaning. ATP is present in all viable microorganisms thus it is widely acceptable for biomass analysis (Hijnen et al. 2011b,

Sanawar et al. 2018, Vrouwenvelder et al. 2008). TOC measurements were carried out to quantify total organic carbon contained in both biofilm cells and extracellular polymeric substances (EPS) (Miller et al. 2012).

#### 4.2.5 EPS extraction and composition

To analyse the EPS composition and adherence properties, EPS was extracted from the accumulated biomass on the membrane. The membrane coupons were cut from membrane sheets. The EPS was extracted under alkaline conditions as previously described by (Felz et al. 2019). The biofilm was initially treated with 0.1 NaOH for 30 minutes at 80°C followed by centrifugation at 20000×g, where the solid residue was separated from the supernatant that contains the soluble EPS.

Polysaccharide and protein contents in the EPS were qualified using colorimetric methods. Polysaccharides concentration was determined based on Dubois method (DuBois et al. 1956) with glucose as the standard. Protein content was determined using Bio-Rad<sup>a</sup> Protein assay using Bovine serum albumin, BSA, as the standard (Bradford 1976). These established EPS analysis were selected due to their reliabilities and accessibility in the practice.

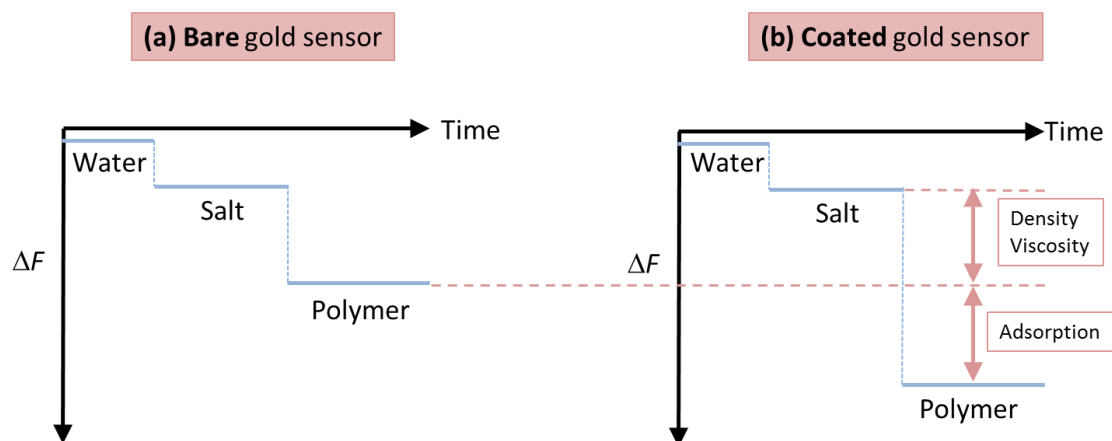
#### 4.2.6 EPS adherence properties using Quartz Crystal microbalance with dissipation (QCM-D)

To determine the adherence properties of EPS, the adsorption kinetics of EPS was measured using Quartz Crystal Microbalance and Dissipation, QCM-D, (Q-Sense E4, Gothenburg, Sweden). EPS adherence properties to a surface were characterized by measuring the change of oscillation frequency of the sensor. Generally, the QCM-D measurements determine the physical properties of the deposited film on the sensor surface. The adsorbed mass on the sensor ( $\Delta m$ ) linearly correlated to the frequency change ( $\Delta F$ ) by Sauerbrey equation  $\Delta m = -\frac{c}{n}\Delta F$  where  $c$  is the mass sensitivity constant (17.7 ng/cm<sup>2</sup>/Hz at F=5 MHz) and  $n$  is the overtone number (1,2,3,..). Thus, the mass uptake on the sensor is linearly correlated with frequency changes (Kwon et al. 2006). The change in frequency could be related to both bulk liquid physical properties such as density and viscosity as well as the adsorbed layer mass on the sensor. **Figure 4.1** indicates an example of frequency results of QCM-D measurements subjected to pure water, salt and polymer solutions on both bare gold and coated sensors. Assuming no adsorption of salt and polymer to the gold sensor, the change in frequency of bare gold sensor is only caused by bulk liquid viscosity and density. However, due to interaction of polymer solution with the coated gold sensor (polymer-polymer interaction), the frequency shift in the coated gold sensor is even higher for the polymer solution compared to bare gold sensor (**Figure 4.1**). This higher reduction in frequency of coated sensor is correlated to the adsorption of thin film of polymer on the coated sensor.

Moreover, the decay of crystal oscillation can be correlated to the energy dissipated in each oscillation. The dissipation factor in every oscillation circuit can be defined as  $D = \frac{\text{Energy dissipated}}{\text{Energy stored in crystal}}$ .  $\Delta D/\Delta F$  ratio provides information on how energy is dissipated per oscillation. A higher  $\Delta D/\Delta F$  ratio is correlated to the non-rigid adsorbed layer as appose to low  $\Delta D/\Delta F$  ratio which correspond to rigid adsorbed film (Al Ashhab et al. 2017).

The variations of frequency,  $F$ , and dissipation factor,  $D$ , were measured for the two overtones  $n=5,7$ ). EPS adherence properties (i.e., rigidity) on the crystal sensor was measured by analysing the correlation between the

shift in frequency and dissipation factor of different EPS biofilms (Al Ashhab et al. 2017, Sweity et al. 2011). The QCM-D measurements were carried out on both on bare-gold sensor and sensor coated with polyamide (Nomex, Sigma-Aldrich) with fundamental resonant frequency of 5 MHz. The sensors were coated with polyamide to mimic the RO membrane surface (Al Ashhab et al. 2017, Sweity et al. 2011). Prior to experiments, the sensors were soaked in 5 mM ethylenediaminetetraacetic acid (EDTA) for 30 min followed by rinsing thoroughly with Milli-Q water and finally dried with pure N<sub>2</sub> as described by Sweity et al. (2011). A background solution containing 8.5 mM NaCl + 0.5 mM CaCl<sub>2</sub> (background solution) was considered the standard solution. EPS solution was diluted into background solution to 5.5 mM of TOC (EPS standard solution). EPS aqueous solution flows above coated sensors at constant temperature of 22 °C and flowrate of 150 μL/min (cross-flow mode). At least two EPS samples were extracted from each membrane module (Al Ashhab et al. 2017). The protocol reported by Al Ashhab et al. (2017) was followed including three steps. i) 20 min Milli-Q water; ii) 20 min 10mM background solution (8.5 mM NaCl + 0.5 mM CaCl<sub>2</sub>); iii) 30 min of 10 mM standard EPS solution (containing 5.5mg/L TOC and diluted by background solution). An identical protocol was carried out on a bare gold sensor in order to subtract the impact of bulk viscosity and density of the frequency shift of the coated sensor.



**Figure 4.1** An example of QCM-D measurements results of frequency shift over time for a) bare (uncoated) gold sensor and b) coated gold sensor (e.g., polyamide) in contact with water, salt solution, and polymer solution. The changes in frequency for bare gold sensor (assuming no adsorption) are only correlated to bulk liquid density and viscosity. However, for the coated sensor, the frequency shifts for polymer solution have adsorption contribution on top of effects of bulk liquid density and viscosity.

#### 4.2.7 Fouling layer morphology: Scanning Electron Microscope (SEM) imaging

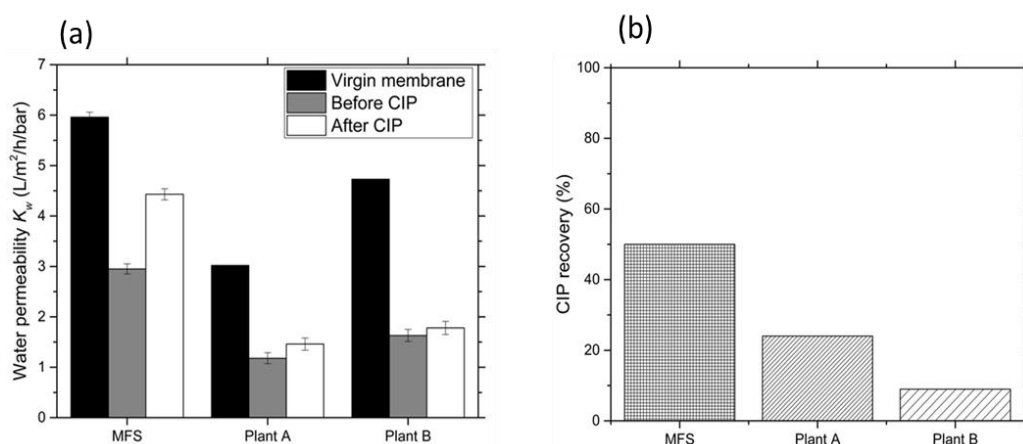
Morphological properties of the fouling layers were observed using Scanning Electron Microscopy (SEM). The dried fouled membrane samples were coated with gold for 30 s. Two different resolutions (500 and 10,000- fold magnifications) were applied to observe and compare the structural properties of different fouling layers (Al Ashhab et al. 2017, Kim et al. 2015). The compositional details of fouling layers were characterized using energy dispersive X-ray (EDX)

### 4.3 Results

A lab-scale MFS and two full-scale RO modules were analysed to compare CIP efficiency (in terms of water flux recovery) and biofouling properties (biomass content and EPS properties) in the typical lab-scale and full-scale conditions. The operational characteristics of the MFS and full-scale RO modules are listed in **Table 4.1**.

#### 4.3.1 Water permeability and CIP recovery

The water flux was measured for the virgin membrane, as well as for the fouled membranes before and after CIP cleaning. The water permeability was derived by normalizing water flux to the applied TMP. The water flux for the virgin membrane was measured to compare the impact of biofouling in water permeability decline. **Figure 2a** shows water permeability for the lab-scale MFS and two full-scale RO modules. The water permeability decreased in the MFS from around 6 to 3 L/m<sup>2</sup>/h/bar due to the fouling. Similarly, for the full-scale modules water permeability was reduced from around 3 to 1 L/m<sup>2</sup>/h/bar for Plant A and from ~ 4.5 to 1.7 L/m<sup>2</sup>/h/bar for Plant B. After CIP, the water permeability recovered significantly more in the MFS compared to the full-scale modules, increasing from ~ 3.0 to 4.5 L/m<sup>2</sup>/h/bar for MFS while only from about 1 to 1.2 L/m<sup>2</sup>/h/bar for plant A (**Figure 4.2a**). Clearly, CIP was more effective in MFS (~ 50% recovery) compared to full-scale Plant A (~ 22%) and Plant B (~9%) (**Figure 4.2b**). Such considerable difference in CIP recovery raises questions on the applicability of CIP results obtained in “typical” MFS experiments as an indication for full-scale plants.

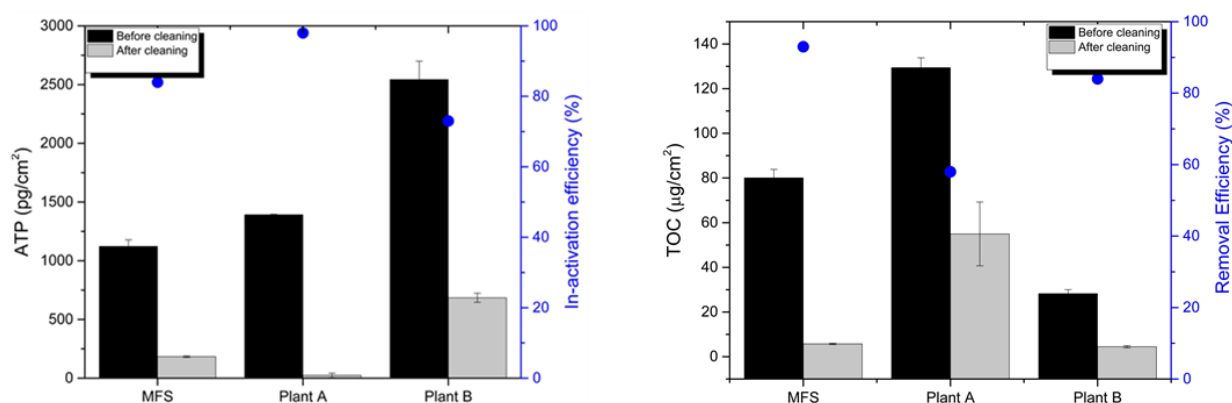


**Figure 4.2** Water permeability and CIP recovery for the lab-scale MFS and two full-scale modules. a) water permeability for virgin membrane, before and after CIP cleaning, b) CIP efficiency in terms of water permeability recovery (%).

#### 4.3.2 Biomass quantification and chemical cleaning efficiency

To evaluate the relation between the water permeability recovery and the biomass accumulation, we measured the amount of biomass deposited on the membrane and the removal of biomass via CIP cleaning. Biomass accumulated on the membrane surface was quantified using typical ATP and TOC measurements before and after chemical cleaning. **Figure 4.3a** shows ATP concentration in the MFS and two full-scale modules. ATP concentration before cleaning for the MFS is around 1000 pg/cm<sup>2</sup> compared to around 1500 and 2500 pg/cm<sup>2</sup> for Plant A and Plant B, respectively. A strong decrease in ATP concentrations in the fouling layer was observed

after chemical cleaning. ATP removal efficiency (which can be regarded as a microbial in-activation efficiency) was relatively high for all the three cases ( $> 70\%$ ) with the highest in-activation efficiency of around 100% for Plant A. The TOC results for the three case studies before and after chemical cleaning are shown in **Figure 4.3b** to reveal the amount of organic matter actually removed by cleaning. TOC concentration before cleaning in Plant A ( $\sim 130 \mu\text{g}/\text{cm}^2$ ) was higher than in the MFS ( $\sim 80 \mu\text{g}/\text{cm}^2$ ) and Plant B ( $\sim 30 \mu\text{g}/\text{cm}^2$ ). TOC removal efficiency demonstrates that Plant A has the most difficult biomass to be removed (removal efficiency around 60%) (**Figure 4.3b**). On the other hand, the MFS showed the highest biomass removal (measured by TOC) and therefore higher cleanability compared to full-scale modules.



**Figure 4.3** Accumulated biofilm for the lab-scale MFS and two full-scale modules. a) Adenosine triphosphate concentration (ATP) ( $\mu\text{g}/\text{cm}^2$ ) before and after chemical cleaning; second Y-axis in blue shows ATP removal efficiency (inactivation efficiency) by chemical cleaning; b) Total organic carbon concentration (TOC) ( $\mu\text{g}/\text{cm}^2$ ) before and after chemical cleaning; second Y-axis in blue shows TOC removal efficiency by chemical cleaning.

### 4.3.3 Extracted EPS properties and EPS compositions

The amount of extracted EPS is much higher for full-scale modules (between  $20\text{-}50 \mu\text{g}/\text{cm}^2$ ) compared to the lab-scale MFS ( $\sim 1\text{-}3 \mu\text{g}/\text{cm}^2$ ) (**Table 4.2**). This considerable difference in EPS concentrations between the MFS and full-scale modules is related to the membrane operation time and biofilm age. Interestingly, the protein to polysaccharide ratio (PN/PS) is much lower in MFS compared to the full-scale plants. The PN/PS ratio for MFS, before cleaning, is around 0.5 compared to 2.2 for both Plant A and Plant B, respectively. The results demonstrate that EPS produced in the lab-scale MFS conditions is polysaccharide-rich as opposed to the full-scale EPS which is much more protein-rich (**Table 4.2**). The PN/PS ratio after chemical cleaning does not follow any consistent trend in favourability in solubilisation of protein or polysaccharide by the CIP protocols.



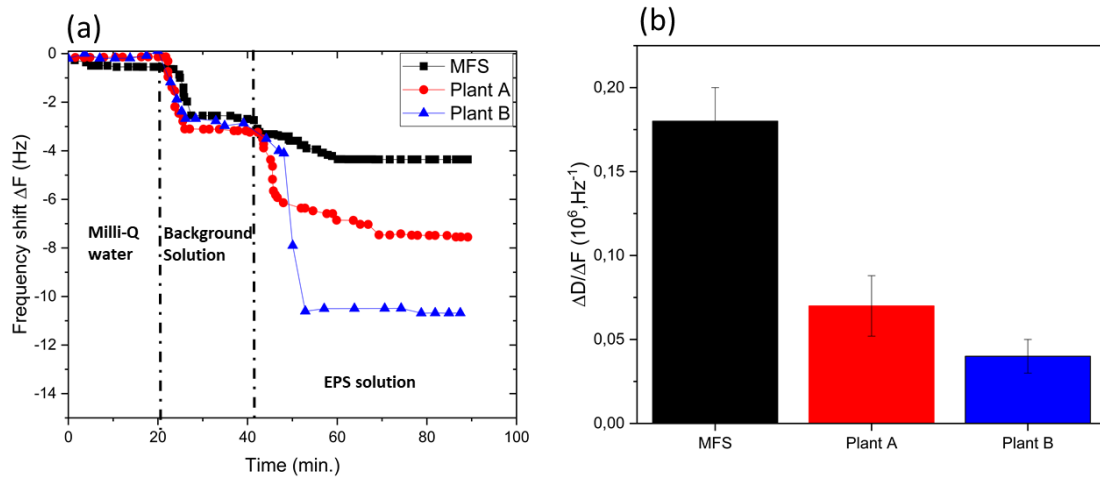
**Table 4.2** EPS composition of different biofilms from full-scale plants and lab-scale MFS before and after cleaning (n=3)

EPS composition	Before cleaning			After cleaning		
	MFS	Plant A	Plant B	MFS	Plant A	Plant B
Polysaccharide ( $\mu\text{g}/\text{cm}^2$ )	1.8	20	6.2	1	4.7	3.4
Protein ( $\mu\text{g}/\text{cm}^2$ )	0.9	45.6	13.8	0.4	5.2	8.5
Protein /Polysaccharide (PN/PS)	0.5	2.2 $\pm$ 0.2	2.2 $\pm$ 0.3	0.45	1.1 $\pm$ 0.1	2.5 $\pm$ 0.2

#### 4.3.4 EPS adherence properties and QCM-D measurements

The EPS extracted from the three biofilms demonstrate similar trends in adherence behaviour when they were adsorbed on the QCM-D coated sensors. Milli-Q water was used to measure the baseline of the adsorption experiments. The frequency shift is almost zero during the baseline measurements, followed by the frequency shift of  $\sim 3$  Hz observed as the background solution was introduced (**Figure 4a**). The shift in frequency for the background solution is due to the changes in the solution viscosity and density compared to Milli-Q water. The frequency shift increased as the EPS solution was introduced to the coated sensor. The adsorption of the polymer (EPS) on the coated sensor caused additional frequency changes of  $\sim 4$  Hz (MFS) and around 8 and 11 Hz for Plant A and B, respectively (**Figure 4.4a**). For the gold (non-coated) sensor, the frequency changes were 2.2 Hz (MFS) and 3.5 and 3.1 Hz (for Plant A and B) (**Supplementary information Figure 4.S1**), indicating only the impact of density and viscosity of the EPS solution. The higher value of frequency shift with EPS solution on coated sensor indicates more deposition (adsorption) of polymer layer on the sensor surface.

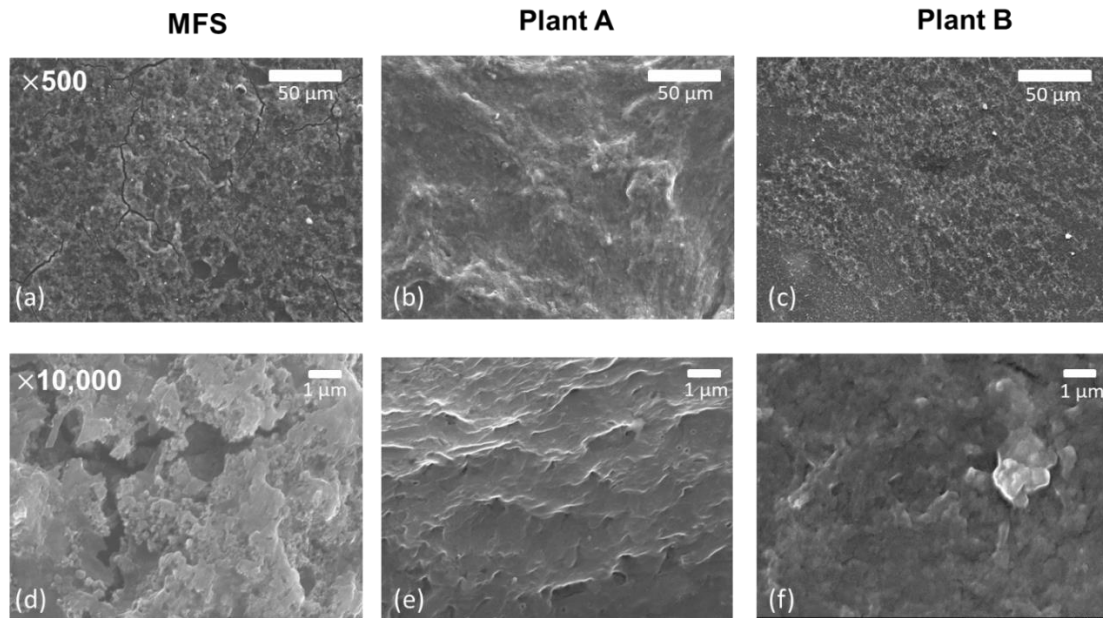
Furthermore, the dissipation of energy per oscillation,  $\Delta D$ , for two overtones ( $n = 5$  and  $7$ ) was also measured to analyse adsorbed EPS layer viscoelastic behaviour. The slope of the linear relationship between frequency shift,  $\Delta F$ , and dissipation change,  $\Delta D$ , during EPS solution measurement gives an indication of the EPS adsorbed layer fluidity on the coated sensors. The  $\Delta D/\Delta F$  ratio is much higher for the lab-scale EPS around 0.18 compared to Plant A EPS  $\sim 0.07$  and Plant B around 0.04 (**Figure 4.4b**). The ratio indicates that the adsorbed EPS layer obtained from full-scale samples have higher rigidity (less fluidity properties) compared to lab-scale EPS, as they are adsorbed on the coated sensor.



**Figure 4.4** EPS adherence properties on sensor coated with polyamide using QCM-D; a) the frequency shift ( $\Delta F$ ) showing EPS adherence to the membrane-like surfaces, b)  $\Delta D/\Delta F$  ratio showing EPS fluidity during adsorption to the coated sensors.

### 4.3.5 Optical analysis and SEM imaging

The biofilms covered almost the entire surfaces of the membrane and spacer. SEM images at two magnifications illustrate the biofouling structures for the three case studies. The structures of all three fouling layers appear different (**Figure 4.5a-c**). Specifically, the biofouling layer in the lab-scale MFS at high magnification (**Figure 4.5d**) is more porous than the full-scale biofouling (**Figure 4.5e,f**).



**Figure 4.5** SEM micrographs of all three biofilm cases, at two zoom levels (500x and 10,000x, upper and lower row respectively).

#### 4.4 Discussion

*CIP efficiency and water permeability.* The virgin membrane water permeability in each studied system was reduced significantly due to membrane fouling (**Figure 4.2a**). The water permeability recovery caused by CIP cleaning was greatly different between the lab-MFS and full-scale modules (**Figure 4.2a**). The CIP efficiency was evaluated based on water permeability change caused by CIP cleaning (Madaeni and Mansourpanah 2004a). The applied CIP cleaning had a much higher efficiency on lab-scale MFS (~50 %) compared to around 20 and 10% for full-scale modules (**Figure 4.2b**). The reduction in water permeability and water flux due to fouling layer are vastly reported in literature (Al Ashhab et al. 2017, Farhat et al. 2019, Kim and Jang 2006, Madaeni and Mansourpanah 2004a, Porcelli and Judd 2010a, Porcelli and Judd 2010b, Vrouwenvelder et al. 2008). The observed difference in the CIP efficiency (in terms of flux recovery) could be attributed to the different CIP history and EPS properties of full-scale and lab-scale biofouling layers. Al Ashhab et al. (2017) observed that CIP efficiency in flux recovery decreases as the number of CIP events increased. They correlated the reduction in the CIP efficiency after several CIP rounds to the selection of more resilient and adhesive cells and EPS following several CIP events. Recently, Tew et al. (2019) reported a significant difference in CIP efficiency when comparing the lab-scale and industrial-scale RO membrane for concentrating milk. They used identical feed water solutions and similar cleaning routines while only the operation time was different (biofouling age). They observed that the chemical cleaning could restore laboratory flux to a high extent (compared to original flux) while the chemical cleanings had little or no impacts on membrane permeability in industrial membranes. The observed differences are attributed to, for example, different lipid type and concentration. In our study, despite considerable biomass removal (**Figure 4.3**), the water flux never fully restored after the CIP events. This confirms previous observations that presence of a thin and dense biofouling layer (i.e., biofilm base layer) would dominate the resistance to water flux and reduce total membrane permeability (Derlon et al. 2016, Jafari et al. 2019, Jafari et al. 2018).

*Biomass quantification.* The biomass quantification results show that ATP and TOC values in this study are in the range of reported data in literature (Beyer et al. 2014). The ATP concentration in the fouling layer of Plant B is higher than the ones in Plant A and MFS (**Figure 4.3a**), which can be related to the observed algae bloom in the source of the feed water. Algae contribute to an increase in the Natural Organic Matter (NOM) (Her et al. 2004) and dissolved organic matter (e.g., EPS) (Castaing et al. 2011) in the feed water. The relative low ATP concentration in Plant A is accompanied with a fairly high TOC concentration (**Figure 4.3b**), which suggests deposition of organic carbon in form of NOM (Beyer et al. 2014) leading to significant reduction to hydraulic permeability (Violleau et al. 2005). The ATP in-activation and TOC removal efficiencies are also in accordance with reported studies (Hijnen et al. 2012, Hijnen et al. 2011b). In the current study, high TOC removal was not linked to the low concentration of divalent cations in the fouling layer, as widely reported in literature (Herzberg et al. 2009, Li and Elimelech 2004). The MFS has higher TOC removal (compared to full-scale cases) while the concentration of divalent cations is also higher than in the full-scale cases (**Table 4.S1**). Thus, the higher TOC removal in MFS can be attributed to more porous morphology of the fouling layer in MFS (**Figure 4.5**), which leads to greater EPS solubilisation (due to better cleanant diffusion) and resulting in higher biomass removal. In our study, the average ATP removal was around 83% compared to the average TOC removal of

~76% (higher organic matter compared to cells), in-line with the general observation that TOC removal is lower than ATP removal (Hijnen et al. 2012). Although chemical cleaning mechanisms of biomass removal (e.g., solubilisation, hydrolysis,...) are widely discussed (Beyer et al. 2014, Madaeni and Mansourpanah 2004b, Porcelli and Judd 2010a, Trägårdh 1989), the ATP and TOC removal efficiencies provide limited information on the actual effect of chemical cleaning and the underlying reason for the observed difference in performance parameters (i.e., membrane permeability recovery) (Beyer et al. 2014, Hijnen et al. 2012). Therefore, EPS as a biofilm matrix, which reveals crucial information about biofouling layer composition and adherence was studied in more detail here.

*EPS composition and protein to polysaccharide ratio (PN/PS).* The significant difference in chemical cleaning efficiency between lab-scale MFS and full-scale plants (**Figure 4.2a, b**) could be attributed to the remarkable differences in the protein to polysaccharide ratio (PN/PS) of extracted EPS (**Table 4.2**). The lab-grown biofilm consisted of polysaccharide-rich EPS (low PN/PS) that can be correlated to the young biofilm and nutrient excess (typical in lab studies). This is in agreement with other studies reporting the EPS composition for biofilms grown in lab-scale RO systems (Al Ashhab et al. 2017, Sanawar et al. 2018). On the other hand, full-scale plant biofilms in our study consisted of mainly protein-rich EPS (high PN/PS). Herzberg et al. (2009) reported polysaccharide-rich EPS for the biofilms grown under lab-scale conditions using a synthetic wastewater. The PN/PS ratio of extracted EPS increased with increasing SRT in MBR. The results suggest PN/PS ratio increases with an increase in biofilm age. In addition, the PN/PS ratio increases as the biofilm age increases during dead-end UF for the biofilms grown under nutrient limitation (Desmond et al. 2018a). The transition from polysaccharide-rich EPS in the young biofilm (low PN/PS) to protein-rich EPS in the mature biofilms (high PN/PS) has been explained by the need to have polysaccharides with high adherence in the initial biofilm development stages, required for structural integrity (Christensen 1989, Limoli et al. 2015, Sweity et al. 2011). However, Fong and Yildiz (2015) reported that not all polysaccharides facilitate biofilm adhesion. Proteins found in EPS are also claimed to contribute importantly to biofilm attachment to the surface and biofilm stabilization (Fong and Yildiz 2015). Thus, it seems that different proteins and polysaccharides with different properties (e.g., electrostatic charge) are preferred for biofilm adhesion in the early stages of biofilm formation. Therefore, the literature on EPS characterization and functionality is speculative and uncertain as described above and in more details by Seviour et al. (2019). For instance, the significant role of polysaccharides on biofilm adhesion often referred to work of Christensen (1989) despite the fact that the authors clearly stated that their speculations have no “direct and conclusive evidence”.

*EPS adherence properties.* The quasi-quantitative results of QCM-D measurements ( $\Delta F$  and  $\Delta D$ ) allow us to compare adherence properties of lab-scale and full-scale EPS on the coated sensor. The lab-scale EPS exhibited a lower adherence to the sensor surface compared to the full-scale EPS (**Figure 4.4**), which can be correlated to differences in their composition and the number of CIP events performed. Al Ashhab et al. (2017) reported that the biofilm adherence to the coated sensor increased only after five rounds of CIP cleaning, due to the selection of specific microbial community with higher adherence to the membrane surface. Moreover, biofilms grown under low substrate concentration have higher adherence to the surface compared to the biofilms grown under nutrient excess (the biofilms had equal age) (Allen et al. 2018). This is in agreement with the finding of

this study where the full-scale biofilm (nutrient-limited) has higher adherence than lab-scale biofilm (nutrient-excess). The  $\Delta D/\Delta F$  ratio (**Figure 4.4b**) was developed to analyse the rigidity of adsorbed EPS layer on the sensors. The higher fluidity (less rigidity) of EPS from lab-scale MFS with no CIP history compared to full-scale EPS with several rounds of CIP is in accordance with reported results by Al Ashhab et al. (2017). One should note that the QCM-D results are only reliable for the comparison only if the EPS samples are extracted using an identical technique. Moreover, the EPS adsorption measurements should be carried out also on the bare (uncoated) gold sensor to evaluate impacts on EPS solution density and viscosity on the frequency changes (**Supplementary information Figure 4.S1**).

*Practical implications and future research.* There have been extensive efforts in the development of novel, cost effective and efficient CIP protocols to reduce fouling impacts in membrane processes. CIP protocols are often optimized in the lab using synthetic feed water and short-term experiments (Tew et al. 2019). However, the CIP efficiency is significantly different in laboratory and industrial conditions, which is likely due to considerable difference in biofilm composition (Beyer et al. 2014, Tew et al. 2019). This study proposed that the observed differences in CIP efficiency are caused by the difference between the EPS composition in the full-scale and lab-scale membranes. Thus, the CIP protocols should not be developed using synthetic feed water and fouling layer developed over a short period of time. We suggest that a more detailed EPS composition analysis (e.g., by mass spectrometry) could give qualitative valuable information on the protein and polysaccharide fraction of EPS.

The knowledge of EPS could help to choose the optimal CIP protocols. In this sense, we could customize chemical solvents and treatments based on different EPS compositions to maximize solubilisation. For example, some EPS compositions are reported to be much more soluble in acidic conditions, as oppose to the others which are solubilized to a higher degrees in alkaline conditions or in ionic liquids (Boleij et al. 2019).

However, lack of unified EPS extraction and characterization protocols makes comparing the available literature data extremely difficult (Seviour et al. 2019). The novel EPS extraction and characterization techniques provide an opportunity to develop better CIP protocols by enhancing EPS solubilisation (Sanawar et al. 2018). However, one should also note the limitations of the current EPS extraction and characterization methods (Felz et al. 2019). The relatively low EPS extraction yield and the impossibility to distinguish between excreted polymer (produced by microorganism) and deposited polymer (from the feed water) limit further understanding of the EPS role in CIP efficiency. Thus, further research should also focus on developing alternative and reliable EPS extraction and characterization methods (Felz et al. 2019). EPS properties in the membrane system should be evaluated in the lab by long-term studies using real wastewater. This would allow to estimate the minimum experimental time required to properly replicate the full-scale membrane biofilms.

## 4.5 Conclusions

The goal of this study was to investigate suitability of CIP results from lab-scale fouling experiments for applications in full-scale RO plants. A fouling experiment under lab-conditions (short-term and synthetic feed water) and two full-scale RO membrane autopsies were carried out. The CIP efficiency measurements as well biomass analysis have been done. The main study findings can be summarized by:

- Chemical cleaning efficiency is much higher for fouled lab-scale MFS than for module full-scale plants.
- Higher CIP efficiency for the lab-scale MFS than the full-scale modules is correlated to a considerable difference in their EPS properties. The extracted lab-scale EPS is polysaccharide-rich while the EPS extracted from full-scale modules mainly consist of protein.
- The EPS extracted from full-scale fouled membranes exhibited higher adherence to the membrane surface compared to the lab-scale EPS.

This study indicates that the lab-scale CIP results are not representative for the full-scale applications. The typical lab-scale fouling experiments (young biofilms which are fed with nutrient excess feed water) are not representative of full-scale conditions. We propose that CIP protocols should be optimized in long-term experiments using the realistic feed water.

#### **4.6 Acknowledgements**

This study was funded by European Union's Horizon 2020 research and innovation program under the Marie Skłodowska-Curie grant agreement No. 676070. The authors gratefully acknowledge Özgür Gölbaşı and David Moed (Evides Industriewater B.V., The Netherlands) and Celestin Claeys (De Watergroep N.V., Belgium) for kindly providing membrane modules and related supports. This communication reflects only the authors' view and the Research Executive Agency of the EU is not responsible for any use that may be made of the information it contains.



# 5

## **Bringing laboratory to full-scale RO installation: A novel approach for membrane fouling analysis and CIP protocol development**

“A concept is a brick. It can be used to build a courthouse of reason. Or it can be thrown through the window.”

Gilles Deleuze

---

This chapter is submitted as: M., Jafari, O., Golbasi, A., Zlopasa, J., Cornelissen, E.R., Vrouwenvelder, J.S., Verliefe, A., van Loosdrecht, M.C.M. and Picioreanu. Bringing laboratory to the full-scale RO installation: A novel approach for membrane fouling analysis and CIP protocol development.



## **Abstract**

In our previous work, we showed that the efficiency of chemical cleaning-in-place (CIP) is significantly higher for flow-cells under lab-conditions (at short-term using synthetic feed water) compared to full-scale Reverse Osmosis (RO) plants (at long term operation, using complex feed water). We proposed that such a difference in CIP efficiency is attributed to the different extracellular polymeric substance (EPS) properties caused by different operational conditions. Therefore, the CIP protocols and the membrane fouling analysis should be developed under full-scale conditions. A novel approach in membrane fouling monitoring and characterization and CIP protocol development is using new RO modules into full-scale RO installation and operated for 30 days.

The suitability of this new method was to evaluate the fouling properties of the new modules and the CIP efficiency (under operation for 30 days) compared to old RO modules (under operations for > 2 years). The results of this study show that the new RO module installed in the full-scale installation for 30 days has similar CIP efficiency and fouling properties (such as ATP, TOC removal rate and EPS properties) compared to the old RO module (> 2 years in the operation). Moreover EPS, which acts like the biofouling matrix, showed to have relatively similar properties both in old and new modules fouling layers. The EPS extracted from both young and old RO modules are polysaccharide-rich and they have very similar adherence properties to the membrane surface. The almost identical CIP efficiency observed in the old and new RO modules in this study is attributed to the similar EPS properties (i.e., composition, adherence) of these two cases. However, the findings of this study contradict our initial hypothesis that the EPS extracted from the old RO modules is protein-rich and has higher adherence to the membrane surface compared to the young RO modules. These observations shows that the feed water properties and operational conditions are more important for fouling properties and CIP efficiency than only the fouling growth time. Finally, the new proposed fouling simulation method indicates the promising results in predicting both CIP efficiency results and fouling properties of the full-scale RO modules under operation for a long time.

## 5.1 Introduction

Fouling is the main challenge for optimal operation of full-scale Reverse Osmosis membrane (RO) plants (Ang et al. 2017, Bucs et al. 2018, Vrouwenvelder et al. 1998). Fouling related costs are considered around 25% of brackish water RO plant operational expenses in Netherlands (Jafari et al. 2021). Fouling studies are often carried out in laboratory conditions (e.g., synthetic feed water, short time) using laboratory flow-cells due to the practical considerations (Hijnen et al. 2011a, Miller et al. 2012, Vrouwenvelder et al. 2006). The differences between typical laboratory and full-scale conditions (e.g., feed water composition, operational time, cleaning history and operational pressure) often lead to different fouling properties (Jafari et al. 2020, Sanawar et al. 2017, Tew et al. 2019) and consequently different fouling control/mitigation results (Al Ashhab et al. 2017, Ang et al. 2006, Beyer et al. 2017, Bucs et al. 2018, Madaeni and Mansourpanah 2004a, Vrouwenvelder et al. 2010a). Chemical cleaning routines are often performed as membrane operational parameters (e.g., permeability and pressure drop) exceed the allowable and acceptable values (Beyer et al. 2017, Beyer et al. 2014, Bucs et al. 2018, Madaeni and Mansourpanah 2004a). The goal of chemical cleaning routine is to remove foulants and restore membrane performance as close as possible to virgin membranes (Hijnen et al. 2012, Madaeni and Mansourpanah 2004a). However, CIP protocols are often optimized in the lab using synthetic feed water and short-term experiments (lab conditions). In our previous work, we showed that the efficiency of chemical cleaning-in-place (CIP) (i.e., fouling removal) is significantly higher for lab-conditions flow-cell (i.e., short-term and synthetic feed water) compared to full-scale Reverse Osmosis (RO) plants (i.e., long term operation, complex feed water) (Jafari et al. 2020). We proposed such difference in CIP efficiency is attributed to different extracellular polymeric substance (EPS) properties (compositions, adherence) caused by different operational conditions (Jafari et al. 2020). Finally, it has been suggested that CIP protocols should be developed in membrane flow cell only using real feed water and in long time experiments (Jafari et al. 2020). However, long term operation of lab flow cells fed with real feed water is often limited by the accessibility of fresh real feed water in the lab. (Simon Vrouwenvelder et al. 2011) (Vrouwenvelder et al. 2006) installed laboratory flow cell parallel to full-scale RO installation and studied typical fouling properties and performance parameters (Normalized Pressure Drop, NPD). However, the role of EPS properties (composition, adherence) have not been well explored for membrane fouled with complex real feed water.

The aim of this study was to investigate fouling properties and CIP efficiency of RO modules fed with real feed water in a short-term (30 days) and long-term (> 2 years) experiments. The novelty of this work lays on installation of virgin modules in the full-scale RO installation to study effect of operational time (i.e., fouling growth/accumulation time) on fouling properties and chemical cleaning efficiency for RO modules fed with real feed water.

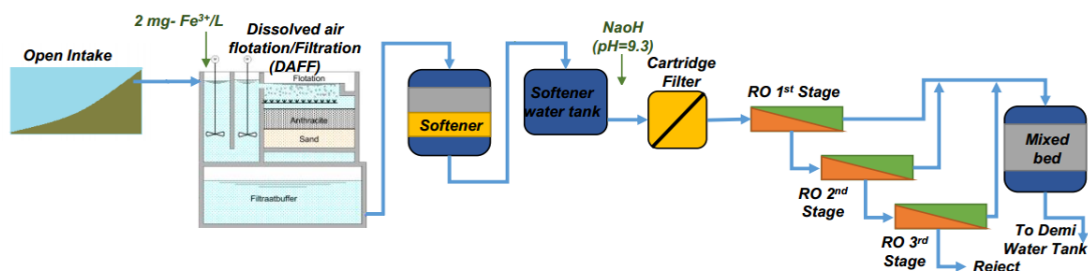
We hypothesized that CIP efficiency is much higher in young RO modules compared to the old RO modules fed with identical feed water. We also hypothesize that EPS extracted from the fouling of young RO modules is polysaccharide-rich as oppose to the old RO module's EPS which is protein-rich. These considerable difference (i.e., in CIP efficiency and EPS composition) are assumed to be attributed to the biofilm growth time (i.e., operation time). In other words, we assumed the CIP efficiency and consequently EPS properties are mainly determined by biofouling growth time (operation time) rather than feed water composition.

We installed new virgin RO modules into full-scale RO plant and operated them for 30 days (new modules) and for more than 2 years (old modules). The goal was to compare “young” fouling layer (30 days) and “old” fouling layer (> 2 years) fed with identical real feed water in terms of i) fouling properties (i.e., biomass indicators, inorganic concentration and morphology) ii) CIP efficiency (i.e., change in NPD,  $K_w$  by a CIP event), and iii) EPS properties (i.e., composition and adherence).

## 5.2 Materials and Methods

### 5.2.1 Full-scale Reverse Osmosis (RO) plant

A full-scale demineralized water production plant in Rotterdam, The Netherlands was selected to study impact of operational time in fouling properties and cleaning efficiency. The plant provides demineralized water to broad range of industries in port of Rotterdam. The plant’s pre-treatment steps include a Dissolved Air Flotation sand Filtration (DAFF), Water softener (cation exchange resin), and three-stages RO in series (as the main purification step). The post-treatment consists of a mixed-bed ion exchange resins to remove the residual ions (**Figure 5.1**). The fouling potential increases usually during spring leading to higher pressure drop and consequently more frequent CIP cleaning. Periodical CIP was performed in the plant as the feed channel pressure increased by 20 %. The details of plant’s operation and specifications is listed in **Table 5.1**.



**Figure 5.1** The scheme of the full-scale demi-water production plant in Rotterdam, Netherlands.

A chemical cleaning was applied as operational parameters reduce more than 20% which includes the following steps *i*) alkaline cleaning (fast circulation with NaOH, 120 m<sup>3</sup>/h, pH 12, 39 °C, 1 hour), *ii*) (slow circulation with NaOH, 40 m<sup>3</sup>/h, pH 12, 39 °C, 3 hours) *iii*) alkaline cleaning (soaking with of NaOH, pH 12, , 39 °C, 1 hour), *iv*) Rinsing with RO permeate for 1 hour with flow rate 70 m<sup>3</sup>/h, *v*) acid cleaning (fast circulation with mixture of HCl and C<sub>2</sub>H<sub>2</sub>O<sub>4</sub>, 120 m<sup>3</sup>/h, pH 2, 39 °C, 1 hour), *vi*) acid cleaning (slow circulation with mixture of HCl and C<sub>2</sub>H<sub>2</sub>O<sub>4</sub>, 50 m<sup>3</sup>/h, pH 2, 39 °C, 3 hours) *vii*) acid cleaning (soaking with mixture of HCl and C<sub>2</sub>H<sub>2</sub>O<sub>4</sub>, pH 12, , 39 °C, 1 hour) and *viii*) final rinsing with RO permeate for 1 hour,

**Table 5.1** Plant general information and the module specifications.

Specification	Plant info
<b>General information</b>	
Location	Rotterdam, The Netherlands
Intake water source	Surface water
Production capacity (m <sup>3</sup> /h)	200
RO Recovery (%)	85
Bumber of CIP per year	52
<b>Module specification*</b>	
Module Manufacturer	DOW FILMTEC
Module model	ECO-PRO 440-iLEC
Membrane material	Polyamide thin film composite
Feed spacer thickness (mil)	28
Water permeability (L/m <sup>2</sup> /h/bar)	5.3
Minimum salt rejection (%)	99.4
Operational time (years)	2
<b>RO Feed water</b>	
Source	Surface water
TOC (mg/L)	2.26±0.4
ATP (ng/L)	9.8±6
pH	9.3
Total Hardness (mmol/L)	0.06
Conductivity (µS/cm)	547

### 5.2.2 Integration of virgin (new) RO modules in the full-scale installation

Four new identical modules were installed in the full-scale installation and operated similar to full-scale conditions (e.g., hydrodynamics, feed water composition, CIP history). The new modules were all installed in lead position of each pressure vessel (**Figure 5.1**). This is due to higher fouling potential of the new modules in lead position. The new modules were operated for 30 days (short-term experiment) and during the operation time, they underwent exact similar operational conditions as the whole plant.

### 5.2.3 RO module autopsy and sampling

From the full-scale installation, four membrane elements (two elements after 30 days and two after more than 2 years) were taken and autopsied for fouling layer characterization. Membrane modules were transported for autopsy within 30 min of extraction from the pressure vessels. Fouling samples were taken from membrane sheets randomly (at least 3 locations along the module). The samples size vary between 10-30 cm<sup>2</sup>. The results of all the analysis were normalized by samples area for further comparative assessment.

#### **5.2.4 Performance parameters and chemical cleaning**

The module performance parameters (NPD,  $K_w$ ) were measured for all the four modules before and after the CIP event to evaluate CIP efficiency of the plant on both “young” and “old” modules. To be able to monitor CIP efficiency on each individual module, the fouled modules were transferred to an in-house single-module RO pilot installation fed with identical feed water and operated under similar conditions as the full-scale RO. The NPD and  $K_w$  before and after each CIP event were used to calculate CIP efficiency (i.e., recovery of performance parameters) by each CIP event (Jafari et al. 2020, Madaeni and Mansourpanah 2004a).

#### **5.2.5 Biomass quantification**

To analyse the amount of active biomass in the fouling layer, Adenosine triphosphate (ATP) measurements were carried out on the fouling layer samples. The ATP measurement procedure has been explained in details in (Farhat et al. 2019, Sanawar et al. 2018, Vrouwenvelder et al. 2008). To quantify the amount of organic carbon in the accumulated fouling layer, TOC measurements were performed on the samples taken from each membrane modules. Details of TOC measurement procedure can be found in (Miller et al. 2012). The procedures were repeated three times. Each measurement for each sample was repeated 3 times.

#### **5.2.6 EPS extraction and composition**

EPS as a biofilm matrix is crucial in biofilm solubilisation and removal in the chemical cleaning mechanisms. EPS composition is important in the extent of biofilm solubilisation (Al Ashhab et al. 2017, Jafari et al. 2020, Sanawar et al. 2018). We measured EPS composition (polysaccharide and protein contents) using colorimetric methods as previously described in our previous work ((Bradford 1976, DuBois et al. 1956). Prior to measurements, the EPS was extracted using alkaline method as reported to be effective in to extracted the soluble EPS of accumulated fouling layer (Felz et al. 2019).

#### **5.2.7 EPS adherence properties and Quartz Crystal Microbalance and Dissipation (QCM-D)**

EPS adherence properties was quantifies using QCM-D measurements on polyamide coated sensor. The sensor was coated with polyamide to mimic the membrane surface. The variations of frequency,  $F$ , and dissipation factor,  $D$ , were measured for the two overtones ( $n=5,7$ ) to evaluate EPS adherence properties (i.e., adherence and rigidity). The procedure of sensor preparation prior to experiments was explained in details in (Jafari et al. 2019). The QCM-D protocols adapted from (Al Ashhab et al. 2017) and follows the following steps: i) 20 min Milli-Q water; ii) 20 min 10mM background solution (8.5 mM NaCl + 0.5 mM CaCl<sub>2</sub>); iii) 30 min of 10 mM standard EPS solution (containing 5.5mg/L TOC and diluted by background solution). This protocols was performed both on coated sensor and bare gold sensor (to identify impact of bulk liquid viscosity and density) (Jafari et al. 2020).

#### **5.2.8 Inorganic concentration in the fouling layer: Inductively coupled plasma-optical emission spectrometer (ICP-OES)**

Elements concentrations in the fouling layer were measured in the urea and the dissolved precipitates using a Varian Vista MPX ICP-OES (Agilent Technologies, USA. Prior to analysis, samples were acidified to 2% Nitric

acid ( $\text{HNO}_3$ ), to ensure all ions were fully dissolved. The inorganic compounds most likely to contribute to biofouling are considered as Calcium, Magnesium and Iron (Chon et al. 2012).

The summary of the experiments carried out in this study is listed in **Table 5.2**.

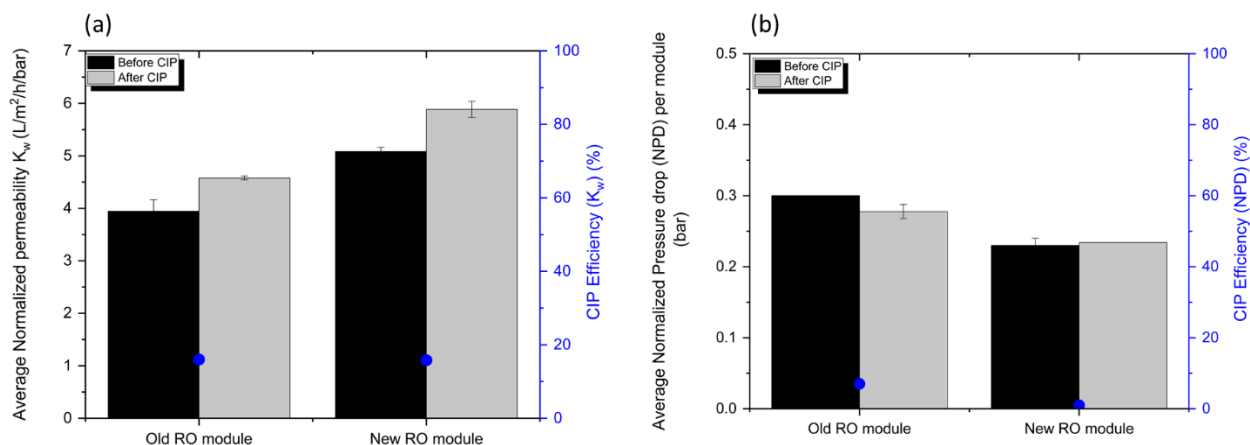
**Table 5.2** The summary of experiments carried out in the current study.

Experiment	New RO module (30 days)	Old RO module (> 2 years)	Remark
Performance parameters before and after CIP			
<i>NPD</i>	✓	✓	To calculate CIP efficiency
$K_w$	✓	✓	To calculate CIP efficiency
Fouling properties (autopsy of 4 modules)			
ATP	✓	✓	Biofilm indicator
TOC	✓	✓	Organic carbon indicator
ICP-OES	-	✓	elemental concentration
EPS composition	✓	✓	Protein/Polysaccharide ratio
QCM-D	✓	✓	EPS adherence

## 5.3 Results

### 5.3.1 Membrane performance parameters and CIP efficiency

The performance parameters namely, average *NPD* and  $K_w$ , were measured before and after in-place CIP for both old and new RO modules. The normalized pressure drop and permeability were adjusted to water temperature, flow rate, transmembrane pressure and flows conductivity (see **Supplementary Information Chapter 5**) to enable a fair comparison among performance parameters. **Figure 5.2a** shows that water permeability before cleaning for old RO module (~ 2 years in operation) is around 4 L/m<sup>2</sup>/h/bar while the permeability of new RO module (30 days in operation) is around 5 L/m<sup>2</sup>/h/bar. This was predicted as water permeability would decrease over time due to accumulation of irreversible fouling on membrane surface. Water Permeability after CIP for old and new modules are 4.5 and 5.5 L/m<sup>2</sup>/h/bar, respectively (**Figure 5.2a**). This means that CIP efficiency in term of permeability recovery is around 18% for both old and new RO modules (**Figure 5.2a**). Also as expected the pressure drop over a module before CIP for an old modules (~ 0.3 bar) is slightly higher than the new module (~ 0.25 bar) (**Figure 5.2b**). Interestingly, CIP efficiency in pressure drop reduction is negligible for both modules (<10%). From the CIP efficiency point of view, it seems that CIP recovery results of new modules operated for 30 days are comparable with CIP efficiency of old modules.

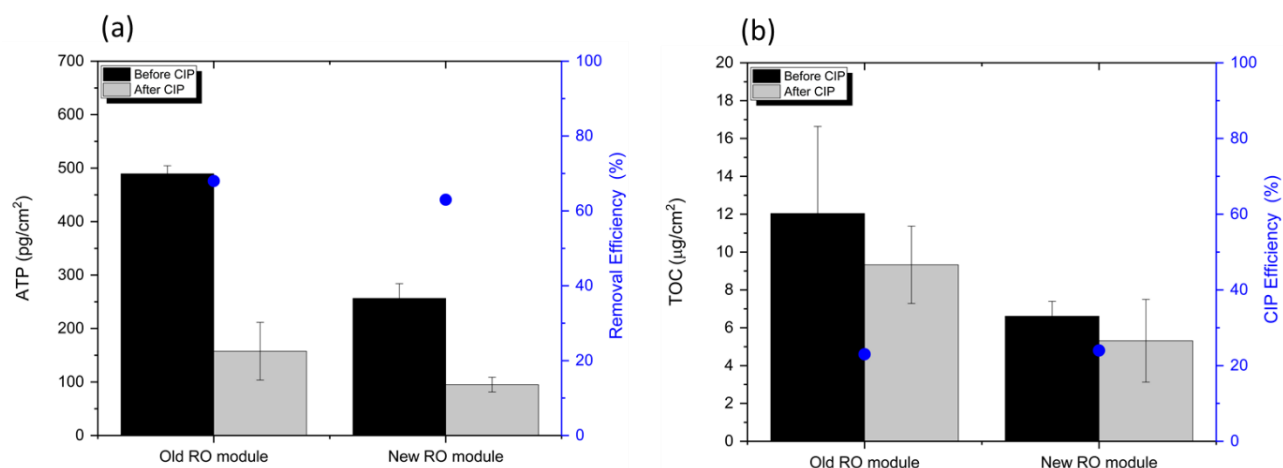


**Figure 5.2** Performance parameters ( $K_w$ , NPD) and CIP efficiency for old and new RO modules before and after in-place CIP. a) Average normalized water permeability for old and new RO modules before and after CIP as well as CIP efficiency in terms of water permeability recovery (%), b) Average normalized pressure drop for old and new RO modules before and after CIP as well as CIP efficiency in terms of pressure drop reduction (%).

### 5.3.2 Biomass quantification and chemical cleaning efficiency

Typical biomass indicators (ATP, TOC) were measured before and after in-place CIP event. Membrane modules before and after cleaning were autopsied and samples of fouling layer were obtained. These measurements are often carried out to quantify the content of accumulated organic carbon (TOC) and biofouling (ATP) on the membrane surface. **Figure 5.3a** shows ATP concentrations in the old and new modules before and after CIP as well as biofilm removal efficiency through a CIP event. ATP concentration before cleaning for the old module (~2 years in operation) is around 500 pg/cm<sup>2</sup> compared to around 250 pg/cm<sup>2</sup> for the new module (30 days in operation). These values generally are much lower than average ATP values for ATP concentration in industrial RO modules indicating that biofouling does not dominate the fouling in this plant. The CIP cleaning, does significantly decrease ATP concentration leading to biofilm removal efficiency of around 60 % for both old and new modules (**Figure 5.3a**).

Similarly, the TOC values of old and new modules before and after CIP are shown in **Figure 5.3b** which shows the amount of organic matter on the membrane surface and how much it was removed by a CIP event. TOC concentration before cleaning in old module (~12 µg/cm<sup>2</sup>) was higher than in the new module (~6 µg/cm<sup>2</sup>). Again, these values are significantly lower than typical TOC values of fouled RO after two year in the operations. TOC removal efficiency demonstrates that both plants have much lower TOC removal (~20%) compared to biofilm removal (~60%) (**Figure 5.3b**). This shows that biomass indicators and specially their removal efficiency is relatively comparable in an old and new modules when there are feed with similar feed water.



**Figure 5.3** Biomass indicators before and after CIP for the old and new RO modules. a) Adenosine triphosphate concentration (ATP) ( $\text{pg}/\text{cm}^2$ ) before and after chemical cleaning; second Y-axis in blue shows ATP removal efficiency (inactivation efficiency) by chemical cleaning; b) Total organic carbon concentration (TOC) ( $\mu\text{g}/\text{cm}^2$ ) before and after chemical cleaning; second Y-axis in blue shows TOC removal efficiency by chemical cleaning.

### 5.3.3 Element concentrations in fouling layer

The calcium concentration in the fouling layer for old module before CIP is around  $5 \mu\text{g}/\text{cm}^2$  while after CIP is around  $5.9 \mu\text{g}/\text{cm}^2$ . Calcium concentration in a fouling layer of new module ( $5.5 \mu\text{g}/\text{cm}^2$ ) before cleaning which is comparable to old modules (> 2 years in operation). Unfortunately, the sampling for ICP-OES measurement from the new module after CIP was not possible as the accumulated fouling was almost negligible (See **Table 5.4**). The elements concentration for samples from new modules after CIP were below detection limits. The magnesium concentrations in all the detectable samples were almost equal ( $1\text{--}1.6 \mu\text{g}/\text{cm}^2$ ). Moreover, Iron concentration in the fouling layer is much higher before CIP ( $0.2 \mu\text{g}/\text{cm}^2$ ) than after CIP ( $<0.01 \mu\text{g}/\text{cm}^2$ ) (**Table 5.3**). However, generally the iron concentrations measured in this study is much lower than expected considering iron was heavily dosed in the plant's pretreatment steps (DAFF).

**Table 5.3** Element concentration in the fouling layer samples of the old and new modules operated in the full-scale installation. The results are shown before and after an in-situ CIP event ( $n=3$ )

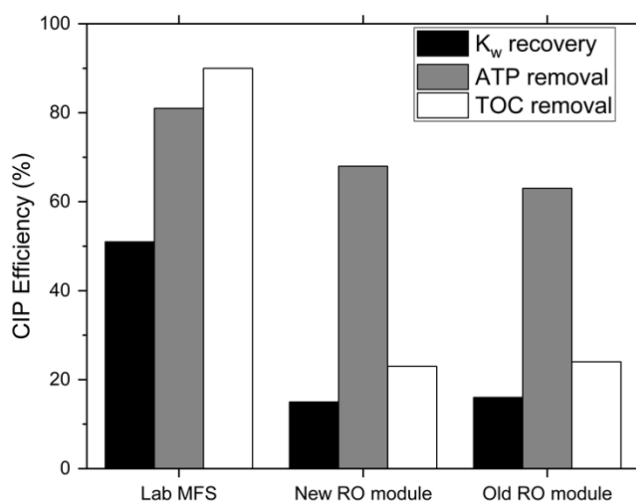
Element concentration	Old modules		New modules	
	Before CIP	After CIP	Before CIP	After CIP
Calcium ( $\mu\text{g}/\text{cm}^2$ )	$4.4 \pm 0.3$	$5.9 \pm 0.8$	5.5	<sup>1</sup> N.D.
magnesium ( $\mu\text{g}/\text{cm}^2$ )	$1 \pm 0.1$	1.3	$1.6 \pm 0.1$	N.D.
Iron ( $\mu\text{g}/\text{cm}^2$ )	0.2	<0.01	<0.01	N.D.

<sup>1</sup> Not enough accumulated fouling for measurement.



### 5.3.4 Predictability of module integration approach in CIP efficiency

We evaluated whether the proposed approach (installation of new modules in the full-scale and its operation for 30 days) is representative for fouling simulation and CIP efficiency in the full-scale RO after a long operation (>2 years). Previously, we showed that laboratory MFS, which are grown for a short time and fed with synthetic water, are not representative of full-scale installations in terms of CIP efficiency and fouling properties. **Figure 5.4** shows that CIP efficiency in permeability ( $K_w$ ) recovery is around 50% for MFS while the value for new and old RO modules which were installed in the full-scale installation and fed with real complex feed water is around 10%. Moreover, ATP removal rate with a CIP event for the lab MFS is around 80% as opposed to ~60% for the old and new modules. Especially, TOC removal efficiency in the new RO modules, fed with complex feed water for 30 days, is much more representative old module RO than MFS fed with synthetic feed water for 30 days.



**Figure 5.4** CIP efficiency in permeability recovery, ATP removal and TOC removal with in between lab-MFS, new modules and old modules. MFS results are extracted from the adapted from (Jafari et al. 2020).

### 5.3.5 Extracted EPS properties and EPS compositions

The amount of polysaccharide and protein in a fouling layer appeared to be crucial in fouling removal and CIP efficiency. The Protein/Polysaccharide ratio (PN/PS) are reported to be important in CIP efficiency. As previously shown, the biofouling is not the major part of the fouling under study (**Figure 5.3**) which leads to lower amount of extracted EPS. The amount of accumulated biomass and consequently the extracted EPS was relatively low for the new modules. This was specially the case for the new module after CIP, where not enough fouling samples could be collected for EPS analysis. **Table 5.4** shows the protein to polysaccharide ratio (PN/PS) is around 0.1 for the old modules before and after CIP and ~ 0.9 for the new module before CIP. On other words, the EPS of old modules is more polysaccharide-rich compared to new modules. Although, one should note that the polysaccharide concentration is very close to the measurement's detection limits which makes any definitive conclusion from the these results difficult to draw (**Table 5.4**).

**Table 5.4** EPS composition of biofouling formed on the old and new modules operated in the full-scale installation. The results are shown before and after an in-situ CIP event (n=3).

EPS composition	Old modules		New modules	
	Before CIP	After CIP	Before CIP	After CIP
Polysaccharide ( $\mu\text{g/L}$ )	31.1	18.7	<sup>1</sup> <2.1	<sup>2</sup> N.D.
Protein ( $\mu\text{g/L}$ )	3.5	2.2	1.8	N.D.
Protein /Polysaccharide (PN/PS)	0.1	0.1	>0.9	N.D.

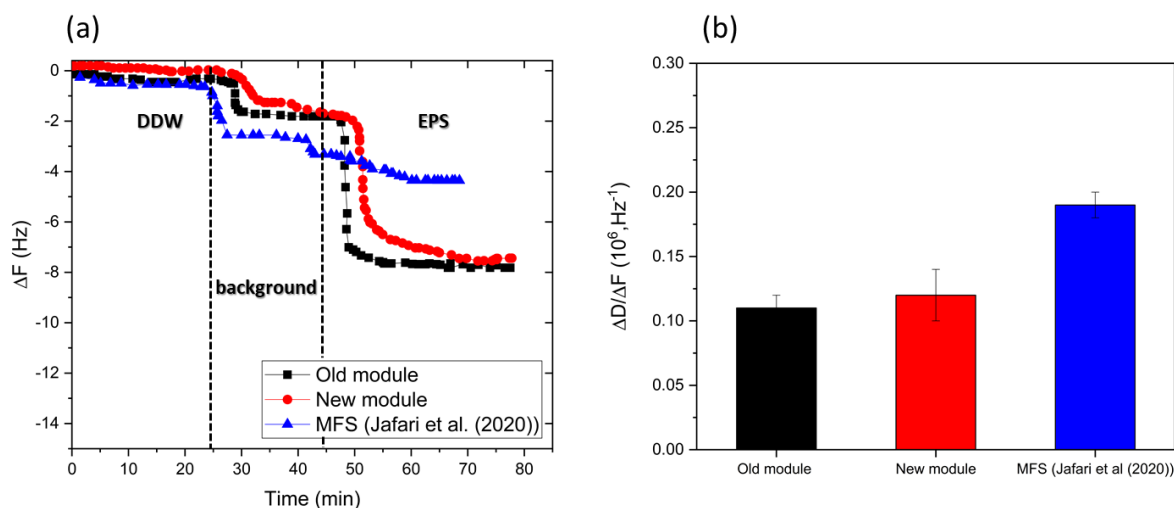
<sup>1</sup> Close to the measurement's detection limit

<sup>2</sup> Not enough accumulated fouling for measurement

### 5.3.6 EPS adherence properties and QCM-D measurements

The EPS extracted from the old and new modules before CIP showed very similar behaviour when they were exposed to the coated QCM-D sensors. The results were compared with MFS EPS adherence properties as shown in our previous work (Jafari et al. 2020). Adherence measurement were only carried out on the modules before CIP, as one round of cleaning would not change the EPS properties (Al Ashhab et al. 2017). Milli-Q water, Double Distilled Water (DDW), was used to measure the baseline of the adsorption experiments. As expected, the frequency shift for the DDW water is almost zero followed by small shift of  $\sim 2$  Hz for the background solution (**Figure 5.5a**). The shift in frequency for the background solution is due to the changes in the solution viscosity and density compared to Milli-Q water. The frequency shift increased as the EPS solution was introduced to the coated sensor. The adsorption of the polymer (EPS) on the coated sensor caused additional frequency changes of  $\sim 5$ - $6$  Hz for both old and new modules (**Figure 5.5a**). A shift in EPS shows adoption to the coated sensor, the higher frequency shift, the more amount of adsorbed polymer of the surface. Again, EPS adherence data shows that old and new modules shows very similar adherence properties and they have much higher adherence properties ( $\sim +50\%$ ) compared with laboratory MFS grown under lab conditions. The dissipation of energy due to viscoelastic behaviour of the coated layer is shown in ( See **supplementary information Figure 5.S1**). The dissipation of energy per oscillation,  $\Delta D$ , for two overtones ( $n = 5$  and  $7$ ) was also measured to analyse adsorbed EPS layer viscoelastic behaviour. The slope of the linear relationship between frequency shift,  $\Delta F$ , and dissipation change,  $\Delta D$ , during EPS solution measurement gives an indication of the EPS adsorbed layer fluidity on the coated sensors. The  $\Delta D/\Delta F$  for old module before CIP is  $\sim 0.11$  and for the new module is around  $0.12$  as oppose to  $\Delta D/\Delta F$  of around  $0.19$  for MFS under study.

$\Delta D/\Delta F$  results show that the EPS extracted in old and new modules have very similar rigidity ( $\sim 0.11$ ) while the lab MFs has much lower rigidity (high fluidity) of around  $0.19$ .



**Figure 5.5** EPS adherence properties on sensor coated with polyamide using QCM-D; a) the frequency shift ( $\Delta F$ ) showing EPS adherence to the membrane-like surfaces, b) EPS fluidity indicator during EPS adsorption on the coated sensor.

## 5.4 Discussion

*CIP efficiency and performance parameters.* Performance parameters such as (NPD, Kw) are often monitored to evaluate plants performance. Chemical cleaning efficiency in membrane system is measured based on the extent that a CIP event can recover the reduced permeability and the elevated pressure drop (Al-Juboori and Yusaf 2012, Al Ashhab et al. 2017, Beyer et al. 2014, Madaeni and Mansourpanah 2004a). It has been widely reported that fouling formation on membrane surface and spacer leads to a reduction in water permeability and such reduction continue to increase during operation. Water permeability values for old RO modules are slightly lower than new RO modules (**Figure 5.2**). This is in-line with the previous reports on the impacts of operational time on water permeability (Beyer et al. 2017, Beyer et al. 2014, Flemming 2002, Hijnen et al. 2012, Li and Elimelech 2004). The lower permeability of the old RO modules is attributed to higher fouling severity of the old RO modules (e.g. higher TOC and fouling consolidation over time)(**Figure 5.3**). (Al Ashhab et al. 2017, Bereschenko et al. 2011) reported that fouling properties will change over time due to accumulation of more organic fouling, biofilm formation and its interaction to other types fouling as well as precipitation and complexation with metal ions (Hijnen et al. 2011a, Shen et al. 2018). Similarly, pressure drop values for old RO modules are slightly higher than new RO modules. Higher pressure drop in the old RO modules was induced by greater fouling accumulation (i.e., organic fouling and biofouling) leading to formation of thicker fouling layer and consequently higher pressure drop. This is in-line with other studies correlating pressure drop increase over time (Beyer et al. 2017, Beyer et al. 2014, Bucs et al. 2016, Vrouwenvelder et al. 2010b, Vrouwenvelder et al. 2009, Vrouwenvelder et al. 2006). Interestingly, CIP efficiency values in both permeability and pressure drop recovery are very similar in old and new modules (**Figure 5.2**). This opposes the Al Ashhab et al. (2017) observation that CIP efficiency decreases significantly as the number of CIP events (CIP history) increases. Such clear difference in the CIP efficiency results can be attributed to the fact that their experiments were carried out in the laboratory conditions (laboratory feed water and flow cells). Surprisingly, CIP efficiency in permeability recovery is higher than CIP efficiency in pressure drop reduction (**Figure 2**). This is due to the

fact fouling removal through sheer force during CIP and removal of thick and patchy biofilm leading to greater recovery of pressure drop (Creber et al. 2010, Wibisono et al. 2015) while EPS solubilisation and removal of thin base layer of fouling is required to significantly recover the permeability (Sanawar et al. 2018). This is in agreement with previous works suggesting the presence thin, rigid and dense base layer determine water permeability (Derlon et al. 2016, Jafari et al. 2019, Jafari et al. 2018) The fouling samples in the current study are very thin (See fouling images in SI) thus, higher CIP efficiency was expected for permeability recovery than for the pressure drop reduction.

*Biomass indicators and CIP efficiency.* The biomass indicators such as ATP and TOC values measured in this study (**Figure 5.3**) are in the range of reported data, however in the lower side of the range (Beyer et al. 2017, Beyer et al. 2014, Hijnen et al. 2012, Jafari et al. 2020). Low TOC values suggest relatively low Natural Organic matter (NOM) in the fouling layer while low ATP values suggest low biofilm/biofouling fraction in the deposited fouling layer of both modules (Beyer et al. 2014, Jafari et al. 2020). This is indeed compatible with the visual investigation as the membranes both old and new modules are lightly fouled (See fouling images in SI). ATP and TOC values are slightly higher for the old modules than for the new modules (**Figure 5.3**). This is in accordance with previous studies which show correlation of fouling accumulation and operation time (Al Ashhab et al. 2017, Hijnen et al. 2011a, Miller et al. 2012, Vrouwenvelder et al. 2009, Vrouwenvelder et al. 2008). CIP efficiency for ATP removal is around 60% and for TOC removal around 20%. CIP efficiency for TOC removal is lower than ATP removal efficiency which in accordance with previous reported studies that TOC removal is often lower than ATP removal (Hijnen et al. 2012, Hijnen et al. 2011a). One should note the higher ATP removal compared to TOC removal rate observed in this study could be explained by the fact that ATP removal actually means ATP in-activation (leading to dead biofilm residual on the membrane surface) (Abushaban et al. 2019, Jafari et al. 2020). Interestingly, CIP efficiency values for both ATP and TOC are similar for old and new modules (**Figure 5.3**) and well below removal efficiency reported in the literature for laboratory studies (e.g, jar test and flow cell)(Cornelissen et al. 2007, Elimelech 2009, Farhat et al. 2019, Hijnen et al. 2012, Sanawar et al. 2018). Another important reason to explain low fouling severity (both ATP, TOC values) observed in this case study is the low concentration of divalent cations (e.g.,  $\text{Ca}^{2+}$ ,  $\text{Mg}^{2+}$ ) as well as Iron found in this study (**Table 5.4**). A softener unit (ion exchange resin) was installed prior to RO in this case study (**Figure 5.1**) in order to lower scaling potentials. Presence of divalent cations in the fouling layer are often linked to formation of stiff fouling layer through formation organic bonds (Shen et al. 2018).

*New approach in fouling research: integration of new modules in full-scale installation.* Recently several studies have shown that the results of CIP efficiency in the laboratory conditions are not applicable of full-scale installations. Tew et al. (2019) reported a significant difference in CIP efficiency results between lab-scale and industrial-scale RO membranes for concentrating milk. Although their feed water was similar in the laboratory and full-scale, they observed very little impact of CIP on permeability recovery in full-scale as oppose to significant flux recovery in lab-scale (identical CIP protocol). In our previous work, Jafari et al. (2020) showed that CIP efficiency is much higher in the laboratory than in full-scale operation. Typical laboratory conditions (synthetic feed water with excess nutrients, short experiment time) lead to formation of fouling which is very different than fouling grown under full-scale conditions (complex feed water with nutrient limitation and long experiment time) (Jafari et al. 2020). We suggested that CIP protocols and their efficiency should be developed

under similar conditions as full-scale (e.g., feed water, operation time, TMP). The approach suggested in this study, integration of new modules in the full-scale installation and operated for 30 days, show promising results from CIP efficiency and biomass removal points of view (**Figure 5.4**). CIP efficiency in terms of permeability recovery is much lower in the full-scale than in laboratory (**Figure 5.4**). This is in line with previous study suggesting that CIP protocols are not as efficient in the full-scale as the laboratory study (Jafari et al. 2020, Tew et al. 2019). Interestingly, CIP efficiency of both old and new modules are almost identical which shows that this proposed approach for fouling simulation and CIP development has high potential to mimic the fouling and predict the CIP efficiency of the full-scale installations. ATP and TOC removal efficiency also shows that that these biomass indicators are removed to much lower extent under the full-scale conditions than in the lab MFS (**Figure 5.4**). Especially, TOC removal efficiency values are much lower in the full-scale (~20%) than in the lab MFS (~90%) which can be attributed to the deposited fouling layer properties (Al Ashhab et al. 2017, Jafari et al. 2020, Sanawar et al. 2018) (e.g., EPS properties). Interestingly, ATP removal rate in the lab MFS (80%) and full-scale modules shows relatively similar removal rate (60%). This can be explained with the fact that ATP removal rate in practice means ATP in-activation which results in in-activation of viable biomass (killing live cells) by a CIP events (Sanawar et al. 2018). Therefore, ATP removal rate is less prone to the different in feed water and operating conditions in the laboratory and full-scale as suggested by (Beyer et al. 2017, Sanawar et al. 2019, Sanawar et al. 2018, Siddiqui et al. 2017). Moreover, the results of this study suggest that impact of similar feed water and operational conditions is more important in predictability of CIP efficiency (permeability recovery, ATP and TOC removal) than operational time (at least for the fouling developed for 30 days).

*EPS composition.* EPS composition was measured to further investigate the underlying reason for observed similarity between the old and new RO modules installed in the full-scale installations in terms of CIP efficiency, ATP and TOC removal rate. Considering chemical cleaning mechanisms (e.g., solubilisation, hydrolysis,...) (Beyer et al. 2014, Madaeni and Mansourpanah 2004b, Porcelli and Judd 2010a, Trägårdh 1989) and important of EPS solubilisation, as biofilm glue, in biofilm removal, EPS properties are reported to determine the solubility of EPS in contact with cleaning solution. As it was previously suggested (Al Ashhab et al. 2014, Jafari et al. 2020), the Protein/Polysaccharide ratio is a good indicator to study the EPS compositions in the membrane systems. The biofouling formed in both old and new RO modules consists of polysaccharide-rich EPS (PN/PS<1). In case of old RO modules, the observed polysaccharide-rich EPS is in contradiction with our initial hypothesis that protein-rich EPS will be formed under full-scale conditions (nutrient imitated feed water, long term operation). The protein-rich EPS under full-scale conditions was previously reported in several studies. For instance, Herzberg et al. (2009) reported the PN/PS ratio of extracted EPS from the fouling layer in a MBR increased with increasing SRT in MBR. In other words, PN/PS ratio increases with an increase in biofilm age. Similar result was observed between biofilm age and PN/PS ratio of extracted EPS from dead-end UF systems (Desmond et al. 2018a). However, the EPS extracted from both old and new RO modules in this study are both polysaccharide-rich. One should note that there are also reports of polysaccharide-rich EPS under full-scale conditions as well. Beyer et al. (2017) reported a sugar-rich EPS for biofouling formed on two of full-scale RO. The polysaccharide-rich EPS under full-scale conditions was attributed to extensive CIP cleanings (leading to formation of very young biofilm) or feed water with relatively high nutrient (e.g., due to seasonal algae bloom). In this case study, the extracted EPS from old RO modules is polysaccharide-rich which could

be attributed to extensive CIP cleaning (52 time per year) leading to formation of sugar-rich EPS which is reported to be essential for the initial biofilm development and early adherence on the surface as well as required for structural integrity (Christensen 1989, Limoli et al. 2015, Sweity et al. 2011).

*EPS adherence properties.* The QCM-D results shows adherence properties of the extracted EPS to the membrane surface (**Figure 5.5**). The frequency change,  $\Delta F$ , and dissipation energy,  $\Delta D$ , values show that the EPS extracted from old RO modules and new RO modules have similar adherence to the membrane surface. This also could be underlying reason for similar CIP efficiency observed for old and new RO modules. Al Ashhab et al. (2017) reported as that EPS adherence to the membrane surface increases as the number CIP events increases. They also observed that CIP efficiency decreased as the number of CIP events performed increases due to formation and/or selection of resilient biofilm with high adherence properties to membrane surface. In other words, the CIP efficiency is correlated to EPS adherence properties (higher adherence properties leads to lower CIP efficiency). This is in accordance to the results of this study which reports the extracted EPS of both old and new modules show similar adherence properties which led to similar CIP efficiency values. Moreover, EPS adherence properties of old and new RO modules integrated in the full-scale installation are very similar as oppose to lab MFS adherence results which shows much lower adherence properties (**Figure 5.5**)(Jafari et al. 2020). These results again suggests that the proposed fouling simulation method to predict CIP efficiency, integration of new modules in the full-scale integration for 30 days, has very good potential to be further investigated for fouling studies.

*Practical implications and future research.* In our previous study we showed that significant CIP efficiency differences observed between laboratory conditions (flow cell fed with synthetic feed water and short time operation) and full-scale RO installation are linked to its EPS properties differences (EPS composition and adherence properties)(Jafari et al. 2020). We also proposed that CIP protocols should be developed using real feed water and over long experiment time. However, long term experiments are often logistically very difficult considering financial, logistics and scientific issues (e.g., number of replicates, research duration and funding). From practical and industrial points of view, long term experiments for fouling analysis and CIP development does not justify the industrial cost-benefit analysis of long-term fouling experiments . Thus, the proposed a novel fouling simulation method in this study, integration of modules in the integration module for 30 days, which does provide a good trade-off between similar conditions with full-scale installations (identical operation, identical feed water and relatively manageable time span of 30 days). Moreover, this approach provides much easier operation compared to laboratory and also consistent results compared to lab results. Therefore, future research should focus on developing a protocol for fouling simulation in the full-scale installations in a systematic manner. Furthers investigations are also required to unravel the i) underlying factor in determining EPS properties ii) the EPS properties transition over time under full-scale installation. Although the proposed method showed promising results at least from CIP efficiency and EPS properties point of view, its main challenges remain the membrane module cost, sampling difficulty and logistical arrangements (i.e., consistency in the operation during experiment) with industrial partner running full-scale plant under study. However, considering the declining trend on membrane price, the cost of experiment should not be the bottleneck to apply the propose method.

## 5.5 Conclusions

The goal of this study was to investigate suitability of new fouling simulation method, integration of new membrane modules in the full-scale operation for 30 days, from CIP efficiency and biomass and EPS properties. The main findings can be concluded in:

- The new RO module installed in the full-scale installation for 30 days has similar CIP efficiency and ATP and TOC removal rate as the old RO module (> 2 years);
- Polysaccharide-rich EPS was identified in both new RO modules and old RO modules in this study. This could be attributed to extensive CIP events which was practiced in the plant.
- The new RO modules shows similar adherence properties to membrane surface than old membrane modules;
- Overall, the new proposed fouling simulation method show promising results and in both CIP efficiency results and fouling properties.

Thus, we suggest that future research should focus to investigate further the fouling properties and its correlation to operation time as the modules are integrated in the full-scale installation.

## 5.6 Acknowledgements

This study was funded by European Union's Horizon 2020 research and innovation program under the Marie Skłodowska-Curie grant agreement No. 676070. The authors gratefully acknowledge David van Lennep (Lenntech B.V., The Netherlands) for kindly providing membrane modules and related supports. This communication reflects only the authors' view and the Research Executive Agency of the EU is not responsible for any use that may be made of the information it contains.

# 6

## **Cost of fouling in full-scale RO & NF installations in The Netherlands**

Believe it or not, once a revolutionary leader, a dictator, publicly said “Economy is for the donkey”

---

This chapter is published as: Jafari, M., Vanoppen, M., van Agtmaal, J.M.C., Cornelissen, E.R., Vrouwenvelder, J.S., Verliefde, A., van Loosdrecht, M.C.M. and Picioreanu, C. (2021) Cost of fouling in full-scale reverse osmosis and nanofiltration installations in the Netherlands. *Desalination*, 114865.



## **Abstract**

The economic impact of fouling in spiral wound membranes is not yet well explored. There has been an established assumption that the cost of fouling in membrane processes is significant, but this hypothesis has not been thoroughly evaluated. We conducted an economic analysis on seven full-scale installations, four nanofiltration (NF) and three reverse osmosis (RO), to estimate the cost of fouling in industrial plants. The cost of fouling was calculated in detail, including costs of increase in feed channel pressure drop, water permeability reduction, early membrane replacement, and extensive cleaning-in-place (CIP). The estimated cost of fouling was expressed as a fraction of operational expenses (OPEX) for each plant and the major cost factors in fouling and CIP costs were identified.

The selected NF plants were fed with anoxic ground water, while the feed water to RO plants was either surface water or municipal wastewater effluent. All the NF plants produce drinking water, while the RO plants produce demineralized water for industrial applications. We found that the cost of fouling in the RO plants was around 24% of OPEX, while the fouling related costs in NF cases was only around 11% due to the low biofouling potential of the anoxic ground water. The major factor in the cost of fouling is the early membrane replacement cost, followed by additional energy and with only a minor contribution from the cleaning costs. The down-time cost (caused by the interruption of water production during a CIP event) can be the major CIP cost factor for the plants with frequent cleaning events, while the cost of chemicals dominates in the plants with non-frequent CIP. In case of manual cleaning-in-place, the cost of fouling is increased by around 2% for the RO plants with frequent CIP. The manual execution of CIP cleaning is an attention point to reconsider, as the reviewed plants hold an automated CIP cleaning, providing membrane productivity advantages.

## 6.1 Introduction

There has been extensive research on fouling and its impacts on membrane processes specifically nanofiltration (NF) and reverse osmosis (RO). The main focus is usually on evaluation and mitigation of adverse impacts of fouling on process operation. Researchers have vastly studied different types of fouling (e.g., biofouling, scaling, organic and colloidal fouling), fouling formation mechanisms (Al Ashhab et al. 2017, Dreszer et al. 2014, Farhat et al. 2019, Kim et al. 2020, Li and Elimelech 2009, P. Hiemstra 1999, Vrouwenvelder et al. 1998), fouling properties (composition, (in)organic fractions and structure) (Beyer et al. 2014, Farhat et al. 2019, Guo et al. 2012, Li and Elimelech 2004, Li and Elimelech 2009, Meng et al. 2009, Miller et al. 2012, Sanawar et al. 2018, Vrouwenvelder et al. 2010b, Vrouwenvelder et al. 2009, Yu et al. 2017), and novel characterization techniques (Al Ashhab et al. 2017, Desmond et al. 2018a, Hijnen et al. 2011a, Jafari et al. 2019, Jafari et al. 2018, Mohle et al. 2007, Vrouwenvelder et al. 2006). Many studies have been dedicated to fouling mitigation (Bucs et al. 2017, Gao et al. 2011a, Jiang et al. 2017b) and control mechanisms (Derlon et al. 2014, Vrouwenvelder et al. 2010a). Development of cost-effective cleaning-in-place (CIP) (Beyer et al. 2017, Madaeni and Mansourpanah 2004a, Porcelli and Judd 2010a, Porcelli and Judd 2010b) as well as physical cleaning methods (e.g., back-washing, air-bubble cleaning) (Basu 2015, Cornelissen et al. 2007, Wibisono et al. 2014) have attracted significant attention. Besides, there has been a strong effort to develop anti-fouling membranes through surface modification to control fouling formation (Bucs et al. 2017, Rana and Matsuura 2010). Moreover, many studies were dedicated to the development of optimal feed spacers (Abid et al. 2017) and pre-treatment steps (Prihasto et al. 2009) to control and mitigate fouling. Mathematical models have been also developed to improve understanding of fouling mechanism and predict the fouling impacts on membrane performance (Picioreanu et al. 2009, Radu et al. 2014, Radu et al. 2010).

However, the economic impact of fouling on membrane processes (i.e., the extent that fouling causes additional costs on membrane processes) received only limited attention in the technical and scientific literatures. There has been an established assumption that the cost of fouling in the membrane process for water treatment is significant, but this hypothesis (to the best of the authors' knowledge) has not been well documented for RO and neither for NF systems. Some studies have reported that the cost of biofouling in a water production membrane system is around 20 to 30% of operating expenditure (OPEX) (Flemming 2020, Johnson 2014), but they did not provide any detailed calculations or background information. Fouling formation leads to an increase in OPEX through higher energy consumption, the need for early membrane replacement and additional CIP cleaning.

Porcelli and Judd (2010b) studied in detail the cost of chemical cleaning in Ultrafiltration (UF) for potable water production. They suggested an operational scenario (including the chemical cleaning protocols) to reduce the production cost. Ang et al. (2017) reported the technical and economic feasibility of brackish water desalination using several commercial RO and NF membranes. They used a common cost model in the economic assessment of water treatment plants (i.e., the Verberne cost model), which uses the practical plant parameters to calculate OPEX and CAPEX of a brackish water desalination plant. Their plant design was based on experimental data using synthetic feed water instead of the real feed water with a more complex composition, which leaves questions about the practicality of the study.

The adverse impact of fouling on RO/NF systems can be translated into: loss in water permeability (Al Ashhab et al. 2017, Farhat et al. 2019), increase in feed channel pressure drop (Cornelissen et al. 2007, Farhat et al. 2019, Hijnen et al. 2011a, Vrouwenvelder et al. 2010b), elevated salt passage (i.e., loss of water quality leading to early membrane replacement) (Beyer et al. 2017, Beyer et al. 2014, Jiang et al. 2017a) and the necessity of periodic chemical Cleaning-In-Place (CIP) (Hijnen et al. 2012, Li and Elimelech 2009, Madaeni and Mansourpanah 2004a). These operational problems lead to more energy consumption, capacity loss, regular membrane replacements, and in general, increasing OPEX of the plants (Flemming 2020, Jiang et al. 2017a). In addition, there are some indirect fouling related costs such as CIP waste management, down-time (during CIP events) and CIP labour that also contribute to the overall cost of fouling in membrane water treatment (Porcelli and Judd 2010b).

In this study, we implemented a comprehensive economic analysis to calculate the cost of fouling in spiral wound membrane systems (i.e., RO, NF) which produce demineralized water and drinking water in The Netherlands. To better evaluate the relative economic impact of fouling on the daily cost of each individual plant, the cost of fouling is normalized to OPEX of each plant as suggested by (Flemming 2020, Johnson 2014, Porcelli and Judd 2010b). When making a comparison of the cost of fouling between different plants, the introduction of a base case (i.e., a plant without any fouling) would not be logical, because fouling is inherently part of any membrane process and it cannot be excluded (R.D. Noble 1995). Therefore, to enable a fair comparison between the plants, the cost of fouling was normalized with the OPEX of each individual plant.

The aims of this study, conducted on seven full-scale water production installations in The Netherlands, were: i) to derive the total cost of fouling in spiral wound membrane systems (i.e., RO and NF) as a fraction of the OPEX, ii) to make a detailed analysis of cost factors and their contributions to CIP and fouling and iii) to evaluate the impact of manual and automated CIP on the OPEX and cost of fouling.

The novelty of this study consists in its methodology and approach to quantify the economic impact of the fouling in full-scale RO/NF. The study uses historical plant performance parameters and robust non-empirical cost models to calculate the cost of fouling in full-scale RO/NF installations. The results and approach proposed in this work improve the reliability of techno-economic analyses in water-treatment plants, which often either neglect fouling or use empirical models (instead of plant's performance data) to calculate the cost of fouling. Moreover, detailed analysis of fouling cost factors allows practitioners to better target fouling prevention/cleaning strategies. Finally, this study contributes to the scientific literature of fouling characterization by introducing a new indicator (i.e., cost of fouling as fraction of OPEX) to quantify the severity of fouling in membrane systems for water treatment.

## 6.2 Methodology

### 6.2.1 Plant description and operation

In total, seven water production plants were compared in this study: four using nanofiltration and three using reverse osmosis processes.

### 6.2.2 Full-scale Nanofiltration (NF) plants for drinking water production

Four NF full-scale installations (NF1, NF2, NF3 and NF4) were selected, which produce drinking water from anoxic groundwater from different groundwater wells in The Netherlands. All these plants operate at constant flux mode by adjusting feed pressure to achieve the desired flux value. All four installations consist of identical pre-treatment steps (10  $\mu\text{m}$  cartridge filter and additional phosphonate-based antiscalant). The high solubility of reduced metal ions (i.e., iron) present in the water under anoxic conditions leads to a much lower fouling potential compared to aerated feed water (van Paassen et al. 1998). In anoxic groundwater, a lower fouling potential is expected compared to aerated water. In anoxic conditions, the metal ions (i.e., iron and manganese) are in their soluble reduced state ( $\text{Fe}^{2+}$  and  $\text{Mn}^{2+}$ ) which leads to less fouling by precipitates, expressed by a lower fouling potential indicator. Moreover, the lack of oxygen in anoxic conditions slows down the biofilm formation (i.e., anoxic microbial growth has lower yield compared to aerobic conditions) and consequently lower biofouling potential. Furthermore, the low fouling potential characteristic of anoxic feed water enables a relatively long operational life ( $> 10$  years) of the membrane modules (**Table 1**).

Periodical CIPs are performed in all NF plants as the feed channel pressure increased by 25-40% compared to the start-up value of the plant (Beyer et al. 2014). The CIP protocol in all the four installations is similar and consists of two steps: *i*) acid cleaning (circulation with citric acid 2% w/w, 35  $^{\circ}\text{C}$ , 3 hours), and *ii*) alkaline cleaning (circulation with NaOH, pH 11-12, 0.01 M, 35  $^{\circ}\text{C}$ , 3 hours). The acid-base cycles are repeated three times, and at the end the modules are rinsed with NF permeate water. The NF plants undergo non-frequent CIP routines (once every two years) due to the low fouling potential of their feed water. All the chosen plants are equipped with automated CIP systems. During acid and base cleanings in all the NF plants, the flow rate alternates between low (5  $\text{m}^3/\text{h}$  per element) and high (10  $\text{m}^3/\text{h}$  per element) values every half an hour. More details about the NF plants and their feed water characteristics can be found in (Beyer et al. 2014). The main characteristics of the chosen NF plants are listed in **Table 1**.

### 6.2.3 Full-scale Reverse Osmosis (RO) plants for demineralized water production

Three full-scale RO plants (RO1, RO2 and RO3) for demineralized water production in The Netherlands were selected. All plants consist of a two-stage RO system, they are all equipped with automated CIP systems and operated at a constant permeate flux mode. The RO1 plant produces demineralized water with a conductivity below 10  $\mu\text{S}/\text{cm}$  from secondary wastewater effluent of a food company. The pre-treatment steps in RO1 consist of coagulation, flocculation and sedimentation processes followed by ultrafiltration (UF). The UF permeate is dosed with antiscalant to lower the scaling potential in the RO step. The RO2 plant produces demineralized water with a conductivity below 0.2  $\mu\text{S}/\text{cm}$  from river water and its pre-treatment steps include 100  $\mu\text{m}$  pore sized strainer, in-line coagulation and UF. The UF permeate is again dosed with antiscalant. The RO3 produces demineralized water from surface water and its pre-treatment steps include a coarse screen, coagulation, flocculation and sedimentation processes followed by UF (no antiscalant dosing).

Periodical CIPs are performed in all the RO plants as the feed channel pressure increase by 15% (Beyer et al. 2017). The CIP protocol for RO1 is as follows: i) alkaline cleaning (circulation (9 m<sup>3</sup>/h) with NaOH with, pH 12, 0.01 M, 35 °C, 1 hour), ii) alkaline cleaning (soaking with NaOH, pH 12, 0.01 M, 35 °C, 30 min), iii) repeat the alkaline cleaning cycle 2 more times, iv) rinsing with demineralized water, v) acid cleaning (circulation (9 m<sup>3</sup>/h) with HCl, pH 2.1, 35 °C, 1 hour), vi) acid cleaning (soaking with HCl, pH 2.1, 35 °C, 30 min), vii) repeat the acid cleaning cycle 2 more times, viii) final rinsing with demineralized water.

The CIP protocol for RO2 includes the following steps: i) alkaline cleaning (circulation (9 m<sup>3</sup>/h) with NaOH, pH 12, 0.01 M, 35 °C, 2 hours), ii) alkaline cleaning (soaking with NaOH, pH 12, 0.01 M, 20 °C, ~ 20 hours), iii) rinsing with demineralized water, iv) acid cleaning (circulation (9 m<sup>3</sup>/h) with Divos 2 (JohnsonDiversey, UK), pH 1.6, 35 °C, 1.5 hour), vi) final rinsing with demineralized water.

The CIP protocol for RO3 plant includes the following steps: i) soaking with demineralized water for 30 min, ii) alkaline cleaning (circulation (9 m<sup>3</sup>/h) with sodium bisulphite, pH 10.5, 1-1.5 % v/v, 35 °C, 1 hour), iii) alkaline cleaning (soaking with sodium bisulphite, pH 10.5, 1-1.5 % v/v, 20 °C, 2 hours), iv) acid cleaning (circulation (9 m<sup>3</sup>/h) with Divos 2 (JohnsonDiversey, UK), pH 2.5, 35 °C, 30 min), v) acid cleaning (soaking with Divos 2, pH 2.5, 20 °C, 1 hour, vi) final rinsing with demineralized water. The RO plants characteristics are listed in **Table 6.1**. More details about these RO plants and their feed water can be found in (Beyer et al. 2017).

The CIP efficiency of different plant varies between both plants and seasonally. For instance, the average CIP efficiency in NPD reduction in RO plants is in the range 9-15% while the average CIP efficiency in  $K_w$  recovery varies in the range of 3-10%. Similar results was observed for NF plant CIP efficiency where the average CIP efficiency based on NPD was around 10% and on  $K_w$  around 3-5%.

**Table 6.1** Plant specifications and feed water parameters included in the current study (Beyer et al. 2017, Beyer et al. 2014).

Plant name → Plant characteristics ↓	NF1	NF2	NF3	NF4	RO1	RO2	RO3
Feed water source	Anoxic groundwater	Anoxic groundwater	Anoxic groundwater	Anoxic groundwater	Secondary wastewater effluent	Surface water	Surface water
Plant product	Drinking water	Drinking water	Drinking water	Drinking water	Demi water	Demi water	Demi water
Pre-treatment steps	Cartridge filter 10 µm	Cartridge filter 10 µm	Cartridge filter 10 µm	Cartridge filter 10 µm	UF	UF	UF
Years of operation	10	9	8.8	9	5.5	5	5
Production capacity (m <sup>3</sup> /day)	2880	1785	4608	2880	7680	4800	5000
Water recovery (%)	80	80	78	80	80	80	80
Membrane type	Trisep-8040- TS82	Trisep-8040- TS82	Trisep-8040- TS82	Trisep-8040- TS82	DOWFILMTEC BW30XFR-400/34i	DOWFILMTEC LE-440i	DOWFILMTEC LE-440i
CIP frequency (CIP/year)	0.7 (~once every two years)	0.6 (~once every two years)	0.6 (~once every two years)	0.7 (~once every two years)	17	17	7
CIP duration (hours/event)	8	8	8	8	8	24	6.5
Membrane area (m <sup>2</sup> ) (number of modules)	2412 (144)	1809 (89)	4221 (215)	2412 (144)	20000 (500)	10000 (250)	10417 (260)

### 6.2.4 Plant performance data and fouling parameters

For these water production plants, the impact of fouling was estimated using the main operational parameters such as water permeability and feed channel pressure drop. These parameters are routinely monitored to ensure the optimal operation of a plant. The operational parameters are often normalized to the standard conditions to allow an objective comparison between different plants (Beyer et al. 2014). The normalized specific water permeability,  $K_w$  [ $\text{m s}^{-1} \text{kPa}^{-1}$ ], is the actual membrane water flux normalized to net driving force (net transmembrane pressure) and corrected for feed water temperature (Beyer et al. 2014, van de Lisdonk et al. 2001). The normalized feed channel pressure drop,  $NPD$  [kPa], is the actual feed channel pressure drop per membrane element adjusted for feed water temperature and volume as explained by (Beyer et al. 2014, van den Broek et al. 2010). Detailed calculations of the performance parameters are given in **Supplementary Information Figure 6.S1**. Performance parameters during operational time for all the seven selected plants were mainly reported in (Beyer et al. 2017, Beyer et al. 2014), unless specified otherwise. To evaluate the effects of fouling on the process parameters, the performance indicators have been considered in average over the operation time (i.e., at least one round of membrane replacement). The initial values of the performance parameters ( $K_{w0}$  and  $NPD_0$ ) have been recorded without the unstable values obtained during the start-up period (~ 4 days after installation) of each plant. The time-averaged performance parameters of the plants were calculated between two CIP events as explained in (Porcelli and Judd 2010b). The performance parameters used to calculate the cost of fouling (i.e., additional costs such as additional energy consumption, loss of capacity and early membrane replacement) as fraction of operation costs have been listed in **Table 6.2**.

**Table 6.2** Performance parameters and clean-in-place (CIP) information for the investigated full-scale installations , used to calculate the cost of fouling as fraction of OPEX (Beyer et al. 2017, Beyer et al. 2014). Performance data are averaged over the entire operational time of plants working with their original membrane modules

Variables	Symbol	Units	NF1	NF2	NF3	NF4	RO1	RO2	RO3
<b>Performance parameters</b>									
Initial normalized pressure drop	$NPD_0$	$kPa$	275	282	251	265	168	125	123
Average normalized pressure drop	$NPD_{avg}$	$kPa$	359	359	293	344	216	173	175
Initial water permeability	$K_{w0}$	$\times 10^{-8} m s^{-1} kPa^{-1}$	1.3	1.3	1.3	1.1	1	1.6	1
Average water permeability	$K_{w avg}$	$\times 10^{-8} m s^{-1} kPa^{-1}$	1.2	1	~1.3	~1.1	0.8	1.1	0.8
Design flux	$J_{design}$	$L m^{-2}/h$	22	22	22	22	20	20	20
Feed flow rate	$Q_f$	$m^3 d^{-1}$	3600	2225	5908	3600	9600	6000	6250
permeate flow rate	$Q_p$	$m^3 d^{-1}$	2880	1785	4608	2880	7680	4800	5000
Average transmembrane pressure	$TMP_{avg}$	$bar$	6.3	6.3	6.3	6.3	13	13	13
<b>CIP info</b>									
Acid solution	$pH_{acid}$	$[-]$	4.7	4.7	4.7	4.7	2.1	1.6	2.5
Alkaline solution	$pH_{base}$	$[-]$	12	12	12	12	12	12	10.5
Acid volume / event	$V_{acid}$	$m^3$	12	7.5	17	12	20	10	10.5
Base volume/event	$V_{base}$	$m^3$	12	7.5	17	12	20	10	10.5
Acid temperature	$T_{acid}$	$^{\circ}C$	35	35	35	35	35	35	20 <sup>a</sup> -35 <sup>b</sup>
Base temperature	$T_{base}$	$^{\circ}C$	35	35	35	35	35	20 <sup>a</sup> -35 <sup>b</sup>	20 <sup>a</sup> -35 <sup>b</sup>

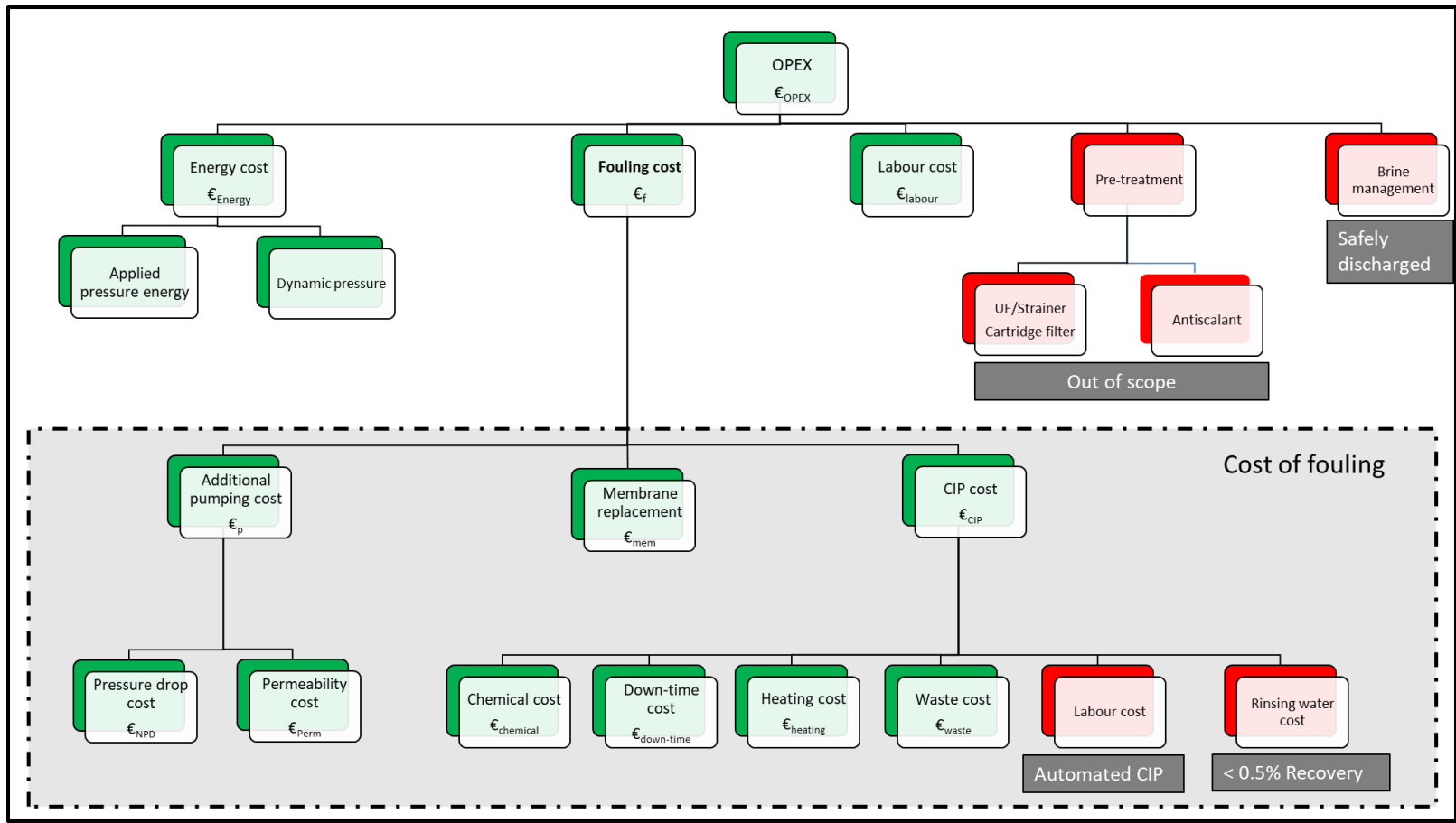
<sup>a</sup> Soaking temperature; <sup>b</sup> Circulation temperature.



### 6.2.5 Economic analysis and cost estimation

A cost calculation spreadsheet has been developed in which all relevant costs caused by fouling in the full-scale installations have been included. **Figure 6.1** illustrates an overview of the scheme used in this study to calculate the cost of fouling as a fraction of OPEX. The economic impact of fouling on the plant OPEX was considered. CAPEX was not included in these calculations, because CAPEX calculations usually are highly case-dependent and subjective. The economic impacts of fouling on the pre-treatment steps have been considered out of the scope of this study. This is due to the fact that the considered NF plants are all equipped with identical pre-treatment steps (i.e., cartridge filter) and the RO plants have all ultrafiltration (UF) in upstream. Therefore, it is reasonable to compare fouling impact only on the main purification steps (RO, NF) and neglect often similar and typical pre-treatment steps prior to NF/RO units.

The fouling formation causes an increased feed channel pressure drop, reduction in water permeability, and an increase in salt passage. The deterioration of these performance parameters is compensated by additional pumping energy (constant flux operation mode) and consequently higher pumping costs. The replacement of membrane modules occurs normally when their lifetime was exceeded or when salt passage exceeds 5% due to extensive fouling formation (typical values of demineralized water quality) (Beyer et al. 2017). CIP cost basically consists of chemical costs (acids and bases), down-time cost, CIP solutions heating costs and waste management costs (**Figure 6.1**). As all the plants in this study are equipped with automated CIP, labour cost in the CIP was neglected. In addition, cost of rinsing water (during rinsing steps of CIP events) is neglected as often the amount of water used is negligible (<0.5% permeate production) (Intellegence 2018). The cost of membrane replacement has been considered in OPEX since membrane replacement is often caused by operational issues such as severe fouling (Johnson 2014, Mendret et al. 2019). In all the investigated plants, the cost of brine management is negligible due to the plants vicinity to the waterbodies which allows a safe discharge of the brine. Moreover, no contractual penalty (additional costs for delayed water delivery to clients) are considered. Contractual penalties in practise are often countered by additional plant capacity (CAPEX).



**Figure 6.1** Schematic overview of the cost of fouling calculation as a fraction of OPEX, used in this study to compare seven full-scale RO and NF installations in The Netherlands. Cost of fouling is considered using cost factors inside the dot-dashed box. Only the cost factors in the green rectangles are considered, while the cost factors in the red rectangles are either negligible or assumed to be out of scope. The justifications for omission are provided below the red boxes. CIP pumping cost is less than 0.01% of total CIP cost.

To determine the cost of fouling ( $\epsilon_f$ ) as a fraction of the OPEX ( $\epsilon_{OPEX}$ ) in each case study per year, the costs of additional pumping energy due to the fouling ( $\epsilon_p$ ), membrane replacement costs ( $\epsilon_{mem}$ ), and CIP costs ( $\epsilon_{CIP}$ ) have been calculated using equation (6.1). The OPEX of each plant consists of costs of energy ( $\epsilon_{energy}$ ), membrane replacement ( $\epsilon_{mem}$ ), cleaning-in-place ( $\epsilon_{CIP}$ ) and labour for operation of the plant ( $\epsilon_{labour}$ ) as stated in equation (6.2). The additional pumping energy cost is caused by both permeability reduction cost ( $\epsilon_{perm}$ ) and pressure drop increase costs due to fouling deposition ( $\epsilon_{NPD}$ ) according to equation (6.3). The CIP cost ( $\epsilon_{CIP}$ ) includes the costs of chemicals ( $\epsilon_{chemical}$ ), down-time ( $\epsilon_{down-time}$ ), heating cost ( $\epsilon_{heating}$ ) and waste management ( $\epsilon_{waste}$ ) according to equation (6.4).

$$\epsilon_f = \epsilon_p + \epsilon_{mem} + \epsilon_{CIP} \quad (6.1)$$

$$\epsilon_{OPEX} = \epsilon_{energy} + \epsilon_{mem} + \epsilon_{CIP} + \epsilon_{labour} \quad (6.2)$$

$$\epsilon_p = \epsilon_{perm} + \epsilon_{NPD} \quad (6.3)$$

$$\epsilon_{CIP} = \epsilon_{chemical} + \epsilon_{down-time} + \epsilon_{heating} + \epsilon_{waste} \quad (6.4)$$

The total cost of energy consumption,  $\epsilon_{energy}$  [€/year], is calculated based on the average applied pressure ( $P_f$ ) (including average transmembrane pressure ( $TMP_{avg}$ ), axial pressure drop due to constant flux mode and dynamic pressure), flow rate of the water, operation time and amount of down-time of the plant due to CIP cleaning (much lower pressure applied during CIP events) using equation (6.5) (Porcelli and Judd 2010b),

$$\epsilon_{Energy} = \frac{Cf_e}{\eta} P_{f_{avg}} \left( Q_f \times (t - N_{CIP} t_{CIP}) \right) \quad (6.5)$$

where  $Cf_e$  is the unit cost of electrical energy in The Netherlands,  $\eta$  is the typical electrical power conversion efficiency (**Table 3**),  $Q_f$  is flow rate,  $t$  is operational time (i.e., one year),  $N_{CIP}$  is the number of CIP events during the time frame, and  $t_{CIP}$  is duration of each CIP event.

Impact of fouling on membrane replacement has been considered by calculating cost of replacing the modules during the operation time according to equation (6.6):

$$\epsilon_{mem} = \frac{Cf_{module}}{t} \cdot N_{module} \quad (6.6)$$

where  $Cf_{module}$  is unit cost of one membrane module (depending on membrane type),  $N_{module}$  is the number of modules in each installation. The membranes are replaced at the end of their life time, as mentioned in **Table 6.1** (“Operation time”). The membrane replacement costs are divided over the operation time to normalize the annual cost of membrane replacement.

Labour cost,  $\epsilon_{labour}$  [€/year], as part of OPEX is calculated based on number of operators ( $N_{labour} = 2$ ) (Personal communication with Evides Industriewater B.V.) and their annual wages ( $Cf_{labour}$ ) as stated in equation (6.7)

$$\epsilon_{labour} = C_{f_{labour}} \cdot N_{labour} \quad (6.7)$$

The cost of feed channel pressure drop increase due to fouling,  $\epsilon_{NPD}$  [€/year], is calculated based on the changes in normalized pressure drop ( $NPD$ ) averaged during operation time ( $t$ ) as stated in equation (6.8) (Porcelli and Judd 2010b):

$$\epsilon_{NPD} = \frac{C_{f_e}}{\eta} \cdot t \cdot (NPD_{avg} - NPD_0) \cdot Q_f \quad (6.8)$$

where  $NPD_{avg}$  is the average  $NPD$  during operation time,  $NPD_0$  is the initial  $NPD$  in the beginning of the operation (prior to fouling).

The reduction in permeability caused by fouling is compensated by pressurizing the feed water and consequently higher energy costs. The permeability costs,  $\epsilon_{perm}$  [€/year], is related to the change in the water permeability ( $K_w$ ) during operation as mentioned in equation (6.9) (Porcelli and Judd 2010b) :

$$\epsilon_{perm} = \frac{C_{f_e}}{\eta} \cdot t \cdot J_{design} \cdot \left( \frac{1}{K_{w_{avg}}} - \frac{1}{K_{w_0}} \right) \cdot Q_f \quad (6.9)$$

where  $K_{w_{avg}}$  is the average water permeability during operation time,  $K_{w_0}$  is the initial permeability in the beginning of the operation (prior to fouling).

The CIP cost and its constituent cost factors are stated in equation (6.4). The chemical cost in CIP events,  $\epsilon_{chemical}$  [€/year], is calculated based on the volume of chemical solutions used in one cleaning event ( $V_{acid}$ ,  $V_{base}$ ), concentration ( $C_{acid}$ ,  $C_{base}$ ), number of CIP events per year ( $N_{CIP}$ ), and unit cost of chemicals ( $C_{f_c}$ ) according to equation (6.10) (Porcelli and Judd 2010b),

$$\epsilon_{chemical} = C_{f_c} \cdot N_{CIP} \cdot (C_{acid} \cdot V_{acid} + C_{base} \cdot V_{base}) \quad (6.10)$$

The down-time cost caused by disruption in water production due to each CIP event is calculated according to equation (6.11) (Porcelli and Judd 2010b)

$$\epsilon_t = Q_p \cdot C_{f_w} \cdot N_{CIP} \cdot t_{CIP} \quad (6.11)$$

where  $Q_p$  is water production ( $m^3/h$ ),  $C_{f_w}$  is the margin of unit of product water €/m<sup>3</sup> and  $N_{CIP}$  is the number of CIP events and  $t_{CIP}$  is the duration of each CIP event.

As CIP solutions need to be heated up before each CIP events, heating cost of CIP solutions are calculated based on the required energy to heat up the chemical solutions from ambient temperature ( $T_{amb}=10$  °C) to cleaning temperature ( $T_{CIP}$ ) equation (6.12) (Porcelli and Judd 2010b)

$$\epsilon_h = \frac{C_{f_e}}{\eta} \cdot \rho \cdot C_p \cdot (T_{amb} - T_{CIP}) \cdot V_{CIP} \quad (6.12)$$

where  $C_p$  is specific heat capacity (4.2 kJ/kg/K), and  $\rho$  is the density of the chemical.

The chemical waste produced during each CIP routine is usually neutralized and the cost of waste management is calculated as suggested by (Zondervan et al. 2008) according to equation (6.13)

$$\epsilon_w = C_{f_{waste}} \cdot V_{CIP} \cdot N_{CIP} \quad (6.13)$$

The relevant cost factors for cost calculations are listed in **Table 6.3**. Other performance parameters can be found in **Table 6.2**.

### 6.2.6 Manual and automated CIP cleaning

Although all the selected plants in this study are equipped with automated CIP, manual CIP practice is still widespread in many full-scale RO/NF plants. The annual cost of manual CIP,  $\epsilon_{\text{manual}}$  [€/year], is calculated based on number of operators considering safety measures ( $N_{\text{operator}}$ ), their annual wages ( $C_{\text{labour}}$ ) and number of CIP events per year ( $N_{\text{CIP}}$ ) according to equation (6.14). Five-day work week has been considered for operators and each CIP event has been count as whole working day.

$$\epsilon_{\text{manual}} = \frac{C_{f_{labour}} \cdot N_{labour} \cdot N_{CIP}}{270} \quad (6.14)$$

This cost calculation only takes into account the “direct cost” of automated and manual CIP. All other related costs for automated CIP (e.g., maintenance and capital investments for the automation) and manual CIP (e.g., safety and incident costs) are neglected. As all the plants under investigation are equipped with automated CIP, this was considered as the baseline and the additional cost of manual CIP was evaluated.

**Table 6.3** Cost factors for cost of fouling calculation as fraction of OPEX.

Cost factors	Symbol (unit)	Value
Power supply efficiency	$\eta$	0.6*
Electricity cost	$C_{f_e}$ (€/kWh)	0.10**
Product's margin	$C_{f_w}$ (€/m <sup>3</sup> )	0.1
Labour cost	$C_{f_{labour}}$ (€/year)	50,000***
Waste management cost	$C_{f_{waste}}$ (€/m <sup>3</sup> )	2.6
Membrane module price	$C_{f_{module}}$ (€/module)	500 <sup>b</sup> -750 <sup>c</sup>
<i>Chemical cleaning cost</i>	$C_{f_c}$	
Caustic soda (50%) <sup>a</sup>	(€/m <sup>3</sup> )	700****
Citric acid (50%)	(€/m <sup>3</sup> )	1500****
Hydrochloric acid (30%)	(€/m <sup>3</sup> )	700****
Divos 2	(€/m <sup>3</sup> )	2000****
sodium bisulphite (10%)	(€/m <sup>3</sup> )	2000****

\* (Porcelli and Judd 2010b), \*\* (Statistica 2019a), \*\*\* (Statistica 2019b), \*\*\*\* (Chauveau 2020)

<sup>a</sup> solution concentration., <sup>b</sup> Average Nanofiltration (NF) module price.

<sup>c</sup> Average Reverse osmosis (RO) module average price.

## 6.3 Results

### 6.3.1 Cost of fouling and CIP costs in relation to plant OPEX

A comprehensive economic analysis has been carried out on seven full-scale RO and NF installations to evaluate cost of fouling as fraction of the OPEX in each plant. The cost of fouling is calculated based on all the considered additional costs caused by fouling (i.e., energy, membrane replacement, and chemical cleaning) as depicted in **Figure 6.1** and described in detail in the methodology section. An estimation of the cost of fouling allows to better quantify the negative impact of fouling in the plants under study. However, to be able to fairly compare the economic impact of fouling among different plants, the cost of fouling is normalized to the OPEX of each plant. By choosing to normalize the cost of fouling to OPEX, a comparison can be made regardless of plant size

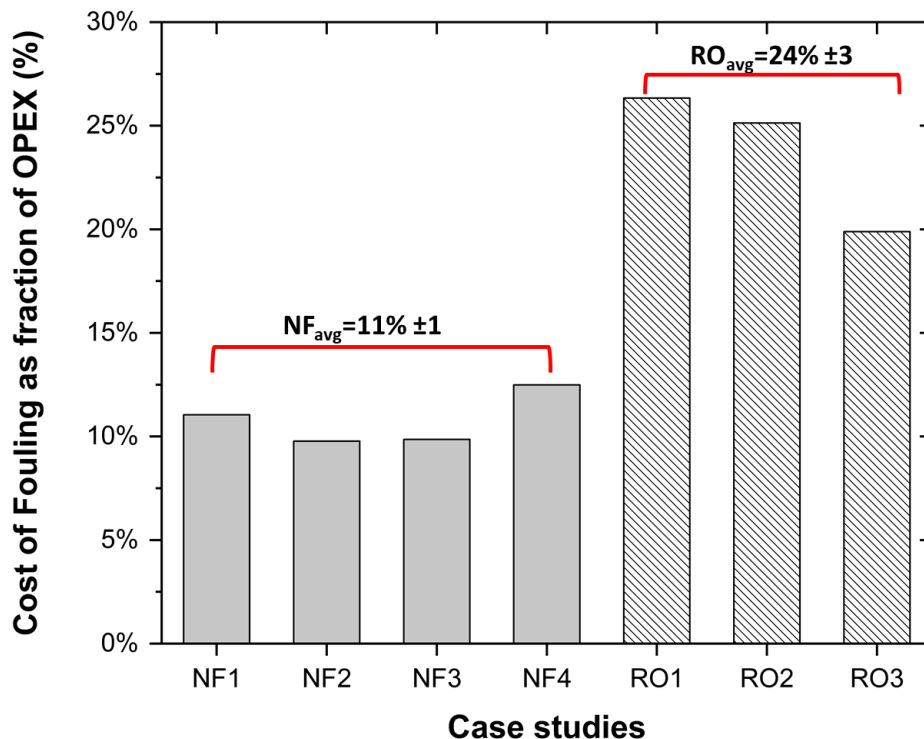
A detailed analysis on the costs of fouling and of CIP was made to identify the major contribution to the cost factors. In addition, the automated and manual CIP costs were compared to evaluate the impact of CIP automation on fouling cost.

The economic evaluation revealed that the average cost of fouling is around 11% of OPEX for the NF cases,

while considerably higher ( $24 \pm 3\%$ ) for the RO plants. The fraction  $\left( \frac{\text{€}_f}{\text{€}_{OPEX}} \times 100 \right)$  is compared for the seven

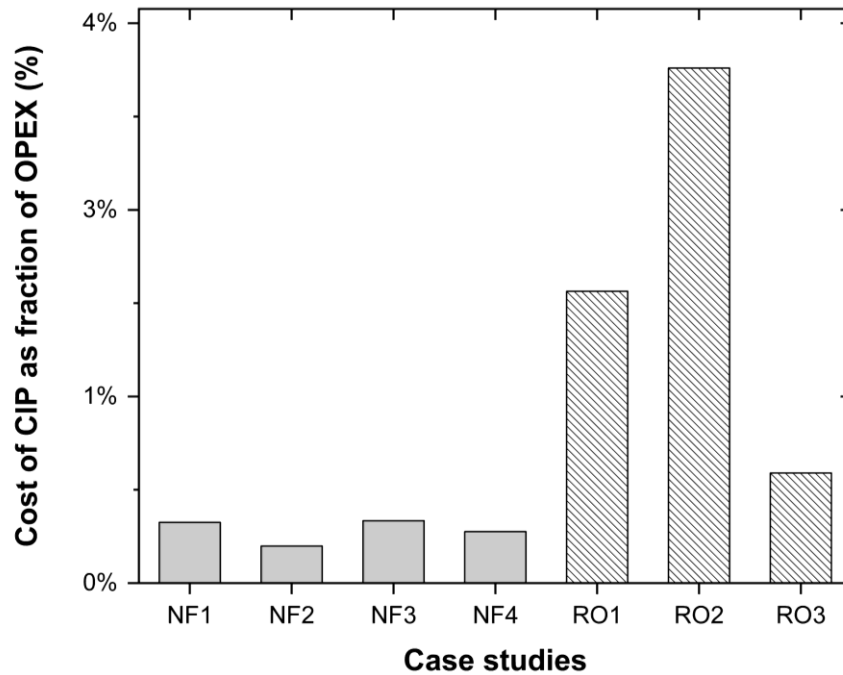
full-scale installations in **Figure 6.2**. The significant difference observed between the cost of fouling in RO and NF plants is caused by a more frequent membrane replacement in RO plants as compared to NF plants, higher energy consumption by the RO and more numerous CIP events (thus, a longer down-time) all caused by higher fouling potential in the ROs operating mainly with surface water compared to NFs that are operating with anoxic ground water. Generally, the OPEX of different NF plants varied between 0.12 to 0.21 Euro/m<sup>3</sup> depending on their production capacities. The OPEX for RO, on the other hand, ranged between 0.15 to 0.18 Euro/m<sup>3</sup>. One should consider that the above OPEX are not the actual plant's OPEX as several OPEX contributors are neglected in this study (e.g., maintenance, brine treatment., pre-treatment steps) (**Figure 6.1**).

In order to understand these notable differences between NF and RO, a more detailed cost calculation follows.



**Figure 6.2.** Cost of fouling as a fraction of OPEX for four NF and three RO full-scale installations.

The cleaning-in-place (CIP) costs as a fraction of the total OPEX (as one of the non-operational costs of fouling) is shown in **Figure 6.3**. The CIP cost as fraction of the total OPEX is relatively low, only ~ 0.5 % for NF installations compared to ~ 2% for the RO cases. The CIP cost is higher in RO as these plants underwent more frequent CIP events compared to the NF ones.

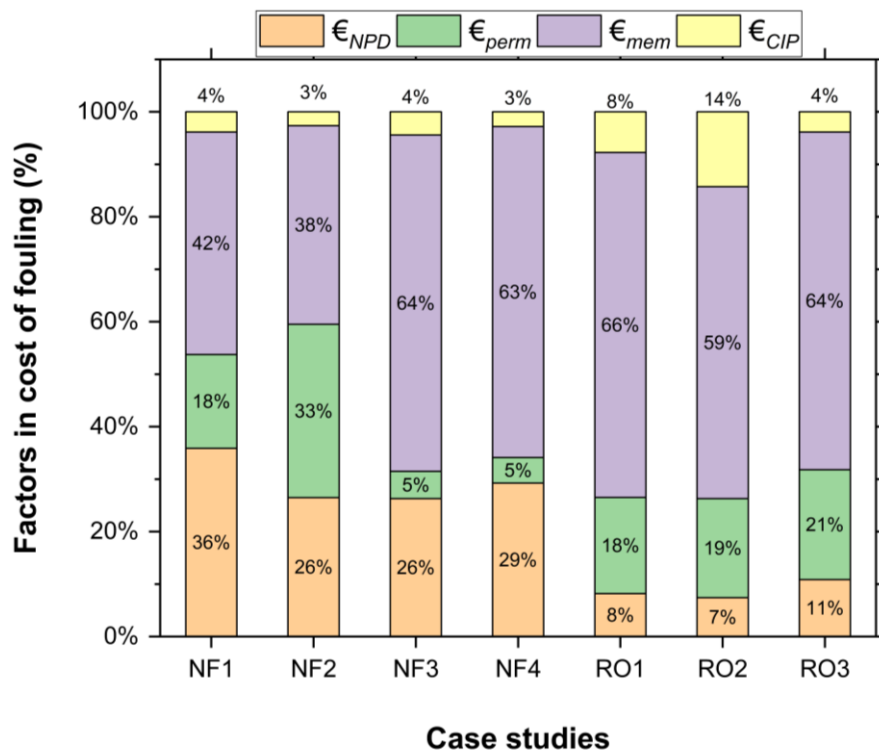


**Figure 6.3.** Cost of CIP as fraction of OPEX for all the four NF and three RO full-scale installations.

### 6.3.2 Cost factors in fouling and CIP

The cost factors contributing to the total cost of fouling are detailed in **Figure 6.4**, these include the costs of feed channel pressure drop ( $\epsilon_{NPD}$ ), water permeability ( $\epsilon_{perm}$ ), membrane replacement ( $\epsilon_{mem}$ ), and CIP ( $\epsilon_{CIP}$ ) for all installations in this study. Clearly, the main contributor to the total cost of fouling in all cases is the cost of membrane replacement ( $\epsilon_{mem} \sim 40$  to  $65\%$ ). The energy cost to compensate for the increased feed channel pressure drop ( $\epsilon_{NPD}$ ) was around 30% of the total cost of fouling for the NF cases, while only  $\sim 9\%$  for RO cases in this study. The least significant in the total cost of fouling was the CIP cost, amounting from  $\sim 4\%$  for non-frequent CIP plants (NF1-4 and RO3) to  $\sim 10\%$  of total cost of fouling for plants that undergo frequent CIP cleaning (RO1 and RO2).

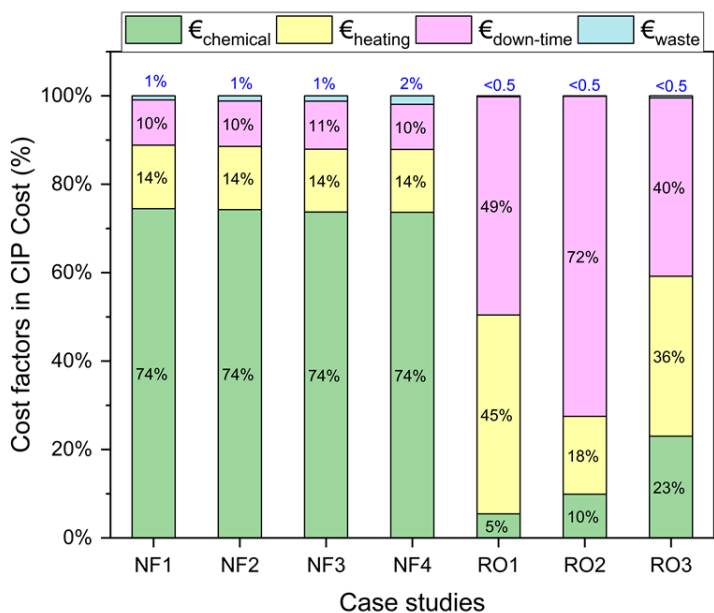




**Figure 6.4.** Factors affecting the cost of fouling for four NF and three RO full-scale installations. Cost factors include additional pumping energy due to an increase feed channel pressure drop ( $\epsilon_{NPD}$ ) and decreased water permeability ( $\epsilon_{perm}$ ), as well as costs for the membrane replacement ( $\epsilon_{mem}$ ) and cleaning-in-place ( $\epsilon_{CIP}$ ).

The CIP cost was furthermore also broken down into several cost factors as shown in **Figure 6.5**. CIP cost factors were analysed in detail, as CIP cost could be optimized more easily compared to other cost factors of fouling (membrane cost and energy cost) from standpoint of utility companies (out the sphere of control of water companies).

For the NF cases, the dominant cost contributor in CIP is by far that of the chemicals (74%), followed by heating (14%), down-time cost (10%) and negligible (<2%) waste management costs (**Figure 6.5**). Because the CIP protocols in all NF plants were very similar, the cost factor distribution was also almost identical in all NF cases. However, the RO plants had a totally different CIP cost factors distribution. The loss of revenues during down-time ranks as the most significant in all the RO cases (~ 40-70 %), followed by heating costs. The cost of CIP waste disposal is negligible (~0.2% of the total CIP cost) due to relatively low amount of CIP solution used (~ 40 L/module) and low frequency of CIP events.

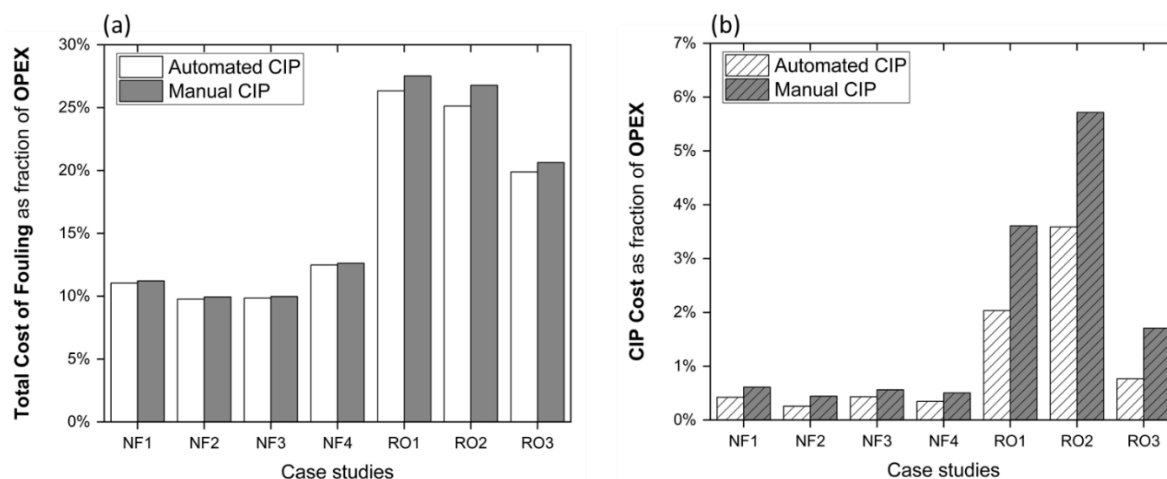


**Figure 6.5.** The CIP cost factors for four NF and three RO full-scale installations, including the cost of chemicals ( $\epsilon_{\text{chemical}}$ ), of heating the CIP solution ( $\epsilon_{\text{heating}}$ ), down-time cost during CIP events ( $\epsilon_{\text{down-time}}$ ) and waste management cost ( $\epsilon_{\text{waste}}$ ).

### 6.3.3 Impact of manual and automated CIP on the costs of fouling and cleaning

Although CIP cleaning was automated in all the case studies, manual CIP cleaning is still widespread in many existing NF/RO full-scale installations. Therefore, we evaluated the potential cost increase in case manual CIP would be performed for all the case studies. **Figure 6.6a** shows that the automated cleaning would not increase the cost of fouling for NF plants (<0.1%), while for RO plants up to ~2% increase in total cost of fouling is estimated because of the higher CIP frequency. The impact of manual versus automated CIP can be seen more clearly in the cost of CIP (**Figure 6.6b**). The observed results clearly suggest that CIP automation would lead to a direct cost saving for the plants with frequent CIP events (i.e., RO plants). However, it may be possible that considering some indirect CIP costs for both manual (e.g., incident and safety costs) and automated CIP (e.g., maintenance costs) could lead to a different conclusion

In the RO cases, with more CIP events per year, the cost of CIP as a fraction of OPEX would decrease in case of automation by a factor of 1.5 to 2 compared to the manual CIP.



**Figure 6.6.** A comparison between manual and automated CIP on four NF and three RO full-scale installations. Impact of manual and automated CIP on (a) total cost of fouling as fraction of OPEX (b) CIP cost as fraction of OPEX. All the cases in this study are equipped to automated CIP. Manual CIP for all the cases were calculated based on a CIP protocol involving two operators during the CIP events.

## 6.4 Discussion

Fouling, as the main bottleneck of membrane processes in water treatment, is generally associated with additional costs (i.e., due to early membrane replacement, additional energy consumption and extensive cleaning) (Flemming 2020, Flemming 2002, Pearce 2008, Schäfer et al. 2001). The impact of fouling on the total costs can be in the form of higher operational cost (e.g., higher energy consumption and cleaning) (Ang et al. 2017, Johnson 2014, Nya 2015, Porcelli and Judd 2010b, Schäfer et al. 2001) and in a higher investment costs (e.g., additional pre-treatment steps and over-sized design) (Ebrahim et al. 1995, Farhat et al. 2020, Gao et al. 2011a, Jiang et al. 2017b). Fouling costs depend on plant design, operational parameters and feed water quality (Flemming 2002). To calculate the cost of fouling as a fraction of operating cost (OPEX), several process and design parameters (Table 6.1 and Table 6.2) as well as the costs of consumables (Table 6.3) are required. In this study we analysed the cost of fouling for several full-scale NF and RO installations in The Netherlands.

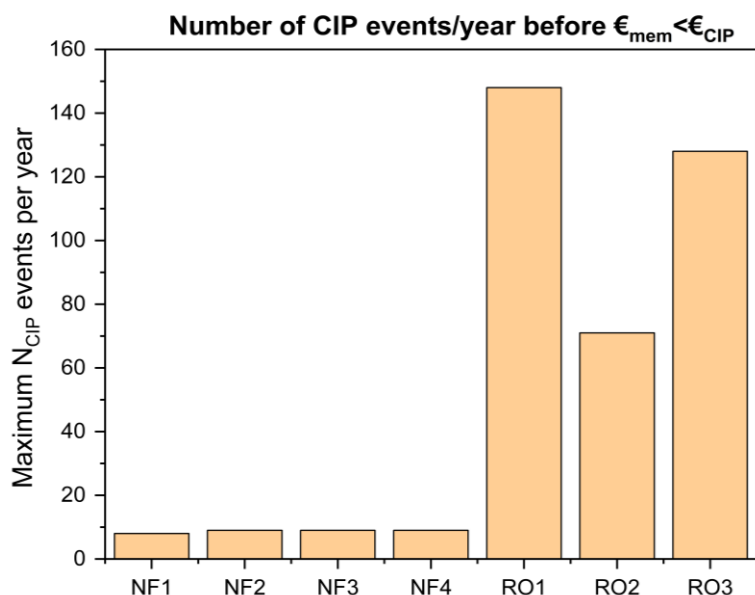
### 6.4.1 Cost of Fouling and CIP as fraction of OPEX

The calculated cost of fouling as a fraction of OPEX was around 24% for RO and 11% for NF systems with automatic CIP systems (Figure 6.2). The cost of fouling in RO systems observed in this study is in the range of other reported data, such as (Flemming 2020, Johnson 2014) who estimated the cost of fouling around 20-30% of the operating costs, however, without providing detailed information on the basis for their estimates. In general, the cost of fouling is mainly correlated to the feed water type, pre-treatment steps, plant design and operational parameters. The higher cost of fouling in RO1 (~27% of OPEX) than in other RO plants (Figure 6.2) can be explained by the feed water type used in this plant (wastewater treatment plant effluent)(Table 6.1). This also agrees with other observations of higher fouling severity in plants using wastewater treatment effluent compared to those using surface water as feed source (Beyer et al. 2017). The higher fouling cost of RO2 compared to RO3, despite their similar type of feed water, is attributed to the longer CIP cleanings for RO2 (Figure 6.3). The cost of fouling in RO1 and RO2 is very similar despite the fact that RO1 is fed with municipal

wastewater treatment effluent compared to RO2 which is fed with surface water. Although the RO1 is expected to be more prone to fouling compared to RO2, membrane autopsy results suggested that RO1 suffers from organic fouling while in RO2 biofouling dominates. This explains the same number of CIP events for RO1 and RO2 (**Supplementary Information Figure 6.S2**).

On the other hand, the cost of fouling in all NF plants was very similar (~ 11% of OPEX) (**Figure 6.2**) due to almost identical feed water type, plant design, and operational conditions (**Table 6.1**). The low fouling potential in the studied NF plants is mainly associated to their feed source (anoxic ground water). The higher solubility of reduced iron ions under anoxic conditions was found to create less gel and colloidal deposits on the membrane, resulting in lower fouling compared to aerated feed water (Beyer et al. 2014, van Paassen et al. 1998). Moreover, in anoxic conditions, biofilm growth is slower leading to lower biomass production compared to aerobic conditions (P. Hiemstra 1999).

Another important issue for practitioners is the choice of frequent CIP (extensive) versus early membrane replacement. The maximum number of CIP event per years (CIP frequency) before the cost of CIP surpasses annual membrane replacement cost was calculated. **Figure 6.7** shows the maximum number of CIP events per year until it is economically favourable to replace the membrane rather than perform more CIP. In RO installations many more cleaning events than in the NF plants can be performed until the CIP cost exceeds the membrane replacement cost: in RO ~1-3 CIP per week, while the maximum economically viable CIP frequency in the NFs under study is around 1 CIP per month. RO2 showed a lower number of economically feasible CIP cycles (~70 CIP events per year) than the other RO plants under study. This is due to much longer down-time (soaking overnight step) in the CIP protocols of the RO2 plant.



**Figure 6.7** Maximum number of CIP events per year until the annual cost of CIP is higher than annual cost of membrane replacement (economically viable conditions).

Although the cost of fouling cannot be estimated in reference to a base case without fouling (due to the inherent fouling in all membrane processes treating water), the NF cases considered here can be regarded as being very close to a base case ("minimum" fouling costs) due to their extremely low fouling potential. On the other hand, it is expected the cost of fouling in large Sea Water Reverse Osmosis (SWRO) plants would be higher than in surface water RO plants (this study) due to significant adverse impact of scaling and cake enhanced concentration polarization (as reported by (Kim et al. 2009b)).

One should note that the cost of fouling as a fraction of OPEX can change depending on what is included or neglected in both OPEX and cost of fouling calculations. For example, the cost of fouling can increase in case of any binding contractual costs (e.g., penalty for water delivery delay) and for any limitation on CIP waste management (e.g., local discharge limits and taxes). On the other hand, extensive brine management can increase the operating costs (Morillo et al. 2014, Zhu et al. 2010) leading to a decrease in the cost of fouling as fraction of OPEX. Therefore, the numbers derived in this study should not be seen as absolute values, but rather as estimation criteria in comparing different plants.

#### 6.4.2 Factors in CIP and fouling costs

Analysing the factors involved in the cost of fouling shows, for all seven plants in this study (NF and RO), that membrane replacement causes the largest costs ( $\epsilon_{mem}$ ) (**Figure 6.4**). Similarly, Pearce (2008) reported that UF membrane replacement as the biggest OPEX cost factors among four full-scale UF plants under their study. The second largest contributor in fouling costs comes from pumping ( $\epsilon_{perm} + \epsilon_{NPD}$ ). In all RO plants, the energy required to compensate permeability reduction ( $\epsilon_{perm}$ ) is greater than the energy required to compensate pressure drop ( $\epsilon_{NPD}$ ) (**Figure 6.4**). This is in-line with previous reports showing that maintaining the designed flux value in a fouled membrane needs more energy compared to pressure drop compensation (Jafari et al. 2019).

For plants using the CIP with a low frequency, i.e., all the NF cases in this paper, the cost of chemicals ( $\epsilon_{chemical}$ ) is the main cost factor in the CIP cost while for the plants that undergo frequent CIP events (ROs), the down-time cost ( $\epsilon_{down-time}$ ) is the main factor in their CIP cost. This is especially visible for RO2, where the plant undergoes 17 CIP events per year and each event takes around 24 hours ( $\epsilon_{down-time} \sim 70\%$  total CIP cost). Pearce (2008) also reported a significant of down-time cost for plants for UF plants with frequent CIP cleaning. In contrast, waste management costs are a negligible fraction of the total CIP costs (<0.2%) for all plants (**Figure 6.5**). However, the waste management cost ( $\epsilon_{waste}$ ) can be significantly higher in case of any local discharge limitation leading to additional transport costs (Pearce 2008). A combined handling of CIP solutions and brine (i.e., merging CIP waste with the brine stream) could lower the waste management costs.

The information shown in **Figure 6.4** and **Figure 6.5** could be used to better target parameters to optimize CIP protocols, as described by (Beyer et al. 2017, Madaeni and Mansourpanah 2004a, Porcelli and Judd 2010b). For example, in RO2, the CIP protocol could be optimized by shortening the soaking time, which is the main contributor of the significant down-time cost in RO2 (**Figure 6.5**).

#### 6.4.3 Manual versus Automated CIP

The impact of CIP automation has been evaluated as part of the OPEX for all selected plants, as shown in **Figure 6.6**. Automation leads to negligible saving in OPEX for processes not needing frequent CIP, such as the

NF, while CIP automation would save around 2% in OPEX for the plants that undergo frequent CIP cleanings (such as the ROs). Although CIP automation might not have a direct economic impact on OPEX for low frequency CIP plants, it could still significantly improve plant safety as reported by (Labs 2014). Even though CIP automation presents some clear technological and economic advantages, it is not yet widespread among many membrane water treatment plants. This could be perhaps due to the economic viability of manual cleaning (i.e., operator low wages often in developing countries) and other societal considerations in some countries (e.g., to secure employment). Others suggested that the labour cost (e.g., number of operators, wages) are heavily dependent on the philosophy of owner (Pearce 2008).

#### **6.4.4 Practical implications and future studies**

There has been extensive research on fouling and its impacts on membrane processes. Several techno-economic analyses of RO/NF installations have been conducted using empirical relations without considering the economic impact of fouling. Thus, the results obtained in this study will help improving the techno-economic analyses by taking into account also the economic impacts of fouling. Considering the cost of fouling as a fraction of OPEX (~ 25%), other costs factors can still be optimized like the plant automation (leading to less labour cost) or “smart” energy consumption (adjusting water production to available excess energy) as described by (Intellegence 2018).

We estimate higher fouling severity for seawater desalination plants compared to fresh water membrane plants (due to higher energy consumption and concentration polarization). Considering different fouling criteria for seawater RO (e.g., higher NPD threshold to perform a CIP), further research is required to calculate the cost of fouling for the seawater desalination plants.

Fouling potential in RO/NF installations is often mitigated using either extensive pre-treatment or cleaning (Jiang et al. 2017b). These fouling mitigation strategies lead to additional costs, however, extensive pre-treatments are often labelled as CAPEX, while cleaning costs are included in OPEX. Thus, the plant designer should take into account several financial considerations to decide their fouling mitigation strategies. For example, cost analysis of the current study illustrates that membrane replacement cost is the biggest cost factor in the fouling cost. To reduce the membrane replacement cost, factors leading to early membrane replacement, such as CIP cleaning, should be minimized. Therefore, the non-invasive physical cleanings such as air-water cleaning and hydraulic cleaning could be the effective and economic alternatives (Cornelissen et al. 2007, Wibisono et al. 2014, Wilson et al. 2013).

## 6.5 Conclusions

An economic study on the cost of fouling on full-scale spiral wound membrane systems has been carried out in seven full-scale RO and NF installations in the Netherlands, using plant-wide performance data. The cost of fouling as a fraction of the plant OPEX was evaluated, together with the factors contributing to the fouling and the cleaning-in-place (CIP) costs. It has been found that:

- The cost of fouling as fraction of OPEX is around 24% for the RO installations, while only 11% for anoxic NF cases, due to the low biofouling potential of the anoxic ground water used. The cost of fouling in the anoxic NF systems can be considered as a “*minimum*” possible in a full-scale water treatment installation because of the overall low fouling propensity of anoxic groundwater;
- The most important factor in the cost of fouling is the early membrane replacement cost, followed closely by additional energy cost. CIP costs have a minor contribution to the overall cost of fouling;
- The down-time cost is the most important CIP cost factor for the plants with frequent CIP events, while the cost of chemicals dominates in the plants with non-frequent CIP;
- CIP automation could save up to 3% of OPEX for the plants with frequent cleanings, while automation would provide only negligible direct cost savings for plants with non-frequent cleaning.

## 6.6 Acknowledgements

This study was funded by European Union's Horizon 2020 research and innovation program under the Marie Skłodowska-Curie grant agreement No. 676070. The authors gratefully acknowledge Martin Pot (Evides Industriewater B.V., The Netherlands) and Sandie Chauveau (Global Water & Energy Group, Belgium) for the fruitful discussion during concept development phase of this study. This communication reflects only the authors' view and the Research Executive Agency of the EU is not responsible for any use that may be made of the information it contains.

# 7

## **A techno-economic analysis of fit-for-multi-purposes Effluent Reclamation Plant (ERP)**

“The essence of the independent mind lies not in what it thinks, but in how it thinks.”

Christopher Hitchens

---

This chapter is accepted as: Kehrein, P.; Jafari, M.; Slagt, M.; Cornelissen, E.; Posada, J.; Osseweijer, P.; van Loosdrecht, M. (2021) A techno-economic analysis of membrane-based advanced treatment processes for different municipal wastewater reuse types. *Journal of Water Reuse and Desalination (IWA)*



## **Abstract**

The reclamation of water from municipal wastewater treatment plant effluents with membrane-based advanced treatment processes has been widely recognized as a practical mitigation of regional water scarcity and is therefore promoted by the European Commission. Despite proven technical feasibility, the high energy consumption and costs of those processes are often stated counter arguments. But the energy and costs depend to a large extent on the water reuse type targeted (i.e. potable, industrial, agricultural reuse). There is a lack of knowledge which reuse type is preferable over another from a process cost and energy consumption perspective because the comparison of existing case studies is impossible due to inconsistent study design. The objective of this paper is to compare the energy consumption and net costs of process designs for the three reuse type. Mass and energy balances of four consistently designed membrane-based advanced treatment processes are conducted to estimate the recovery rates that allow to compare costs and energy consumption of the processes per m<sup>3</sup> reclaimed water. By combining different process modelling tools the energy consumption and cost and benefits are calculated to reveal the performance of each process design under Dutch market conditions. The results indicate that the application of reverse osmosis is needed to reclaim high quality water for industrial and potable reuse but not for irrigation water which offers significant energy savings but may not lead automatically to lower net costs. However, while a reclamation process for industrial reuse is economically most promising, irrigation water reclamation processes are not cost effective despite lower energy consumption. This is due to low water prices which determine the economic feasibility of municipal wastewater reclamation to a large extent. Assuming a 20 year process lifetime, operational expenditures may exceed capital expenditures which is important for tender procedures. A significant cost factor for membrane-based advanced treatment processes are waste management costs that may exceed energy costs. Process recovery rates could be significantly enhanced through the integration of a softener/biostabilizer unit prior to reverse osmosis which leads to an optimized process performance. Moreover, the energy consumption of wastewater reclamation processes could be supplied on-site with solar energy. Finally, the possibility of designing a 'fit for multi-purpose' reclamation process that can supply water for different reuse types is discussed. The presented comparative analysis allows for a better informed decision making about which reuse type is preferably targeted in a municipal wastewater reuse project from a process design perspective.

## 7.1 Introduction

Humans consume water across the globe for domestic consumption, for industrial manufacturing purposes and for agriculture. The share of each water usage type of the total water abstraction may differ greatly between countries. While the industrial sector and especially the power generation industry, is in many western countries the largest consumer of abstracted freshwater, agriculture is responsible for the highest water abstraction rates in other countries (Blackhurst et al. 2010; Ranade and Bhandari 2014). Water scarcity is the geographic and temporal mismatch between freshwater demand and availability and is expected to be increased due to climate change. In addition, increasing population, improving living standards, changing consumption patterns, and expansion of irrigated agriculture drive the growth in global water demand (Mekonnen and Hoekstra 2016). The reclamation of water from municipal wastewater treatment plant (WWTP) effluents has been widely recognized as a practical alleviation of regional water scarcity and is therefore promoted politically by the European Commission (European Commission 2018). It creates a yet untapped water source which guarantees a high level of supply reliability because its production is relatively constant (Garcia and Pargament 2015). Since WWTPs are inherently located close to cities, reclaimed effluents become available where water is demand is high (Rietveld et al. 2009).

Several technologies have been proposed to reclaim water from municipal wastewater, such as membrane filtration, advanced oxidation, activated carbon or constructed wetlands. Membrane-based technologies have attracted significant attention because membranes act as a physical barrier for a wide range of contaminants including contaminants of emerging concerns (CECs) (Fatta-Kassinos et al. 2016). Especially ultrafiltration (UF) and reverse osmosis (RO) have been successfully applied in full scale WWTP effluent reclamation processes (Shang et al. 2011; Helmecke et al. 2020). Another advantage of membrane processes is that they can flexibly be scaled up with different unit operations and membrane types to add treatment capacity if necessary (Quist-Jensen et al. 2015). Various full scale studies have demonstrated that MATPs can be designed to reclaim WWTP effluents for all three water usage types: (i) (in)direct potable reuse for domestic consumption (Ortuño et al. 2012; Chalmers and Patel 2013; Van Houtte and Verbauwhede 2013), (ii) demineralised process water for industrial reuse (Majamaa et al. 2010; Shang et al. 2011) and (iii) irrigation water for agricultural reuse (Hamoda et al. 2015).

Despite the proven applicability and advantages, two main bottlenecks have been repeatedly identified in scientific literature that need to become optimized to make membrane driven wastewater reuse even more feasible. Those are the high energy consumption due to required operational pressure and high process costs (Verstraete et al. 2009; Yangali Quintanilla 2010; Batstone et al. 2015; Eslamian 2016; Helmecke et al. 2020). Little is known about the generic differences in energy consumption and costs of MATPs that reclaim WWTP effluents for different reuse types.

This is because a generic comparison between existing case studies that reclaim wastewater for the three reuse types is impossible due to different unit operations applied in each case study, differing feed water compositions, and different methods to calculate energy consumption and process costs. Therefore, it is difficult to state from an energy and cost perspective which reuse type should be preferably targeted by a wastewater reuse project and why. To provide decision guidance from a reclamation process performance perspective and enable a fair

comparison, a common reference has to be defined. The WWTP effluent quality, the applied unit operations and the process assessment methodology should be consistent. Only then a valid comparison of MATP performances for different reuse types can be carried out (Raffin et al. 2013).

It is unquestionable that the energy consumption and process net costs of MATPs depend on the targeted reuse type because it defines the required water quality and consequently the process design. This implies also that each MATP has different water recovery rates and therefore, revealing the different energy consumption and costs of each reuse type requires to compare results based on m<sup>3</sup> reclaimed water. In addition, market prices for reclaimed water may differ significantly (e.g. potable water is usually more expensive than irrigation water) and a fair net cost comparison needs to take this into account.

The primary goal of this study is to estimate and compare the net costs and the energy consumption of MATPs that reclaim wastewater for industrial, potable, and agricultural use. This is achieved by theoretically designing and modelling four different MATPs that are all based on the same core process (**Figure 7.1**). The reclamation of WWTP effluents to alleviate water scarcity can conflict with other sustainability related goals of water utilities. Due to a high energy consumption and brine production of MATPs the environmental footprint of wastewater reuse has been criticized (Daigger 2008; Delacamera et al. 2016). We argue that due to renewable energy conversion technologies energy is no longer a limited resource while water remains more critical and should therefore be prioritised. The second goal of this study is therefore to present two different process optimisation possibilities that further improve the sustainability of MATPs. One possibility is the integration of renewable energy technologies (i.e. solar energy and biogas). The area of photovoltaic modules required to run the modelled MATPs solely on solar energy is calculated assuming Dutch climate conditions. Another possible renewable energy integration system investigated is the recovery of electricity from the chemical oxygen demand (COD) contained in municipal wastewater via anaerobic digestion (Rulkens 2008).

The second process optimisation possibility studied is the integration of a softener/biostabilizer RO pre-treatment to increase the RO recovery rate. Membrane based processes are often presented as reliable to remove a wide range of organic pollutants which makes them a suitable option to cope with variations in WWTP effluent qualities (Hamoda et al. 2015). However, practical experiences from full scale UF-RO reclamation processes report severe biofouling potential in RO which leads to extensive membrane cleaning (Majamaa et al. 2010). Although the UF is successful in TSS removal, its capability to provide a high quality RO feed water is limited as it does not remove pollutants responsible for scaling, organic and bio-fouling. Designing a RO pre-treatment that is more robust to variable feed water qualities would improve RO recovery rates, energy consumption and brine production (Slagt and Henkel 2019).

Since this study is based on the idea that a fair of MATPs for different reuse types requires a consistency in unit operations applied in each process model, it also shows what changes are needed to design a 'fit for multi-purpose' instead of a fit for single-purpose MATP. Therefore, in the outlook the possibility of designing a fit for multi-purpose MATP that can reclaim wastewater for different reuse types and cope with temporarily changing water demand patterns (e.g. from agriculture) is presented.

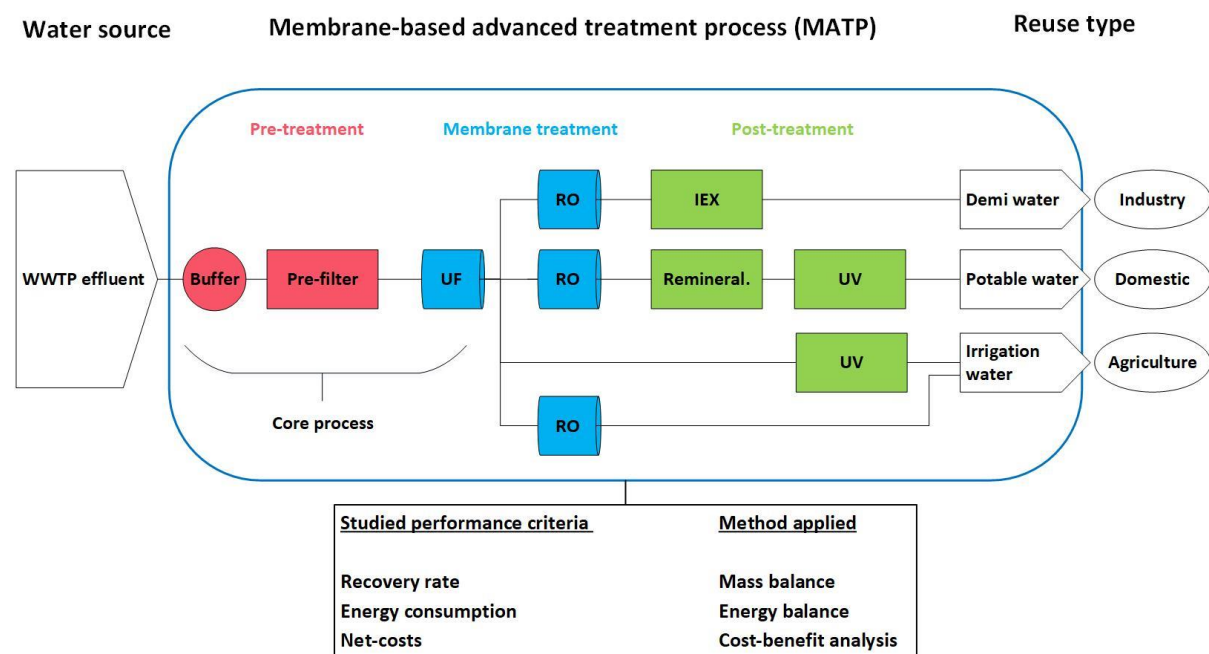
To the best of the authors’ knowledge this is the first study to generically compare different reuse types and associated MATP process designs in the performance criteria of energy consumption and net costs. Beyond that, the introduction of new technical process optimization possibilities is urgent to reduce the trade-off between (i) the sustainability goal of decreasing water scarcity and (ii) carbon footprint reduction and cost effectiveness. The results allow to make better informed decisions because knowing in which range the differences in energy consumption and net costs lie helps to decide for a particular wastewater reuse type.

## 7.2 Methodology

In the following section the modelled membrane-based advanced treatment processes are described including the rationale for process design choices. Studied MATPs are shown in **Figure 7.1** while important process parameters and assumptions of each operational unit are presented in **Table 7.1**. More detailed information of operational parameters can be found in the SI.

### 7.2.1 Estimation of recovery rates and energy consumption

All studied MATPs are modelled with a fixed feed flow of  $100 \text{ m}^3 \text{ h}^{-1}$  which represents a small WWTP and provides a generic scalable number. Each MATP is based on the same core process design including a buffer tank, a pre-filtration step and an ultrafiltration unit. Depending on the specific water quality requirements of a reuse type, the core process is extended by reverse osmosis, ion-exchange, remineralisation and/or ultraviolet light treatment (**Figure 7.1**). All materials and process units applied in this study are commercially available technologies ready for full scale application. In total, three performance criteria have been investigated for each MATP: (i) recovery rates, (ii) energy consumption and (iii) net costs.



**Figure 7.1** Scope and concept of the study with system boundaries in blue rectangle. Four individual MATP designs have been modelled. Irrigation water is reclaimed by two processes where “irrigation water+” has higher quality (UF-RO) compared to Irrigation water (UF-UV) and consequently higher net price.

To obtain generically comparable results, a “standard” WWTP effluent quality was defined that meets the Dutch legal effluent quality standards (**Table 7.1**) (Shang et al. 2011). A sensitivity analysis has been conducted at the end of the study to reveal the impact of possible effluent quality fluctuations ( $\pm 20\%$ ) on the measured performance criteria.

**Table 7.1** Modelled WWTP effluent quality (Shang et al. 2011)

Parameter	Value
Na <sup>+</sup> (ppm)	311
Cl <sup>-</sup> (ppm)	463
Mg <sup>2+</sup> (ppm)	31
HCO <sub>3</sub> <sup>-</sup> (ppm)	325
SO <sub>4</sub> <sup>2-</sup> (ppm)	96.5
Ca <sup>2+</sup> (ppm)	83
Ortho-phosphate	0.7
SDI <sub>15</sub>	5
TSS (ppm)	6
Turbidity (NTU)	4
Conductivity ( $\mu$ S/cm)	2187
pH (15 °C)	7.5

Mass and energy balances (MEBs) are conducted to estimate the recovery rates and energy requirements of designed processes using different modelling tools. The “DuPont Water Solutions Water Application Value Engine” (WAVE) software is used for integrated modelling of the UF, RO, and ion exchange mixed bed (IEX). It uses harmonized data for all products and processes and provides complete mass and energy flows (DuPont).

The impact of fouling and the required chemical cleaning-in-place (CIP) in the RO are added using an in-house calculation method (Jafari et al. 2021). This means that both economical and operational impacts of fouling are calculated based on plant performance data (e.g., pressure drop, permeability and CIP events) using non-empirical cost models as explained in detail by (Jafari et al. 2021). This way, the energy consumption and costs caused by RO fouling have been taken into account through operational downtime, chemical use and CIP heat requirements. To model those unit operations not available in the WAVE software (i.e. pre-filtration, remineralisation, ultraviolet light) performance data have been used from full-scale installations described in scientific articles and/or estimated in consultation with technology providers (Trojan Technologies inc., WeUVcare, Xylem Water Solutions Nederland B.V., Global Water Engineering B.V., Evides Industriewater B.V., DuPont Water Solutions). **Table 7.2** summarizes the major process parameters applied in the models unit operations. More detailed model metrics can be found in the SI.

**Table 7.2** General process parameters shown for each unit operation applied in the model.

<b>Pre-filter</b>	
Pore size ( $\mu\text{m}$ )	100
<b>Ultrafiltration</b>	
Applied pressure (bar)	2.3
Operation mode	Constant flux
Total number of elements	28
Elements type	DOW™ UF SFP-2880
Design flux (LMH)	50
<b>UF Cleaning protocol</b>	
Forward flush	UF feed water
Backward flush interval (h)	1
Backward flush with UF permeate (min)	3.8
CEB water with UF permeate (min)	16.1
CEB water interval (h)	12
CIP cleaning interval (h)	30
CIP water with UF permeate (min)	312.8
<b>Reverse osmosis</b>	
Configuration	Double stages (2:1)
Total number of elements	90
Element type	FilmTec™ ECO-PRO 400
RO average flux (LMH)	22.5
Antiscalant (mg/l)	3.5
RO feed flow rate ( $\text{m}^3/\text{h}$ )	94.2
RO recovery (%)	80
<b>RO Cleaning protocol</b>	
CIP frequency (events/yr)	40
CIP duration (h)	8
CIP step 1 acid cleaning (HCl)	4 hours at pH 2
CIP step 2 Alkaline cleaning (NaOH)	4 hours at pH 12
Rinsing after each step	demineralized water
<b>Ion-exchange (mixed-bed)</b>	
Vessel type	Amberpack™ Sandwich
SAC (internal regeneration)	AmberLite™ HPR1200 H
SBC (internal regeneration)	AmberLite™ HPR4200 Cl
Linear Velocity (m/h)	38
Design flow rate ( $\text{m}^3/\text{h}$ )	75
Design run time (h)	48

Regeneration time (h)	4.5
SAC Volume (m <sup>3</sup> )	2,2
SBA Volume (m <sup>3</sup> )	4.5
Regeneration (SAC) (HCl g/l)	80
Regeneration (SBA) (NaOH g/l)	80
Regeneration Temperature (°C)	15
<b>Remineralisation</b>	
Total hardness achieved (mmol/L) (Ca + Mg)	>1
Type of remineralisation process	Lime saturator
<b>Ultraviolet light disinfection</b>	
Assumed UV dosage (mJ/cm <sup>2</sup> )	80
Assumed log removal	4
Lifetime of lamps (h)	12000
Energy consumed per lamp (W)	100
<b>Softener/biostabilizer</b>	
Vessel type	Amberpack™ Sandwich
SAC (internal regeneration)	AmberLite™ HPR1100 Na
SBC (internal regeneration)	AmberLite™ HPR4580 Cl
Internal bed area (m <sup>3</sup> )	4,4
Linear Velocity (m/h)	23
Design flow rate (m <sup>3</sup> /h)	100 (SAC); 94 (SBA)
Design run time (h)	10 (SAC); 10 (SBA)
Regeneration time (h)	1.71 (SAC); 3.46 (SBA)
SAC Volume (m <sup>3</sup> )	8.3
SBA Volume (m <sup>3</sup> )	5.3
Regeneration Temperature (°C)	15
Regeneration solution	RO brine

## 7.2.2 Modelled MATPs and process design choices

### 7.2.2.1 Core process

Prior to the core process, a buffer tank functions to balance out hydraulic load variations during day/night or seasons (**Figure 7.1**) (Majamaa et al. 2010). The following pre-filter (100µm) protects the downstream UF from larger suspended solids. This combination of unit operations has been applied in various full scale WWTP effluent reclamation processes (Van Houtte and Verbauwhe 2013; Hamoda et al. 2015). Instead of UF, microfiltration (MF) membranes have been applied for wastewater reclamation in the Netherlands (Shang et al. 2011) but UF has distinct advantages. Firstly, it gives process designers more flexibility to choose a suitable membrane for a given feed quality as UF pore sizes have a wider range between 0,1 – 0,001 µm (Rao 2013). Secondly, in contrast to microfiltration, UF membranes also remove soluble organic particles including coliform

bacteria more effectively and therefore may produce a permeate quality that lies closer to the legal standards for irrigation water (Oron et al. 2006). Sand filtration has also been discussed as an alternative unit operation to UF but the removal efficiency of suspended solids may vary greatly and the effluent still contains colloidal matter which can cause problems in the RO (Verstraete et al. 2009). However, in this study the UF unit is modelled with full redundancy of equipment to ensure a steady operation despite the operational downtime during membrane cleaning.

### **7.2.2.2 Process extension for industrial reuse**

**Figure 7.1** illustrates the process extension for demi water reclamation. Due to industrial water applications at high temperatures together with internal water evaporation processes, industrial process water should have a low hardness and a low salt concentration (Rietveld et al. 2011). In the past two decades, RO in combination with ion-exchange mixed bed (IEX) has become the standard process to treat water for industrial applications to a quality that prevents scale formation and/or corrosion in equipment, like e.g. high pressure steam systems. The IEX resins are regenerated using hydrochloric acid and sodium hydroxide. To ensure a steady operation during resin regeneration the IEX unit is applied with full redundancy of equipment. Moreover, an open tank degasification unit is applied prior to the mixed-bed IEX to remove 70% of CO<sub>2</sub> from the RO permeate.

### **7.2.2.3 Process extension for potable reuse**

Removal of pathogens and toxic pollutants is paramount in reclamation of potable water to avoid potential health risks. Related to this, safe guarding the membrane integrity is very important (Trussel 2012). Generally speaking and dependent on the membrane type, RO is expected to reach a log removal value (LRV) of 6 while UF reaches a LRV of 4 (Warsinger et al. 2018). Recent studies even suggest that RO membranes can reach a LRVs of >7 for different natural viruses (Hornstra et al. 2019). But due to its modular design, a full-scale membrane installation contains a large number of O-ring seals, interconnectors, glue lines and other potential locations which could be vulnerable for integrity breaching (Pype et al. 2016). Consequently, the modelled MATP for potable reuse includes a final UV disinfection step to reach an additional LRV of 4 (Pype et al. 2016).

Moreover, WWTP effluents still contain a wide range of unregulated inorganic and organic CECs (Helmecke et al. 2020). It has been stated that assessing only pathogen indicators is therefore not safe in case of potable reuse (Wang et al. 2015) and that post-treatment with advanced oxidation or adsorption process for CEC removal have to be applied (Stefanakis 2016). For example, the incomplete removal of certain chemicals has been reported, e.g. for boron or di-butyl phthalate (DBP) (Trussel 2012). The removal of CECs might become a requirement in the future due to changing legislations and additional quality indicators (Hendry and Benidickson 2017). Nevertheless, the modelled process for potable reuse does not include a final advanced oxidation process because it is not clear which CECs could be primarily subject to new legislation nor which advanced oxidation process is most suitable to be applied then.

To ensure that no sand particles or other debris enter the RO system in case of potential UF system leakages or due to other unforeseen problems it is common practice to install cartridge filters before a RO (Farhat et al. 2020). Since the UF permeate is still biologically active, cartridge filter costs cannot be neglected. Therefore,



the model includes cartridge filters as integral part of the RO system without labelling them as a separate filtration step.

The permeate of the RO unit is not directly potable due its low alkalinity and must be remineralized with hardening components ( $\text{Ca}^{2+}$  and  $\text{Mg}^{2+}$ ). The model follows the remineralisation process described by (El Azhar et al. 2012), to reach a total hardness higher than 1 mmol/l required to meet Dutch potable water quality legislation (Beyer et al. 2014). Considering the low solubility of lime in water this process applies a lime saturation tank and a mixer that feeds an adequate amount of lime saturated water into the RO permeate (El Azhar et al. 2012). Remineralisation of water after reverse osmosis can improve drinking water quality significantly and even allows to adjust total dissolved solid contents to empirically confirmed concentrations that provide users with the most favourable taste intensity (Vingerhoeds et al. 2016).

#### 7.2.2.4 Process extension for agricultural reuse

The discussion whether to apply UF or UF-RO for irrigation water reclamation from municipal wastewater is controversial due to the trade-offs between process costs and microbial and chemical safety (Helmecke et al. 2020). The EU guidelines on water quality for irrigation water from municipal wastewater (**Table 7.3**) differentiate between four water qualities depending on the targeted crop, its intended use and the irrigation method applied (European Commission 2018):

Quality A allows direct contact of the reclaimed water with the edible part of the crop

Quality B is not allowed to have direct contact with the edible parts of the crop but is suitable for food crops that are processed before consumption and for crops used as feed

Quality C is only allowed when drip irrigation is applied to crops mentioned in quality B.

Quality D only allows to irrigate crops for industrial use, energy and seeded crops.

**Table 7.3** Recommendation of the European Commission to implement water quality standards for irrigation water reclaimed from municipal WWTPs (European Commission 2018).

	A ( $\leq$ )	B ( $\leq$ )	C ( $\leq$ )	D ( $\leq$ )
<i>E.coli</i> (cfu/100ml)	10	100	1000	10000
BOD5 (mg/l)	10	25		
TSS (mg/l)	10	35		
Turbidity (ntu)	5	-		
<i>Legionella spp.</i> (cfu/l)	1000 (greenhouse use)			
Intestinal nematodes (eggs/l)	1 (feed and pasture)			

Reaching the highest quality for safe direct contact of the reclaimed water with the edible part of the crop requires the following LRVs to be reached by any wastewater reclamation process: *E. coli*  $\geq 5$ ; total coliphages  $\geq 6$ ; *clostridium perfringens*  $\geq 5$  (European Commission 2018). Since UF alone can be expected to not consistently reach these LRVs (Warsinger et al. 2018), one might evaluate the use of UF permeate for irrigation

as too risky. Although several studies suggest that UF alone can successfully remove bacteria and nematode eggs from effluents (Gómez et al. 2006; Sabater Prieto et al. 2012), in practice, UF membranes operated at reuse facilities did not always achieve complete bacterial rejection (Warsinger et al. 2018). Therefore it is recommendable to integrate a subsequent disinfection step which is usually achieved with UV light treatment. This might be especially valid for greenhouse irrigation where the risk of aerosolisation of pathogens is given (European Commission 2018).

Due to these uncertainties regarding UF, RO has been claimed to be the better option because it is a total barrier for pathogens and also salts and CECs are rejected at a high rate (Warsinger et al. 2018). Irrigating crops with lower quality water may require to add fresh water to prevent salt accumulation in the soil causing significant yield losses (Quist-Jensen et al. 2015). An additional argument in favour of RO integration is potentially higher crop yields achieved with RO permeate compared to UF permeate (Oron et al. 2006).

Considering these controversial results, two different processes are modelled for agricultural reuse. One consists of UF-UV treatment and reclaims irrigation water while the other uses UF-RO treatment, which is referred to as “irrigation water+” in this study. The plus sign indicates that it may easily meet quality standards for a wide range of other applications outside of the agricultural sector since RO can reach a LRV of >7 and removes most CECs (Hornstra et al. 2019).

### 7.3 Economic analysis

To estimate the economic performance of each MATP, cost-benefit analyses (CBA) have been conducted calculating their net present value (NPV). The procedure has been described in the field of wastewater resource recovery elsewhere in greater detail (Kehrein et al. 2020) and applies equation 7.1.

$$NPV = \sum_{t=0}^m \frac{NB_0}{(1+i)^0} + \frac{NB_1}{(1+i)^1} + \dots + \frac{NB_n}{(1+i)^n} \quad (7.1)$$

Where the net present value (NPV) at time t, calculated for a time horizon of n years, is the sum of discounted annual net benefits (NB) assuming a discount rate i (Kehrein et al. 2020).

A discount rate of 5% has been applied in the CBA which accounts for the opportunity cost of time by discounting future costs and benefits because of the profit that could be earned in alternative investments (European Commission 2015). All net benefits have been discounted along a 20 year time horizon which represents the life time of the reclamation process. Cost factors as well as water prices assumed in the CBA are representative for The Netherlands in the year 2020. Electricity costs are assumed to be 0,1 € per kWh which represents an average price for non-household electricity consumers below 2000 MWh/yr in the Netherlands (CBS Statline 2020).

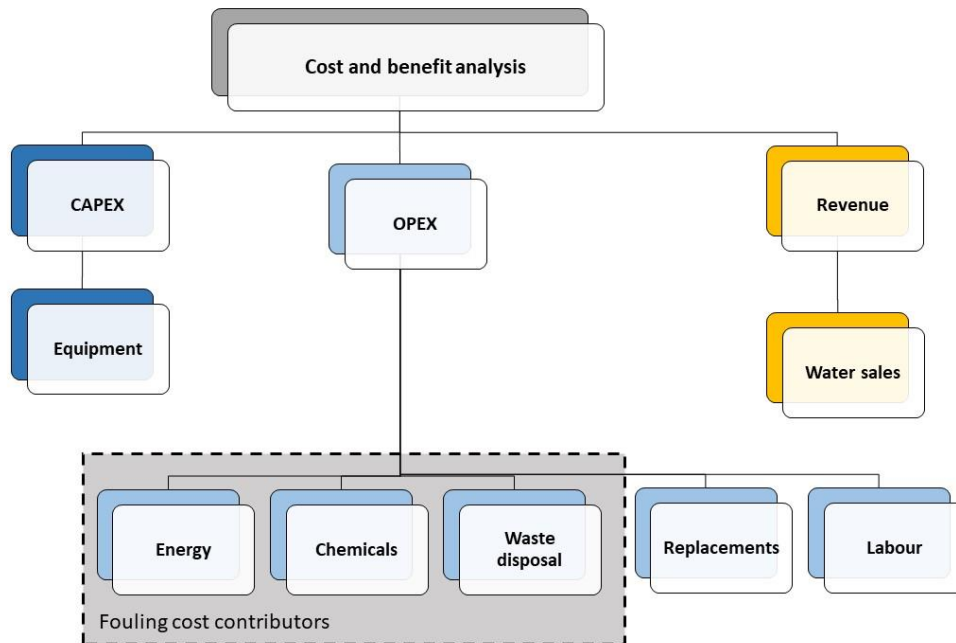
As shown in equations 7.2-7.4 and **Figure 7.2**, the CBA includes revenues from water sales of either demi water (€<sub>demi</sub>), potable water (€<sub>potable</sub>), irrigation water (€<sub>irrigation</sub>), irrigation water+ (€<sub>irrigation+</sub>) as the only benefits. Costs

include operational expenditures (opex) for energy ( $\epsilon_{energy}$ ), input of chemicals ( $\epsilon_{chem}$ ), waste disposal costs ( $\epsilon_{waste}$ ), equipment replacements ( $\epsilon_{replace}$ ) and labour for process operation ( $\epsilon_{labour}$ ). Labour requirements and costs are estimated based on personal communication with sector specific companies and are typical for The Netherlands to operate a process of similar size. For the calculation of capital expenditures (capex) only costs related to the purchase of process equipment and its installation ( $\epsilon_{equip \& install}$ ) are considered. The equipment purchase prices of each unit operation have been estimated in close consultation with existing technology providers to obtain realistic “plug and play” prices of each unit operation. Real prices are more accurate because prices of individual unit operations vary considerably in literature studies and at online market places. However, other possible capex factors, like e.g. land acquisition, planning, and construction of buildings are excluded from the capex calculations. The reason is that those cost factors are highly case dependent or underlie strongly effects of economy of scale.

$$\epsilon_{OPEX} = \epsilon_{Energy} + \epsilon_{chemical} + \epsilon_{replacement} + \epsilon_{Labour} \quad (7.2)$$

$$\epsilon_{CAPEX} = \epsilon_{equip\&install} \quad (7.3)$$

$$\epsilon_{Revenues} = \epsilon_{demi} + \epsilon_{potable} + \epsilon_{irrigation} + \epsilon_{irrigation+} \quad (7.4)$$



**Figure 7.2** Cost factors (capex, opex) and benefits (revenues) included in the CBA calculations.

The water prices applied in the CBA represent Dutch gross market values and have been corrected for 9% value-added tax to obtain net prices (**Table 7.4**).

**Table 7.4** Assumed market prices (€/m<sup>3</sup>) for reclaimed water for different reuse types.

Water prices	Gross price	Net price (excl. 9% VAT)
<b>Demi water</b>	1.10	1.00
<b>Drinking water</b>	0.93	0,85
<b>Irrigation water</b>	0.19	0.17
<b>Irrigation water+</b>	0.60	0.55

Gross potable water prices have been estimated to be 0.93 €/m<sup>3</sup> which is the price charged in 2020 to households by the water company ‘‘Evides Waterbedrijf N.V.’’ that serves over two million inhabitants in South-West Netherlands (Evides 2020). Gross demi water prices paid by industries may depend on different factors, like e.g. the delivered water quality (e.g. demineralised) and especially on the purchased volume. The modelled flow rate of 100 m<sup>3</sup> h<sup>-1</sup> WWTP effluent leading to a typical recovery rate of 70-80% demi water represents a relatively small water quantity in an industrial context. Considering this low purchase volume, a gross price of 1.1 €/m<sup>3</sup> was assumed for demi water which may be lower ( $\approx 1$  €/m<sup>3</sup>) when purchased at large industrial scale (>1000 m<sup>3</sup> h<sup>-1</sup>). Irrigation water+ has been accounted for with a gross price of 0.6 €/m<sup>3</sup> which is paid by fruit growers in the Dutch region Zuid-Beveland for potable water to irrigate fruit trees (STOWA 2019). The lower quality irrigation water is estimated to cost 0.19 €/m<sup>3</sup> which is the fee that farmers pay for the allowance to pump and use groundwater in the Dutch region of Brabant (STOWA 2019). These low prices for irrigation water have also been confirmed by studies from other European countries that have shown that farmers may perceive reclaimed municipal wastewater as of minor quality and therefore have a low willingness to pay if alternative water sources are available (Quist-Jensen et al. 2015).

Moreover it is assumed that all water prices remain constant over the 20 year time horizon applied in the CBA. The residual value of each reclamation process has been calculated by using the NPV of cash flows occurring for an additional five years after the computed time horizon is over. Costs of finance are not considered in the CBA.

## 7.4 Process optimisation and integration for more sustainability

As stated above, this study also aims to explore the potential to further improve the sustainability of MATPs by (i) modelling a process optimisation approach that increases RO recovery rates; and (ii) by integrating renewable energy sources into MATPs.

### 7.4.1 Increasing RO recovery rates

Although the UF is successful in TSS removal, its capability to provide a high quality RO feed water is limited as it does not remove pollutants responsible for scaling, organic and bio fouling. Applying a RO pre-treatment that is more robust to variable feed water qualities than only UF, would improve RO recovery rates, energy consumption and brine production. Consequently, an optimized process design for demi water reclamation is modelled and compared to the initially modelled standard process. It integrates a softener and a biostabilizer unit prior to the RO to maximize process recovery rates. The applied ion exchangers target the specific problem species that can influence RO performance.

First, a pre-softening unit is integrated that removes multivalent cations ( $\text{Ca}^{2+}$ ,  $\text{Mg}^{2+}$ ,  $\text{Fe}^{2+}$ ) which lowers the RO's scaling potential and therefore may improve membrane performance (Salvador Cob et al. 2015; Hijnen et al. 2016). This can be achieved by exchanging those ions with monovalent ions ( $\text{Na}^+$ ) under slightly acidic conditions. Secondly, to decrease the biofouling potential of the RO feed even further an anion exchange step is integrated that removes also fractions of TOC including organic contaminants from the RO feed, like e.g. humic acids. In addition, it removes multivalent anions (e.g.  $\text{PO}_4^{3-}$  and  $\text{SO}_4^{2-}$ ) from the RO feed which provides a bio-stabilizing effect (Slagt and Henkel 2019). Such a combined cation/anion exchange unit prior to the RO, named here softener/biostabilizer, allows to increase RO recovery to significantly higher values (>90%) due to negligible risk of scaling and low biofouling potential due to phosphate limitation (known as biofouling control strategy) (Vrouwenvelder et al. 2010; Slagt and Henkel 2019). Therefore 50% less CIP events have been modelled for the optimized demi water MATP design.

### 7.5 Integration of renewable energy sources

Water reclamation is generally referred to as an energy intensive process leading to an increased carbon footprint of WWTPs (Eslamian 2016). To better understand how renewable energy sources can lower the carbon footprint the photovoltaic (PV) net energy that can be generated in the city of Delft (The Netherlands) has been calculated using the "Photovoltaic Geographical Information System" database and calculator provided by the European Commission's Joint Research Centre (European Commission 2020). Assumed parameters are shown in **Table 7.5**. It is estimated how much PV area is needed to operate studied MATPs which is an important number to show if PV installations can be integrated on-site of a WWTP.

**Table 7.5** Parameters applied to calculate required PV area to operate MATPs with solar energy.

Database used for calculation	PVGIS-SARAH
1 kWp PV capacity ( $\text{m}^2$ )	10
PV technology	Crystalline silicon
Yearly in-plane irradiation ( $\text{kWh}/\text{m}^2$ )	1263
Total loss (%)	-18.85
Yearly PV energy production (kWh)	1025

The second renewable energy integration system investigated is the recovery of electricity from the chemical oxygen demand (COD) contained in the WWTP influent via anaerobic digestion (Rulkens 2008). The obtained methane is assumed to be converted into electricity in a combined heat and power unit to be then consumed by the MATP. **Table 7.6** shows the realistic assumptions made in the calculations of electricity recoverable from the anaerobic sludge digestion route.

**Table 7.6** Assumptions made to estimate the electricity recovery from municipal wastewater.

	<b>Assumption</b>	<b>Reference</b>
Influent COD concentration (mg/l)	750	(Henze and Comeau 2008)
Flow rate (m <sup>2</sup> /h)	100	Own assumption
Energy content COD (kJ/g)	17.8	(Heidrich et al. 2011)
Primary COD capture (%)	60	(Wan et al. 2016)
COD into secondary sludge (%)	40	(Winkler et al. 2013)
COD converted into biogas (%)	50	(Khiewwijit et al. 2016)
Methane content biogas (%)	65	(Frijns et al. 2013)
Electrical efficiency (%)	40	(Verstraete and Vlaeminck 2011)

## 7.6 Results and discussion

In the following section the energy consumption and net costs are presented and discussed for all studied MATPs. To make a fair comparison between studied wastewater reuse types, the results need to be compared not only in absolute values but also based on 1 m<sup>3</sup> reclaimed water. Therefore, the recovery rate of each MATP was estimated first. Any detailed process design information can be found in the SI.

### 7.6.1 Recovery rates

The results show the recovery rates for each reuse type taking an upstream perspective in the process designs that all consider 100 m<sup>3</sup> h<sup>-1</sup> WWTP effluent as a feed (**Figure 7.3**). The recovery rate is highly dependent on the RO unit which has 19% loss as brine leading to an overall process recovery rate of ca. 75% for demi, potable, and irrigation water+ reclamation. Applying no RO but only UF followed by UV light disinfection would lead to a significantly higher recovery rate above 90%. The reclamation of quality irrigation water provides therefore advantages due to less brine production and more water actually reused.

The model predicts that UF meets easily the turbidity and TSS requirements of all EU guidelines on water quality for irrigation water from municipal wastewater (**Table 7.3**). But as explained in the methodology section, it is questionable if microbial standards can be reliably reached. However, the significantly lower overall process recovery rate associated with RO integration could be a valid argument to design processes for irrigation water reclamation only with UF to decrease process costs.

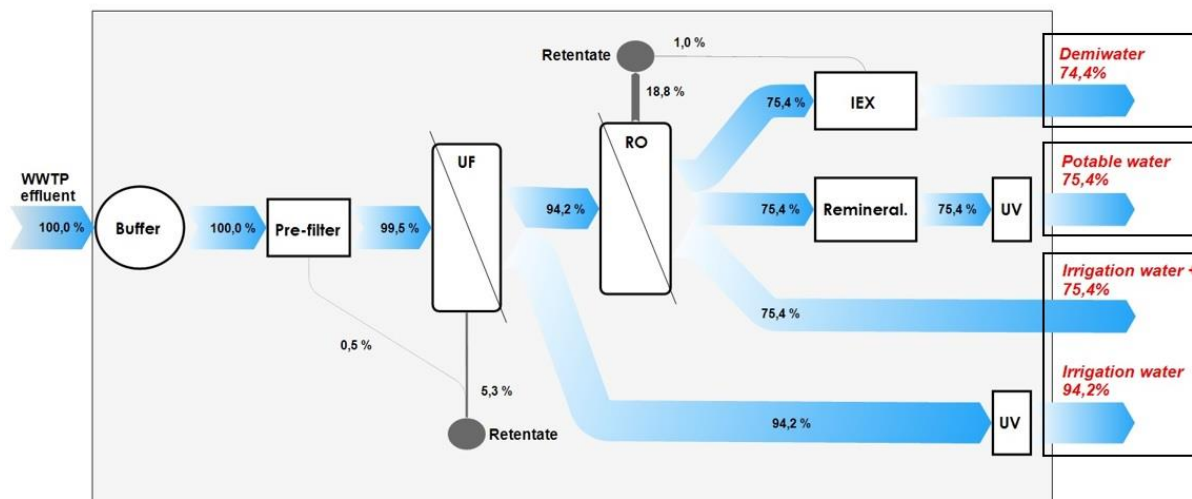


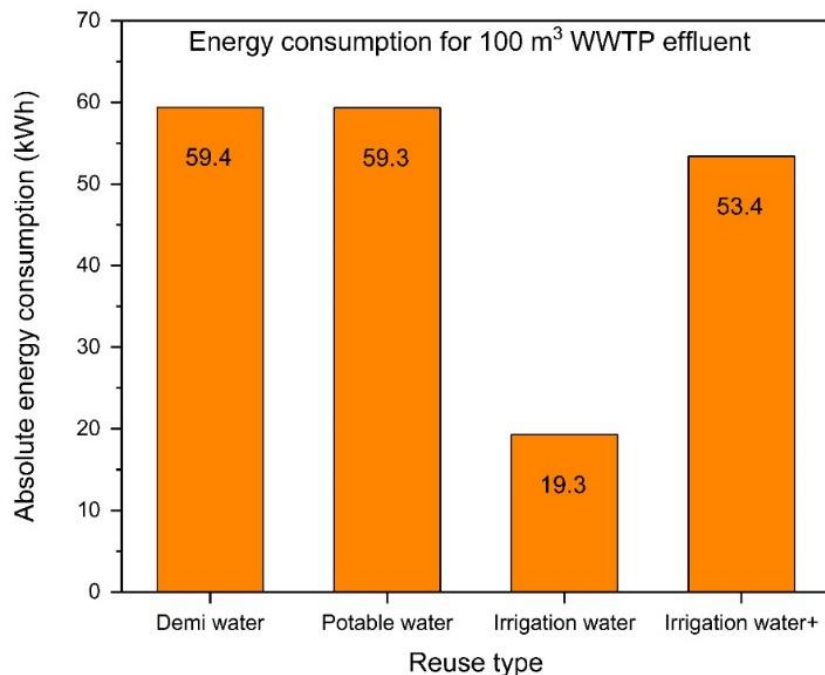
Figure 7.3 Modelled process designs showing water flows in %. Final recovery rates are highlighted in red.

### 7.6.2 Energy consumption

The operation of a WWTP in Europe has been estimated to require ca. 0.15 – 0.25 kWh/m<sup>3</sup> (Pearce 2008) and can account for a significant share of the total energy consumption of a small municipality (Berger et al. 2013). The energy consumption of MATPs covers in literature also a broad range of 0.7 – 2.3 kWh/m<sup>3</sup> reclaimed water depending on the system boundaries of the respective study (Quist-Jensen et al. 2015). The study at hand confirms previous results that the energy consumption of an MATP is largely determined by the integration of RO. **Figure 7.4** shows the absolute energy consumption of MATPs defined as the kWh required to treat 100 m<sup>3</sup> WWTP effluent. In absolute numbers, the treatment of 93.7 m<sup>3</sup> h<sup>-1</sup> UF permeate with RO requires ca. 43 kWh which is significantly higher than all other operational units. The specific energy consumption of each MATP (**Table 7.7**) reveals the energy required per 1 m<sup>3</sup> of reclaimed water and allows a fair comparison between modelled MATPs. Reclamation of irrigation water with UF and subsequent UV disinfection consumes much less energy compared to the other processes, because of the absence of RO and the higher recovery rate of the process. The energy consumption of UV disinfection shows that despite the fact that the larger UF permeate stream for irrigation water reclamation requires more UV lamps than the smaller and cleaner RO permeate stream for potable water reclamation, both UV units have similar specific energy consumption.

Table 7.2 Energy requirements of modelled unit operations as specific energy in kwh/m<sup>3</sup> reclaimed water.

	Demi water	Potable water	Irrigation	Irrigation water+
<b>Pre-filter</b>	0.003	0.003	0.002	0.003
<b>UF</b>	0.15	0.14	0.11	0.14
<b>RO</b>	0.60	0.59	-	0.59
<b>IEX</b>	0.08	-	-	-
<b>Remin.</b>	-	0.002	-	-
<b>UV</b>	-	0.08	0.09	-
<b>Total</b>	<b>0.83</b>	<b>0.82</b>	<b>0.20</b>	<b>0.74</b>

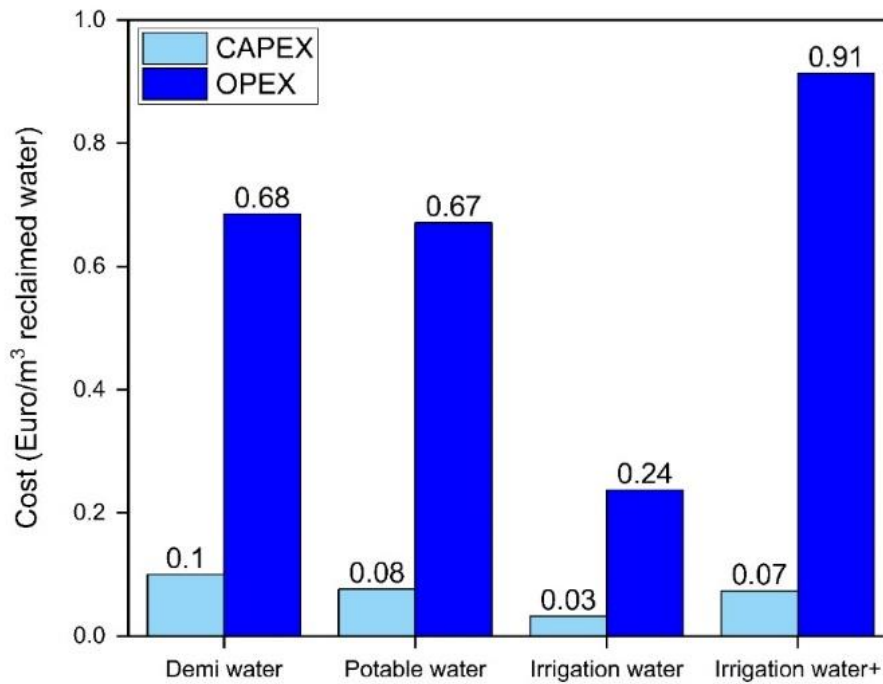


**Figure 7.4** Absolute energy in kWh required to treat 100 m<sup>3</sup> WWTP effluent with modelled MATPs.

### 7.6.3 Cost and benefit analysis

The European water framework directive expects that urban water systems are managed in an economically self-sustained way. This requires that costs are covered by the system itself through pricing of reclaimed water and service fees for wastewater treatment (Castillo et al. 2017). Therefore, the economic performance of MATPs is critical for successful water reuse. To assess this a CBA has been conducted revealing the specific costs per m<sup>3</sup> reclaimed water and the NPVs of modelled MATPs. More detailed cost information can be found in the SI. **Figure 7.5** shows that the opex per m<sup>3</sup> reclaimed water are far higher than the capex needed for initial process equipment and installation. The difference is due to the fact that capex occur only once at the beginning of the assumed 20 year lifetime while opex are due constantly. Therefore, it is arguably more important to design MATPs with the goal to optimize its operation and to save opex rather than saving capex. This is especially important to consider in tender procedures where decisions are usually capex driven. Nevertheless, it should be noted again that other potential capex factors, like e.g. land acquisition or buildings have been excluded in this study due to highly site specific variations. The inclusion of those cost factors would increase capex further but unlikely exceed opex. **Table 7.8** reveals that the RO, UF determine the operational costs of MATPs to the largest extend compared to other unit operations and that labour costs are the second largest opex factor after RO. To show how to possibly design a more cost effective process an optimized process for demi water reclamation that decreases total opex by increasing RO recovery rates is presented below. When RO is applied the highest operational cost factor of MATPs is waste management which refers to the discharge or additional treatment of RO brines (**Table 7.9**) followed by labour costs. If irrigation water is reclaimed without RO, labour costs represent the highest opex factor.





**Figure 7.5** Total opex and capex in € per m<sup>3</sup> of reclaimed water. All values are undiscounted.

**Table 7.8** Overview of capex and opex of each unit operation applied in each MATP (€ct per m<sup>3</sup> reclaimed water per year). All values are undiscounted. Capex consists only of initial process equipment and installation costs.

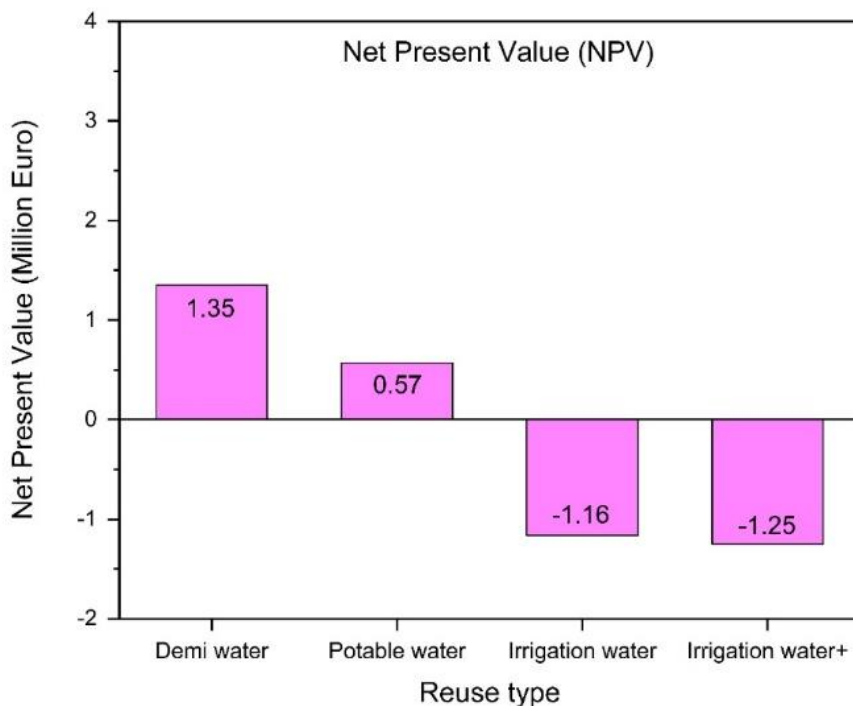
	Demi water		Potable water		Irrigation water		Irrigation water+	
	Capex	Opex	Capex	Opex	Capex	Opex	Capex	Opex
<b>Buffer</b>	0.7	-	0.7	-	0.5	-	0.7	-
<b>Pre-filter</b>	0.1	0.1	0.1	0.1	0.1	0.1	0.1	0.1
<b>UF</b>	3.2	10.6	3.2	10.6	2.5	8.1	3,2	10.5
<b>RO</b>	3.4	32.9	3.4	32.9	-	-	3,4	32.5
<b>IEX</b>	2.5	8.9	-	-	-	-	-	-
<b>Remin.</b>	-	-	0.1	4.1	-	-	-	-
<b>UV</b>	-	-	0.2	3.6	0.2	3.5	-	-
<b>Labour</b>	-	15.9	-	15.7	-	12.1	-	15.7

**Table 7.9** Opex factor distribution (%) in total opex for modelled MATPs based on opex per m<sup>3</sup> reclaimed water.

	<b>Demi</b>	<b>Potable</b>	<b>Irrigation</b>	<b>Irrigation+</b>
<b>Energy</b>	12%	14%	10%	13%
<b>Chemicals</b>	11%	7%	2%	4%
<b>Waste</b>	42%	44%	21%	47%
<b>Replacement</b>	11%	10%	10%	10%
<b>Labour</b>	23%	25%	57%	26%

The discounting of future cash flows reveals that both process costs and water prices determine the economic feasibility of MATPs significantly. Demi water reclamation is the most economically attractive reuse type showing a positive NPV of 1.3 Mil € (**Figure 7.6**). This is due to the relatively high price of demi water (**Table 7.4**). A lower price becomes realistic for very large scale industrial clients that purchase much higher quantities (>1000 m<sup>3</sup> h<sup>-1</sup>) than the 100 m<sup>3</sup> h<sup>-1</sup> assumed in this study which would lower the NPV. In contrast to demi water, it might be very difficult to develop an economically viable business case for irrigation water reclamation. Given the low prices for irrigation water it is not even economically attractive to forego the RO unit and only apply UF in combination with UV disinfection which implies relatively low opex and capex but still shows a highly negative NPV of ca. -1,2 Mil €. To generate a positive NPV a net price for low quality irrigation water of minimum 0,3 € per m<sup>3</sup> needs to be applied. At the first glance it seems surprising that the irrigation water+ (UF-RO) shows a similar negative NPV as the irrigation water (UF-UV) as process costs are higher and recovery rates lower. But the significantly large price difference of 0,38 €/m<sup>3</sup> between irrigation water and irrigation water+ leads to an equal NPV. This shows that from an economic perspective the application of RO for irrigation water reclamation is as feasible as the application of UF-UV if the difference in water quality is also reflected in the water prices.

When it comes to potable water reclamation, process costs may be covered by the revenues from water sales as a positive NPV is achieved. However, it is important to state that a positive NPV does not suggest an automatic profit can be earned with the reclamation of wastewater but only that the main process costs can be covered by the projected revenues. The positive net benefits can be used for covering cost factors which are excluded in this study, like e.g. construction and non-process related cost factors that occur in water reuse projects, like e.g. water distribution costs (Pearce 2008). Whether an overall solid business case can be developed for a reuse project depends therefore strongly on site specific cost factors, like e.g. distance to customers, land purchase costs and/or right of way costs. Nevertheless, this study shows that the highest probability to operate a municipal wastewater reuse scheme in an economically feasible way is the reclamation of demi water for industrial purposes.



**Figure 7.6** Net present value (€) of modelled MATPs.

## 7.6.4 Process optimisation and integration for more sustainability

### 7.6.4.1 Increasing RO recovery rates

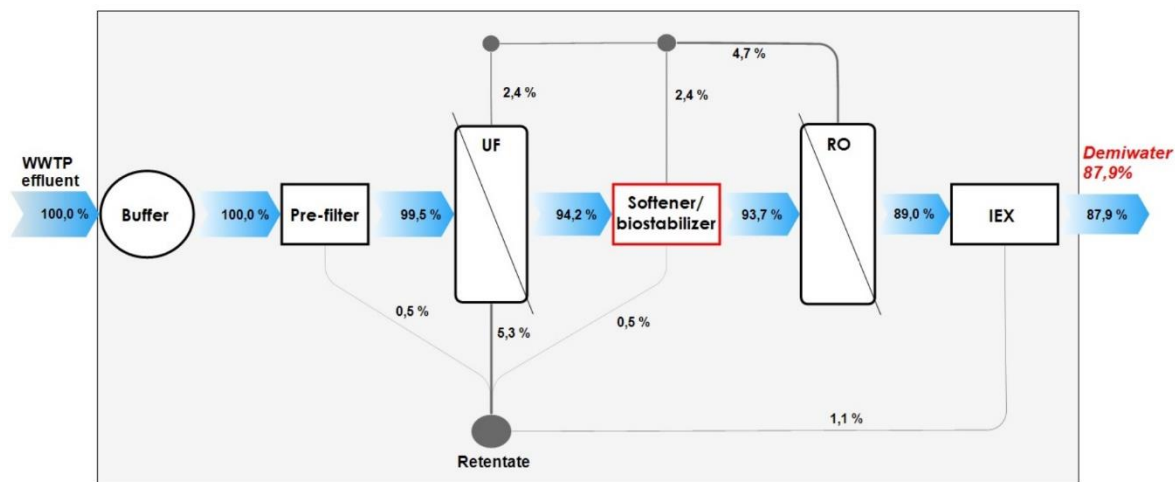
The presence of multivalent ions in the feed water of RO systems contributes significantly to scaling and biofouling on the membrane surface which results into limited RO system recovery (Hilal and Wright 2018). To increase the RO recovery rate a softener/biostabilizer can be integrated to pre-treat the RO feed (Slagt and Henkel 2019). We applied this concept to the initially modelled MATP for demi water reclamation to compare both process performances in recovery rates, energy consumption and net costs. Since the obtained RO brine is due to the installation of softener/biostabilizer, free of any risk of biofouling and scaling it can be used for UF cleaning. Moreover, due to the absence of both multivalent cations and anions the brine is chemically suitable for the regeneration of the ion exchange resins of the softener/biostabilizer unit (Vanoppen et al. 2016). This has the advantage that no fresh water has to be subtracted from the process for these purposes and also the process's chemical consumption is lower (chemicals are often used in the IEX regeneration) (Slagt and Henkel 2019). For the presented optimized process an addition of only 2,2 g NaCl l<sup>-1</sup> brine is enough to obtain a useful resin regeneration solution which saves costs. However, since the number of operational units is increasing the process complexation does too. Nevertheless, all applied technologies are mature and often used solutions that are in this concept only operated in a different manner than usually.

The comparison of recovery rates of the initially modelled demi water process (**Figure 7.3**) and the optimized process (**Figure 7.7**) shows that the overall recovery rate increases from 74,4 to 87,3%. As discussed above, this is mainly due to negligible scaling and biofouling potential of the RO feed which allows for elevated RO

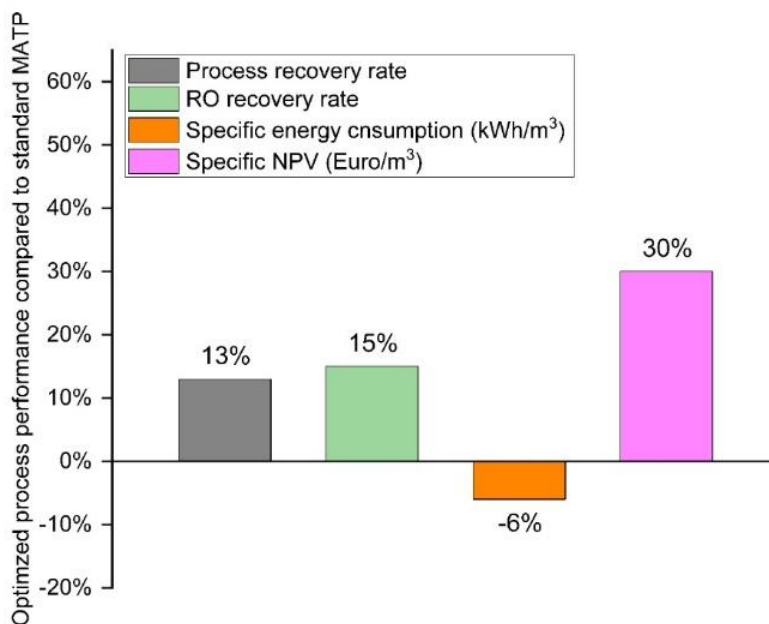
recovery rate from 80 to 95%. Moreover, lower number of CIP events are required for RO in the optimized process (due to lower fouling) leading to a lowered operational down-time of the plant which contributes to a higher process recovery rate too.

The overall performance improvement of the optimized process compared to the initially modelled demi water process is shown in **Figure 7.8**. The energy consumption of the RO is lowered due to less scaling and biofouling and since RO is the most energy intensive unit the energy consumption per reclaimed m<sup>3</sup> of demi water of the optimized process is decreased by 11%. The comparison of the CBAs of both process designs reveals that absolute capex for the optimized process are 31% higher than for the standard process. This is not only due to the softener/biostabilizer unit but also due to an overall higher requirement of RO modules.

On the contrary, the optimized process requires lower opex per m<sup>3</sup> reclaimed demi water due to its higher recovery rate. Especially the significantly less brine production leads to brine management cost savings. In addition, the higher salt concentration of the brine would facilitate the extraction of solids to comply with zero liquid discharge policies. After discounting future cash flows the final NPV per m<sup>3</sup> reclaimed water is 30% higher for the optimized process. This shows that the initially higher capex are easily offset by the decreased opex. Thus a potential economic advantage has been revealed in this study by integration of a softener/biostabilizer as a RO pre-treatment. The decreased opex are a positive argument for the optimized process from an operators point of view (opex oriented) while a technology supplier (capex oriented) may be deterred by the high capex at first but should consider the full economic performance over time. This should especially be considered for tender procedures in public water reuse projects.



**Figure 7.7** Optimized process design for demi water reclamation showing water flows in %. Final recovery rate in red.



**Figure 7.8** Performance of the optimized process design for demi water reclamation compared to the performance of the standard process for demi water reclamation shown in %. ‘Specific’ refers to results are based on m<sup>3</sup> reclaimed water.

#### 7.6.4.2 Integration of renewable energy sources

The results presented in **Table 7.10** reveal how much photovoltaic (PV) area is required under Dutch climate conditions to operate each MATP with solar energy. For demi water reclamation a PV area of ca. 5000 m<sup>2</sup> would be required which represents 70% of the size of a football field. This shows that it is realistic to operate MATPs on solar energy as probably only relatively little extra space than the plant itself is required. However, the calculations are based on the assumption that the PV system is connected to the grid. If an off-grid system is applied, energy storage facilities are necessary which implies that additional energy conversion losses have to be considered and the required PV area would increase.

**Table 7.3** Photovoltaic module area required to operate modelled MATPs (flow rate: 100 m<sup>3</sup> h<sup>-1</sup>) on solar energy in the City of Delft (The Netherlands).

MATP	PV area required (m <sup>2</sup> )	PV area required (m <sup>2</sup> /m <sup>3</sup> reclaimed)
Demi water	5077	0.0081
Potable water	5072	0.0080
Irrigation water	1647	0.0020
Irrigation water+	4564	0.0072
Optimized demi	5728	0.0076

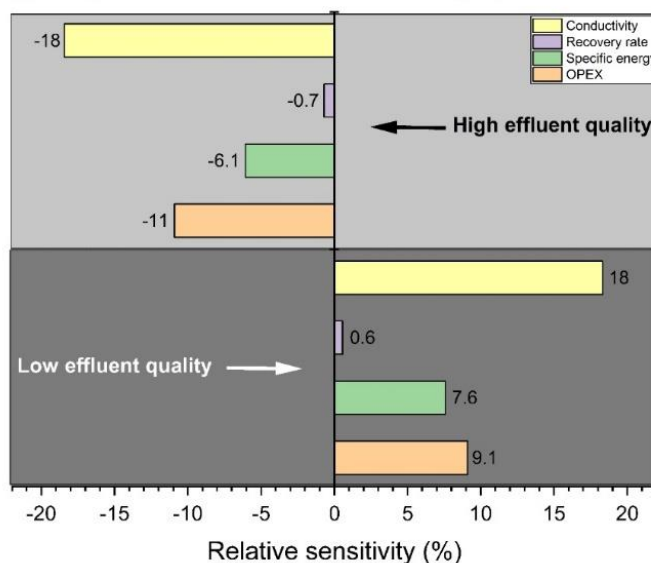
In addition to solar energy, the energy that can be recovered in a WWTP from COD via the anaerobic digestion and combined heat and power biogas combustion was estimated (Frijns et al. 2013). The question arises how much energy could come from anaerobic sludge digestion to offset the energy consumption of the MATP and achieve a good overall energy balance of both the WWTP and MATP. The realistic assumptions presented in **Table 7.6** lead to only  $2,6 \times 10^{-5}$  kWh electricity that could be recovered from the  $100 \text{ m}^3$  raw wastewater entering the WWTP. This is a negligible amount of electricity compared to the absolute electricity required to operate an MATP as shown in **Figure 7.4**. This estimation excludes a similar amount of heat energy that is additionally recoverable from the biogas combustion process. It should also be mentioned that if a WWTP is designed to recover not only chemical energy but additionally also the heat energy from the effluent via heat exchangers, the total WWTP energy recovery could be significantly further increased (Hao et al. 2019).

### 7.6.5 Sensitivity analysis

The results of this study may be sensitive to the WWTP effluent quality assumed in the modelled (**Table 7.1**). Therefore, a sensitivity analysis has been conducted for the demi water reclamation MATP (**Figure 7.9**). The impact of the effluent quality was tested by changing the concentrations of selected ions ( $\text{Na}^+$ ,  $\text{Cl}^-$ ,  $\text{Mg}^{2+}$ ,  $\text{Ca}^{2+}$ ), TSS and turbidity by  $\pm 20\%$  of the initially modelled values. Total organic carbon (TOC) is not considered although it is possible that effluent TOC concentrations impact membrane fouling and thus would impact the process energy consumption. Since the distinct correlation of TOC composition and membrane permeability is not clear (Kennedy et al. 2008) and there is a lack of operational data about the impacts of other changing effluent quality parameters and membrane fouling, fouling costs are assumed to be linearly correlated to the effluent quality.

However, the results in **Figure 7.9** show that changing ion concentrations would change the conductivity of the effluent by  $\pm 18\%$  leading to opex changes of ca.  $\pm 10\%$ . While labour costs have been assumed to not be affected by WWTP effluent quality changes the other opex factors (i.e. energy, chemical reagents, brine management, and equipment replacements) have been included in the sensitivity analysis. The specific process energy consumption increases by 8% if effluent qualities decrease by 20%. In contrast to this, no significant changes in recovery rates occur due to changing WWTP effluent qualities.

Changes in performance criteria due to changing WWTP effluent quality



**Figure 7.9** Sensitivity of WWTP effluent quality changes measured in  $\text{Na}^+$ ,  $\text{Cl}^-$ ,  $\text{Mg}^{2+}$ ,  $\text{Ca}^{2+}$ , TSS, turbidity. High WWTP effluent quality represents 20% lower concentrations compared to the initially modelled WWTP effluent quality while low WWTP effluent quality represents 20% higher concentrations. These variations in effluent quality is often reported during extreme weather conditions. Results are shown in % change.

## 7.7 Outlook and future research

Most studies in the field of WWTP effluent reclamation investigate potable or agricultural reuse possibilities but the results of this study suggest that industrial reuse is economically most attractive and deserves therefore more attention in future research. A process design approach that aims to improve RO performance is needed. RO pre-treatment steps, such as e.g. lime softening, and coagulation and flocculation could be more effective than only UF. They can better eliminate substances leading to scaling, organic and biofouling. It is therefore important to understand how those formerly applied technologies worked and to challenge the current standardized approach of applying for example UF-RO-IEX subsequently for demi water reclamation. It is necessary to find new ways of how to integrate these three key technologies in the most efficient and effective way to improve robustness and recovery rates of RO systems (Slagt and Henkel 2019). This study indicates that the integration of a softener/biostabilizer could be very promising to improve the performance of RO driven water reuse and therefore this concept should be investigated further.

### 7.7.1 Fit for multi-purpose process design

The choice to design a MATP for a certain reuse type depends on the specific demands for reclaimed water (Garcia and Pargament 2015). The demand for a certain water quality can underlie high temporal variations (Wang et al. 2015). For example, a major difficulty for agricultural reuse is that a varying demand of irrigation water throughout a year or vegetation period meets a relatively steady supply potential as WWTP effluent quantities are relatively steady. It could be increasingly necessary in the future to supply high loads of irrigation water in short drought periods that threaten harvest losses in summer due to increasing heat wave events (Buras et al. 2020). Therefore, it is necessary to study the usefulness of designing a ‘fit for multi-purpose’ MATP that

can be adjusted flexibly to changing water demand patterns and reclaim different water qualities. Since this study is based on the idea that a fair comparison of MATPs for different reuse types requires a consistency in chosen unit operations in each process model, it shows also how many changes are needed to design a fit for multi-purpose instead of a fit for single-purpose MATP.

From **Figure 7.3** it becomes obvious that, if a demi or potable water reclamation process is installed at a WWTP already, it may be relatively simple to react on such a temporary urgent demand. Either RO or UF permeate (or both) needs to be abstracted from the process to supply irrigation water. If UF permeate is used, only a stand-by UV disinfection unit is required to treat it further to meet irrigation water quality regulations (**Table 7.3**). The RO permeate instead has the advantage of being suitable to satisfy several non-potable applications with varying temporal demand patterns at once. Examples are firefighting, dust control or fish farm basin refilling (Garcia and Pargament 2015). Also the supply of additional water to river banks or other natural habitats that may fall dry in drought periods and lose their ecosystem services (Cazurra 2008) can be achieved with the irrigation water+. Other possible applications include landscaping or urban irrigation (Wang et al. 2015), vehicle washing, recreational activities and street cleaning (Meneses et al. 2010). A fit for multi-purpose MATP design that could reclaim water of different qualities to supply it to various usage types and switch flexibly between them if necessary, would require that all unit operations studied in this paper are installed which implies higher initial capex. Another bottleneck to overcome would be the cost effective distribution of reclaimed water to its users possibly requiring costly infrastructure. Since WWTPs are usually located at the lowest point of a catchment area to use gravity flow, uphill pumping or transportation of reclaimed water is often necessary to reach the demand location (Lee et al. 2013). Nevertheless, a fit for multi-purpose concept could be a solution to ensure that wastewater is not only fully reused in a water stressed city or region but also that it is available at times and places where needed most and with the required quality.

## 7.8 Conclusion

This study contributes to better informed decision making in water reuse projects revealing differences in recovery rates, energy consumption and costs of MATPs designed for different reuse types (industrial, potable, agricultural) under Dutch conditions. The main findings are:

- The most economically feasible water reuse type is demi water for industrial purposes followed by drinking water while the water price is too low to reclaim irrigation water cost effectively;
- High quality irrigation water (UF-RO) has a similar net present value as low quality irrigation water (UF-UV) if the difference in water quality is also reflected in the water price;
- When RO is applied waste management is the main opex cost factor for water reclamation while labour costs are most significant for irrigation water reclamation with UF-UV;
- MATP process costs are mainly determined by the opex instead of capex and therefore processes with higher capex may be even more cost effective over a 20 year process lifetime (important for tender procedures);
- The integration of a softener/biostabilizer prior to RO may significantly improve a process's recovery rate, energy consumption and net present value;



## 7.9 Acknowledgements

This study was funded by European Union's Horizon 2020 research and innovation programme, under Marie Skłodowska-Curie Grant Agreement no. 676070. It reflects the authors' views alone. The Research Executive Agency of the EU is not responsible for any use that may be made of the information it contains.

For the support and information sharing we want to thank especially people and organisations:

Jochen Henkel	DuPont Water Solutions
Noor Holland	Xylem Water Solutions Nederland B.V.
Donya Fakhravar	Global Water Engineering B.V.
Arielle Nombro	WeUVcare
Elena Slaston	Trojan Technologies inc.
Ralf Lindeboom	Faculty of Civil Engineering and Geosciences, TU Delft
Pakyien Au	Bachelor Student TU Delft & Leiden University
Amir Assadbeigi	Faculty of Applied Sciences, TU Delft
The operational team	Evides Industriewater B.V.

# 8

## Conclusions & outlook

“If you would be a real seeker after truth, it is necessary that at least once in your life you doubt, as far as possible, all things.”

René Descartes

## **8.1 General conclusions**

The objective of this thesis was to evaluate membrane fouling properties and their (inter)relation to membrane performance parameters in different membrane processes. We employed a combination of mathematical methods and experimental study (in both lab and full-scales) to analyse fouling properties and its impact on membrane performance.

### **8.1.1 Novel method to extract fouling layer properties**

A new techniques was developed to obtain mechanical, structural and hydraulic properties of fouling layer in membrane systems. The new proposed method couples a fluid-structural interaction model (FSI) with a membrane flow cell with integrated OCT camera. Therefore, fouling layer morphology and deformation as well as water flux was measured simultaneously. Coupling of OCT results with FSI models enables extraction of fouling properties in an in-situ and non-destructive manner. The elastic modulus, porosity, permeability, thickness and roughness of fouling layers developed on the dead-end UF systems were measured under different operating conditions. (**Chapter 2 and 3**).

### **8.1.2 Fouling layer morphology is crucial in determining hydraulic resistance in dead-end UF.**

The surface thickness and roughness of the fouling layer plays a significant role in determination of hydraulic resistance of total membrane systems. A double layer morphology with a thin and dense base layer and a thick and porous top layer would most accurately explain the behaviour of fouling layer formed in a dead-end UF system fed with surface water (**Chapter 3**).

### **8.1.3 EPS properties of biofouling layer which are grown in lab-conditions are significantly different from biofouling developed under full-scale conditions.**

The chemical cleaning efficiency of RO systems which are operated under laboratory conditions (synthetic feed water, short operational time) is significantly higher than Clean-In-Place (CIP) efficiency of full-scale installations using an identical cleaning protocol. This is very important as most of CIP protocols are developed under lab-conditions and then applied in the industrial installations. Analysis of typical biomass indicators (e.g., ATP, TOC) before and after cleaning illustrates that typical biomass indicators of fouling layers (sampling via membrane autopsy) are not good indicators to evaluate efficiency of a CIP protocol (**Chapter 4**). However, EPS properties of fouling layer provide more important information about membrane cleanability. For instance, biofouling under lab-conditions contains sugar-rich EPS as oppose to the protein-rich EPS formed in the fouling layer full-scale RO. Moreover, Full-scale EPS shows much higher adherence to the membrane surface compared to lab EPS (**Chapter 4**) which explain lower CIP efficiency observed in full-scale systems.

### **8.1.4 The proposed approach for fouling simulation, integration of new RO modules in full-scale installations for 30 days, demonstrated promising results in term of CIP efficiency.**

New membrane modules were integrated at full-scale RO installation of Evides Industriewater for 30 days and were operated under exact same conditions as full-scale installations. Membrane performance parameters and CIP efficiency in recovery of performance parameters were compared between new RO modules (30 days) and old RO modules (>2 years). The results show that the CIP efficiency of the old and new modules are very

similar in terms of permeability recovery and pressure drop reduction (**Chapter 5**). We also observed significant similarity between fouling properties of old and new modules in full-scale installation (in terms of ATP and TOC removal rate, EPS properties) as oppose to lab-condition MFS (**Chapters 4 and 5**).

### **8.1.5 Fouling cost is around quarter of OPEX in BWRO systems and around 10% of OPEX in NF systems in The Netherlands.**

A comprehensive cost model was developed to calculate cost of fouling using plant's performance data from RO/NF plants in The Netherlands. The results show that cost of fouling is around 25% of OPEX in brackish water RO while around 11% for anoxic NF (**Chapter 6**). Membrane replacement cost is the greatest cost factor in cost of fouling while, CIP cost is just around 5% of total cost of fouling. We also observed different cost distribution patterns in the plants with non-frequent CIP compared to the plant with frequent CIP events. Cost of chemicals is the main CIP cost factor for non-frequent CIP plants as oppose to down-time cost for the plant with frequent CIP. These results gave better overview for real cost of fouling in membrane systems and allow better execution of techno-economic analysis (which would include cost of fouling).

### **8.1.6 Techno-economic analysis of a fit-for-purpose water reuse plant with focus on improved recovery rate and integrated cost of fouling**

A membrane-based water reuse plant, using municipal wastewater treatment plant effluent as feed water, was designed with a fit-for-purpose approach. The plant was intended to produce three water qualities (potable, industrial and irrigation reuse type). The results show that demi-water production for industrial purpose is the most economically viable reuse type as opposed to irrigation water. We also showed that as water reuse projects are often driven by local water scarcity, it is logical to increase the RO water recovery rate to around 95% (by installation of softener/stabilizer prior to RO unit) in expense of additional capital cost (**Chapter 7**).

## 8.2 Future of fouling research: Opportunities and challenges

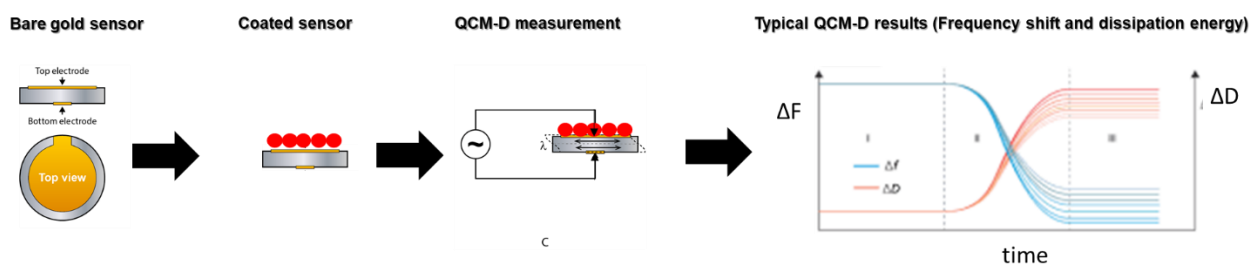
In the final part of this thesis, I tried to share my views about the future research directions in the field and what, at least to my opinion, needs to be focused on and further investigated.

### 8.2.1 Fouling composition and focus on EPS properties.

Typical biofouling indicators such as TOC and ATP are not robust indicators in prediction of (bio)fouling potential in the membrane systems. Significant efforts have been made to find a correlation between feed water compositions (e.g., TOC, ATP) and (bio)fouling severity in membrane systems (Farhat et al. 2019, Sanawar et al. 2019, Sanawar et al. 2017). Unfortunately, no clear correlation has been drawn yet. Recently, for instance, Abushaban et al. (2020) attempted to propose ATP-based biofilm growth potential (BGP) as indicator for biofouling development in SWRO in The Netherlands. However, no clear correlation was observed between BGP in the feed water and fouling severity in the RO membranes. EPS formed in the membrane systems are reported to act as a glue to hold the biofilm together as well as to the membrane surface. Thus, solubilisation of EPS can significantly improve fouling removal (Sanawar et al. 2018). However, the first step for better EPS solubilisation is to better characterize EPS composition. At this moment, one of the major bottlenecks in EPS research is lack of unified EPS extraction and characterization protocol which limits the ability to collect reliable data from existing literature (Seviour et al. 2019).

Relatively low EPS extraction yield and the impossibility to distinguish between excreted polymer (produced by microorganism) and deposited polymer (from the feed water) limit further understanding of the EPS role in CIP efficiency. Thus, further research should also focus on developing alternative and reliable EPS extraction and characterization methods (Felz et al. 2019).

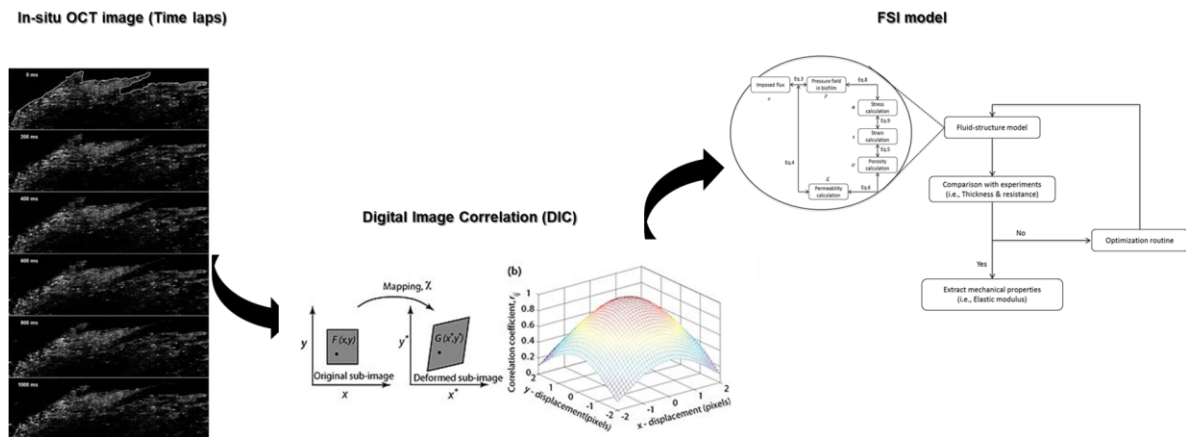
Furthermore, EPS composition and its dynamic changes under different operational conditions should be investigated in order to enhance EPS solubilisation. For instance, impact of membrane operational time, operational mode (dead-end versus cross flow), shear stress, pH and salinity should be analysed on EPS composition as previously partially were carried out by (Al Ashhab et al. 2014, Sweity et al. 2011). One should also eagerly investigate the impacts of operational parameters not only on the EPS composition but also on the functionality of extracted EPS with different properties. For instance, EPS adherence properties are good indicators to correlate EPS composition to its functionality. QCM-D measurement offer relatively reliable results to correlate EPS composition to its functionality. In addition, the device also offers the possibility to measure adherence properties on difference surfaces (**Figure 8.1**).



**Figure 8.1** Potential QCM\_D measurements and sensor coating to study of adherence properties of fouling and EPS to the surface of interest.

### 8.2.2 Biofouling mechanics and morphology

The new trend of research in biofilm mechanics provides significant advancements in techniques to extract biofilm mechanical properties (Bauer et al. 2019, Blauert et al. 2015, Jafari et al. 2019, Jafari et al. 2018, Picioreanu et al. 2018). To accurately extract mechanical properties, further developments of image processing techniques are required. Local and in-situ deformation of biofilm should be measured in order to accurately extract the local mechanical properties. Picioreanu et al. (2018) provided local biofilm mechanical properties, however, did not use an in-situ imaging method. Application of Digital Image Correlation (DIC) provides the full-field displacement maps and local deformation of fouling layer which allow more accurate integration of fluid-structural model (FSI) with an image processing technique. Mathias and Stoodley (2009) already used DIC to measure mechanical behaviour of biofilm under shear stress. However, they did not use in-situ OCT images and coupling of their DIC with FSI model. By using DIC and time resolved OCT images of biofilm deformation and coupling them with FSI, the local mechanical properties can be extracted through calculation of local applied load using computational FSI model while the local deformation and displacement can be derived using DIC measurement of in-situ OCT images (**Figure 8.2**).

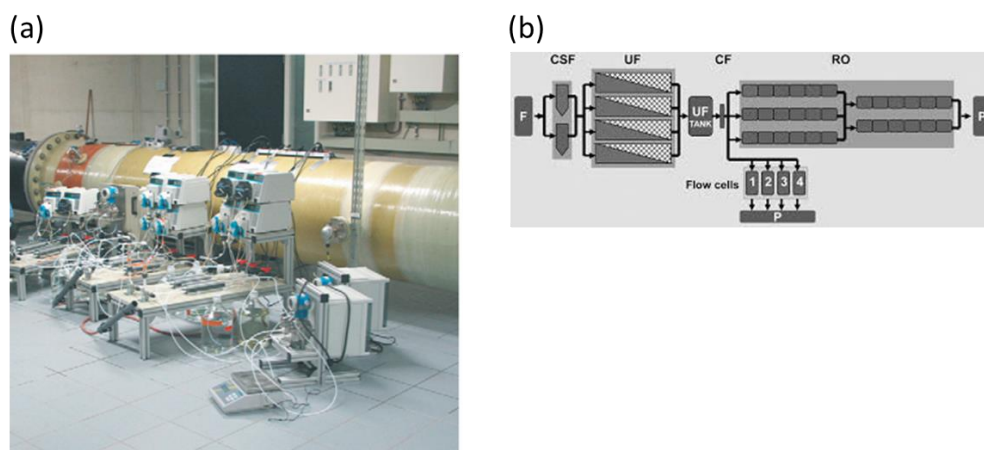


**Figure 8.2** Application of Digital Image Correlation (DIC) coupled with Fluid-Structure Interaction model (FSI model) on time-resolved OCT images of biofilm to extract mechanical properties. OCT images from (Blauert et al. 2015).

Although the recent advancements in the extraction of fouling mechanical properties unravel new insights into biofouling properties, the exact mechanical properties values, at least directly, does not provide much information for practitioners in the membrane industry. From practical point of view, information about fouling hydraulic properties such as porosity and permeability are much more important. These mechanical properties can be used in fluid-structure models to extract more accurate hydraulic properties (permeability, porosity). Therefore, future research should also focus on development on FSI model with focus to extract hydraulic properties and frequent calibration using operational data such as water flux, cross flow velocity and axial pressure drop.

### 8.2.3 Experimental design and Operating conditions

Tremendous amount of researches have focused on fouling in laboratory conditions to mimic fouling formation in full-scale membrane systems. Fouling laboratory studies often use synthetic feed water and, model organisms. Laboratory flow cells are often operated under less-intensive operational conditions (e.g., lower pressure) and for shorter operational time. The main limitation in the laboratory fouling research is lack of access to fresh feed water in the lab. Moreover, long experimental time are also not often logical in a time-frame of typical research projects. On the other hands, full-scale fouling experiments are mainly limited due to lack of frequent fouling sampling as the fouling sampling is only possible via destructive method (e.g., membrane autopsy). We proposed integration of new/virgin modules in the full-scale installations to better mimic and study fouling layer formation, prevention and cleaning strategies under comparable operational conditions and feed water compositions. However, the experimental time (biofilm growth time) and the logistic of new modules integrations in the full-scale installation are the limiting factors. Vrouwenvelder et al. (2006) reported the integration of an in-house MFS installation parallel to the full-scale membrane system to analyse suitability of MFS for the fouling research in the full-scale installation (**Figure 8.3**).



**Figure 8.3** MFS test rig integrated in full-scale installation. a) A MFS test rig in a RO plant (Vrouwenvelder et al. 2010a), b) scheme of MFS test rig integrated in a water treatment plant and fed with UF permeate to mimic fouling in RO modules.

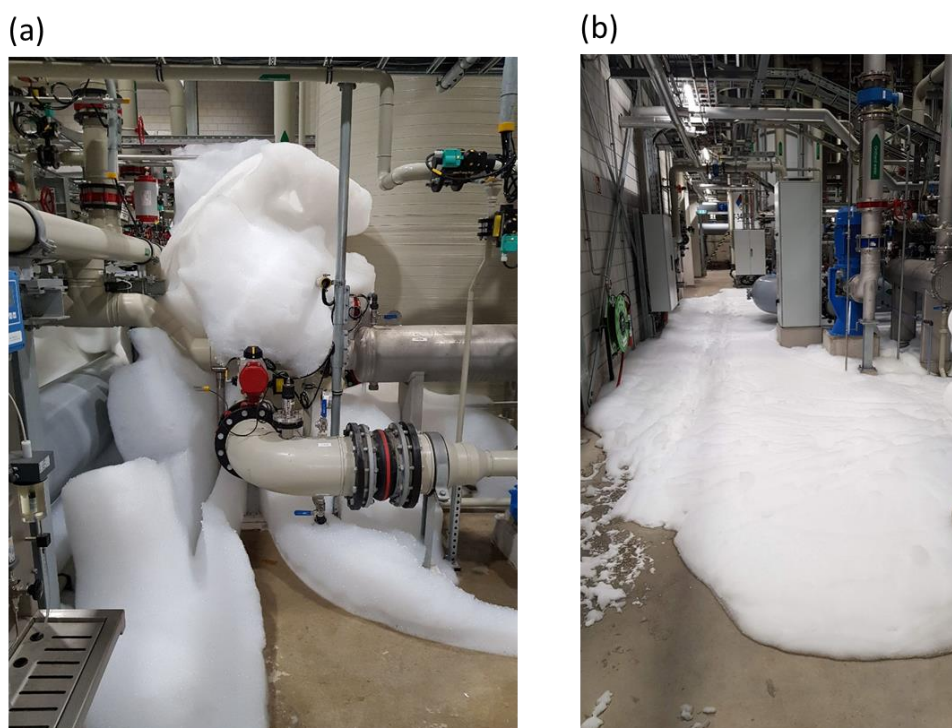
Installation of MFS set-up parallel to main stream provide an easy and cost effective opportunity for membrane and fouling samplings. This provides useful information about fouling properties which can be used to better optimize the pre-treatment steps and the optimal cleaning strategies. In other words, the MFS set-up can be used as a sampling port for to access to the membrane samples and fouling layer formed in under very conditions as the full-scale modules.

### 8.2.4 Fouling mitigation strategies

#### 8.2.4.1 Membrane chemical cleaning.

Chemical cleaning is widely applied in industrial membrane installations. Conventional cleaning protocols, namely acid and alkaline cleanings are often used in industrial membrane installations due to their financial advantages. The CIP protocols in the industrial plants are often adjusted based on the severity of fouling

indicated via typical performance parameters (NPD,  $K_w$ ). However, there is a significant gap between membrane cleaning strategies developed in the academic research and those applied in the practice. Recently, biological control strategies such as quorum quenching, enzyme cleaning have received significant attractions as the biofouling control mitigation strategies (Kim et al. 2009a, Oh et al. 2017, Yeon et al. 2009). However, these cleaning methods are barely applied in the industrial scale. Moreover, several commercial and advance cleaning agents are also available which claim to enhance membrane performances (Beyer et al. 2017, Sanawar et al. 2019). However, their industrial applications are limited mainly due to the trade-off between their price and the performance's enhancement achieved by these cleaning agents. Moreover, companies are sometimes sceptical to novel cleaning agents due to their unexpected side-effect (**Figure 8.4**).



**Figure 8.4** Unexpected and severe foaming in RO membrane caused by novel chemical cleaning agents

Future research on membrane chemical cleanings should focus on EPS solubilisation based on fouling analysis (sampling via in-house MFS installations). Application of EPS extraction protocols can be also used to further increase yield of EPS solubilisation (e.g., acid soluble EPS and/or alkaline soluble EPS) (Boleij et al. 2019, Pronk et al. 2017). Application of physical cleaning such as new solubilized  $\text{CO}_2$  cleaning should also be further investigated specially in its compatibility with plants which are fed with feed water high scaling potential (Ngene et al. 2010).

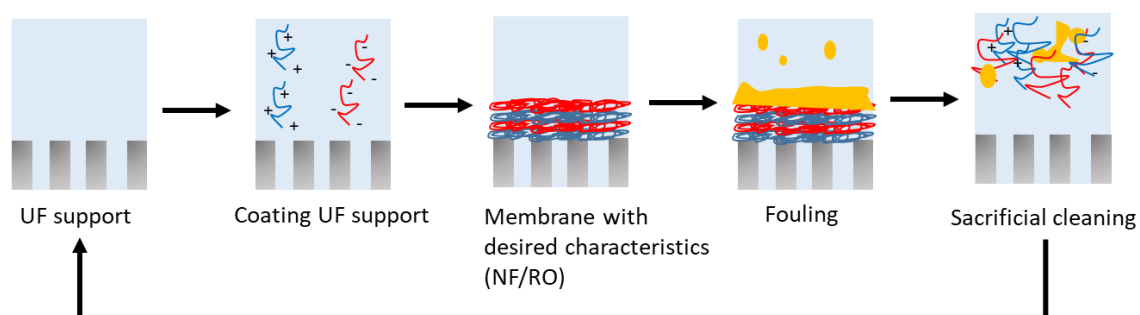
#### **8.2.4.2 Surface modification and new membrane fabrication**

Membrane surface properties such as degree of hydrophilicity, surface roughness and surface charges significantly impact biofouling adhesion in the early stages of fouling formation. Numerous studies on membrane surface modification have been done using both conventional (e.g., layer by layer modification or interfacial polymerization) and advance methods (surface and UV grafting) (Deng et al. 2021, Pichardo-Romero



et al. 2020, Saqib and Aljundi 2016, Zhao et al. 2021). However, the challenge is still manufacturing of reliable and stable modified membrane. The anti-fouling layer are usually removed during fouling test or in contact with relatively harsh conditions (e.g., extreme pH) (Li et al. 2019, Nava-Ocampo et al. 2020). Moreover, these anti-fouling membrane are not actually successful in fully fouling mitigation while they only delay fouling formation (Nava-Ocampo et al. 2020). Therefore, “*low fouling membrane*” should be used rather than “*anti-fouling membrane*” as correct term since (bio)fouling formation is just matter of time. In addition, these *low-fouling membranes* are often tested using model foulant and under laboratory conditions. Thus, future research should focus on reliability of these membranes under pilot and large scales operations (fed with complex feed water and operated for long time).

Considering all the challenges of low-fouling membranes, it might be favourable from both economic and manufacturing point of view to develop a modified layer which is removable. The so called “sacrificial” layer can be peeled off under control and be replaced (Ilyas et al. 2015, Nava-Ocampo et al. 2020). So, fouling will be removed rather than prevented. Future research should focus on application polyelectrolytes coating as a sacrificial layer (**Figure 8.5**).



**Figure 8.5** Scheme of membrane surface modification and mechanism of sacrificial layer membrane cleaning for fouling removal

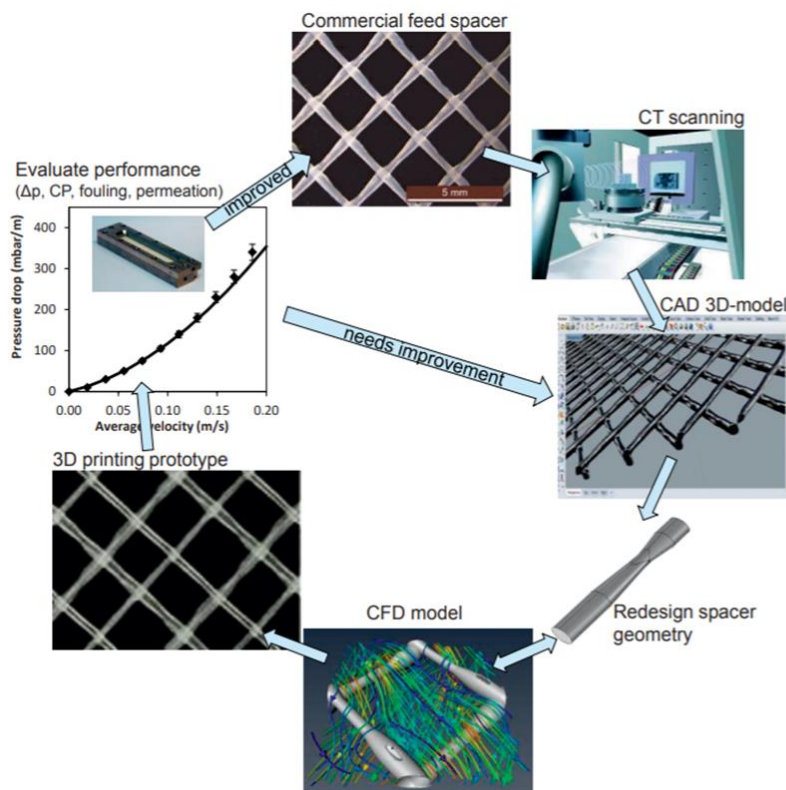
Although low-fouling membranes can delay biofouling formation and consequently increase water flux, one should note that these coating layers often reduce membrane performance parameters such as membrane water permeability and rejection. Therefore, it worth to mention that the strive to find a low-fouling membranes can be also redirected in a more efficient way if it focuses more on manufacturing and synthesizing of membrane modules with much higher water permeability and lower pressure drop (to compensate fouling impact).

### 8.2.4.3 New spacer designs

Presence of feed channel spacer impacts hydrodynamic, mass transfer and fouling potential in membrane systems. There have been extensive efforts to optimize spacer geometry (e.g., filament thickness, filament configuration) to lower concentration polarization and consequently increase the water flux (Bucs et al. 2015, Haaksman et al. 2017, Picioreanu et al. 2009). The objective was to find a feed spacer which decreases concentration polarization and feed channel pressure drop simultaneously. This aim seems, at least theoretically, very challenging as in order to decrease concentration polarization we need higher flow turbulence which leads to higher pressure drop (Haaksman et al. 2017) (**Figure 8.6**). However, the extensive knowledge on spacer will

help us to decide about spacer type depending on plant priority (to aim better which parameters (NPD,  $K_w$ ) should be optimized).

There have been also numerous investigations on how to design and manufacture the optimal spacer design using iterative computational models and 3-D printing (Yanar et al. 2018). Although developments of novel CT-CFD approach in spacer design would provide some new research pathways, its industrial applications is relatively limited. This is mainly due to fact that the optimal spacer offers marginal pressure drop reduction (~50-100 mbar/m) compared to conventional spacer. These performance parameters improvements (e.g., lower pressure drop) are not, at least yet, significant enough to overcome the considerable additional production cost of the new feed spacer. Moreover, in the event of feed channel spacer fouling, fouling formation can hinder the details design of spacer filaments.



**Figure 8.6** Scheme of feed spacer design and optimization for membrane system (Haaksman et al. 2017)

### 8.2.5 Economic impact of fouling

Fouling formation in the membrane system leads to an increase in feed channel pressure drop, reduction in membrane permeability, early membrane replacement, additional cleaning events and generally an increase in both OPEX and CAPEX of the plants. The economic impact of fouling is barely investigated, at least in the academic literature. Most of economic studies take in to account cost of fouling using empirical cost models and not based on plants performance data. We proposed a cost calculation model to calculate cost of fouling using plant's performance data using a non-empirical cost model (Jafari et al. 2021). The economic analysis of fouling for the brackish water RO/NF plants provided new insights on the main cost contributors in the cost of fouling and fouling severity (Jafari et al. 2021). Future research should investigate cost of fouling in seawater

desalination plant (SWRO). Fouling in SWRO is naturally more severe than brackish water due to much higher biofouling and scaling potential in seawater.

Furthermore, the normalized cost of fouling (e.g., normalized to plant's OPEX) could be a good additional indicators to monitor plant performance from fouling severity point of view. Another useful parameter to monitor in RO/NF plants, besides typically performance parameters, is the energy consumption of high pressure pump. This parameter provides complementary information about fouling severity and suitability of the plant's normalization method for the performance parameters (personal communication with Evides industriewater).

### **8.2.6 Bird eye's view**

Fouling remains the main challenge in membrane systems mainly for water and wastewater treatment. Fouling has both direct and indirect economic impacts on membrane systems in water and wastewater treatment plants (see **Chapter 6**). Many utility companies accepted rather severe fouling as normal operational limitations and their so-called "operational window" is quite wide for fouling impacts. In other words, utility companies are only "concerned" about fouling if the fouling impacts on the performance parameters exceed their threshold values (and often they have relatively high threshold values). This shows that academic researches and membrane industry (especially technology providers which do not operate membrane systems) should be more aligned. Future research should focus on how to incorporate some of the novel and promising technologies for fouling control and mitigation in the existing membrane systems.

Membrane-based water treatment plants are often designed mainly from process design point of view and less from water composition and chemistry point of view (**Chapter 7**). Thus, membrane-based water treatment systems are very sensitive to feed water fluctuation. Future research should focus on how to design a "robust process" on the basis of water chemistry (see **Chapter 7**). Robust membrane-based water treatment plant can better cope with feed water variation and reduce the significant operational cost caused by unexpected maintenance of the plant and/or application of alternative and expensive water sources (often for dilution of the feed water) (Majamaa et al. 2010).

Fouling and specially scaling potential are the main bottleneck in maximizing RO and NF water recovery. The membrane system recovery determines the quantity of RO/NF concentrate stream (brine) to be discharged. In the recent years, extensive efforts have been focus to develop novel brine treatment technologies (Panagopoulos et al. 2019). Many researchers investigated brine handling technologies from a resource recovery point of view which leads to the introduction of new approaches to extract and recycle the valuable nutrients. However, one should note that water is still the most valuable resources in the brine stream. Thus, future research should focus how to recover the maximum water by increasing membrane system recovery rate in an economically viable manner (leading to less brine production).

# Supplementary Information

## Chapter 2

### Simplification of model equations in the one-dimensional uniaxial strain case

- **Model geometry**

The one-dimensional biofilm domain extends in the  $y$  direction from 0 to biofilm thickness  $L$ .

- **Flow in the biofilm:**

The uniaxial flow equations become:

$$\frac{d\varphi}{dt} + \frac{du}{dy} = 0 \quad (\text{continuity}), \text{ with } u = \frac{-K\varphi}{\mu} \frac{dp}{dy} \quad (\text{Darcy}) \quad (2.S1)$$

with the local water velocity  $u$  in the  $y$  direction only, pressure  $p$ , water viscosity  $\mu$ , biofilm permeability  $K$  and biofilm porosity  $\varphi$ . This leads to equation (2S.2) solved for water pressure  $p$  in the biofilm

$$\frac{d\varphi}{dt} + \frac{d}{dy} \left( \frac{-K\varphi}{\mu} \frac{dp}{dy} \right) = 0 \quad (2.S2)$$

The variable biofilm porosity and permeability can be calculated with the same equations:

$$\varphi(t) = \varphi_0 \frac{L_0 - \int_0^{L(t)} \varepsilon_y(t) dy}{L_0} \quad (2.S3)$$

$$K(t) = A\varphi^n \quad (2.S4)$$

where  $\varphi_0$  and  $L_0$  are the initial biofilm porosity and thickness,  $A$  is biofilm permeability coefficient and  $n$  permeability exponent. In case of the applied step-wise permeate flux, the velocity  $u$  is imposed on the biofilm base ( $y=0$ ) and constant pressure ( $p=p_{top}=1$  bar) is set on the biofilm-liquid interface ( $y=L$ ).

- **Solid mechanics**

The stress tensor  $\sigma$  can be expanded in three dimensions for linear elastic material as following:

$$\sigma_x = -p + \frac{E}{(1+\nu)(1-2\nu)} \left[ (1-\nu)\varepsilon_x + \nu(\varepsilon_y + \varepsilon_z) \right] \quad (2.S5)$$

$$\sigma_y = -p + \frac{E}{(1+\nu)(1-2\nu)} \left[ (1-\nu)\varepsilon_y + \nu(\varepsilon_x + \varepsilon_z) \right] \quad (2.S6)$$

$$\sigma_z = -p + \frac{E}{(1+\nu)(1-2\nu)} \left[ (1-\nu)\varepsilon_z + \nu(\varepsilon_x + \varepsilon_y) \right] \quad (2.S7)$$

$$\sigma_{xy} = \frac{E}{(1+\nu)} \varepsilon_{xy} \quad , \quad \sigma_{xz} = \frac{E}{(1+\nu)} \varepsilon_{xz} \quad , \quad \sigma_{yz} = \frac{E}{(1+\nu)} \varepsilon_{yz} \quad (2.S8-10)$$

Because no shear force has been applied to biofilm under dead-end conditions,  $\sigma_{xy} = \sigma_{xz} = \sigma_{yz} = 0$  and

$\varepsilon_{xy} = \varepsilon_{xz} = \varepsilon_{yz} = 0$ . Furthermore, the uniaxial strain condition implies no strains in the  $x$  and  $z$  directions,

$\varepsilon_x = \varepsilon_z = 0$ . From the strain tensor, only the strain in the axial direction  $y$  is not zero:

$$\varepsilon_y = \frac{d\delta}{dy} \quad (2.S11)$$

with  $\delta$  being here the relative biofilm deformation with respect to the initial biofilm structure. This also means

that deformation can be calculated as  $\delta = \int_0^y \varepsilon_y dy$ .

With these simplifications, the constitutive equations for the axial stress  $\sigma_y$  and lateral stresses  $\sigma_x$  and  $\sigma_z$

including Hooke's elastic stress correlation with elastic strain and the fluid pressure in pores  $p$  become:

$$\sigma_x = \sigma_z = -p + \frac{E\nu}{(1+\nu)(1-2\nu)} \frac{d\delta}{dy} \quad (2.S12)$$

$$\sigma_y = -p + \frac{E(1-\nu)}{(1+\nu)(1-2\nu)} \frac{d\delta}{dy} \quad (2.S13)$$

The quasi-static balance of momentum of a linear elastic material becomes in the case of uniaxial strain, with

the lateral stress components  $\sigma_x$  and  $\sigma_z$  invariable  $x$  and  $z$  directions, respectively:

$$\frac{d\sigma_y}{dy} = 0 \tag{2.S14}$$

from which after substitutions one obtains the following Poisson equation:

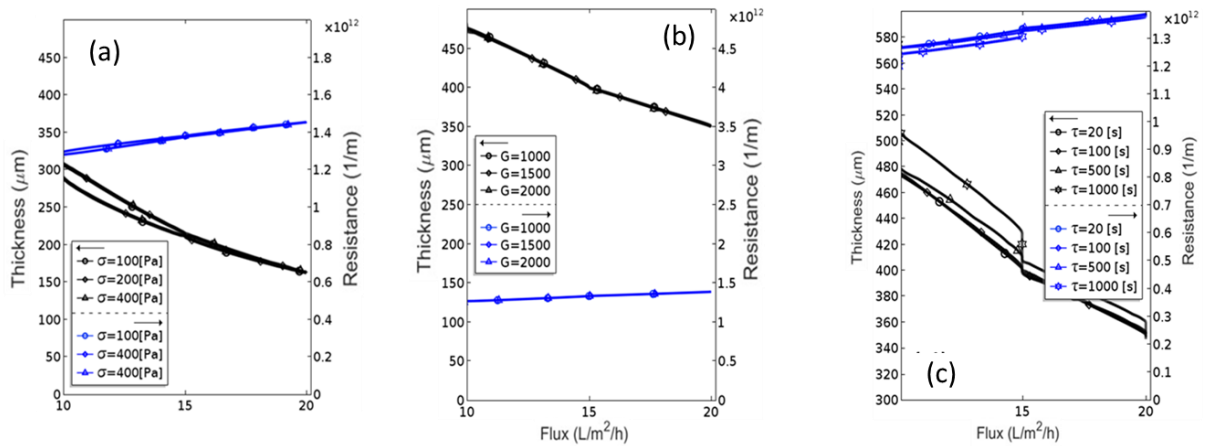
$$-\frac{dp}{dy} + C \frac{d^2\delta}{dy^2} = 0 \tag{2.S16}$$

solved for the local values of deformation  $\delta$ , by using fluid pressure from equation (2.S2). The constant  $C$  is

equal to 
$$\frac{E(1-\nu)}{(1+\nu)(1-2\nu)}$$
.

In case of the step-wise permeate flux, the constant pressure applied on the biofilm surface leads to a zero elastic stress condition ( $\delta=0$  at  $y=L$ ), while the biofilm base is fixed (i.e. zero deformation,  $\delta=0$  at  $y=0$ ).

### Sensitivity analysis



**Figure 1.S1** Parametric study of biofilm thickness and resistance over a flux range for different model parameters: a) initial yield stress,  $\sigma_{ys0}$ ; b) viscous shear modulus,  $G_v$ ; d) viscous relaxation time,  $\tau_v$ . Black lines refer to biofilm thickness variation and blue line show hydraulic resistance. For interpretation of the references to colour in this figure legend, the reader is referred to the Web version of this article.

### Feed water composition

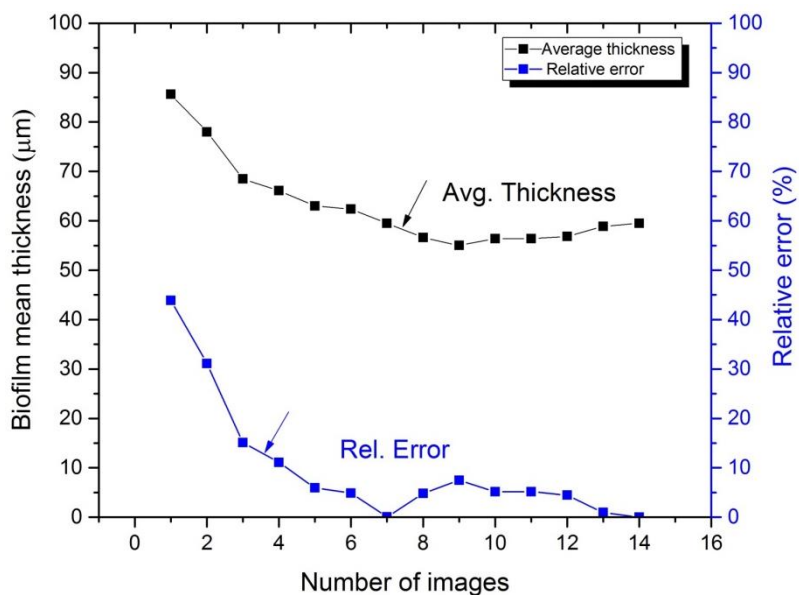
*Table 2.S1 Details of feed water characteristics for biofilm growth condition*

Feed water type	Carbon (acetate)	$\text{NH}_4^+$	$\text{PO}_4^{3-}$
P-Limiting	5 mg C/L	1.5 mg N/L	0.0 mg P/L
River water	1-2 mg C/L	$\leq 0.1$ mg N/L	$\leq 0.01$ mg P/L

## Chapter 3

### Importance of the number of acquired images in the determination of biofilm morphology

In order to have representative biofilm thickness values, biofilm morphology should be quantified based on multiple OCT images. Therefore, the mean biofilm thickness was calculated based on OCT images taken at random locations, while biofilm hydraulic resistance derived from permeate mass collected from the whole flow-cell area. **Figure 3.S1** shows that the mean biofilm thickness converges to steady values of  $\sim 60 \mu\text{m}$  as the number of images increases. For the biofilm under study, a minimum of 10 OCT images would be sufficient to gain representative measures of biofilm morphology.

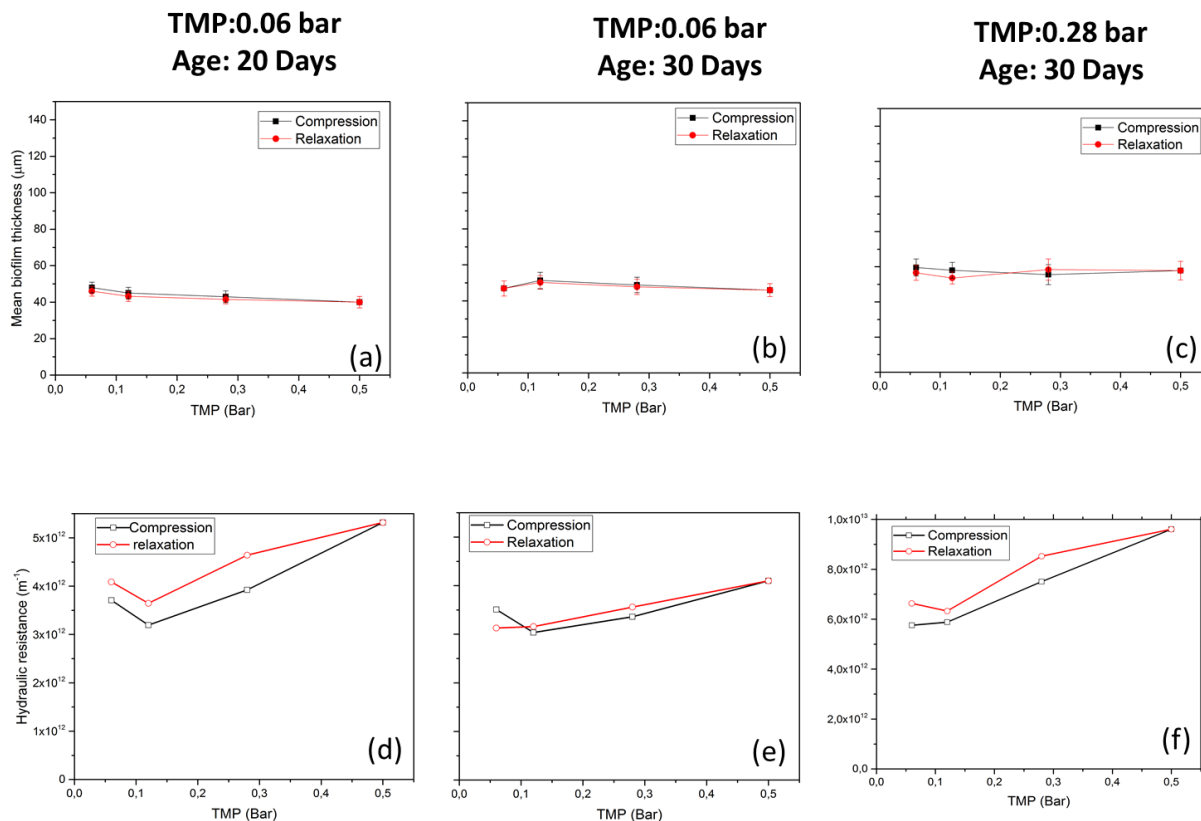


**Figure 3. S1** Biofilm average thickness and relative error around average, as a function of number of OCT images. As number of images increases the average biofilm thickness stabilized and the relative error approaches zero.

### Correlation of biofilm hydraulic resistance with the structural deformation

Biofilm thickness and hydraulic resistance were measured in several flow cells, for biofilms developed under different conditions during compression. **Figure 3.S2** shows an additional series of measurements besides those reported in the main paper. It is clear that the biofilm did undergo only a slight deformation (average thickness change  $\sim 5\text{-}10 \mu\text{m}$ ) while biofilm hydraulic resistance increased significantly up to 60%. Results in all replicate measurements show similar trends.





**Figure 3.S2** Change in mean biofilm thickness (a-c) and hydraulic resistance (d-f) of river water biofilms developed in three conditions during compression/relaxation tests: (a,d) TMP = 0.06 bar for 20 days, (b,e) TMP = 0.06 bar for 30 days, (c,f) TMP = 0.28 bar for 20 days. Biofilm thickness was calculated based on 10 images taken at random locations.

Videos below demonstrate the time-lapse of biofilm displacement under compression. A relatively constant biofilm thickness is also observed in the time-lapse videos in 3.SI-V1 and 3.SI-V2, while the membrane displacement clearly indicates the applied pressure steps (available on the online version of the paper)

*3.SI-V1: Biofilm compression under step-wise change in applied TMP=0.5 bar*

*3.SI-V2: Biofilm compression under step-wise change in applied TMP=0.5 bar.*

### Feed water characteristics for biofilm growth

The detailed characteristics (Total organic carbon, dissolved organic carbon, assimilable organic carbon, etc) of feed water used for biofilm growth can be found in (Derlon et al. 2013) and in supplementary information

**Table 3.S1.**

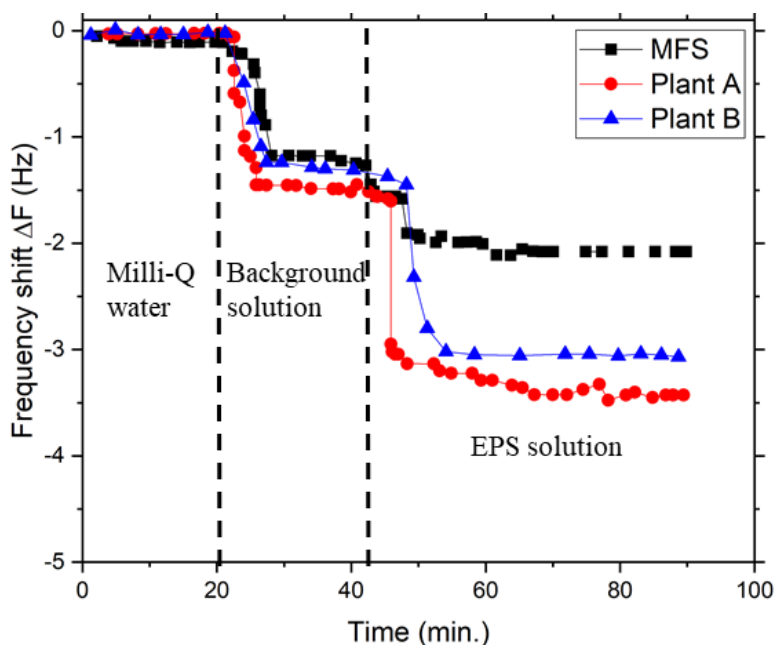
*Table 3.S1 Details of feed water characteristics for biofilm growth condition*

Parameter	Unit	Value
Conductivity	$\mu\text{S}/\text{cm}$	$687\pm 2$
pH	-	$8.1\pm 1.5$
Ammonium Concentration	$\mu\text{g N}/\text{L}$	$19.4\pm 1.8$
Chloride concentration	$\text{mg}/\text{L}$	$34.2\pm 1.2$
TOC	$\text{mg}/\text{L}$	2.5-3
DOC	$\text{mg}/\text{L}$	$2.8\pm 0.2$
AOC	$\text{mg}/\text{L}$	0.3

## Chapter 4

### Frequency result of QCM-D measurements on bare gold sensor (not coated)

The frequency shift for bare gold sensor is almost zero for all three cases for milli-Q water. The frequency shift increased to around 1.5 Hz as the sensor was introduced to background solution. For the gold (non-coated) sensor, the frequency changes of EPS solutions were 2.2 Hz (MFS) and 3.5 and 3.1 Hz (for Plant A and B), indicating only the impact of density and viscosity of the EPS solution.



**Figure 4.S1** Frequency shift results of gold sensors using QCM-D measurements. The results show impacts of bulk density and viscosity on frequency shift.

### Inorganic concentration in the fouling layer

- **Elemental analysis of fouling layer: inductively coupled plasma-optical emission spectrometer (ICP-OES)**

Elements concentrations in the fouling layer were measured in the urea and the dissolved precipitates using a Varian Vista MPX ICP-OES (Agilent Technologies, USA, detection limits of 2.5 to 100 mg/L at an average accuracy of 3%). Prior to analysis, samples were acidified to 2% Nitric acid (HNO<sub>3</sub>), to ensure all ions were fully dissolved. The inorganic compounds most likely to contribute to biofouling are considered as Calcium, Magnesium and Iron (Chon et al. 2012).

The calcium concentration in the fouling layer for MFS is around 20  $\mu\text{g}/\text{cm}^2$  compared to Plant A (8  $\mu\text{g}/\text{cm}^2$ ) and Plant B (3  $\mu\text{g}/\text{cm}^2$ ). The magnesium concentration is higher for Plant A (~0.9  $\mu\text{g}/\text{cm}^2$ ) compared to the MFS and Plant B (~0.4  $\mu\text{g}/\text{cm}^2$ ). Moreover, Iron concentration adsorbed in the fouling layer is much higher for Plant B (18.3  $\mu\text{g}/\text{cm}^2$ ) than Plant A (~1  $\mu\text{g}/\text{cm}^2$ ). The results from inorganic elemental analysis cannot be consistently correlated to the biomass adsorption and CIP recovery.

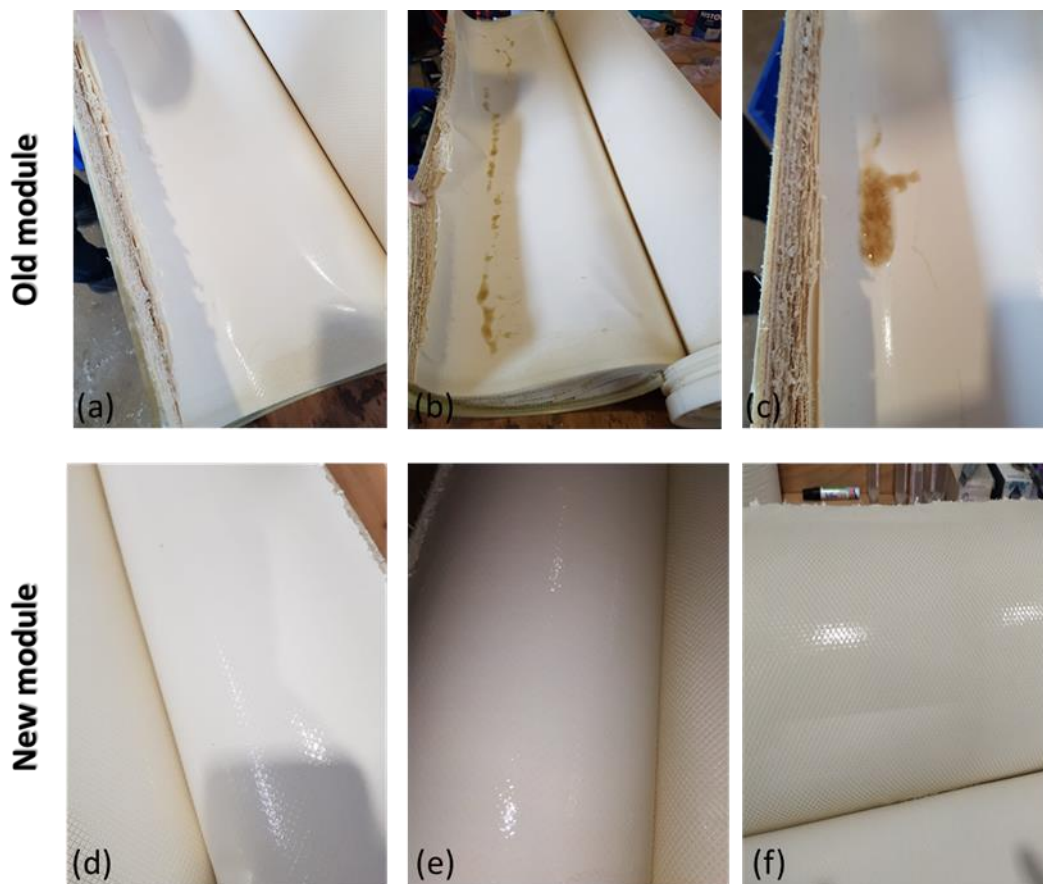
**Table 4.S1** Element concentration in biofouling layer of full-scale and lab-scale membrane system (n=3).  
Before CIP

Element concentration	Before CIP		
	MFS	Plant A	Plant B
Calcium ( $\mu\text{g}/\text{cm}^2$ )	19.8 $\pm$ 0.4	7.7 $\pm$ 0.3	2.7 $\pm$ 0.5
magnesium ( $\mu\text{g}/\text{cm}^2$ )	0.3	0.9	0.4
Iron ( $\mu\text{g}/\text{cm}^2$ )	6.2	0.8 $\pm$ 0.3	18.3 $\pm$ 0.1

## Chapter 5

### Images of membrane modules operated in full-scale installation

The modules under study was autopsied and the fouling layer was evaluated visually. **Figure 5.S1** shows that the modules under study were lightly fouled. **Figure 5.S1 d-f** also demonstrate that the new modules are really slightly fouled during 30 days of operation.

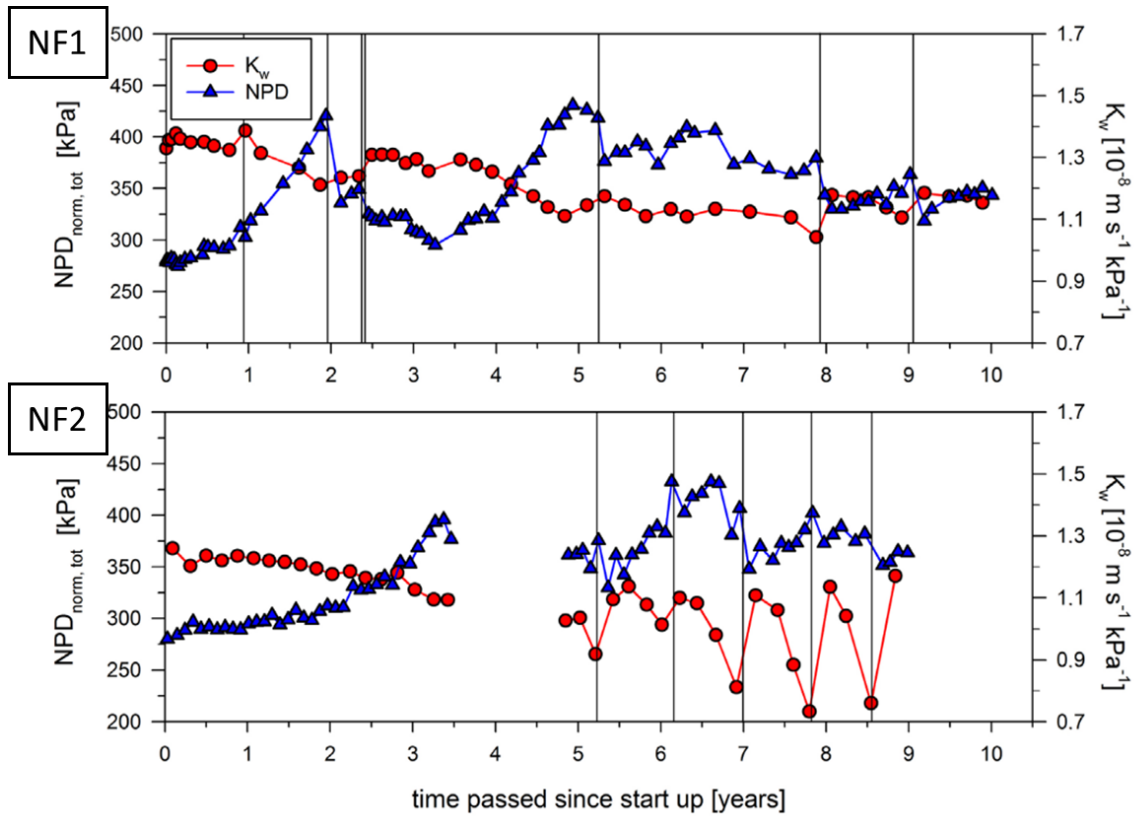


**Figure 5.S1** Images of autopsied modules and the fouling layer formed on the old and new modules. a-c) images of fouling layer formed in the old module after 2 years in the operation, d-f) images of fouling layer formed in the old module after 30 days.

## Chapter 6

### Performance parameters and operation time of the plants

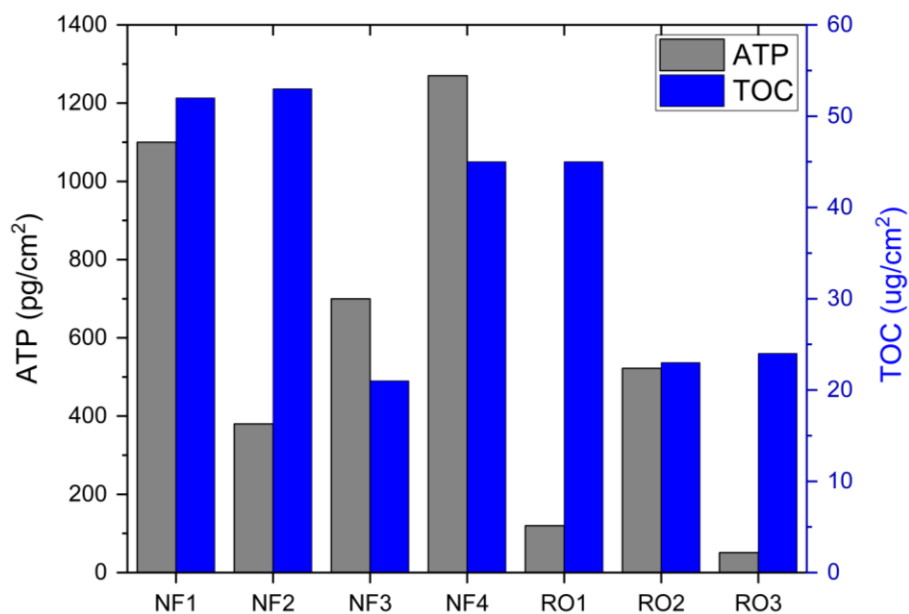
The performance parameters in this study is extracted for the NF plants from (Beyer et al. 2014) and for the RO plants from (Beyer et al. 2017). The performance parameters are extracted and averaged over the entire operation time (using the original membrane modules).



**Figure 6.S1** Example of performance parameters data for the plant NF1 and NF2. Figure is a reproduction from (Beyer et al. 2014).

## Membrane autopsy and fouling characterization

In order to better understand the different in cost of fouling among the plants under study, the membrane autopsy was executed and reported by (Beyer et al. 2017, Beyer et al. 2014). Here are the typical organic fouling and biofouling indicators, TOC and ATP of lead modules, for seven different plants under study.



**Figure 6.S2** Autopsy results for ATP and TOC concentration values of lead membrane modules from seven different plants. Figure is adapted from (Beyer et al. 2017, Beyer et al. 2014).

## Chapter 7

- **Process design parameters, energy consumptions and costs**

### Buffer tank

Design and cost parameters-Buffer Tank <sup>1</sup>	
Buffer capacity (h)	10
Size (m <sup>3</sup> )	1000
Material	steel
Price (Euro)	85000

Reference:

1. Personal communication with Global Water Engineering B.V.

### Pre-filter

Pre-filter	
Type	Disk filter
<b>Energy</b>	
Pressure (bar)	0.05
Pump efficiency	0.6
Flow rate (m <sup>3</sup> /h)	100
Energy consumption (kwh)	0.2
<b>OPEX</b>	
Energy cost (Euro/d)	0.55
Energy cost (cent/m <sup>3</sup> )	0.02
Lifetime filter (year)	10
Cost filter	5000
Replacement events	1
Replacement costs (cent/m <sup>3</sup> )	0.028
Total OPEX (cent/m <sup>3</sup> )	0.051
<b>CAPEX</b>	
Full unit cost (Euro)	10000

Reference:

1. Personal communication with Global Water Engineering B.V.



## Ultrafiltration

UF	
<b>General Info <sup>1</sup></b>	
Operation mode	constant module flux
Number of online-train	1
Number of standby train	1
Number of elements per train	28
Element type	UF SFP-2880
UF recovery (%)	94.2
Design flux (LMH)	50
<b>General Operation info <sup>1</sup></b>	
Feed flow rate (m <sup>3</sup> /h)	99.5
Permeate flow rate (m <sup>3</sup> /h)	94.2
Applied pressure (bar)	2.3
Average net driving pressure	0.52
UF average flux (LMH)	50
<b>Cleaning protocol</b>	
Forward flush	with UF feed water
Backward flush interval (h)	1
Backward flush with UF permeate (min)	3,8
CEB water with UF permeate (min)	16,1
CEB water interval (h)	12
CIP cleaning interval (d)	30
CIP water with UF permeate (min)	312,8
<b>Flow properties ( UF Feed) <sup>1</sup></b>	
Turbidity (NYU)	4
TOC (mg/L)	9.8
SDI 15	5
TSS (mg/L)	6
<b>Flow properties ( UF permeate) <sup>1</sup></b>	
Turbidity (NYU)	<0.1
TOC (mg/L)	8.8
SDI 15	<2.5
<b>OPEX <sup>1</sup></b>	

---

Utility and chemicals (Euro/m <sup>3</sup> )	0.06
Membrane replacement ( Euro/m <sup>3</sup> )	0.02
<b>CAPEX<sup>2</sup>- Per train</b>	
Single element cost (Euro/module)	2000
Total module cost <sup>3</sup> (Euro)	14000
Feed pump <sup>3</sup> (Euro)	5000
Feed buffer tank <sup>3</sup> (Euro)	9000
Filtrate tank <sup>3</sup> (Euro)	8100
Concentrate tank <sup>3</sup> (Euro)	900
Automation control, electrics (Euro)	100000
CEB chemical dosing pump (Euro)	500
Compressor (Euro)	10000
CIP (pumps, tanks etc.) (Euro)	20000
Miscellaneous <sup>3</sup> (Valves, piping) (Euro)	8000

## Reference:

1. Water Application Value Engine (WAVE) software (DuPont Water Solutions)
2. (Hitsov et al. 2018)
3. Full redundancy is considered.

**Cartridge filter**

<b>General info <sup>1</sup></b>	
CF operation model	Inside-out
Type	String wound filtration
CF housing material	PVC
Flow rate (m <sup>3</sup> /h)	100
Micron rating	5 µm
Length (in)	40
Operational pressure (bar)	1
Pressure drop (bar)	0.2
net applied pressure (bar)	1.2
Number of filters	22
Lifetime (month)	1
Operation time (year)	20
Unit cost (Euro/piece)	2
<b>Energy consumption</b>	
Unit cost of electricity (Euro/kWh)	0.1
pump efficiency	0.6
Energy consumption (kWh)	5.56
<b>OPEX</b>	
Energy (Euro/year)	4393
Replacement (Euro/year)	10560
OPEX (Euro/year)	14953
<b>CAPEX</b>	
Pump (Euro)	5000
Cartridge filters (Euro)	440
CF housing (Euro)	1000

Reference:

1. (Farhat et al. 2020)
2. Personal communication Evides Industriewater B.V.

**Reverse osmosis**

<b>General Info <sup>1</sup></b>	
Configuration	Double stages
Stage 1 (No. PV)	10
Stage 2 (No. PV)	5
Number of elements per PV	6
Total number of elements	90
Elements type	ECO-PRO 400
RO recovery (%)	80
<b>General Operation <sup>1</sup></b>	
Feed flow rate (m <sup>3</sup> /h)	94.2
Permeate flow rate (m <sup>3</sup> /h)	75.3
Feed pressure (bar)	9.6
Average net driving pressure	6.7
Specific Energy (kWh/m <sup>3</sup> )	0.42
RO average flux (LMH)	22.5
Antiscalant (mg/l)	3.5
<b>Flow properties <sup>1</sup></b>	
RO feed flow rate (m <sup>3</sup> /h)	94.2
Pressure (bar)	9.6
TDS (mg/L)	1314
RO concentrate	18.9

Pressure (bar)	8
TDS (mg/L)	6500
RO permeate (m <sup>3</sup> /h)	75
Pressure (bar)	1
TDS (mg/L)	12.13
<b>CIP cleaning</b> <sup>2</sup>	
CIP frequency (events/yr)	40
CIP duration (h)	8
CIP chemicals	HCl/NaOH
CIP cleaning pH	2/12
<b>OPEX</b> <sup>1</sup>	
Energy, waste disposal and antiscalant (Euro/day)	423.6
Cost of fouling (Euro/m <sup>3</sup> )	0.03
Cartridge filter (Euro/m <sup>3</sup> )	0.02
<b>CAPEX</b> <sup>3</sup>	
Single element (Euro/module)	600
90 Elements (Euro)	54000
Pressure vessel (Euro/module)	600
15 Pressure vessels (Euro)	9000
Feed Pumps (Euro)	200000
Feed buffer tank (Euro)	9000
Filtrate tank (Euro)	7200
Concentrate tank (Euro)	1800
Automation control, electrics (Euro)	100000
CIP (pumps, tanks etc.) (Euro)	30000
Valves, piping etc. (Euro)	15000

## Reference:

1. Water Application Value Engine (WAVE) software (DuPont Water Solutions)
2. (Shang et al. 2011)
3. (Hitsov et al. 2018)

### Fouling and cleaning in Reverse Osmosis

<b>Feed Channel pressure drop increase <sup>1</sup></b>	
Initial Normalized feed pressure drop (NPD0) (kPa)	120
Average Normalized feed pressure drop (NPD) (kPa)	140
Unit cost of electricity (Euro/kWh)	0.1
pump efficiency	0.6
feed flow rate (m <sup>3</sup> /d)	2248.8
Annual energy consumption due to pressure drop (Euro)	7600
Annual cost of pressure drop (Euro)	760
<b>Permeability reduction <sup>1</sup></b>	
Virgin membrane permeability (m/s/kPa)	3.6
Average fouled membrane permeability (m/s/kPa)	2.88
permeate flow rate (m <sup>3</sup> /h)	1800
Design flux( constant value) (LMH)	20
Annual energy consumption due to permeability (Euro)	43452
Annual cost of permeability reduction (Euro)	4345
<b>Membrane replacement <sup>1</sup></b>	
RO module (Euro/stuck)	600
Total number of membrane replaced	90
Life time (year)	5
<b>CIP cleaning <sup>1</sup></b>	
<b>Chemicals:</b>	
C HCl (pH=2)	0.36
C NaOH (pH=12)	0.4
Cost of acid (Euro/kg)	100
Cost of base (Euro/kg)	100
acid volume (m <sup>3</sup> )	2.88
Base volume (m <sup>3</sup> )	2.88
Number of CIP	40
Annual cost of Chemical cost (Euro)	8,801
<b>Waste disposal</b>	
waste cost factor (Euro/m <sup>3</sup> )	0.6
Annual cost of down-time	2400
<b>Down-time cost (Due to CIP)</b>	
Water production capacity (m <sup>3</sup> /d)	1800
Profit loss due to down-time (Euro/m <sup>3</sup> )	0.1
<b>CIP solution heating</b>	
pump efficiency	0.9
Ambient Temperature (C)	10
T base (C)	35
T acid (C)	35
specific heat capacity kJ/kg/C	4.2
Density (kg/m <sup>3</sup> )	1000
Total energy consumption (kWh)	7467
Annual heating cost (Euro)	747

Reference:

1. (Jafari et al. 2021)

**Degasifier**

<b>Designed for saturated stream</b>	
CO <sub>2</sub> removal (%)	70
Type	Tank/Agitator
Design flow (m <sup>3</sup> /h)	75
Residence time (min)	10
Agitation power intensity (W/m <sup>3</sup> )	50
Mixing tank volume (m <sup>3</sup> )	12.5
Specific Energy (kWh/m <sup>3</sup> )	0.01
<b>OPEX</b>	
Energy cost (Euro/m <sup>3</sup> )	0.01
<b>CAPEX</b> <sup>1</sup>	
Tank (Euro)	7000
Agitator (Euro)	2500
Instrumentations (Euro)	2375

## Reference:

1. Personal communication (Global Water and Energy)

**Ion exchange mixed-bed permeate polishing**

<b>Ion Exchange mixed bed- Permeate polishing <sup>1</sup> [SAC SBA]</b>		
Resin form	SAC	SBA
Layout	[SAC SBA]	
Vessel type	Amberpack sandwich	
Resin type	AMBERLITE™ HPR1200 H	AMBERLITE™ HPR4200 C1
Feed flow rate (m <sup>3</sup> /h)	75	75
Regeneration bypass (m <sup>3</sup> /h)	0.6	
Design flow rate (m <sup>3</sup> /h)	75	75
Permeate flow rate (m <sup>3</sup> /h)	74.4	74.4
Design run time (h)	48	48
Regeneration time (h)	4.47	
Bed volume (m <sup>3</sup> )	2.23	4.47
Feed water pH	9.8	
Product pH	7.9	
Vessel pressure drop (bar)	1.5	
Safety factor	0.95	0.95
<b>Resin info</b>		
Volume (m <sup>3</sup> )	2.23	4.47
Ionic load (eq)	2282	2527
Regenerate	HCl	NaOH
Regenerate dose (g/L)	80	80
Regeneration ratio (g/L)	160	370
<b>Vessel type</b>		
Linear Velocity (m/h)	38	
Vessel diameter (inside) mm	1580	
Vessel diameter (outside) mm	1600	
<b>Inert resin</b>		
Resin	AMBERLITE™ 14i	
<b>OPEX<sup>1</sup></b>		
Utility-service-Chemical cost (Euro/d)	€ 125.17	
Specific Energy cost (Euro/m <sup>3</sup> )	€ 0.01	
Resin replacement (Euro/h)	€ 1.03	
Resin replacement (Euro/m <sup>3</sup> )	€ 0.01	
Total OPEX (per m <sup>3</sup> )	€ 0.02	
<b>CAPEX<sup>2</sup></b>		
SAC (Euro/m <sup>3</sup> )	€ 2,000	
SBA (Euro/m <sup>3</sup> )	€ 5,000	
IEX vessel (plug and play)	€ 120,000	
Pumps	€ 3,000	
Buffer tank	€ 4,000	
Total net CAPEX	€ 319,495	

Reference:

1. Water Application Value Engine (WAVE) software (DuPont Water Solutions)
2. Personal communication (DuPont Water Solutions)

### Remineralisation

<b>Remineralisation <sup>1</sup></b>	
<b>General info (lime milk)</b>	
	$2\text{CO}_2 + \text{Ca}(\text{OH})_2 \rightarrow \text{Ca}^{2+} + 2\text{HCO}_3^-$
Ca(OH) <sub>2</sub> concentration (gr/m <sup>3</sup> )	144.1
inlet flow rate (m <sup>3</sup> /h)	75
outlet flow rate (m <sup>3</sup> /h)	75
Energy consumption (kWh)	0.17
<b>OPEX <sup>1</sup></b>	
Lime consumption (kg/day)	259
Lime consumption (tone/year)	95
Cost of Lime (Euro/year)	14199
RO Permeate (m <sup>3</sup> /year)	657000
Cost of lime (Euro/m <sup>3</sup> )	0.02
Electricity cost (Euro/m <sup>3</sup> )	0.008
Total OPEX	0.03
<b>CAPEX <sup>1</sup></b>	
Lime milk prep tank (Euro)	€ 1000
Pumps (Euro)	€ 1000
Saturators (Euro)	€ 10000
Total CAPEX (Euro)	€ 12000

Reference:

1. (El Azhar et al. 2012)



**UV disinfection**

<b>UV disinfection<sup>1</sup></b>		
	Potable (RO permeate)	Irrigation (UF permeate)
Assumed UV dosage (mJ/cm <sup>2</sup> )	80	80
Assumed log removal	4	4
TDS (mg/l)	41.2	1333.3
<b>CAPEX calculation</b>		
Price of unit	12000	15000
Lifetime of unit (year)	10	10
Total CAPEX	€ 24000	€ 30000
<b>Cost of lamp energy consumption</b>		
Flow (m <sup>3</sup> /h)	75.4	94.2
Required lamps	16	24
Lifetime of lamps (h)	12000	12000
Energy consumed per lamp (kW)	0.1	0.1
Unit cost of electricity (Euro/kWh)	0.1	0.1
<b>Cost of pumping energy consumption</b>		
Average feed pressure (bar)	0.05	0.05
Pump efficiency (eta)	0,6	0.6
Flow rate (m <sup>3</sup> /h)	75.4	94.2
<b>Other energy requirements</b>		
Cleaning automation etc. (kWh)	4	6
Cost of other energy requirements (Euro)	0.005	0.006
<b>Cost of lamp replacements</b>		
Price of one lamp (Euro)	100	100
Required lamps	16	24
Total price lamps (Euro)	1600	2400
Lifetime of lamps (h)	12000	12000
Lifetime of lamps (year)	1.4	1.4
Remaining lifetime (year)	18.6	18.6
Required lamp replacement events	13.6	13.6

Reference:

1. Personal communication (Xylem Water Solutions Nederland B.V & WeUVcare)

***Labour costs***

It is assumed that each MATP can be operated by 2 operators that earn a gross salary of 50.000 Euros per year each. Labour requirements and costs are estimated based on personal communication with sector specific companies.

- **Process optimization for increased RO recovery**

**Softener/biostablizer**

<b>Softener/biostablizer [SAC-SBA]<sup>1,2</sup></b>		
Resin form	SAC	SBA
Resin Type	Amberlite-HPR1100 Na	Amberlite-HPR4580 Cl
Layout	[SAC-SBA]	
Vessel type	Amberpack sandwich	
Resin type	Amberlite-HPR1100 Na	Amberlite-HPR4580 Cl
Feed flow rate (m <sup>3</sup> /h)	93.7	93.7
Regeneration bypass (m <sup>3</sup> /h)	2.4	2.4
Design flow rate (m <sup>3</sup> /h)	100	94
Permeate flow rate (m <sup>3</sup> /h)	93.7	93.7
Design run time (h)	10	10
Regeneration time (h)	1.71	3.46
bed volume (m <sup>3</sup> )	8.3	5.25
Feed water pH	12	12
Product pH	7	7
Vessel pressure drop (bar)	1	
Safety factor	0.49	0.79
<b>Resin info</b>		
Volume (m <sup>3</sup> )	8.3	5.25
Effective ionic capacity (eq/L)	0.81	0.54
Ionic load (eq)	6686	7221
Regenerate	RO Brine+ 2.2 g/L NaCl	RO Brine+ 2.2 g/L NaCl
Regeneration dose (g/L)	80	80
Regeneration ratio (g/L)	485	485
<b>Vessel type</b>		
Linear Velocity (m/h)	23	
Internal bed area(m <sup>2</sup> )	4.426	
Vessel diameter (inside) mm	2374	
Vessel diameter (outside) mm	2400	
<b>Inert resin</b>		
Resin	Amberlite 14i	
Volume (m <sup>3</sup> )	0.747	
Height (mm)	169	
<b>OPEX<sup>1</sup></b>		
Utility-service-Chemical cost (Euro/d)	€ 24.55	
Specific Energy cost (Euro/m3)	€ 0.01	
Resin replacement (Euro/h)	€ 0.76	
Resin replacement (Euro/m3)	€ 0.01	
Total OPEX (per m3)	€ 0.02	
<b>CAPEX<sup>2</sup></b>		
SAC (Euro/m3)	€ 2,000	
SBA (Euro/m3)	€ 5,500	
IEX vessel (plug and play)	€ 200,000	
pumps	€ 3,000	
Buffer tank	€ 4,000	
Total net CAPEX	€ 447,200	

Reference:

1. Water Application Value Engine (WAVE) software (DuPont Water Solutions)
2. Personal communication (DuPont Water Solutions)

### Reverse osmosis

<b>General Info <sup>1</sup></b>	
Configuration	Double stages
Stage 1 (No. PV)	12
Stage 2 (No. PV)	6
Number of elements per PV	6
Total number of elements	108
Elements type <sup>2</sup>	ECO Pro-400
RO recovery (%)	95
<b>General Operation <sup>1</sup></b>	
Feed flow rate (m <sup>3</sup> /h)	93.8
Permeate flow rate (m <sup>3</sup> /h)	89.06
Feed pressure (bar)	10.3
Average net driving pressure	6.7
Specific Energy (kWh/m <sup>3</sup> )	0.38
RO average flux (LMH)	22.2
Antiscalant (mg/l)	0
<b>Flow properties <sup>1</sup></b>	
RO feed flow rate (m <sup>3</sup> /h)	93.8
Pressure (bar)	10.3
TDS (mg/L)	933.8
RO concentrate (m <sup>3</sup> /h)	4.64
Pressure (bar)	9.4
TDS (mg/L)	15224
RO permeate (m <sup>3</sup> /h)	89.06
Pressure (bar)	1
TDS (mg/L)	129.2
<b>CIP cleaning <sup>2</sup></b>	
CIP frequency (events/yr)	20
CIP duration (h)	8
CIP chemicals	HCl/NaOH
CIP cleaning pH	2/12
<b>OPEX <sup>1</sup></b>	
Energy, waste disposal and antiscalant (Euro/m <sup>3</sup> )	0.07
Cost of fouling (Euro/m <sup>3</sup> )	0.24
Cartridge filter (Euro/m <sup>3</sup> )	0.02
<b>CAPEX <sup>3</sup></b>	
Single element (Euro/module)	€ 600
108 Elements (Euro)	€ 64,800
Pressure vessel (Euro/module)	€ 600
18 Pressure vessels (Euro)	€ 10,800
Feed Pumps (Euro)	€ 200,000
Feed buffer tank (Euro)	€ 9,000
Filtrate tank (Euro)	€ 7,200
Concentrate tank (Euro)	€ 1,800
Automation control, electrics (Euro)	€ 100,000
CIP (pumps, tanks etc.) (Euro)	€ 30,000
Valves, piping etc. (Euro)	€ 15000

Reference:

1. Water Application Value Engine (WAVE) software (DuPont Water Solutions)
2. (Shang et al. 2011)
3. (Hitsov et al. 2018)

### Fouling and cleaning in Reverse Osmosis

<b>Feed Channel pressure drop increase <sup>1</sup></b>	
Initial Normalized feed pressure drop (NPD0) (kPa)	120
Average Normalized feed pressure drop (NPD) (kPa)	140
Unit cost of electricity (Euro/kWh)	0.1
Pump efficiency	0.6
Feed flow rate (m <sup>3</sup> /d)	2248.8
<b>Permeability reduction <sup>1</sup></b>	
Virgin membrane permeability (m/s/kPa)	3.6
Average fouled membrane permeability (m/s/kPa)	2.88
Permeate flow rate (m <sup>3</sup> /d)	2138
Design flux( constant value) (LMH)	20.2
<b>Membrane replacement <sup>1</sup></b>	
RO module (Euro/stuck)	600
Total number of membrane replaced	108
Life time (year)	5
Annual cost of module replacement (Euro)	10800
<b>CIP cleaning <sup>1</sup></b>	
<b>Chemicals:</b>	
C HCl (pH=2)	0.36
C NaOH (pH=12)	0.4
Cost of acid (Euro/kg)	100
Cost of base (Euro/kg)	100
acid volume (m <sup>3</sup> )	2.88
Base volume (m <sup>3</sup> )	2.88
Number of CIP per year	20
<b>Waste disposal</b>	
Waste cost factor (Euro/m <sup>3</sup> )	0.6
<b>Down-time cost (Due to CIP)</b>	
Water production capacity (m <sup>3</sup> /d)	1800
Profit loss due to down-time (Euro/m <sup>3</sup> )	0.1
<b>CIP solution heating</b>	
Pump efficiency	0.9
Ambient Temperature (C)	10
T base (C)	35
T acid (C)	35
Specific heat capacity kJ/kg/C	4.2
Density (kg/m <sup>3</sup> )	1000

Reference:

1. (Jafari et al. 2021)

**Degasifier**

<b>Designed for saturated stream <sup>1</sup></b>	
CO <sub>2</sub> removal (%)	70
Type	Tank/Agitator
Design flow (m <sup>3</sup> /h)	89.6
Residence time (min)	10
Agitation power intensity (W/m <sup>3</sup> )	50
Mixing tank volume (m <sup>3</sup> )	14.9
Specific Energy (kWh/m <sup>3</sup> )	0.01
<b>OPEX</b>	
Energy cost (Euro/m <sup>3</sup> )	0.01
<b>CAPEX <sup>1</sup></b>	
Tank (Euro)	€ 7,000
Agitator (Euro)	€ 2,500
Instrumentations (Euro)	€2,375

Reference:

1. Personal communication (Global Water and Energy)

**Ion Exchange Mixed bed-Permeate polishing**

<b>Ion exchange mixed-bed permeate polishing <sup>1</sup> [SAC SBA]</b>		
Resin form	SAC	SBA
Layout	[SAC SBA]	
Vessel type	Amberpack sandwich	
Resin type	AMBERLITE™ HPR1200 H	AMBERLITE™ HPR4200 CI
Feed flow rate (m <sup>3</sup> /h)	89.6	89.6
Regeneration bypass (m <sup>3</sup> /h)	1.7	
Design flow rate (m <sup>3</sup> /h)	90	90
Permeate flow rate (m <sup>3</sup> /h)	87.9	87.9
Design run time (h)	20	20
Regeneration time (h)	3.76	
Bed volume (m <sup>3</sup> )	2.52	5.77
Feed water pH	9.8	
Product pH	7.9	
Vessel pressure drop (bar)	1.34	
Safety factor	0.95	0.95
<b>Resin info</b>		
Volume (m <sup>3</sup> )	2.52	5.77
Ionic load (eq)	3113	3114
Regenerate	HCl	NaOH
Regenerate dose (g/L)	80	80
Regeneration ratio (g/L)	165	370
<b>Vessel type</b>		
Linear velocity (m/h)	36	
Vessel diameter (inside) mm	1780	
Vessel diameter (outside) mm	1800	
<b>Inert resin</b>		
Resin	AMBERLITE™ 14i	
<b>OPEX<sup>1</sup></b>		
Utility-service-chemical cost (Euro/d)	€ 389	
Specific utility and chemical cost (Euro/m <sup>3</sup> )	€ 0.18	
Resin replacement (Euro/h)	€ 1.03	
Resin replacement (Euro/m <sup>3</sup> )	€ 0.01	
Total OPEX (per m <sup>3</sup> )	€ 0.2	
<b>CAPEX<sup>2</sup></b>		
SAC (Euro/m <sup>3</sup> )	€ 2,000	
SBA (Euro/m <sup>3</sup> )	€ 5,000	
IEX vessel (plug and play)	€ 120,000	
Pumps	€ 3,000	
Buffer tank	€ 4,000	
Total net CAPEX	€ 333,665	

Reference:

1. Water Application Value Engine (WAVE) software (DuPont Water Solutions)
2. Personal communication (DuPont Water Solutions)

- **Renewable energy integration**

**Electricity recoverable with anaerobic sludge digestion**

Unit	Assumptions & Calculations	Value	Unit	Reference
<b>Influent</b>	Total influent	100	m <sup>3</sup> /h	
	COD []	750	mg/l	(Henze and Comeau 2008)
		750000	mg/m <sup>3</sup>	
		0.75	kg/m <sup>3</sup>	
	COD load	75	kg	
	Energy content COD	17.8	kJ/gCOD	(Heidrich et al. 2011)
	Chemical energy in influent COD	1335000	kJ	
		1335	MJ	
<b>Primary COD capture</b>	COD capture	0.6	%	(Wan et al. 2016)
	COD into primary sludge	45	kg	
<b>CAS</b>	COD load	30	kg	
	COD oxidised into CO <sub>2</sub>	0.6	%	(Winkler et al. 2013)
	COD into secondary sludge	12	kg	
<b>AD</b>	COD load	57		Primary + secondary sludge
	COD converted into biogas	0.5	%	(Khiewwijit et al. 2016), Mesophilic-35°C
		29	kg	
	CH <sub>4</sub> content biogas	0.65	%	(Frijns et al. 2013)
	COD converted into CH <sub>4</sub>	19	kg	
	Theoretical max CH <sub>4</sub> production	0.35	Nm <sup>3</sup> CH <sub>4</sub> /kg COD	(Frijns et al. 2013)
	Produced CH <sub>4</sub>	6	Nm <sup>3</sup> CH <sub>4</sub>	
	Calorific value CH <sub>4</sub>	35.9	MJ/Nm <sup>3</sup>	(Frijns et al. 2013)

	Produced energy	233	MJ	
	Recovery efficiency CH <sub>4</sub>	17	%	
<b>CHP</b>	Electricity conversion efficiency	0.4	%	(Verstraete and Vlaeminck 2011)
	Electricity produced	93	MJ	
	1 MJ=	0.000278	MWh	Conversion factor
	Electricity produced	0,026	MWh	
		0,001	MW	(Wh)/(h) = (W)
		$2.59 \times 10^{-5}$	kWh	per 100m <sup>3</sup> WWTP effluent
		$2.59 \times 10^{-7}$	kWh/m <sup>3</sup>	
		$6.21 \times 10^{-4}$	kWh/d	
	Recovery efficiency electricity	7,0	%	



## Required photovoltaic area

The calculations are based on the Photovoltaic Geographical Information System (PVGIS) of the European Commission and an assumed ratio of 1 kWp PV capacity per 10m<sup>2</sup> installed PV area. (European Commission 2020).

<b>PVGIS results</b>		-
<b>Provided inputs</b>		
Latitude/Longitude (Delft)		52.010, 4.349
Horizon		Calculated
Database used		PVGIS-SARAH
PV technology		Crystalline silicon
PV installed (kWp)		1
System loss (%)		14
<b>Simulation outputs</b>		
Slope angle (°)		39
Azimuth angle (°)		3
Yearly PV energy production (kWh)		1024.66
Yearly in-plane irradiation (kWh/m <sup>2</sup> )		1262.75
Year-to-year variability (kWh)		47.61
Changes in output due to:		
Angle of incidence (%)		-3
Spectral effects (%)		1.74
Temperature and low irradiance (%)		-4.39
Total loss (%)		-18.85
		<b>Energy producible</b>
		(kWh/yr)
<b>Delft: 1 kWp PV capacity</b>		1024.66
		<b>PV module sizing</b>
		(m <sup>2</sup> )
<b>1 kWp PV capacity</b>		10
Field size Johan Cruyff Arena (m <sup>2</sup> )		7,140

# List of Abbreviations

Abbreviation	Definition
UF	Ultrafiltration
MF	Microfiltration
NF	Nanofiltration
RO	Reverse Osmosis
FO	Forward Osmosis
EPS	Extracellular Polymeric substances
AOC	Assimilable organic Carbon
DOC	Dissolved Organic Carbon
GDM	Gravity Driven Membrane
OPEX	Operational Expenditure
CAPEX	Capital Expenditure
OCT	Optical Coherence Tomography
TMP	Trans membrane Pressure
FSI	Fluid-Structure Interaction
CIP	Cleaning-In-Place
DBNPA	2,2-Dibromo-3-nitrilopropionamide
SBS	Sodium bisulfite
MFI	Membrane Fouling Index
MWCO	Molecular Weight Cut-Off
SRSSE	square root of the averaged sum of squares of errors
CLSM	Confocal Laser Scanning Microscopy
TOC	Total Organic Carbon
ATP	Adenosine triphosphate
DAFF	Dissolved Air Flotation sand Filtration
QCM-D	Quartz Crystal Microbalance and Dissipation
PN/PS	Protein to Polysaccharide ratio
SRT	Solid Retention Time
MBR	Membrane Bioreactor
NOM	Natural Organic Matter
SEM	Scanning Electron Microscope
NPD	Normalized Pressure Drop
ICP-OES	Inductively coupled plasma-optical emission spectrometer
CECs	contaminants of emerging concerns
WWTP	WasteWater Treatment Plant
MATP	Membrane Advance Treatment Plant

## List of abbreviations

---

TSS	Total Suspended Solid
CEB	Chemical Enhanced Backwash
MEB	Mass and Energy balance
IEX	Ion Exchange bed
WAVE	Water Application Value Engine
NPV	Net Present Value
LRV	Log removal value
CBA	Cost benefit analysis
UV	Ultraviolet
SWRO	Sea Water Reverse Osmosis
DIC	Digital Image Correlation

---

# References

- Abid, H.S., Johnson, D.J., Hashaikeh, R. and Hilal, N. (2017) A review of efforts to reduce membrane fouling by control of feed spacer characteristics. *Desalination* 420, 384-402.
- Abushaban, A., Salinas-Rodriguez, S.G., Dhakal, N., Schippers, J.C. and Kennedy, M.D. (2019) Assessing pretreatment and seawater reverse osmosis performance using an ATP-based bacterial growth potential method. *Desalination* 467, 210-218.
- Abushaban, A., Salinas-Rodriguez, S.G., Dhakal, N., Schippers, J.C. and Kennedy, M.D. (2020) Monitoring Biofouling Potential Using ATP-Based Bacterial Growth Potential in SWRO Pre-Treatment of a Full-Scale Plant. *Membranes (Basel)* (10), 360.
- Al-Juboori, R.A. and Yusaf, T. (2012) Biofouling in RO system: Mechanisms, monitoring and controlling. *Desalination* 302, 1-23.
- Al Ashhab, A., Gillor, O. and Herzberg, M. (2014) Biofouling of reverse-osmosis membranes under different shear rates during tertiary wastewater desalination: microbial community composition. *Water Research* 67, 86-95.
- Al Ashhab, A., Sweity, A., Bayramoglu, B., Herzberg, M. and Gillor, O. (2017) Biofouling of reverse osmosis membranes: effects of cleaning on biofilm microbial communities, membrane performance, and adherence of extracellular polymeric substances. *Biofouling* 33(5), 397-409.
- Allen, A., Habimana, O. and Casey, E. (2018) The effects of extrinsic factors on the structural and mechanical properties of *Pseudomonas fluorescens* biofilms: A combined study of nutrient concentrations and shear conditions. *Colloids and Surfaces Biointerfaces* 165, 127-134.
- Ang, W.L., Nordin, D., Mohammad, A.W., Benamor, A. and Hilal, N. (2017) Effect of membrane performance including fouling on cost optimization in brackish water desalination process. *Chemical Engineering Research and Design* 117, 401-413.
- Ang, W.S., Lee, S. and Elimelech, M. (2006) Chemical and physical aspects of cleaning of organic-fouled reverse osmosis membranes. *Journal of Membrane Science* 272(1-2), 198-210.
- Anis, S.F., Hashaikeh, R. and Hilal, N. (2019) Reverse osmosis pretreatment technologies and future trends: A comprehensive review. *Desalination* 452, 159-195.
- Antony, A., Low, J.H., Gray, S., Childress, A.E., Le-Clech, P. and Leslie, G. (2011) Scale formation and control in high pressure membrane water treatment systems: A review. *Journal of Membrane Science* 383(1), 1-16.
- Aravas, N. and Lapidou, C.S. (2008) On the calculation of the elastic modulus of a biofilm streamer. *Biotechnology and Bioengineering* 101(1), 196-200.

- Asano, T. and Levine, A.D. (1996) Wastewater reclamation, recycling and reuse: past, present, and future. *Water Science and Technology* 33(10), 1-14.
- Basu, O.D. (2015) *Encyclopedia of Membranes*. Drioli, E. and Giorno, L. (eds), pp. 1-3, Springer Berlin Heidelberg, Berlin, Heidelberg.
- Bauer, A., Wagner, M., Saravia, F., Bartl, S., Hilgenfeldt, V. and Horn, H. (2019) In-situ monitoring and quantification of fouling development in membrane distillation by means of optical coherence tomography. *Journal of Membrane Science* 577, 145-152.
- Bereschenko, L.A., Prummel, H., Euverink, G.J., Stams, A.J. and van Loosdrecht, M.C. (2011) Effect of conventional chemical treatment on the microbial population in a biofouling layer of reverse osmosis systems. *Water Research* 45(2), 405-416.
- Bereschenko, L.A., Stams, A.J.M., Euverink, G.J.W. and van Loosdrecht, M.C.M. (2010) Biofilm Formation on Reverse Osmosis Membranes Is Initiated and Dominated by. *Applied Microbiology and Biotechnology* 76(8), 2623-2632.
- Beyer, F., Laurinonyte, J., Zwijnenburg, A., Stams, A.J.M. and Plugge, C.M. (2017) Membrane Fouling and Chemical Cleaning in Three Full-Scale Reverse Osmosis Plants Producing Demineralized Water. *Journal of Engineering* 2017, 1-14.
- Beyer, F., Rietman, B.M., Zwijnenburg, A., van den Brink, P., Vrouwenvelder, J.S., Jarzembowska, M., Laurinonyte, J., Stams, A.J.M. and Plugge, C.M. (2014) Long-term performance and fouling analysis of full-scale direct nanofiltration (NF) installations treating anoxic groundwater. *Journal of Membrane Science* 468, 339-348.
- Billings, N., Birjiniuk, A., Samad, T.S., Doyle, P.S. and Ribbeck, K. (2015) Material properties of biofilms-a review of methods for understanding permeability and mechanics. *Reports on Progress in Physics* 78(3), 036601.
- Bishop, P.L., Zhang, T.C. and Fu, Y.-C. (1995) Effects of biofilm structure, microbial distributions and mass transport on biodegradation processes. *Water Science and Technology* 31(1), 143-152.
- Bland, D.R. (1957) The associated flow rule of plasticity. *Journal of the Mechanics and Physics of Solids* 6(1), 71-78.
- Blauert, F. (2017) Investigating biofilm deformation using optical coherence tomography and fluid-structure interaction simulation, *Karlsruher Instituts für Technologie, Karlsruhe*.
- Blauert, F., Horn, H. and Wagner, M. (2015) Time-resolved biofilm deformation measurements using optical coherence tomography. *Biotechnology and Bioengineering* 112(9), 1893-1905.

- Boleij, M., Seviour, T., Wong, L.L., van Loosdrecht, M.C.M. and Lin, Y. (2019) Solubilization and characterization of extracellular proteins from anammox granular sludge. *Water Research* 164, 114952.
- Boretti, A. and Rosa, L. (2019) Reassessing the projections of the World Water Development Report. *npj Clean Water* 2(1), 15.
- Bradford, M.M. (1976) A rapid and sensitive method for the quantitation of microgram quantities of protein utilizing the principle of protein-dye binding. *Analytical Biochemistry* 72(1), 248-254.
- Bucs, S., Valladares Linares, R., Siddiqui, A., Matin, A., Khan, Z., van Loosdrecht, M.C.M., Yang, R., Wang, M., Gleason, K.K., Kruithof, J.C. and Vrouwenvelder, J.S. (2017) Coating of reverse osmosis membranes with amphiphilic copolymers for biofouling control. *Desalination and Water Treatment* 68, 11.
- Bucs, S.S., Farhat, N., Kruithof, J.C., Picioreanu, C., van Loosdrecht, M.C.M. and Vrouwenvelder, J.S. (2018) Review on strategies for biofouling mitigation in spiral wound membrane systems. *Desalination* 434, 189-197.
- Bucs, S.S., Valladares Linares, R., Marston, J.O., Radu, A.I., Vrouwenvelder, J.S. and Picioreanu, C. (2015) Experimental and numerical characterization of the water flow in spacer-filled channels of spiral-wound membranes. *Water Research* 87, 299-310.
- Bucs, S.S., Valladares Linares, R., Vrouwenvelder, J.S. and Picioreanu, C. (2016) Biofouling in forward osmosis systems: An experimental and numerical study. *Water Research* 106, 86-97.
- Casey, E. (2007) Tracer measurements reveal experimental evidence of biofilm consolidation. *Biotechnology and Bioengineering* 98(4), 913-918.
- Castaing, J.B., Massé, A., Séchet, V., Sabiri, N.E., Pontié, M., Haure, J. and Jaouen, P. (2011) Immersed hollow fibres microfiltration (MF) for removing undesirable micro-algae and protecting semi-closed aquaculture basins. *Desalination* 276(1-3), 386-396.
- Cense, A.W., Peeters, E.A., Gottenbos, B., Baaijens, F.P., Nuijs, A.M. and van Dongen, M.E. (2006) Mechanical properties and failure of *Streptococcus mutans* biofilms, studied using a microindentation device. *Journal of microbiological methods* 67(3), 463-472.
- Chauveau, S. (2020) Cost of biofouling in Reverse Osmosis. Jafari, M. (ed).
- Chon, K., Kim, S.J., Moon, J. and Cho, J. (2012) Combined coagulation-disk filtration process as a pretreatment of ultrafiltration and reverse osmosis membrane for wastewater reclamation: an autopsy study of a pilot plant. *Water Research* 46(6), 1803-1816.
- Christensen, B.E. (1989) The role of extracellular polysaccharides in biofilms. *Journal of Biotechnology* 10(3), 181-202.

- Cornelissen, E.R., Vrouwenvelder, J.S., Heijman, S.G.J., Viallefont, X.D., Van Der Kooij, D. and Wessels, L.P. (2007) Periodic air/water cleaning for control of biofouling in spiral wound membrane elements. *Journal of Membrane Science* 287(1), 94-101.
- Coussy, O. (2004) *Poromechanics*, Wiley, UK.
- Creber, S.A., Vrouwenvelder, J.S., van Loosdrecht, M.C.M. and Johns, M.L. (2010) Chemical cleaning of biofouling in reverse osmosis membranes evaluated using magnetic resonance imaging. *Journal of Membrane Science* 362(1-2), 202-210.
- Cui, Z.F., Jiang, Y. and Field, R.W. (2010) *Membrane Technology*. Cui, Z.F. and Muralidhara, H.S. (eds), pp. 1-18, Butterworth-Heinemann, Oxford.
- Deng, L., Li, S., Qin, Y., Zhang, L., Chen, H., Chang, Z. and Hu, Y. (2021) Fabrication of antifouling thin-film composite nanofiltration membrane via surface grafting of polyethyleneimine followed by zwitterionic modification. *Journal of Membrane Science* 619, 118564.
- Derlon, N., Grutter, A., Brandenberger, F., Sutter, A., Kuhlicke, U., Neu, T.R. and Morgenroth, E. (2016) The composition and compression of biofilms developed on ultrafiltration membranes determine hydraulic biofilm resistance. *Water Research* 102, 63-72.
- Derlon, N., Koch, N., Eugster, B., Posch, T., Pernthaler, J., Pronk, W. and Morgenroth, E. (2013) Activity of metazoa governs biofilm structure formation and enhances permeate flux during Gravity-Driven Membrane (GDM) filtration. *Water Research* 47(6), 2085-2095.
- Derlon, N., Massé, A., Escudié, R., Bernet, N. and Paul, E. (2008) Stratification in the cohesion of biofilms grown under various environmental conditions. *Water Research* 42(8), 2102-2110.
- Derlon, N., Mimoso, J., Klein, T., Koetzsch, S. and Morgenroth, E. (2014) Presence of biofilms on ultrafiltration membrane surfaces increases the quality of permeate produced during ultra-low pressure gravity-driven membrane filtration. *Water Research* 60, 164-173.
- Derlon, N., Peter-Varbanets, M., Scheidegger, A., Pronk, W. and Morgenroth, E. (2012) Predation influences the structure of biofilm developed on ultrafiltration membranes. *Water Research* 46(10), 3323-3333.
- Desmond, P., Best, J.P., Morgenroth, E. and Derlon, N. (2018a) Linking composition of extracellular polymeric substances (EPS) to the physical structure and hydraulic resistance of membrane biofilms. *Water Research* 132, 211-221.
- Desmond, P., Böni, L., Fischer, P., Morgenroth, E. and Derlon, N. (2018b) Stratification in the physical structure and cohesion of membrane biofilms — Implications for hydraulic resistance. *Journal of Membrane Science* 564, 897-904.



- Desmond, P., Morgenroth, E. and Derlon, N. (2018c) Physical structure determines compression of membrane biofilms during Gravity Driven Membrane (GDM) ultrafiltration. *Water Res* 143, 539-549.
- Desmond, P., Morgenroth, E. and Derlon, N. (2018d) Physical structure determines compression of membrane biofilms during Gravity Driven Membrane (GDM) ultrafiltration. *Water Research* 143, 539-549.
- Dreszer, C., Vrouwenvelder, J.S., Paulitsch-Fuchs, A.H., Zwijnenburg, A., Kruithof, J.C. and Flemming, H.C. (2013) Hydraulic resistance of biofilms. *Journal of Membrane Science* 429, 436-447.
- Dreszer, C., Wexler, A.D., Drusova, S., Overdijk, T., Zwijnenburg, A., Flemming, H.C., Kruithof, J.C. and Vrouwenvelder, J.S. (2014) In-situ biofilm characterization in membrane systems using Optical Coherence Tomography: formation, structure, detachment and impact of flux change. *Water Research* 67, 243-254.
- DuBois, M., Gilles, K.A., Hamilton, J.K., Rebers, P.A. and Smith, F. (1956) Colorimetric Method for Determination of Sugars and Related Substances. *Anal. Chem* 28(3), 350-356.
- Ebrahim, S.H., Abdel-Jawad, M.M. and Safar, M. (1995) Conventional pretreatment system for the Doha Reverse Osmosis Plant: Technical and economic assessment. *Desalination* 102(1), 179-187.
- Eke, J., Yusuf, A., Giwa, A. and Sodiq, A. (2020) The global status of desalination: An assessment of current desalination technologies, plants and capacity. *Desalination* 495, 114633.
- Elimelech, Q.L.a.M. (2009) Organic Fouling and Chemical Cleaning of Nanofiltration Membranes: Measurements and Mechanisms. *Environmental Science & Technology* (43), 4393–4398.
- Fabrizi, S., Johnston, D.A., Rmaile, A., Gottenbos, B., De Jager, M., Aspiras, M., Starke, E.M., Ward, M.T. and Stoodley, P. (2016) *Streptococcus mutans* biofilm transient viscoelastic fluid behaviour during high-velocity microsprays. *Journal of the Mechanical Behavior of Biomedical Materials* 59, 197-206.
- FAO (2017) *The future of food and agriculture – Trends and challenges*. Rome (ed).
- Farhat, N.M., Christodoulou, C., Placotas, P., Blankert, B., Sallangos, O. and Vrouwenvelder, J.S. (2020) Cartridge filter selection and replacement: Optimization of produced water quantity, quality, and cost. *Desalination* 473.
- Farhat, N.M., Javier, L., Van Loosdrecht, M.C.M., Kruithof, J.C. and Vrouwenvelder, J.S. (2019) Role of feed water biodegradable substrate concentration on biofouling: Biofilm characteristics, membrane performance and cleanability. *Water Research* 150, 1-11.
- Felz, S., Vermeulen, P., van Loosdrecht, M.C.M. and Lin, Y.M. (2019) Chemical characterization methods for the analysis of structural extracellular polymeric substances (EPS). *Water Research* 157, 201-208.
- Flemming, H.-C. (2011) *Biofilm Highlights*, pp. 81-109.

- Flemming, H.-C. (2020) Biofouling and me: My Stockholm syndrome with biofilms. *Water Research*, 115576.
- Flemming, H.C. (2002) Biofouling in water systems – cases, causes and countermeasures. *Applied Microbiology and Biotechnology* 59(6), 629-640.
- Fong, J.N.C. and Yildiz, F.H. (2015) Biofilm Matrix Proteins. *Microbiology spectrum* 3(2), 10.1128/microbiolspec.MB-0004-2014.
- Fortunato, L., Qamar, A., Wang, Y., Jeong, S. and Leiknes, T. (2017) In-situ assessment of biofilm formation in submerged membrane system using optical coherence tomography and computational fluid dynamics. *Journal of Membrane Science* 521, 84-94.
- Galy, O., Latour-Lambert, P., Zrelli, K., Ghigo, J.M., Beloin, C. and Henry, N. (2012) Mapping of bacterial biofilm local mechanics by magnetic microparticle actuation. *Biophysical Journal* 103(6), 1400-1408.
- Gao, W., Liang, H., Ma, J., Han, M., Chen, Z.-l., Han, Z.-s. and Li, G.-b. (2011a) Membrane fouling control in ultrafiltration technology for drinking water production: A review. *Desalination* 272(1), 1-8.
- Gao, W.J., Lin, H.J., Leung, K.T., Schraft, H. and Liao, B.Q. (2011b) Structure of cake layer in a submerged anaerobic membrane bioreactor. *Journal of Membrane Science* 374(1-2), 110-120.
- Gaublomme, D., Strubbe, L., Vanoppen, M., Torfs, E., Mortier, S., Cornelissen, E., De Gussemme, B., Verliefde, A. and Nopens, I. (2020) A generic reverse osmosis model for full-scale operation. *Desalination* 490, 114509.
- Gloag, E.S., Fabbri, S., Wozniak, D.J. and Stoodley, P. (2020) Biofilm mechanics: Implications in infection and survival. *Biofilm* 2, 100017.
- Guo, W., Ngo, H.H. and Li, J. (2012) A mini-review on membrane fouling. *Bioresource Technology* 122, 27-34.
- Haaksman, V.A., Siddiqui, A., Schellenberg, C., Kidwell, J., Vrouwenvelder, J.S. and Picioreanu, C. (2017) Characterization of feed channel spacer performance using geometries obtained by X-ray computed tomography. *Journal of Membrane Science* 522, 124-139.
- Helmig, R., Flemisch, B., Wolff, M., Ebigbo, A. and Class, H. (2013) Model coupling for multiphase flow in porous media. *Advances in Water Resources* 51, 52-66.
- Her, N., Amy, G., Park, H.-R. and Song, M. (2004) Characterizing algogenic organic matter (AOM) and evaluating associated NF membrane fouling. *Water Research* 38(6), 1427-1438.
- Herzberg, M. and Elimelech, M. (2007) Biofouling of reverse osmosis membranes: Role of biofilm-enhanced osmotic pressure. *Journal of Membrane Science* 295(1), 11-20.

- Herzberg, M., Kang, S. and Elimelech, M. (2009) Role of Extracellular Polymeric Substances (EPS) in Biofouling of Reverse Osmosis Membranes. *Environmental Science & Technology* 43(12), 4393-4398.
- Hijnen, W.A., Castillo, C., Brouwer-Hanzens, A.H., Harmsen, D.J., Cornelissen, E.R. and van der Kooij, D. (2012) Quantitative assessment of the efficacy of spiral-wound membrane cleaning procedures to remove biofilms. *Water Research* 46(19), 6369-6381.
- Hijnen, W.A., Cornelissen, E.R. and van der Kooij, D. (2011a) Threshold concentrations of biomass and iron for pressure drop increase in spiral-wound membrane elements. *Water Research* 45(4), 1607-1616.
- Hijnen, W.A.M., Cornelissen, E.R. and van der Kooij, D. (2011b) Threshold concentrations of biomass and iron for pressure drop increase in spiral-wound membrane elements. *Water Research* 45(4), 1607-1616.
- Hilal, N., Ogunbiyi, O.O., Miles, N.J. and Nigmatullin, R. (2005) Methods Employed for Control of Fouling in MF and UF Membranes: A Comprehensive Review. *Separation Science and Technology* 40(10), 1957-2005.
- Huertas, E., Herzberg, M., Oron, G. and Elimelech, M. (2008) Influence of biofouling on boron removal by nanofiltration and reverse osmosis membranes. *Journal of Membrane Science* 318(1), 264-270.
- Ilyas, S., de Grooth, J., Nijmeijer, K. and de Vos, W.M. (2015) Multifunctional polyelectrolyte multilayers as nanofiltration membranes and as sacrificial layers for easy membrane cleaning. *Journal of Colloid and Interface Science* 446, 386-393.
- Intellegence, G.W. (2018) Big data desalination approach pays off for ACWA Power, pp. 12-13.
- Jafari, M., D'Haese, A., Zlopasa, J., Cornelissen, E.R., Vrouwenvelder, J.S., Verbeken, K., Verliefdde, A., van Loosdrecht, M.C.M. and Picioreanu, C. (2020) A comparison between chemical cleaning efficiency in lab-scale and full-scale reverse osmosis membranes: Role of extracellular polymeric substances (EPS). *Journal of Membrane Science* 609, 118189.
- Jafari, M., Derlon, N., Desmond, P., van Loosdrecht, M.C.M., Morgenroth, E. and Picioreanu, C. (2019) Biofilm compressibility in ultrafiltration: A relation between biofilm morphology, mechanics and hydraulic resistance. *Water Research* 157, 335-345.
- Jafari, M., Desmond, P., van Loosdrecht, M.C.M., Derlon, N., Morgenroth, E. and Picioreanu, C. (2018) Effect of biofilm structural deformation on hydraulic resistance during ultrafiltration: A numerical and experimental study. *Water Research* 145, 375-387.
- Jafari, M., Vanoppen, M., van Agtmaal, J.M.C., Cornelissen, E.R., Vrouwenvelder, J.S., Verliefdde, A., van Loosdrecht, M.C.M. and Picioreanu, C. (2021) Cost of fouling in full-scale reverse osmosis and nanofiltration installations in the Netherlands. *Desalination* 500, 114865.

- Jiang, A., Wang, H., Lin, Y., Cheng, W. and Wang, J. (2017a) A study on optimal schedule of membrane cleaning and replacement for spiral-wound SWRO system. *Desalination* 404, 259-269.
- Jiang, S., Li, Y. and Ladewig, B.P. (2017b) A review of reverse osmosis membrane fouling and control strategies. *Science of The Total Environment* 595, 567-583.
- Johnson, J. (2014) Effect of fouling on the operating expenses (OPEX) of reverse osmosis systems, Las Vegas, USA.
- Jones, W.L., Sutton, M.P., McKittrick, L. and Stewart, P.S. (2011) Chemical and antimicrobial treatments change the viscoelastic properties of bacterial biofilms. *Biofouling* 27(2), 207-215.
- Jorgensen, M.K., Bugge, T.V., Larsen, P., Nielsen, P.H. and Christensen, M.L. (2017) Membrane filtration device for studying compression of fouling layers in membrane bioreactors. *PLoS ONE* 12(7), e0181652.
- Kelly, P. (2008) *Mechanics Lecture Notes: An introduction to Solid Mechanics*.
- Kim, I.S. and Jang, N. (2006) The effect of calcium on the membrane biofouling in the membrane bioreactor (MBR). *Water Research* 40(14), 2756-2764.
- Kim, S.-J., Oh, B.S., Yu, H.-W., Kim, L.H., Kim, C.-M., Yang, E.-T., Shin, M.S., Jang, A., Hwang, M.H. and Kim, I.S. (2015) Foulant characterization and distribution in spiral wound reverse osmosis membranes from different pressure vessels. *Desalination* 370, 44-52.
- Kim, S., Lee, S., Hong, S., Oh, Y., Seoul, M., Kweon, J. and Kim, T. (2009a) Biofouling of reverse osmosis membranes: Microbial quorum sensing and fouling propensity. *Desalination* 247(1), 303-315.
- Kim, S., Lee, S., Lee, E., Sarper, S., Kim, C.-H. and Cho, J. (2009b) Enhanced or reduced concentration polarization by membrane fouling in seawater reverse osmosis (SWRO) processes. *Desalination* 247(1), 162-168.
- Kim, Y., Li, S. and Ghaffour, N. (2020) Evaluation of different cleaning strategies for different types of forward osmosis membrane fouling and scaling. *Journal of Membrane Science* 596.
- Klapper, I., Rupp, C.J., Cargo, R., Purvedorj, B. and Stoodley, P. (2002) Viscoelastic fluid description of bacterial biofilm material properties. *Biotechnology and Bioengineering* 80(3), 289-296.
- Ko, M.K. and Pellegrino, J.J. (1992) Determination of osmotic pressure and fouling resistance and their effects on performance of ultrafiltration membranes. *Journal of Membrane Science* 74(1), 141-157.
- Korstgens, Flemming., H.-C., Wingender., J. and W. Borchard (2001a) Uniaxial compression measurement device for investigation of the mechanical stability of biofilms. *Journal of microbiological methods* 46, 9-17.

Korstgens, Flemming., H.-C., Wingender., J. and W. Borchard (2001b) Uniaxial compression measurement device for investigation of the mechanical stability of biofilms. *J Microbiol Methods*.

Kundukad, B., Seviour, T., Liang, Y., Rice, S.A., Kjelleberg, S. and Doyle, P.S. (2016) Mechanical properties of the superficial biofilm layer determine the architecture of biofilms. *Soft Matter* 12(26), 5718-5726.

Kwon, K.D., Green, H., Bjöörn, P. and Kubicki, J.D. (2006) Model Bacterial Extracellular Polysaccharide Adsorption onto Silica and Alumina: Quartz Crystal Microbalance with Dissipation Monitoring of Dextran Adsorption. *Environmental Science & Technology* 40(24), 7739-7744.

Labs, W. (2014) Automated cleaning and sanitation saves time, produces better results, *Food Engineering*.

Lapidou, C.S. (2007) Variation in the mechanical properties of a porous multi-phase biofilm under compression due to void closure. *Water Science & Technology* 55(8-9), 447.

Lapidou, C.S., Spyrou, L.A., Aravas, N. and Rittmann, B.E. (2014) Material modeling of biofilm mechanical properties. *Mathematical Biosciences* 251, 11-15.

Lee, H. and Tan, T.P. (2016) Singapore's experience with reclaimed water: NEWater. *International Journal of Water Resources Development* 32(4), 611-621.

Lee, S., Boo, C., Elimelech, M. and Hong, S. (2010) Comparison of fouling behavior in forward osmosis (FO) and reverse osmosis (RO). *Journal of Membrane Science* 365(1), 34-39.

León Ohl, A., Horn, H. and Hempel, D.C. (2004) Behaviour of biofilm systems under varying hydrodynamic conditions. *Water Science and Technology* 49(11-12), 345-351.

Li, C., Wagner, M., Lackner, S. and Horn, H. (2016) Assessing the influence of biofilm surface roughness on mass transfer by combining optical coherence tomography and two-dimensional modeling. *Biotechnology and Bioengineering* 113(5), 989-1000.

Li, Q. and Elimelech, M. (2004) Organic Fouling and Chemical Cleaning of Nanofiltration Membranes: Measurements and Mechanisms. *Environmental Science & Technology* 38(17), 4683-4693.

Li, Q. and Elimelech, M. (2009) Organic Fouling and Chemical Cleaning of Nanofiltration Membranes: Measurements and Mechanisms. *Environmental Science & Technology* (43), 4393-4398.

Li, X., Liu, C., Yin, W., Chong, T.H. and Wang, R. (2019) Design and development of layer-by-layer based low-pressure antifouling nanofiltration membrane used for water reclamation. *Journal of Membrane Science* 584, 309-323.

Limoli, D.H., Jones, C.J. and Wozniak, D.J. (2015) Bacterial Extracellular Polysaccharides in Biofilm Formation and Function. *Microbiology spectrum* 3(3).

- Lin, H., Zhang, M., Wang, F., Meng, F., Liao, B.-Q., Hong, H., Chen, J. and Gao, W. (2014) A critical review of extracellular polymeric substances (EPSs) in membrane bioreactors: Characteristics, roles in membrane fouling and control strategies. *Journal of Membrane Science* 460, 110-125.
- Lubliner, J. and Papadopoulos, P. (2013) *Introduction to Solid Mechanics: An Integrated Approach*, Springer New York.
- Lyster, E., Kim, M.-m., Au, J. and Cohen, Y. (2010) A method for evaluating antiscalant retardation of crystal nucleation and growth on RO membranes. *Journal of Membrane Science* 364(1), 122-131.
- Lyu, S., Chen, W., Zhang, W., Fan, Y. and Jiao, W. (2016) Wastewater reclamation and reuse in China: Opportunities and challenges. *Journal of Environmental Sciences* 39, 86-96.
- MacMinn, C.W., Dufresne, E.R. and Wettlaufer, J.S. (2016) Large Deformations of a Soft Porous Material. *Physical Review Applied* 5(4), 044020.
- Madaeni, S. and Mansourpanah, Y. (2004a) Chemical cleaning of reverse osmosis membranes fouled by whey. *Desalination* 161, 13-24.
- Madaeni, S.S. and Mansourpanah, Y. (2004b) Chemical cleaning of reverse osmosis membranes fouled by whey. *Desalination* 161(1), 13-24.
- Majamaa, K., Aerts, P.E.M., Groot, C., Paping, L.L.M.J., van den Broek, W. and van Agtmaal, S. (2010) Industrial water reuse with integrated membrane system increases the sustainability of the chemical manufacturing. *Desalination and Water Treatment* 18(1-3), 17-23.
- Martin, K.J., Bolster, D., Derlon, N., Morgenroth, E. and Nerenberg, R. (2014) Effect of fouling layer spatial distribution on permeate flux: A theoretical and experimental study. *Journal of Membrane Science* 471, 130-137.
- Mathias, J.D. and Stoodley, P. (2009) Applying the digital image correlation method to estimate the mechanical properties of bacterial biofilms subjected to a wall shear stress. *Biofouling* 25(8), 695-703.
- McCarthy, A.A., Walsh, P.K. and Foley, G. (2002) Experimental techniques for quantifying the cake mass, the cake and membrane resistances and the specific cake resistance during crossflow filtration of microbial suspensions. *Journal of Membrane Science* 201(1), 31-45.
- McDonogh, R., Schaule, G. and Flemming, H.-C. (1994) The permeability of biofouling layers on membranes. *Journal of Membrane Science* 87(1), 199-217.
- Mendret, J., Azais, A., Favier, T. and Brosillon, S. (2019) Urban wastewater reuse using a coupling between nanofiltration and ozonation: Techno-economic assessment. *Chemical Engineering Research and Design* 145, 19-28.

Meng, F., Chae, S.R., Drews, A., Kraume, M., Shin, H.S. and Yang, F. (2009) Recent advances in membrane bioreactors (MBRs): membrane fouling and membrane material. *Water Research* 43(6), 1489-1512.

Meng, F., Zhang, S., Oh, Y., Zhou, Z., Shin, H.S. and Chae, S.R. (2017) Fouling in membrane bioreactors: An updated review. *Water Research* 114, 151-180.

Miller, D.J., Araujo, P.A., Correia, P.B., Ramsey, M.M., Kruithof, J.C., van Loosdrecht, M.C., Freeman, B.D., Paul, D.R., Whiteley, M. and Vrouwenvelder, J.S. (2012) Short-term adhesion and long-term biofouling testing of polydopamine and poly(ethylene glycol) surface modifications of membranes and feed spacers for biofouling control. *Water Research* 46(12), 3737-3753.

Millington, R. and Quirk, P. (1960a) Permeability of porous solids. *Transactions of the Faraday Society* 57, 1200-1207.

Millington, R. and Quirk, P. (1960b) Permeability of porous solids. *Trans. Faraday Soc.* 57, 1200-1207.

Mohle, R.B., Langemann, T., Haesner, M., Augustin, W., Scholl, S., Neu, T.R., Hempel, D.C. and Horn, H. (2007) Structure and shear strength of microbial biofilms as determined with confocal laser scanning microscopy and fluid dynamic gauging using a novel rotating disc biofilm reactor. *Biotechnology and Bioengineering* 98(4), 747-755.

Morillo, J., Usero, J., Rosado, D., El Bakouri, H., Riaza, A. and Bernaola, F.-J. (2014) Comparative study of brine management technologies for desalination plants. *Desalination* 336, 32-49.

Murga, R., Stewart, P.S. and Daly, D. (1995) Quantitative analysis of biofilm thickness variability. *Biotechnology and Bioengineering* 45(6), 503-510.

Namoodiri, V. and Rajagopalan, N. (2014) *Comprehensive Water Quality and Purification*. Ahuja, S. (ed), pp. 98-119, Elsevier, Waltham.

Nava-Ocampo, M.F., Bucs, S.S., Farinha, A.S.F., Son, M., Logan, B.E. and Vrouwenvelder, J.S. (2020) Sacrificial coating development for biofouling control in membrane systems. *Desalination* 496, 114650.

Ngene, I.S., Lammertink, R.G.H., Kemperman, A.J.B., van de Ven, W.J.C., Wessels, L.P., Wessling, M. and Van der Meer, W.G.J. (2010) CO<sub>2</sub> Nucleation in Membrane Spacer Channels Remove Biofilms and Fouling Deposits. *Industrial & Engineering Chemistry Research* 49(20), 10034-10039.

Nya, E.J. (2015) Biofilms and biofouling - Cost and effect on drinking water quality for human development.pdf. *Journal of Global Biosciences* 4(2), 7.

Öchsner, A. (2016) *Elasto-Plasticity of Frame Structure Elements: Modeling and Simulation of Rods and Beams*, Springer, Berlin, Heidelberg.

Oh, H.-S., Tan, C.H., Low, J.H., Rzechowicz, M., Siddiqui, M.F., Winters, H., Kjelleberg, S., Fane, A.G. and Rice, S.A. (2017) Quorum quenching bacteria can be used to inhibit the biofouling of reverse osmosis membranes. *Water Research* 112, 29-37.

Okabe, S., Hiratia, K., Ozawa, Y. and Watanabe, Y. (1996) Spatial microbial distributions of nitrifiers and heterotrophs in mixed-population biofilms. *Biotechnology and Bioengineering* 50(1), 24-35.

Okabe, S., Kuroda, H. and Watanabe, Y. (1998) Significance of biofilm structure on transport of inert particulates into biofilms. *Water Science and Technology* 38(8), 163-170.

Olivieri, A.W., Pecson, B., Crook, J. and Hultquist, R. (2020) *Advances in Chemical Pollution, Environmental Management and Protection*. Verlicchi, P. (ed), pp. 65-111, Elsevier.

Özkaya, N., Nordin, M., Goldsheyder, D. and Leger, D. (2012) Mechanical Properties of Biological Tissues. 221-236.

P. Hiemstra, J.v.P., B. Rietman, J. Verdouw. (1999) *Aerobic versus anaerobic nanofiltration: fouling of membranes*, Long Beach, CA,.

Pal, P. (2017) *Industrial Water Treatment Process Technology*. Pal, P. (ed), pp. 173-242, Butterworth-Heinemann.

Panagopoulos, A., Haralambous, K.-J. and Loizidou, M. (2019) Desalination brine disposal methods and treatment technologies - A review. *Science of The Total Environment* 693, 133545.

Paramonova, E., de Jong, E.D., Krom, B.P., van der Mei, H.C., Busscher, H.J. and Sharma, P.K. (2007) Low-load compression testing: a novel way of measuring biofilm thickness. *Applied and Environmental Microbiology* 73(21), 7023-7028.

Paramonova, E., Kalmykova, O.J., van der Mei, H.C., Busscher, H.J. and Sharma, P.K. (2009) Impact of hydrodynamics on oral biofilm strength. *Journal of Dental Research* 88(10), 922-926.

Pearce, G.K. (2008) A cost optimization study of flux and fouling rate for UF in the water industry. *Water Supply* 8(1), 113-120.

Peiris, R.H., Jaklewicz, M., Budman, H., Legge, R.L. and Moresoli, C. (2013) Assessing the role of feed water constituents in irreversible membrane fouling of pilot-scale ultrafiltration drinking water treatment systems. *Water Research* 47(10), 3364-3374.

Peterson, B.W., Busscher, H.J., Sharma, P.K. and van der Mei, H.C. (2012) Environmental and centrifugal factors influencing the visco-elastic properties of oral biofilms in vitro. *Biofouling* 28(9), 913-920.



- Peterson, B.W., He, Y., Ren, Y., Zerdoum, A., Libera, M.R., Sharma, P.K., van Winkelhoff, A.J., Neut, D., Stoodley, P., van der Mei, H.C. and Busscher, H.J. (2015) Viscoelasticity of biofilms and their recalcitrance to mechanical and chemical challenges. *FEMS Microbiology Reviews* 39(2), 234-245.
- Phani, K.K. and Niyogi, S.K. (1987) Young's modulus of porous brittle solids. *Journal of Materials Science* 22(1), 257-263.
- Pichardo-Romero, D., Garcia-Arce, Z.P., Zavala-Ramírez, A. and Castro-Muñoz, R. (2020) Current Advances in Biofouling Mitigation in Membranes for Water Treatment: An Overview. *Processes* (8).
- Picioreanu, C., Blauert, F., Horn, H. and Wagner, M. (2018) Determination of mechanical properties of biofilms by modelling the deformation measured using optical coherence tomography. *Water Research* 145, 588-598.
- Picioreanu, C., Vrouwenvelder, J.S. and van Loosdrecht, M.C.M. (2009) Three-dimensional modeling of biofouling and fluid dynamics in feed spacer channels of membrane devices. *Journal of Membrane Science* 345(1), 340-354.
- Pintelon, T.R.R., Picioreanu, C., Loosdrecht, M.C.M.v. and Johns, M.L. (2012) The effect of biofilm permeability on bio-clogging of porous media. *Biotechnology and Bioengineering* 109(4), 1031-1042.
- Poorasgari, E., Farsi, A. and Christensen, M.L. (2016) Fouling of a microfiltration membrane by humic-like substances: a mathematical approach to modelling permeate flux and membrane retention. *Water Science and Technology* 73(12), 3033-3040.
- Poorasgari, E., Vistisen Bugge, T., Lykkegaard Christensen, M. and Koustrup Jørgensen, M. (2015) Compressibility of fouling layers in membrane bioreactors. *Journal of Membrane Science* 475, 65-70.
- Porcelli, N. and Judd, S. (2010a) Chemical cleaning of potable water membranes: A review. *Separation and Purification Technology* 71(2), 137-143.
- Porcelli, N. and Judd, S. (2010b) Chemical cleaning of potable water membranes: The cost benefit of optimisation. *Water Research* 44(5), 1389-1398.
- Prihasto, N., Liu, Q.-F. and Kim, S.-H. (2009) Pre-treatment strategies for seawater desalination by reverse osmosis system. *Desalination* 249(1), 308-316.
- Pronk, M., Neu, T.R., van Loosdrecht, M.C.M. and Lin, Y.M. (2017) The acid soluble extracellular polymeric substance of aerobic granular sludge dominated by *Deffluviicoccus* sp. *Water Research* 122, 148-158.
- Pronk, W., Ding, A., Morgenroth, E., Derlon, N., Desmond, P., Burkhardt, M., Wu, B. and Fane, A.G. (2019) Gravity-driven membrane filtration for water and wastewater treatment: A review. *Water Research* 149, 553-565.
- R.D. Noble, S.A.S. (1995) *Membrane Separations Technology: Principles and Applications*, Elsevier Science.

Radu, A.I., Bergwerff, L., van Loosdrecht, M.C.M. and Picioreanu, C. (2015a) Combined biofouling and scaling in membrane feed channels: a new modeling approach. *Biofouling* 31(1), 83-100.

Radu, A.I., van Steen, M.S.H., Vrouwenvelder, J.S., van Loosdrecht, M.C.M. and Picioreanu, C. (2014) Spacer geometry and particle deposition in spiral wound membrane feed channels. *Water Research* 64, 160-176.

Radu, A.I., Vrouwenvelder, J.S., van Loosdrecht, M.C.M. and Picioreanu, C. (2010) Modeling the effect of biofilm formation on reverse osmosis performance: Flux, feed channel pressure drop and solute passage. *Journal of Membrane Science* 365(1), 1-15.

Radu, M., Bou-Said, B. and Cicone, T. (2015b) Experimental determination of viscoelastic properties of a highly compressible porous materials imbibed with water. *Mechanics & Industry* 16(6), 606.

Rana, D. and Matsuura, T. (2010) Surface Modifications for Antifouling Membranes. *Chemical Reviews* 110(4), 2448-2471.

Richards, R. (2000) *Principles of Solid Mechanics*, CRC Press, Florida, US.

Rmaile, A., Carugo, D., Capretto, L., Zhang, X., Wharton, J.A., Thurner, P.J., Aspiras, M., Ward, M. and Stoodley, P. (2013) Microbial tribology and disruption of dental plaque bacterial biofilms. *Wear* 306(1-2), 276-284.

Rosenthal, A.F., Griffin, J.S., Wagner, M., Packman, A.I., Balogun, O. and Wells, G.F. (2018) Morphological analysis of pore size and connectivity in a thick mixed-culture biofilm. *Biotechnology and Bioengineering* 115(9), 2268–2279.

Ryshkewitch, E. (1953) Compression Strength of Porous Sintered Alumina and Zirconia. *Journal of the American Ceramic Society* 36(2), 65-68.

Safari, A., Tukovic, Z., Walter, M., Casey, E. and Ivankovic, A. (2015) Mechanical properties of a mature biofilm from a wastewater system: from microscale to macroscale level. *Biofouling* 31(8), 651-664.

Sanawar, H., Bucs, S.S., Pot, M.A., Zlopasa, J., Farhat, N.M., Witkamp, G.J., Kruithof, J.C., van Loosdrecht, M.C.M. and Vrouwenvelder, J.S. (2019) Pilot-Scale Assessment of Urea as a Chemical Cleaning Agent for Biofouling Control in Spiral-Wound Reverse Osmosis Membrane Elements. *Membranes (Basel)* 9(9).

Sanawar, H., Pinel, I., Farhat, N.M., Bucs, S., Zlopasa, J., Kruithof, J.C., Witkamp, G.J., van Loosdrecht, M.C.M. and Vrouwenvelder, H.S. (2018) Enhanced biofilm solubilization by urea in reverse osmosis membrane systems. *Water Research* 1.

Sanawar, H., Siddiqui, A., Bucs, S.S., Farhat, N.M., van Loosdrecht, M.C.M., Kruithof, J.C. and Vrouwenvelder, J.S. (2017) Applicability of short-term accelerated biofouling studies to predict long-term biofouling accumulation in reverse osmosis membrane systems. *Desalination and Water Treatment* 97, 72-78.

Saqib, J. and Aljundi, I.H. (2016) Membrane fouling and modification using surface treatment and layer-by-layer assembly of polyelectrolytes: State-of-the-art review. *Journal of Water Process Engineering* 11, 68-87.

Schäfer, A.I., Fane, A.G. and Waite, T.D. (2001) Cost factors and chemical pretreatment effects in the membrane filtration of waters containing natural organic matter. *Water Research* 35(6), 1509-1517.

Seviour, T., Derlon, N., Ducholm, M.S., Flemming, H.-C., Girbal-Neuhauser, E., Horn, H., Kjelleberg, S., van Loosdrecht, M.C.M., Lotti, T., Malpei, M.F., Nerenberg, R., Neu, T.R., Paul, E., Yu, H. and Lin, Y. (2019) Extracellular polymeric substances of biofilms: Suffering from an identity crisis. *Water Research* 151, 1-7.

Shao, S., Wang, Y., Shi, D., Zhang, X., Tang, C.Y., Liu, Z. and Li, J. (2018) Biofouling in ultrafiltration process for drinking water treatment and its control by chlorinated-water and pure water backwashing. *Science of The Total Environment* 644, 306-314.

Shen, Y., Huang, P.C., Huang, C., Sun, P., Monroy, G.L., Wu, W., Lin, J., Espinosa-Marzal, R.M., Boppart, S.A., Liu, W.T. and Nguyen, T.H. (2018) Effect of divalent ions and a polyphosphate on composition, structure, and stiffness of simulated drinking water biofilms. *NPJ Biofilms Microbiomes* 4, 15.

Shi, X., Tal, G., Hankins, N.P. and Gitis, V. (2014) Fouling and cleaning of ultrafiltration membranes: A review. *Journal of Water Process Engineering* 1, 121-138.

Siddiqui, A., Pinel, I., Prest, E.I., Bucs, S.S., van Loosdrecht, M.C.M., Kruithof, J.C. and Vrouwenvelder, J.S. (2017) Application of DBNPA dosage for biofouling control in spiral wound membrane systems. *Desalination and Water Treatment* 68, 12-22.

Silva, T.L.D., Sánchez-Román, R.M., Queluz, J.G.T. and Pletsch, T.A. (2020) *Advances in Chemical Pollution, Environmental Management and Protection*. Verlicchi, P. (ed), pp. 1-31, Elsevier.

Simon Vrouwenvelder, J., Kruithof, J. and van Loosdrecht, M. (2011) *Biofouling of spiral wound membrane systems*, IWA Publishing.

Statistica (2019a) Energy cost in EU countries.

Statistica (2019b) Salary indicator in EU countries.

Stoodley, P., Zbigniew Lewandowski, John D. Boyle and Lappin-Scott, H.M. (1999) Structural deformation of bacterial biofilms caused by short-term fluctuations in fluid shear: An in situ investigation of biofilm rheology. *Biotechnology and Bioengineering* 65(1).

Sweity, A., Ying, W., Ali-Shtayeh, M.S., Yang, F., Bick, A., Oron, G. and Herzberg, M. (2011) Relation between EPS adherence, viscoelastic properties, and MBR operation: Biofouling study with QCM-D. *Water Research* 45(19), 6430-6440.

- Tang, C.Y., Chong, T.H. and Fane, A.G. (2011) Colloidal interactions and fouling of NF and RO membranes: A review. *Advances in Colloid and Interface Science* 164(1), 126-143.
- Tang, F., Hu, H.Y., Sun, L.J., Sun, Y.X., Shi, N. and Crittenden, J.C. (2016) Fouling characteristics of reverse osmosis membranes at different positions of a full-scale plant for municipal wastewater reclamation. *Water Research* 90, 329-336.
- Tew, X.W., Fraser-Miller, S.J., Gordon, K.C. and Morison, K.R. (2019) A comparison between laboratory and industrial fouling of reverse osmosis membranes used to concentrate milk. *Food and Bioproducts Processing* 114, 113-121.
- Thompson, J., Lin, N., Lyster, E., Arbel, R., Knoell, T., Gilron, J. and Cohen, Y. (2012) RO membrane mineral scaling in the presence of a biofilm. *Journal of Membrane Science* 415-416, 181-191.
- Towler, B.W., Rupp, C.J., Cunningham, A.B. and Stoodley, P. (2003) Viscoelastic properties of a mixed culture biofilm from rheometer creep analysis. *Biofouling* 19(5), 279-285.
- Trägårdh, G. (1989) Membrane cleaning. *Desalination* 71(3), 325-335.
- Valladares Linares, R., Fortunato, L., Farhat, N.M., Bucs, S.S., Staal, M., Fridjonsson, E.O., Johns, M.L., Vrouwenvelder, J.S. and Leiknes, T. (2016) Mini-review: novel non-destructive in situ biofilm characterization techniques in membrane systems. *Desalination and Water Treatment* 57(48-49), 22894-22901.
- Valladares Linares, R., Wexler, A.D., Bucs, S.S., Dreszer, C., Zwijnenburg, A., Flemming, H.C., Kruithof, J.C. and Vrouwenvelder, J.S. (2015) Compaction and relaxation of biofilms. *Desalination and Water Treatment* 57(28), 12902-12914.
- van de Lisdonk, C.A.C., Rietman, B.M., Heijman, S.G.J., Sterk, G.R. and Schippers, J.C. (2001) Prediction of supersaturation and monitoring of scaling in reverse osmosis and nanofiltration membrane systems. *Desalination* 138(1), 259-270.
- van den Broek, W.B.P., Boorsma, M.J., Huiting, H., Dusamos, M.G. and van Agtmaal, S. (2010) Prevention of Biofouling in Industrial RO Systems: Experiences with Peracetic Acid. *Water Practice and Technology* 5(2).
- van Paassen, J.A.M., Kruithof, J.C., Bakker, S.M. and Kegel, F.S. (1998) Integrated multi-objective membrane systems for surface water treatment: pre-treatment of nanofiltration by riverbank filtration and conventional ground water treatment. *Desalination* 118(1), 239-248.
- Vanoppen, M., Stoffels, G., Buffel, J., De Gussemé, B. and Verliefde, A.R.D. (2016) A hybrid IEX-RO process with brine recycling for increased RO recovery without chemical addition: A pilot-scale study. *Desalination* 394, 185-194.

- Vanoppen, M., Stoffels, G., Demuytere, C., Bleyaert, W. and Verliefde, A.R.D. (2015) Increasing RO efficiency by chemical-free ion-exchange and Donnan dialysis: Principles and practical implications. *Water Research* 80, 59-70.
- Violleau, D., Essis-Tome, H., Habarou, H., Croud, J.P. and Pontie, M. (2005) Fouling studies of a polyamide nanofiltration membrane by selected natural organic matter: an analytical approach. *Desalination* 173, 223-238.
- Voutchkov, N. (2017) Pretreatment for Reverse Osmosis Desalination. Voutchkov, N. (ed), pp. 43-64, Elsevier, Amsterdam.
- Vrouwenvelder, H.S., van Paassen, J.A.M., Folmer, H.C., Hofman, J.A.M.H., Nederlof, M.M. and van der Kooij, D. (1998) Biofouling of membranes for drinking water production. *Desalination* 118(1), 157-166.
- Vrouwenvelder, J.S., Beyer, F., Dahmani, K., Hasan, N., Galjaard, G., Kruithof, J.C. and Van Loosdrecht, M.C. (2010a) Phosphate limitation to control biofouling. *Water Research* 44(11), 3454-3466.
- Vrouwenvelder, J.S., Buitter, J., Riviere, M., van der Meer, W.G.J., van Loosdrecht, M.C.M. and Kruithof, J.C. (2010b) Impact of flow regime on pressure drop increase and biomass accumulation and morphology in membrane systems. *Water Research* 44(3), 689-702.
- Vrouwenvelder, J.S., Hinrichs, C., Van der Meer, W.G.J., Van Loosdrecht, M.C.M. and Kruithof, J.C. (2009) Pressure drop increase by biofilm accumulation in spiral wound RO and NF membrane systems: role of substrate concentration, flow velocity, substrate load and flow direction. *Biofouling* 25(6), 543-555.
- Vrouwenvelder, J.S., Manolarakis, S.A., van der Hoek, J.P., van Paassen, J.A., van der Meer, W.G., van Agtmaal, J.M., Prummel, H.D., Kruithof, J.C. and van Loosdrecht, M.C. (2008) Quantitative biofouling diagnosis in full scale nanofiltration and reverse osmosis installations. *Water Research* 42(19), 4856-4868.
- Vrouwenvelder, J.S., van Paassen, J.A.M., Wessels, L.P., van Dam, A.F. and Bakker, S.M. (2006) The Membrane Fouling Simulator: A practical tool for fouling prediction and control. *Journal of Membrane Science* 281(1), 316-324.
- Wagner, M. and Horn, H. (2017) Optical coherence tomography in biofilm research: A comprehensive review. *Biotechnology and Bioengineering* 114(7), 1386-1402.
- Wagner, M., Taherzadeh, D., Haisch, C. and Horn, H. (2010) Investigation of the mesoscale structure and volumetric features of biofilms using optical coherence tomography. *Biotechnology and Bioengineering* 107(5), 844-853.
- Wang, Y.-N. and Tang, C.Y. (2011) Protein fouling of nanofiltration, reverse osmosis, and ultrafiltration membranes—The role of hydrodynamic conditions, solution chemistry, and membrane properties. *Journal of Membrane Science* 376(1), 275-282.

- Wang, Y., Fortunato, L., Jeong, S. and Leiknes, T. (2017) Gravity-driven membrane system for secondary wastewater effluent treatment: Filtration performance and fouling characterization. *Separation and Purification Technology* 184, 26-33.
- Warsinger, D.M., Swaminathan, J., Guillen-Burrieza, E., Arafat, H.A. and Lienhard V, J.H. (2015) Scaling and fouling in membrane distillation for desalination applications: A review. *Desalination* 356, 294-313.
- Wibisono, Y., Cornelissen, E.R., Kemperman, A.J.B., van der Meer, W.G.J. and Nijmeijer, K. (2014) Two-phase flow in membrane processes: A technology with a future. *Journal of Membrane Science* 453, 566-602.
- Wibisono, Y., El Obied, K.E., Cornelissen, E.R., Kemperman, A.J.B. and Nijmeijer, K. (2015) Biofouling removal in spiral-wound nanofiltration elements using two-phase flow cleaning. *Journal of Membrane Science* 475, 131-146.
- Wilson, R., Fazel, M., Jarrige, S. and Chesters, S. (2013) Air bubbles enhance membrane cleaning: A future perspective, Tianjin, China.
- Xie, M., Lee, J., Nghiem, L.D. and Elimelech, M. (2015) Role of pressure in organic fouling in forward osmosis and reverse osmosis. *J. Memb. Sci* 493, 748-754.
- Yanar, N., Son, M., Yang, E., Kim, Y., Park, H., Nam, S.-E. and Choi, H. (2018) Investigation of the performance behavior of a forward osmosis membrane system using various feed spacer materials fabricated by 3D printing technique. *Chemosphere* 202, 708-715.
- Yeon, K.-M., Cheong, W.-S., Oh, H.-S., Lee, W.-N., Hwang, B.-K., Lee, C.-H., Beyenal, H. and Lewandowski, Z. (2009) Quorum Sensing: A New Biofouling Control Paradigm in a Membrane Bioreactor for Advanced Wastewater Treatment. *Environmental Science & Technology* 43(2), 380-385.
- Yu, T., Meng, L., Zhao, Q.B., Shi, Y., Hu, H.Y. and Lu, Y. (2017) Effects of chemical cleaning on RO membrane inorganic, organic and microbial foulant removal in a full-scale plant for municipal wastewater reclamation. *Water Research* 113, 1-10.
- Zhang, T.C. and Bishop, P.L. (1994) Density, porosity, and pore structure of biofilms. *Water Research* 28(11), 2267-2277.
- Zhang, T.C., Bishop, P.L. and Gibbs, J.T. (1994) Effect of roughness and thickness of biofilms on external mass transfer resistance. In: *Critical Issues in Water and Wastewater Treatment*. National Conference in Environmental Engineering. New York: ASCE., 593-600.
- Zhao, S., Liao, Z., Fane, A., Li, J., Tang, C., Zheng, C., Lin, J. and Kong, L. (2021) Engineering antifouling reverse osmosis membranes: A review. *Desalination* 499, 114857.

## References

---

Zhu, A., Rahardianto, A., Christofides, P.D. and Cohen, Y. (2010) Reverse osmosis desalination with high permeability membranes — Cost optimization and research needs. *Desalination and Water Treatment* 15(1-3), 256-266.

Zondervan, E., Betlem, B.H.L., Blankert, B. and Roffel, B. (2008) Modeling and optimization of a sequence of chemical cleaning cycles in dead-end ultrafiltration. *Journal of Membrane Science* 308(1), 207-217.

# Acknowledgments

After more than four years of membrane and fouling research, it is time to thank people who contributed to this work.

First of all, I would like to express my gratitude to all the **EU tax payers** who made this EU-funded program possible. I also would like to thank my promoters for offering me this PhD opportunity. **Cristian**, I learned a lot from working with you and your fantastic eyes on details. Our friendship went beyond the formal and academic works. I truly enjoyed our travels to Iran and Romania together. **Mark**, you always supported me from application process to the final defence. Meetings with you always stimulated my ambitions and motivation and helped me to keep the long-term goals in perspective. I really appreciate our informal discussions on the wide range of topics from water treatment and membranes to politics and society.

I would like to thank my UGent supervisor, Arne! **Arne**, thanks for being always there when I needed you. I really enjoyed working with you and learned a lot from your practical insights. I really appreciate your efforts to arrange all the administrations of the double degree. My sincere thanks also to **Emile Cornelissen** who has been extensively involved in this research. Emile, this thesis gained valuable insights from your inputs.

During my PhD, I had the chance to spend some fantastic months at EAWAG, Switzerland. I would like to thank **Eberhard Morgenroth!** Eberhard, I truly appreciate your dedication and involvement in this project and introducing me to the concept of “outline of the paper”. I still use it every day. I also would like to thank **Peter Desmond** for facilitating the research stay and helping with OCT imaging. My dearest gratitude goes to **Nico Derlon** for his enthusiasm, unlimited trust and full support during my stay at EAWAG. Nico, our friendship went beyond the academic relationship! I still miss those Champions League games in the Irish pub in Zurich.

During my PhD I was lucky to collaborate and interact with several industrial and academic partners. Particularly, I would like to thank **Hans Vrouwenvelder** (KAUST); **Özgür Gölbasi**, **David Moed** and **Martin Pot** (Evides Industriewater); **Marc Slagt** and **Jochem Henkel** (Dupont Water Solutions); **Celestin Claeys** (De Watergroep); **David van Lennep** (Lenntech) and **Sjack van Agtmaal** (BCF Systems).

I also had the chance to supervise master and bachelor students, therefore, I would like to thank **Pakyien Au** and **Amir Assadbeigi** for all of their help and dedications.

I absolutely enjoyed my time during my PhD and this is mainly because of the great colleagues that I met and the fantastic friends that I made.

**Jure**, you were my office mate, my neighbour and above all my mate! You are a wonderful person! A man with stories! We had fantastic long talks on the bike rides about books, philosophy, politics, football and science! You never ceased to surprise me with your mind-blowing observations and comments. We cycled almost every day for around 2 years and if I want to be totally honest, this is the things that I've missed the most. Thanks for everything.



**Gerben**, our friendship started late but grew fast and rooted deep. You are a true friend, actually more than a friend. You are my mate. You are fantastic in making people reflecting on themselves. This is a very rare quality and I cannot express how much I appreciate it. Thanks for all those quality time we spent together.

I would like to express my dearest gratitude to **Philipp Kehrein** for being such a wonderful friend during my PhD! Phil, we shared lots of ups and downs together and we had a chance to work on a fantastic collaborative project. We spent several good occasions together, from the secondments in Ghent to the conference in Venice, I'm happy that I shared those moments with you.

I would like also express my deep appreciation to **Robbert Kleerebezem** for always showing willingness to listen, help and keeping a positive outlook. I would like to thank my dear office mate and friend, **Viktor Haaksman** for listening and sharing all those amazing but crazy stories of B2.210.

During my time at Delft, we often had a very good lunch group. I would like to thank **Diana, Michel and Jelmer** for all those fantastic lunches we had with heavy and abstract discussions about random topics. It was always a detachment from work and very helpful for me. I would also like to thank **Ingrid** for all those enjoyable coffee breaks which we shared our feelings about being the EBT's outsiders.

Among all the groups that I've worked in, EBT is the most special one to me. I would like to express my gratitude to all the **EBT current and former group members** who made this fantastic and unique atmosphere. Particularly, **Miranda, Michele and Monica** for their kind supports during my PhD.

I had a chance to spend a research stay at PAINT group at Ghent University. I would like to thank **Arnout D'Haese, John Buffel and Marjolein Vanoppen** for their valuable contributions to this work. Your inputs definitely improved the quality of this project. I would like also to express my deepest gratitude to my dear friend **Sepide** for the time she spent with us in Ghent. Sepide, you bring so much joy with you.

I would like to acknowledge **SuPER-W consortium** for coordinating the project. I met several good colleagues and friends through this program. I would like to thank **Marco Hartl** for being such a wonderful friend. Marco, we had amazing times in Ghent and you were a big part of it. I would like to thank **all the ESRs** within SuPER-W program for making all those long meetings very more enjoyable. My special thanks goes to **Kazem, Alexandra, Kasper and Mojtaba** for all those fantastic moments during SUPER-W project.

این موفقیت بدون حمایت و محبت‌های خانواده‌ام مخصوصاً مادرم ممکن نبود. **مامان**، بابت همه‌ی زحماتی که در تمام این سال‌ها کشیدی بینهایت ازت ممنونم. همینطور پدر بزرگ مهربانم که حامی و مشوق همیشگی من بوده و هست. **آقاچون**، حضور شما همیشه باعث دلگرمی من هست. حتی این سالهای اخیر که از هم دور هستیم. قدردان همه‌ی زحماتت هستیم.

And finally to **Donya**, you know this PhD was not possible without you! From the interview process to the final editing of the book! You were always there for me with your incredible patience and support! I'm the luckiest and happiest person when I'm with you...

Morez Jafari

Rotterdam, September 2021

# List of publications

**Jafari, M.**, Desmond, P., van Loosdrecht, M.C.M., Derlon, N., Morgenroth, E. and Picioreanu, C. (2018) Effect of biofilm structural deformation on hydraulic resistance during ultrafiltration: A numerical and experimental study. *Water Research* 145, 375-387.

**Jafari, M.**, Derlon, N., Desmond, P., van Loosdrecht, M.C.M., Morgenroth, E. and Picioreanu, C. (2019) Biofilm compressibility in ultrafiltration: A relation between biofilm morphology, mechanics and hydraulic resistance. *Water Research* 157, 335-345.

**Jafari, M.**, D'Haese, A., Zlopasa, J., Cornelissen, E.R., Vrouwenvelder, J.S., Verbeke, K., Verliefe, A., van Loosdrecht, M.C.M. and Picioreanu, C. (2020) A comparison between chemical cleaning efficiency in lab-scale and full-scale reverse osmosis membranes: Role of extracellular polymeric substances (EPS). *Journal of Membrane Science* 609, 118189.

**Jafari, M.**, Vanoppen, M., van Agtmaal, J.M.C., Cornelissen, E.R., Vrouwenvelder, J.S., Verliefe, A., van Loosdrecht, M.C.M. and Picioreanu, C. (2021) Cost of fouling in full-scale reverse osmosis and nanofiltration installations in the Netherlands. *Desalination* 500, 114865.

Kehrein, P., **Jafari, M.**, Slagt, M., Cornelissen, E., Posada, J., Osseweijer, P., van Loosdrecht, M. (2021) A techno-economic analysis of membrane-based advanced treatment processes for different municipal wastewater reuse types. *Journal of Water Reuse and Desalination (IWA)*. *Accepted- Chapter 7 of this thesis.*

## *Manuscript under review*

**Jafari, M.**, Golbasi, O., Zlopasa, J., Cornelissen, E.R., Vrouwenvelder, J.S., Verliefe, A., van Loosdrecht, M.C.M. and Picioreanu, C. Bringing laboratory to the full-scale RO installation: A novel approach for membrane fouling analysis and CIP protocol development. *Chapter 5 of this thesis.*





## About the author

Mohammadreza (Morez) Jafari Eshlaghi was born on 19 November 1989 in Tehran, Iran. In 2009 he started his study at the University of Tehran, becoming a chemical Engineer in 2012. Later, he worked for less than 2 years in oil and gas sector and also he was active as a private tutor of Mathematics. In 2014, he started his M.Sc. in chemical and process engineering at University of Bologna, Italy where in 2016 he could successfully obtain his M.Sc. in Chemical and process engineering. During this time, he spend 3 months in France at Université de Technologie de Compiègne, France working on modelling of sugar caking during transport. He also performed his M.Sc. thesis on phosphate recovery from wastewater using Electro-dialysis (ED) at Delft University of Technology, The Netherlands. In December 2016, he started his PhD under Marie Skłodowska–Curie program at Delft university of Technology (Environmental Biotechnology group) in collaboration with Ghent University (Particle and Interface Technology Group) under supervision of Mark Van Loosdrecht, Cristian Picioreanu and Arne Verliefde. The research of his PhD was focus on the importance fouling properties and their interaction in membrane processes for water treatment. During his PhD, he spent around 3 months in Swiss Federal Institute of Aquatic Science and Technology (EAWAG), Switzerland working on optimization dead-end Ultrafiltration membrane.

He made a switch from academia to industry as he currently working as a R&D project manager at the drinking water company PWN technologies.

This doctoral research has been carried out in the context of agreement on joint doctoral supervision between Ghent University, Belgium and Delft University of Technology, the Netherlands. The research project was funded by European Union's Horizon 2020 research and innovation programme, under Marie Skłodowska–Curie Grant Agreement no. 676070.